

Development of enhanced furin inhibitors with
reduced toxicity as potential broad spectrum
antiviral drugs

Entwicklung optimierter Furinhemmstoffe mit
reduzierter Toxizität als potenzielle antivirale
Wirkstoffe mit breitem Wirkungsspektrum

Dissertation

zur

Erlangung des Doktorgrades

der Naturwissenschaften

(Dr. rer. nat.)

dem

Fachbereich Pharmazie der

PHILIPPS-UNIVERSITÄT MARBURG

vorgelegt von

Thuy Van Lam van

aus Dortmund

Marburg an der Lahn, 2021

Erstgutachter: **Prof. Dr. Torsten Steinmetzer**

Zweitgutachter: **Prof. Dr. Eva Böttcher-Friebertshäuser**

Eingereicht am 27.07.2021

Tag der mündlichen Prüfung: 17.09.2021

Hochschulkennziffer: 1180

*Dedicated to
my parents*

Table of contents

List of publications.....	III
Share of author contributions	IV
Abbreviations	V
Summary	1
Zusammenfassung.....	3
1 Introduction	5
1.1 The family of proprotein convertases.....	5
1.2 Furin	8
1.2.1 Autoactivation of furin.....	9
1.2.2 Furin-catalyzed physiological and pathological processes	10
1.3 Coronaviruses	13
1.3.1 Genome and structure of SARS-CoV-2.....	16
1.3.2 Life cycle of SARS-CoV-2	17
1.3.3 Viral entry – the structure and furin cleavage site of the spike protein	19
1.4 Furin inhibitors.....	21
1.5 Crystal structures of furin in complex with inhibitors.....	21
1.6 Toxicity study in mice.....	24
2 Aim of the thesis	25
3 Results and discussion.....	27
3.1 Novel macrocyclic inhibitors of the basic proprotein convertase furin	27
3.2 Development of improved furin inhibitors with reduced basicity residues showing potent antiviral activity against SARS-CoV-2 in human airway cells.....	31
3.3 Cleavage of SARS-CoV-2 S1/S2 and S2' site fluorescence resonance energy transfer (FRET)-substrates by furin.....	37
3.3.1 S1/S2 site FRET-substrates	37
3.3.2 S2' site FRET-substrates	39
3.4 Novel AMC substrates for basic proprotein convertases.....	41
4 Publications	45
4.1 Design, synthesis, and characterization of macrocyclic inhibitors of the proprotein convertase furin.....	45
4.2 The basicity makes the difference – Improved canavanine-derived inhibitors of the proprotein convertase furin.....	65
4.3 TMPRSS2 and furin are both essential for proteolytic activation of SARS-CoV-2 in human airway cells	98

4.4	Design, synthesis, and characterization of novel fluorogenic substrates of proprotein convertases furin, PC1, PC2, PC5, and PC7	115
5	Conclusion and future perspectives	138
6	References.....	141
7	Statutory declaration	154
8	Acknowledgment	155
9	Curriculum vitae	157

List of publications

Thuy Van Lam van, Teodora Ivanova, Kornelia Harges, Miriam Ruth Heindl, Rory E. Morty, Eva Böttcher-Friebertshäuser, Iris Lindberg, Manuel E. Than, Sven O. Dahms, and Torsten Steinmetzer

Design, synthesis, and characterization of macrocyclic inhibitors of the proprotein convertase furin

***ChemMedChem*. 2019**, 14(6), 673-685

Thuy Van Lam van, Miriam Ruth Heindl, Christine Schlutt, Eva Böttcher-Friebertshäuser, Ralf Bartenschlager, Gerhard Klebe, Hans Brandstetter, Sven O. Dahms, and Torsten Steinmetzer
The basicity makes the difference – Improved canavanine-derived inhibitors of the proprotein convertase furin

***ACS Medicinal Chemistry Letters*. 2021**, 12, 3, 426–432

Dorothea Bestle*, Miriam Ruth Heindl*, Hannah Limburg*, **Thuy Van Lam van**, Oliver Pilgram, Hong Moulton, David A. Stein, Kornelia Harges, Markus Eickmann, Olga Dolnik, Cornelius Rohde, Hans-Dieter Klenk, Wolfgang Garten, Torsten Steinmetzer, and Eva Böttcher-Friebertshäuser

TMPRSS2 and furin are both essential for proteolytic activation of SARS-CoV-2 in human airway cells

***Life Science Alliance*. 2020**, 3(9)

Thuy Van Lam van, Teodora Ivanova, Iris Lindberg, Eva Böttcher-Friebertshäuser, Torsten Steinmetzer, and Kornelia Harges

Design, synthesis, and characterization of novel fluorogenic substrates of proprotein convertases furin, PC1, PC2, PC5, and PC7

(Manuscript in preparation; planned for the Journal: ***Analytical Biochemistry***)

*These authors contributed equally to this work.

Share of author contributions

Publication	Authors	Estimated equity ratio [%]	Submitted / Accepted
Design, synthesis, and characterization of macrocyclic inhibitors of the proprotein convertase furin <i>ChemMedChem</i> . 2019, 14(6), 673-685	Lam van, T.V. ; Ivanova, T.; Harges, K.; Heindl, M.R.; Morty, R.E.; Böttcher-Friebertshäuser, E.; Lindberg, I.; Than, M.E.; Dahms, S.O.; Steinmetzer, T.	55	Accepted
The basicity makes the difference – Improved canavanine-derived inhibitors of the proprotein convertase furin <i>ACS Medicinal Chemistry Letters</i> . 2021, 12, 3, 426–432	Lam van, T.V. ; Heindl, M.R.; Schlutt, C.; Böttcher-Friebertshäuser, E.; Bartenschlager, R.; Klebe, G.; Brandstetter, H.; Dahms, S.O.; Steinmetzer, T.	60	Accepted
TMPRSS2 and furin are both essential for proteolytic activation of SARS-CoV-2 in human airway cells <i>Life Science Alliance</i> . 2020, 3(9)	Bestle, D.*; Heindl, M.R.*; Limburg, H.*; Lam van, T.V. ; Pilgram, O.; Moulton, H.; Stein, D.A.; Harges, K.; Eickmann, M.; Dolnik, O.; Rohde, C.; Klenk, H.-D.; Garten, W.; Steinmetzer, T.; Böttcher-Friebertshäuser, E.	5	Accepted
Design, synthesis, and characterization of novel fluorogenic substrates of proprotein convertases furin, PC1, PC2, PC5, and PC7 (planned for the Journal: <i>Analytical Biochemistry</i> .)	Lam van, T.V. ; Ivanova, T.; Lindberg, I.; Böttcher-Friebertshäuser, E.; Steinmetzer, T.; Harges, K.	65	Manuscript in preparation

*These authors contributed equally to this work.

Signature candidate

Signature supervisor

Abbreviations

For units the international system of units has been used. For the proteinogenic amino acids, the one and three letter codes recommended by IUPAC-IUBMM *Joint Commission on Biochemical Nomenclature* (JCBN) were applied. Unless otherwise indicated, all amino acids and derivatives are L-configured.

4-Amba	4-amidinobenzylamide
6-Cl-HOBt	6-Chloro-1-hydroxybenzotriazole
Ac	acetyl
ACE-2	Angiotensin-converting enzyme 2
ACTH	adrenocorticotrophic hormone
AMC	7-amino-4-methylcoumarin
AMe	aminomethyl
Cav	canavanine
CMK	chloromethyl ketone
CoV	coronavirus
COVID-19	Coronavirus disease 2019
CPP	cell-penetrating peptide
DCM	dichloromethane
Dde	1-(4,4-dimethyl-2,6-dioxocyclohex-1-ylidene)ethyl
DENV-2	Dengue virus serotype 2
DIPEA	<i>N,N</i> -Diisopropylethylamine
DMF	<i>N,N</i> -Dimethylformamide
DMSO	Dimethyl sulfoxide
eq	equivalent
Fmoc	9-fluorenylmethoxycarbonyl
FRET	fluorescence resonance energy transfer
HIV	human immunodeficiency virus
HuH7	human liver carcinoma cell line
<i>ip.</i>	intraperitoneal
IUBMB	International Union of Biochemistry and Molecular Biology
IUPAC	International Union of Pure and Applied Chemistry
k_{cat}	turnover number
K_i	inhibition constant
K_i^*	apparent inhibition constant
K_M	Michaelis-Menten constant
MBHA	4-Methylbenzhydrylamine
MERS	Middle Eastern Respiratory Syndrome
MMP	matrix metalloproteases
PACE4	paired basic amino acid-cleaving enzyme 4
Pbf	2,2,4,6,7-Pentamethyldihydrobenzofuran-5-sulfonyl
PC	proprotein convertase
PCSK9	proprotein convertase subtilisin/kexin type 9
RBD	receptor binding domain
RFU	relative fluorescence unit

Abbreviations

RSV	Respiratory syncytial virus
RT	room temperature
S protein	spike protein
SARS	Severe Acute Respiratory Syndrome
S1P	Site-1 protease
SPPS	Solid phase peptide synthesis
TFA	Trifluoroacetic acid
TGN	trans-Golgi network
Tle	tert-leucine
V_{\max}	maximum reaction rate
WNV	West-Nile virus

Summary

At the beginning of the twentieth century, the focus of peptide research was largely on human signalling hormones. A breakthrough in the field of peptide therapeutics was the first medicinal application of insulin isolated from animal pancreas, which revolutionized the treatment of type 1 diabetes. Since then, more than 80 peptide drugs have been used for a variety of diseases, including diabetes, cancer, osteoporosis, multiple sclerosis, HIV infection, and chronic pain. The production of synthetic therapeutic peptides has become possible with the development of solid-phase peptide synthesis by Merrifield in the year 1963. This milestone has provided access to pure and sufficient amounts of peptides enabling countless research projects to determine the functional and structural bioactive properties of peptides.

In the context of drug discovery, this thesis focused on the development of synthetic inhibitors of the Ca^{2+} -dependent type-I transmembrane protein furin, which belongs to the proprotein convertase (PC) family of serine endoproteases. It is ubiquitously expressed in vertebrates and invertebrates and activates a large number of proprotein substrates in the secretory pathway, including prohormones, proenzymes, and proforms of receptors or extracellular matrix proteins. Furin also plays a crucial role in tumorigenesis, neurodegenerative disorders, and diabetes or arteriosclerosis as well as in many bacterial and viral diseases. It cleaves numerous precursors of bacterial toxins such as *Pseudomonas* exotoxin A, Shiga-, and diphtheria toxin. Some enveloped viruses possess surface proteins that contribute to the fusion between viral and host cell membranes and have to be activated by furin or related PCs. Examples of such glycoproteins include those from highly pathogenic avian Influenza viruses, Measles, Ebola, and Flaviviruses such as Dengue-, West Nile-, and Zika-virus. Recent studies revealed that furin is implicated in the activation of the spike (S) protein of the new SARS-CoV-2. Given its implications in a variety of biological processes and diseases, furin emerged as a target of paramount importance in drug discovery. To suppress the propagation cycle of furin-dependent viruses, novel peptidomimetic furin inhibitors were developed in this work. Based on the preferred multibasic cleavage motif of furin ($-\text{Arg}-\text{X}-\text{Lys}/\text{Arg}-\text{Arg}\downarrow-$) and on previous work from our group, novel inhibitors of furin were synthesized by a combination of solid-phase peptide synthesis and solution synthesis.

In a first manuscript, several series of new macrocyclic furin inhibitors have been designed and synthesized. The development of cyclic peptides is a widely used strategy to improve the

stability and bioavailability of peptide drugs. The cyclization was performed between different positions of these substrate-analogue inhibitors and by incorporating different linker segments. The inhibitory potency of these compounds was determined in enzyme kinetic assays with soluble human furin. In cooperation with other groups the binding mode of selected cyclic inhibitors in complex with furin was determined and their antiviral potency was tested in cells infected with Respiratory syncytial virus (RSV).

A second paper describes the optimization of a non-cyclic inhibitor starting from a previously designed linear inhibitor MI-1148 that inhibits furin with a K_i value of 5 pM but suffers from a considerably toxicity in mice and rats. Additional studies with structurally related compounds suggested that the severe toxicity of these compounds is caused by the multibasic character of this inhibitor type and not by the inhibition of the host protease furin. By replacing the arginine residues (pKa of side chain 13.5) with the noncanonical amino acid canavanine (pKa 7.0), a new series of potent furin inhibitors was prepared. The best compound MI-1851 inhibits furin with a K_i value of 10.1 pM. Furthermore, the toxicity of this compound was significantly reduced. In cell culture studies, the novel canavanine-containing compounds also showed a significant antiviral activity against furin-dependent viruses, such as RSV, WNV, and Dengue-2 virus, and most importantly, the current SARS-CoV-2 virus.

In a third co-authored paper, this inhibitor MI-1851 was also used to demonstrate an antiviral effect on the new SARS-CoV-2. Moreover, through a series of newly synthesized FRET-substrates derived from the sequence of the potential S1/S2 cleavage site of the SARS-CoV-2 spike protein, it was possible to prove the SARS-CoV-2 S protein activation at this sequence by furin.

In a fourth paper, the synthesis and characterization of a small series of 11 new fluorescence substrates are described, which were tested with five basic PCs including furin, PC1, PC2, PC5A, and PC7. For four of the tested PCs, improved substrates have been identified, which are more efficiently cleaved than the known reference substrates. The improved furin substrates enabled kinetic measurements at significantly reduced enzyme concentrations, thereby avoiding tight-binding conditions. At these reduced furin concentrations, a slow-binding behaviour was observed for the first time with inhibitor MI-1148, which enabled the determination of its individual k_{on} and k_{off} rate constants. The new inhibitors and substrates may help further elucidate the role of furin and related PCs in physiology and disease.

Zusammenfassung

Zu Beginn des 20. Jahrhunderts konzentrierte sich die Peptidforschung weitestgehend auf menschliche Signale. Der erste Durchbruch gelang mit der medizinischen Anwendung des Insulins aus tierischen Bauchspeicheldrüsen, das die Behandlung von Typ-1-Diabetes revolutionierte. Seitdem werden mehr als 80 therapeutisch wirksame Peptide bei unterschiedlichsten Krankheitsbildern wie Diabetes, Krebs, Multiple Sklerose, HIV-Infektion und chronische Schmerzen eingesetzt. Die Synthese therapeutischer Peptide wurde mit der Entwicklung der Festphasenpeptidsynthese durch Merrifield im Jahr 1963 möglich. Dieser Meilenstein ermöglichte den Zugang zu reinen und ausreichenden Mengen an Peptiden und ermöglichte unzählige Forschungsprojekte zur Bestimmung ihrer Funktion und Struktur.

Der Fokus dieser Arbeit lag auf der Entwicklung synthetischer Inhibitoren der calciumabhängigen subtilisinartigen Serinprotease Furin, die zur Familie der Proproteinkonvertasen (PCs) gehört. Es wird ubiquitär in Vertebraten und Invertebraten exprimiert und aktiviert zahlreiche Proproteinsubstrate wie Prohormone, Proenzyme und Proformen von Rezeptoren oder extrazellulärer Matrixproteine. Furin ist auch an der Tumorigenese, neurodegenerativen Erkrankungen, Diabetes oder Arteriosklerose beteiligt, sowie an zahlreichen bakteriellen und viralen Erkrankungen. Beispielsweise spaltet es Vorstufen bakterieller Toxine wie *Pseudomonas* Exotoxin A, Shiga-Toxin und Diphtherietoxin. Einige Viren besitzen Oberflächenproteine, die zur Fusion viraler und Wirtszellmembranen beitragen und durch Furin oder verwandte PCs aktiviert werden. Beispiele sind die Glykoproteine hochpathogener Vogelgrippeviren, von Masern-, Ebola- oder Flaviviren wie Dengue-, West-Nil- und Zika-Viren. Interessanterweise ist Furin auch an der Aktivierung des Spike-Oberflächenproteins des neuen SARS-CoV-2 beteiligt. Im Rahmen dieser Arbeit wurden neuartige Furininhibitoren entwickelt, synthetisiert, enzymkinetisch und strukturell charakterisiert, sowie ihre antivirale Wirksamkeit bestimmt.

Im ersten Manuskript wurden mehrere Serien makrozyklischer Furininhibitoren synthetisiert. Die Entwicklung zyklischer Peptide ist eine weit verbreitete Strategie zur Verbesserung der Stabilität und Bioverfügbarkeit therapeutischer Peptide. Die Zyklisierung erfolgte zwischen verschiedenen Resten an unterschiedlichen Positionen dieser substratanalogen Inhibitoren mittels verschiedener Linkersegmente. Die inhibitorische Wirksamkeit dieser Verbindungen wurde durch enzymkinetische Untersuchungen mit löslichem humanen Furin bestimmt. In

Zusammenarbeit mit Kooperationspartnern wurde der Bindungsmodus ausgewählter zyklischer Inhibitoren im Komplex mit Furin und ihre antivirale Wirksamkeit in mit dem Respiratorischen Synzytial-Virus (RSV) infizierten Zellen ermittelt.

Die zweite Arbeit beschreibt die Optimierung des bereits bekannten linearen Inhibitors MI-1148, der Furin mit einem K_i -Wert von 5 pM hemmt, sich jedoch an Mäusen und Ratten als relativ toxisch erwiesen hat. Zusätzliche Studien mit strukturell verwandten Verbindungen legten nahe, dass die Toxizität dieser Verbindungen durch den stark multibasischen Charakter dieses Verbindungstyps und nicht durch die eigentliche Hemmung der Wirtsprotease Furin verursacht wird. Durch Austausch der Argininreste (pKa der Seitenkette 13.5) durch die nicht-kanonische Aminosäure Canavanin (pKa 7.0) wurde eine neue Serie wirksamer Furinhemmstoffe hergestellt. Die effektivste Verbindung MI-1851 hemmt Furin mit einem K_i -Wert von 10.1 pM. Wie erwartet, hat sich diese Verbindung in Mäusen als deutlich weniger toxisch erwiesen. In Zellkulturstudien zeigten die neuartigen canavaninhaltigen Verbindungen eine signifikante antivirale Aktivität gegen furinabhängige Viren, wie RSV, West-Nil- und Dengue-2-Virus.

In einer dritten Arbeit aus dem Arbeitskreis von Prof. Friebertshäuser wurde für den Inhibitor MI-1851 auch eine antivirale Wirkung auf das neue SARS-CoV-2 nachgewiesen. Darüber hinaus konnte durch eine Reihe neu synthetisierter FRET-Substrate, die von der Sequenz der potenziellen S1/S2-Spaltstelle im Spike-Protein verschiedener Coronaviren abgeleitet wurden, die Aktivierung der SARS-CoV-2 Sequenz durch Furin nachgewiesen werden.

In einer vierten Arbeit wird die Synthese und Charakterisierung einer kleinen Serie von 11 neuen Fluoreszenzsubstraten beschrieben, die mit den fünf basischen PCs Furin, PC1, PC2, PC5A und PC7 vermessen wurden. Für vier der getesteten PCs (außer PC5A) wurden verbesserte Substrate identifiziert, die effizienter als die bekannten Referenzsubstrate gespalten werden. Die verbesserten Furinsubstrate gestatteten Messungen bei deutlich reduzierten Enzymkonzentrationen, bei denen erstmals ein sogenanntes *slow-binding* Verhalten für den Inhibitor MI-1148 festgestellt wurde. Unter diesen Bedingungen konnten die individuellen Assoziations- und Dissoziations-Geschwindigkeitskonstanten k_{on} und k_{off} bestimmt werden. Die neuen Inhibitoren und Substrate können zukünftig helfen, die Rolle des Furins und verwandter PCs bei physiologischen Prozessen und Erkrankungen weiter aufzuklären.

1 Introduction

1.1 The family of proprotein convertases

The diversity of proteins encoded by an organism is increased by post-translational modifications. They can influence the function of modified products and through specific enzymatic steps, new proteins and peptides with altered function and activity are formed.¹ Currently, more than 200 types of post-translational alterations are known, which affect many aspects of cellular functionalities, including metabolism, signal transduction, and protein stability.² Proteases often generate irreversible post-translational modifications of proteins through a specific cleavage of peptide bonds to release and /or further modify the products and ultimately convert them into their active form. In rare cases, this can also lead to the deactivation of the corresponding substrates. Analysis of the human genome suggests the presence of around 600 different proteolytic enzymes.³ According to their catalytic mechanism, these human proteases can be divided into five groups: metalloproteinases, serine, cysteine, threonine, and aspartic proteases.^{4,5} Considering that humans express around 200 different serine proteases, which corresponds to about 1% of all proteins, serine proteases belong to one of the most abundant and diverse classes of enzymes.³ Most of the catalytic domains of the serine proteases possess a chymotrypsin or subtilisin-like folding pattern.⁶

The proprotein convertases (PCs) belong to the subtilisin-like proteases of the family S8 (**Figure 1.1**). The S8 family is further subdivided into the prokaryotic subfamily S8A that is similar to the subtilisin Carlsberg, and the eukaryotic subfamily S8B related to kexin from *Saccharomyces cerevisiae*.⁵ In addition to furin, the kexin-like and calcium-dependent PCs include PC1, PC2, PC4, PC5 (exists in two forms, the soluble A and membrane-bound B)⁷, PACE4, and PC7 as well as SKI-1/S1P, and PCSK9. While the PCs of the subfamily S8B cleave after single or paired basic residues (basic or furin-like PCs), the two of S8A preferentially cleave after non-basic residues. Many different substrates are known for SKI-1/S1P⁸, whereas PCSK9 only cleaves one substrate, its own proform after residue 152 at the VFAQ↓ sequence.¹ Both, SKI-1/S1P and PCSK9 are implicated in cholesterol and/or fatty acid metabolism.⁷ In general, PCs are responsible for the post-translational proteolytic maturation of numerous proproteins, i.e., the activation and rarely also inactivation of proforms of peptide hormones, enzymes, and growth factors. Therefore, these proteases play a crucial role in numerous

physiological processes. However, a deregulated processing of numerous endogenous, but also the cleavage of some exogenous proteins, can cause detrimental pathological effects.

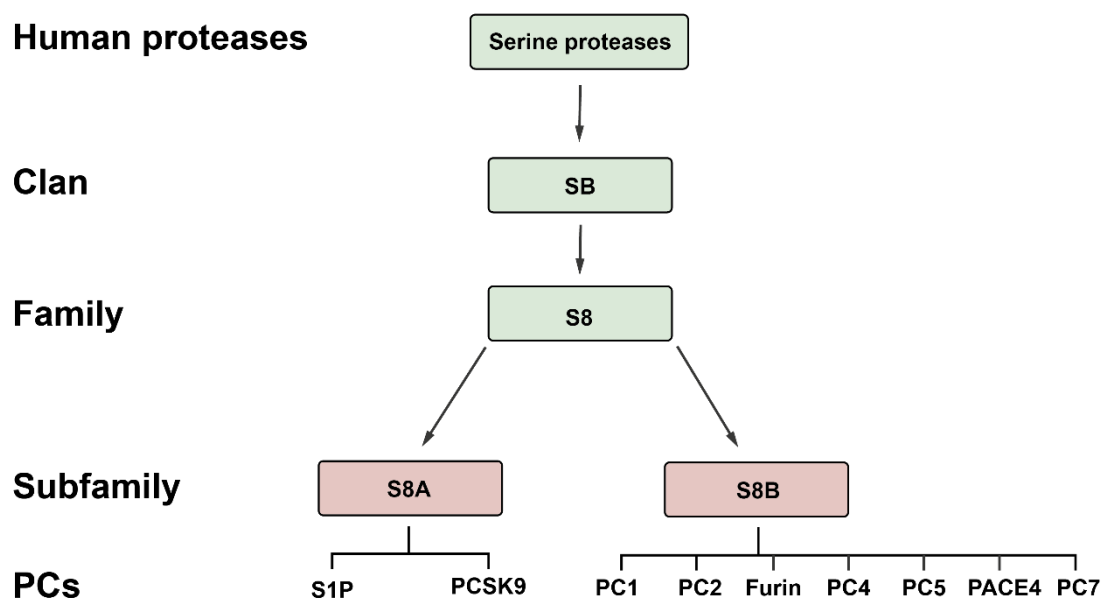


Figure 1.1 Classification of the proprotein convertases within the human serine proteases.

The importance of the furin-like PCs has been demonstrated with various knock-out studies.^{1,9–11} In summary, the absence of furin, PC5, PACE4, and S1P leads to embryonic death of the mice. Complicated and difficult growth disorders arise from the loss of both PC1 and PC2. The absence of PC4 in knock-out mice leads to fertility impairment, especially for male mice, while the lack of PC7 shows no apparent abnormal phenotype despite its ubiquitous expression pattern.¹² This result is surprising, given that in vitro many substrates can be cleaved by PC7. However, the same substrates are usually also cleaved by furin and PACE4, and the expression pattern of furin largely overlaps with that of PC7. Thus, it is possible that PC7 is largely redundant, or that only a subset of non-essential substrates is dependent upon PC7. Further studies with tissue-specific knockout of furin in the liver of adult mice suggest partial redundancy within the PCs. For example, some furin substrates, like insulin receptor or albumin could also be processed in the absence of furin.¹³ Possibly, this redundancy is caused by a significant sequence homology resulting in a very similar active site architecture within the furin-like PCs (**Figure 1.2**).

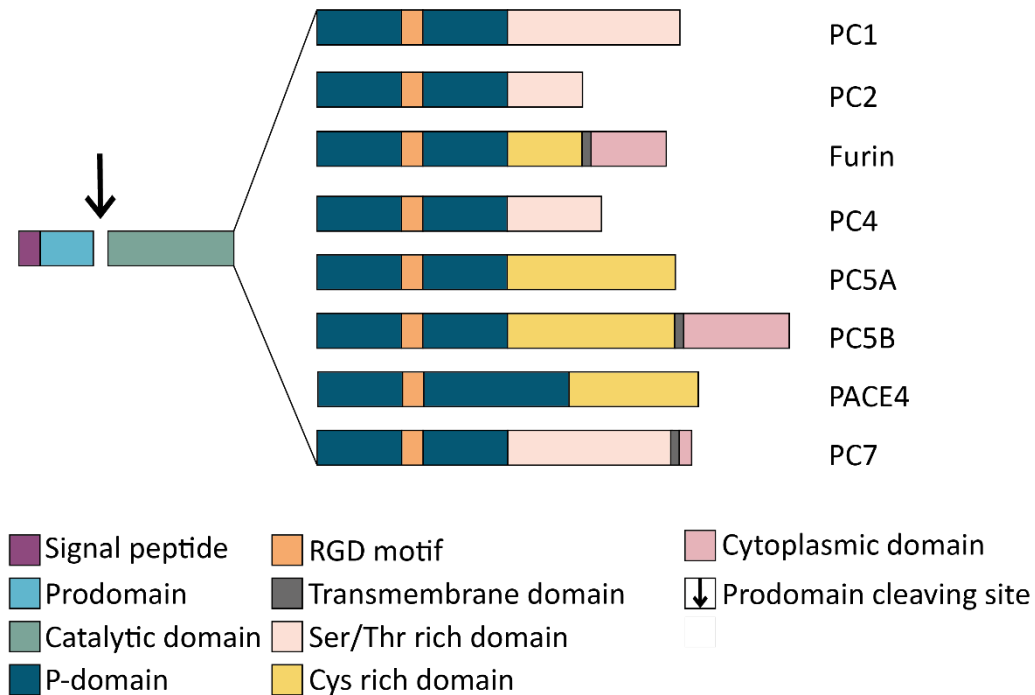


Figure 1.2 Domain architecture of the basic PCs.^{10,14} The seven S8B family members exhibit sequence homology and possess structurally characteristic domains. The signal peptide (magenta) is located at the N-terminus and followed by the prodomain (light blue) and catalytic domain (green). The prodomain plays a key role in the appropriate folding of the PCs. It also acts as an intramolecular inhibitor keeping the enzyme in its inactive form until its autocatalytic processing and subsequent dissociation from the activated protease. The catalytic domain is located immediately downstream of the prodomain and contains the catalytic triad composed of Ser368, His194, and Asp153. It is followed by the P-domain (dark blue), which is essential for the stability and enzymatic activity of the PCs, as well as for their calcium and pH dependency. The P-domain contains also an RGD motif (orange). The lowest sequence homologies are in the C-terminal region of the PCs. Furin, PC5B and PC7 belong to the type I transmembrane proteins and accordingly, possess additional transmembrane (grey) and cytoplasmic (pink) domains. Depending on the intracellular localization, the C-terminal domain of each PC can vary and may contain serine/threonine (light pink) or cysteine-rich (yellow) domains.¹⁵

Furin, PC5, PACE4, and PC7 are widely or ubiquitously expressed. As shown in **Figure 1.3**, they are mainly found in the trans-Golgi network (TGN), in secretory granules, on the cell surface, and in endosomes. They are implicated in major processing events that occur within the constitutive/basolateral secretory pathway.¹⁶ In contrast, PC1 and PC2 are mainly located in the immature and dense secretory nuclear granules of neural and endocrine cells and are known to process most polypeptide prohormones within the regulated secretory pathway.¹⁷ The membrane-bound S1P from the subfamily S8A is typically located in the cis- and medial-Golgi and usually, does not reach the cell surface.¹ PCSK9, the second non-basic PC, is secreted from the TGN directly into the extracellular milieu.¹

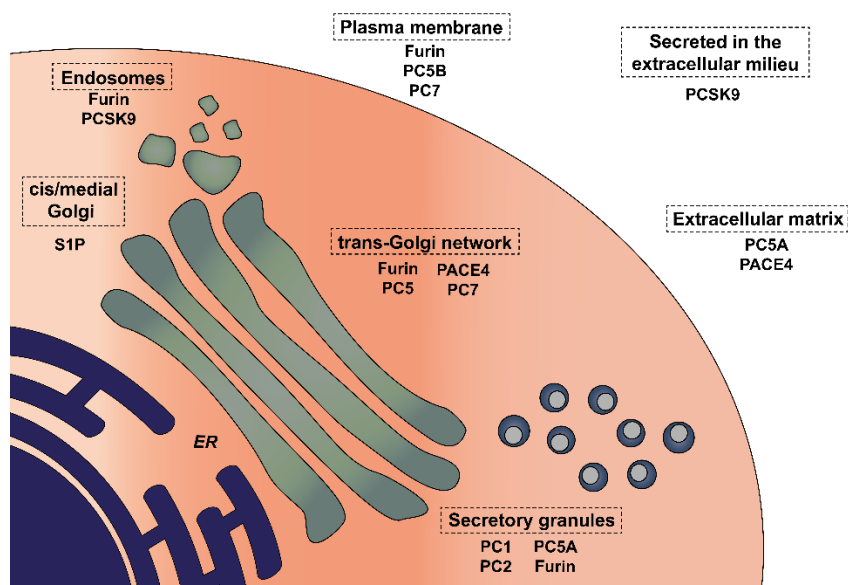


Figure 1.3 Localization of proprotein convertases. An illustration from the literature served as a template.¹⁴

Based on findings of the inducible liver-specific furin knock-out mouse model¹³, the results suggest that furin inhibition could be tolerable as part of a time-limited drug treatment without severe side effects. Therefore, and due to its contribution in numerous diseases, furin emerged as a potential drug target. Its discovery and properties are described in the following paragraphs.

1.2 Furin

Furin is expressed by the *fur*-gene, an upstream region of the *c-fes/fps* proto-oncogene, which was discovered in the year 1986. Roebroek *et al.* demonstrated evidence that the *fur*-sequence encodes for a protein with receptor-like characteristics.¹⁸ At the same time, it was found that the *fur*-gene shows homologies to the gene of the known protease Kex2 of yeast, for which the substrate specificity (proteolytic cleavage after paired basic amino acid residues, e.g. –Lys-Arg-↓ or –Arg-Arg-↓ sequences, where ↓ defines the cleavage site) was already determined.¹⁹ In the following years, furin was intensively investigated and in 1989, it was recognized as the first human PC with a 50 % sequence homology to the catalytic domain of Kex2.^{20,21} Since 1990, furin has been considered as the prototype and best-characterized member of the human PCs. Furin is an omnipresent expressed 794 amino acids long type-I-transmembrane enzyme, which is found in all vertebrates and many invertebrates.^{10,22,23} In the presence of approximately 1 mM calcium and a pH-value between 5-8, furin preferably

cleaves at the following consensus site: –Arg–X–Lys/Arg–Arg↓– (where X is any amino acid).^{10,24} Modelling studies using the solubilized structure of *Bacterial thermitase*, a well-characterized subtilisin that shares 29% sequence identity with the sequence identity of the catalytic domain of furin, suggested that furin contains two calcium-binding pockets, which show different affinities for calcium.²⁵ More recent crystal structures of furin revealed three calcium binding sites and one additional sodium binding site in its protease domain.²⁶

1.2.1 Autoactivation of furin

The activation of furin is a multistep process in which the active enzyme is formed by a twofold autocatalytic cleavage. After translation of the mRNA, the inactive furin proenzyme is translocated via its 24 amino acids long signal peptide into the ER and enters the secretory pathway. The short signal peptide is removed cotranslationally at the sequence –Ala22-Asp-Ala24↓–.²⁷ The proenzyme of furin contains an 83-amino acid propeptide, which acts in the ER as an intramolecular chaperone and enables the correct folding of the catalytic protease domain under neutral pH conditions.²⁸ The first autocatalytic and calcium-dependent cleavage of the propeptide occurs after the sequence –Arg104-Thr-Lys-Arg107↓–. In the environment of the ER²⁹, the propeptide remains non-covalently associated and functions as an autoinhibitor. Then, the furin-propeptide complex enters the TGN via the Golgi apparatus.³⁰ The second intramolecular cleavage takes place in the mildly acidic environment of the TGN, where the propeptide is cleaved by furin after –Arg70-Gly-Val-Thr-Lys-Arg75↓– and subsequently dissociates from the catalytic domain.²⁷ From the TGN, the final activated form of furin can now reach different intracellular compartments such as endosomes and as well the cell membrane. The transport back to the TGN is also possible.¹⁰ The detailed intracellular transport of furin is shown in **Figure 1.4**.

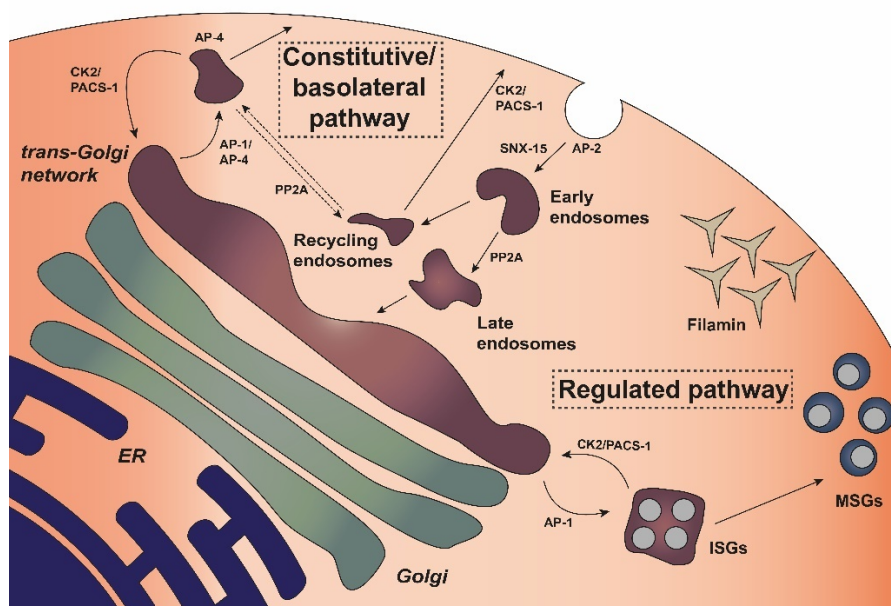


Figure 1.4 Model of the intracellular localization and trafficking of furin. The intracellular transport of furin takes place in two different pathways: the regulated and constitutive/basolateral pathway. The regulated pathway involves the transport of activated furin from the TGN via the immature secretory granules (ISGs) to the mature secretory granules (MSGs) by budding of furin from the TGN caused by adaptor protein (AP)-1. The casein kinase 2 (CK2)-phosphorylated furin acidic cluster is connected by the phosphor furin acidic cluster sorting protein-1 (PACS-1) to AP1 to return furin from the ISGs or in case for the constitutive/basolateral pathway, from the endosomes back to the TGN.³¹ Within the basolateral pathway, furin can also bind to AP-4 to leave the TGN towards the cell surface. When furin molecules arrive at the plasma membrane, there, they can be attached by a cytoskeletal protein, called filamin. The dynamin/clathrin-mediated internalization begins with the binding of the tyrosine-based motif of furin to AP-2. If furin molecules are now in the early endosome, they are dephosphorylated by specific protein phosphatase 2A (PP2A) and then transported back to the TGN via late endosomes. In contrast to that, furin molecules can also be recycled by being phosphorylated by CK2 and returned to the plasma membrane in a PACS-1-mediated step, whereas the sorting nexin-15 protein (SNX-15) is responsible for sorting furin through the endosomal compartments. An illustration from the literature served as a template.¹⁰

Through the localization of furin and its recurrent transport from the TGN across the individual compartments to the plasma membrane and back to the TGN, furin is involved in various physiological processes within the secretory pathway, which are discussed in the next chapter.

1.2.2 Furin-catalyzed physiological and pathological processes

Numerous physiological processes are regulated by proteolytic cleavage, which is one of the most important post-translational modifications.³² Due to its different localization and the ubiquitous presence of furin, it catalyses the cleavage of numerous substrates.³³ Furin is also implicated in numerous diseases including cancer, cardiovascular disorders, and autoimmune diseases.³⁴ Furin activates more than 150 mammalian, bacterial, and viral substrates.³⁵ Among

them are cellular factors that promote tumour development and growth when hyperactivated as well as viral envelope glycoproteins and bacterial toxins.

Many endogenous precursor proteins are cleaved by furin typically leading to their activation. Besides plasma proteins such as proalbumin and proforms of proteases of the blood-clotting factors (pro-factor IX, pro-factor X, pro-von Willebrand factor, pro-protein C), also growth factors (pro- β -nerve growth factor (β -NGF), pro-insulin like growth factor 1 (IGF-1), pro-endothelin 1), receptors (insulin pro-receptor, hepatocyte growth factor pro-receptor), and hormones (prorenin, pro-parathyroid²⁴) can be activated by furin.³⁶ However, furin can also perform inactivating cleavage steps with PCSK9³⁷ and endothelial lipase.³⁸ The essential physiological importance of furin is particularly evident during embryonic development. This was demonstrated by the inactivation of the *fur* gene in mice, as the embryos already died on day 11 due to cardiac ventral closure defects and hemodynamic insufficiency.³⁹ Furthermore, an endothelial cell-specific knock out of the furin gene similarly led to cardiac malformations and early postnatal death.⁴⁰ In addition, further studies with mutations in the furin cleavage site of some substrates revealed genetic disorders leading to haemophilia B⁴¹ or X-linked hypohidrotic ectodermal dysplasia.⁴² Thus, furin can have adverse effects on the organism due to its pleiotropic effects.

In 2005, Bassi *et al.* described furin and other PCs as „master switches in the regulation of tumor growth and progression“.⁴³ As already mentioned, PC substrates include cancer-related proteins such as growth factors, growth factor receptors, integrins, and matrix metalloproteases (MMPs). For example, the furin substrate IGF-1 is increased in colon, breast, prostate, and lung carcinoma. The corresponding receptor IGF-1R is equally dependent on furin and increasingly found on the surfaces of tumour cells.⁴⁴ Another substrate of furin is transforming growth factor beta (TGF- β), which significantly contributes to tissue growth and differentiation in the embryonic phase.³⁹ However, a TGF- β dysregulation provokes different effects. In early stages of cancer, TGF- β revealed tumour suppressive effects by inhibiting cell cycle progression and promoting apoptosis. Though, in late stages, it exerts tumour-promoting effects by increasing tumour invasiveness and metastasis.⁴⁵ Angiogenic and lymphangiogenic factors such as vascular endothelial growth factor C (VEGF-C) and vascular endothelial growth factor D (VEGF-D) may also be hyperactivated by furin and promote tumour vascularization and growth.⁴⁶ Increased furin expression also correlates with overexpression of transmembrane metalloprotease MT1-MMP⁴⁷, which can activate MMP-2

thereby enhancing subsequent tumour growth and neovascularization.⁴⁸ Beyond that, MT1-MMP/MMP-2 are required for alveolus formation in the embryonic lung. Furthermore, a furin inhibition and subsequent reduction of MMP2 activity may exerts an anti-inflammatory and protective effect against atherosclerotic coronary artery disease (CAD)⁴⁹ as well as the autoimmune rheumatoid arthritis (AR) disease⁵⁰. Besides furin, other related basic PC s are involved in the progression of certain tumours, e.g., PACE4 in prostate⁵¹ and estrogen-receptor-positive breast⁵² cancer.

In addition to cellular precursor proteins, a number of bacterial exotoxins (AB toxins) are activated by furin.¹⁰ These are secreted by bacteria and can exert their effect in certain cell compartments. They commonly consist of an enzymatically active A subunit and B subunits, the latter mediates membrane binding, pore formation and translocation of the A subunit into the cell. Furin induces the cleavage between the A and B subunits, a prerequisite for toxicity.⁵³ Examples of furin-activatable AB toxins comprise anthrax toxin (expressed by *Bacillus anthracis*⁵⁴), diphtheria toxin (secreted by *Corynebacterium diphtheriae*⁵⁵), *Pseudomonas* Exotoxin A (from *Pseudomonas aeruginosa*), Shiga and Shiga-like toxins (caused by *Shigella dysenteriae*⁵⁶).

Numerous surface glycoproteins of enveloped viruses must be proteolytically cleaved by furin as a prerequisite for virus entry into host cells and to achieve fusion competence. Therefore, the furin-catalyzed activation of these glycoproteins is necessary for the infectivity and pathogenicity of these viruses. Viruses bind to the host cell membrane via corresponding receptors and can then enter the cell either via direct fusion with the outer cell membrane (e.g., Paramyxoviruses like measles virus) or, in other cases, via endocytic uptake (e.g., highly pathogenic avian influenza viruses). In **Table 1.1** several examples of furin-dependent viruses are summarized.

These viral furin substrates include the envelope protein gp160 from Human immunodeficiency virus Typ 1 (HIV-1), which is cleaved into gp120 and gp41.⁵⁷ Additional glycoproteins such as those from Ebola virus, Eppstein-Barr virus, and Marburg viruses, mumps and measles viruses, as well as hemagglutinins of certain HPAIV influenza viruses⁵⁸ are also activated at multibasic recognition sequences by furin.^{59,60}

Table 1.1 Examples of furin-activated viruses including the type of genome, name of the cleaved viral glycoprotein and cleavage sequence (Abbreviations: Env, envelope; F, fusion protein; gB, glycoprotein B; GP, glycoprotein; HA, hemagglutinin; HbeAg, hepatitis B external core antigen; prM, premembrane protein; S, spike protein; ↓, cleavage site).

Genom	Virus	Protein	Polybasic cleavage site
dsDNA	<i>Herpesviridae</i>		
	Epstein-Barr virus	gB	LRRRRR↓DA
(+) ssRNA	<i>Coronaviridae</i>		
	Infectious bronchitis virus	S	TRRFRR↓SI
	SARS-CoV-2	S	SPRRAR↓SV
	<i>Flaviviridae</i>		
	Dengue virus type 2	prM	HRREKR↓SV
	West Nile virus	prM	SRRSRR↓SL
	Zika virus	prM	ARRSRR↓AV
(-) ssRNA	<i>Filoviridae</i>		
	Ebola virus	GP	GRRTRR↓EA
	<i>Orthomyxoviridae</i>		
	HPAIV (H5, H7, H9)	HA	H5: TRRQKR↓GL
	<i>Paramyxoviridae</i>		
	Respiratory syncytial virus	F	KKRKRR↓FL
ssRNA-RT	<i>Retroviridae</i>		
	Human immunodeficiency virus 1	Env	VQREKR↓AV
dsDNA-RT	<i>Hepadnaviridae</i>		
	Hepatitis B virus	HBeAG	VRRRGR↓SP

Similarly, certain coronaviruses possess a spike surface protein S, which mediates the host cell binding and fusion process. In late 2019, a new variant of this virus emerged, causing a pandemic of acute respiratory disease, named COVID-19.⁶¹ Related to the third publication in the context of this thesis, SARS-CoV-2 is discussed in more detail in the following chapter.

Due to its involvement in these many diseases, furin emerged as an attractive target for drug development. However, due to its manifold functions in normal physiological processes, a strong sustained furin inhibition could also lead to side effects. Therefore, furin inhibitors should be preferably used for a short-term treatment in acute infections.

1.3 Coronaviruses

In 1968, a novel group of viruses was observed under the electron microscope by eight virologists and named as coronavirus (CoV), due to its crown-like morphology.^{62,63} Coronaviruses are enveloped, non-segmented positive-sense and so far the largest known

RNA viruses (their genome contains up to ≈ 30 kb).⁶⁴ They belong to the subfamily *Coronavirinae* of the family of *Coronaviridae* and the order *Nidovirales* (International Committee on Taxonomy of Viruses), depicted in **Figure 1.5**. The subfamily is grouped into four genera: alpha- and beta-coronaviruses, that primarily can infect mammals, and gamma- and delta coronaviruses, where their occurrence has been observed only in animals until now. Coronaviruses have been actively studied for more than 60 years. The prototype of a murine coronavirus strain was isolated and reported in the year 1949.⁶⁵ And since the 1970s, the molecular mechanisms of replication as well as the pathogenesis of several coronaviruses have been described. Generally, coronaviruses cause mild upper respiratory tract illness, resembling a cold⁶⁶, and intestinal infections in humans and animals. However, since 2002 and 2003, coronaviruses moved into the focus of the public, due to the outbreak of the lethal *Severe Acute Respiratory Syndrome* (SARS) caused by coronaviruses in Guangdong, a province in China.^{67,68} Spreading through human transmission chains, the consequence of this outbreak led to a near-pandemic with 8437 cases reported worldwide and 813 deaths. Ten years later, another highly pathogenic β -coronavirus, not previously found in humans, was detected for the first time in a patient in Saudi Arabia.⁶⁹ This new coronavirus was named as *Middle Eastern Respiratory Syndrome* (MERS) coronavirus and caused a fatality rate of 34.4% in 2012.⁷⁰

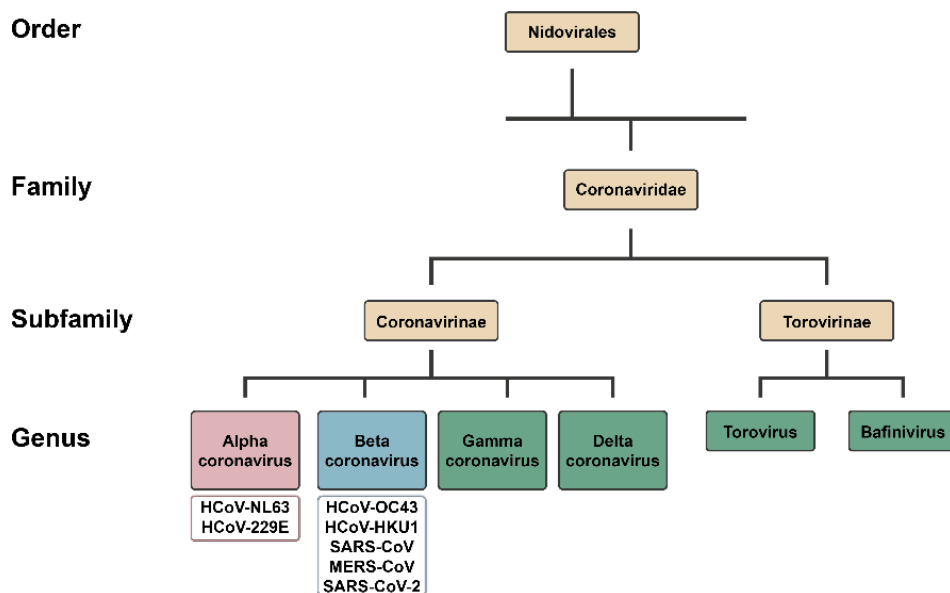


Figure 1.5 Present taxonomy of *Coronaviridae*⁷¹ according to the International Committee on Taxonomy of Viruses.

Most recently, a contemporary outbreak of an “old new viral enemy”⁷², named *Severe Acute Respiratory Syndrome Coronavirus 2* (SARS-CoV-2) was declared by the World Health

Organization as a public health emergency. In December 2019, the coronavirus disease (COVID-19) was identified in Wuhan, Hubei Province, China. Since then, it has spread rapidly via human-to-human transmission across the world at a worrying rate. Most patients with COVID-19 report symptoms such as cough, fatigue, dyspnoea, headache, and mild-to-severe fever. Some patients also report gastrointestinal infections with diarrhoea, nausea, and vomiting as symptoms.⁷² The spread and lethality of the COVID-19 outbreak is higher than previous epidemics, due to international travel density and immune naivety of the population.⁷² It is now a serious medical problem in more than 200 countries with over 190 million confirmed cases and with over 4 million dead worldwide (Johns Hopkins Coronavirus Resource Center, status July, 2021).

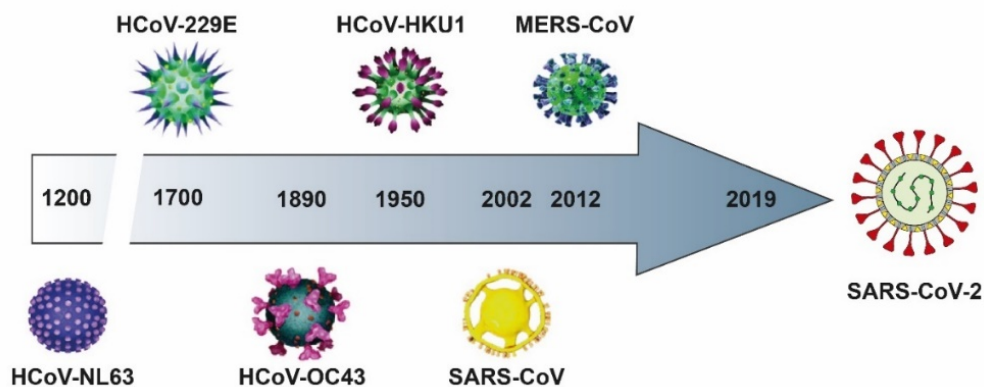


Figure 1.6 The appearance of the seven human coronaviruses over the time. Alpha-CoVs (HCoVs-NL63, HCoVs-229E) and beta-CoVs (HCoVs-OC43, HCoVs-HKU1, SARS-CoV, MERS-CoV and SARS-CoV-2). The illustration was taken from literature and slightly modified.⁷³

During the rapid global spreading of COVID-19 last year, as case numbers rose expeditiously, several already approved drugs were described for the potential treatment of COVID-19.⁷⁴ For example, at the onset of the pandemic, remdesivir and hydroxychloroquine/chloroquine were suggested for the treatment of COVID-19.⁷⁵ Very rapidly, since the beginning of the pandemic manifold information about this new virus became available. For examples, Coutard *et al.* described for the first time a potential S1/S2-furin-like cleavage site within the S glycoprotein. Using molecular modelling, Chen *et al.* analysed the receptor binding domain (RBD) of the SARS-CoV-2 S protein and revealed a stronger interactions with the host receptor ACE-2 than found for SARS-CoV.^{76,77} The spike protein of SARS-CoV-2 is crucial for host cell entry and requires a priming by furin and TMPRSS2. Therefore, these two host cell proteases emerged as potential drug targets.⁷⁸ More details about these results are described in Chapter 4.3.

Genetic structure and pathogenic mechanism of SARS-CoV-2 are explained in more detail in the following Section.

1.3.1 Genome and structure of SARS-CoV-2

In January 2020, the genome sequence of SARS-CoV-2 was published in GenBank with accession no. MN908947.3. As already mentioned in **Figure 1.5**, based on evolutionary tree analysis and sequence alignment, SARS-CoV-2 belongs to the genus *beta*-coronavirus as its newest member. According to genomic analysis, SARS-CoV-2 has 79.6% sequence identity to SARS-CoV and 50% to MERS-CoV.^{79,80} The genome structure of SARS-CoV-2 is shown below in **Figure 1.7**.

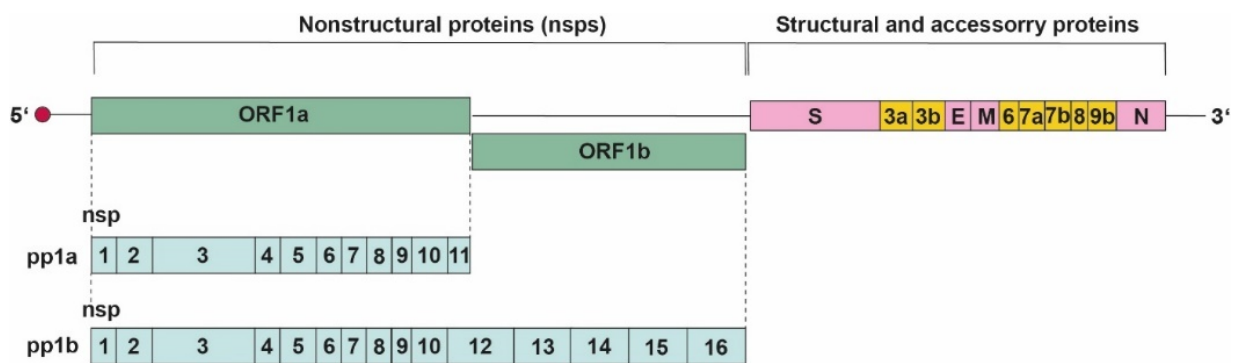


Figure 1.7 Schematic viral genomic organization of SARS-CoV-2. The virions contain an outer lipid envelope and are spherical with diameters from 60 to 140 nm.⁸¹ The genome possesses 14 open reading frames (ORFs) encoding 27 different proteins. There are two categories of proteins: non-structural proteins (nsp) and structural and accessory proteins. At least, the SARS-CoV-2 genome contains six accessory proteins, their genes are located between the structural genes. However, their functions are currently not fully understood.⁸²

SARS-CoV-2 is an enveloped, non-segmented, positive single stranded RNA virus of nearly 29.9 kB in size, which belongs to one of the largest known genomes among RNA viruses.^{83,84} Structurally, SARS-CoV-2 possesses four distinct structural proteins that include the so called spike or S glycoprotein, small envelope (E) glycoprotein, membrane (M) glycoprotein, and nucleocapsid (N) protein, and as well several accessory proteins.⁸⁵ The SARS-CoV-2 virion structure is depicted in **Figure 1.8**.

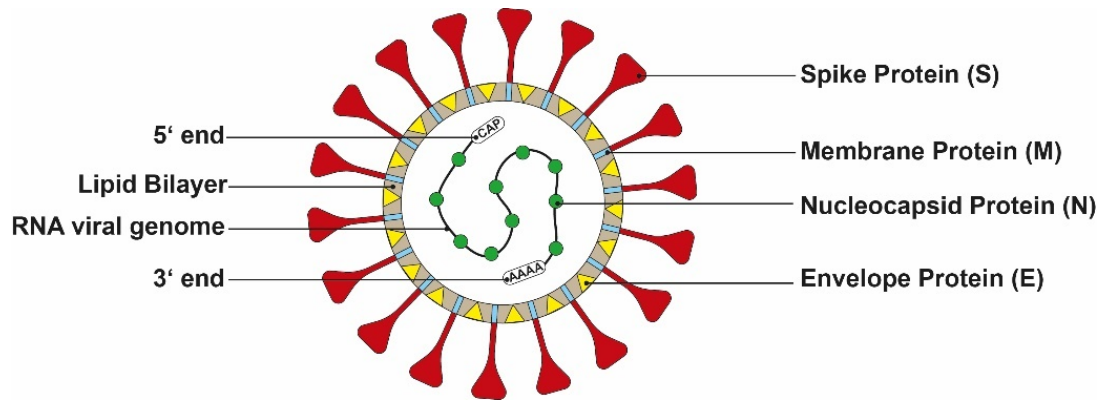


Figure 1.8 Structure of SARS-CoV-2. The S protein, which coats the entire outer lipid membrane, gives the coronavirus the appearance of a crown under the electron microscope.⁸⁶ This homotrimeric transmembrane protein contains a molecular weight of ≈ 150 kDa and is involved in the entry into host cells after binding to the receptor ACE2. The nucleocapsid (N) is a phosphorylated protein that is located in the endoplasmic reticulum-Golgi region. It is bound to the genome of the virus and assists the replication cycle and cellular response of host cells to viral infections.^{85,87,88} An additional structured protein of the virus is the M protein, which is the most abundant protein present in coronavirus and determines the shape of the virus envelope. The small transmembrane envelope protein (E) plays a role as an ion channel to release the viral genomic material to the host cell. Furthermore, it is involved in the assembly and release of the virus.⁸⁷

1.3.2 Life cycle of SARS-CoV-2

It has been known for some time, that human coronaviruses, like HCoV-229E, HCoV-OC43, and HCoVs-HKU1 (**Figure 1.6**) circulate in the population and cause seasonal, usually mild respiratory tract infections associated with symptoms of the "common cold." In contrast, the highly pathogenic coronaviruses that have emerged in the human population in the last 20 years can be lethal, especially for the elderly. By infecting the upper respiratory tract in humans, SARS-CoV, MERS CoV, and more recently SARS-CoV-2 infections can develop into severe, life-threatening respiratory pathologies and lung injuries for which no effective specific prophylactic or therapeutic treatment has yet been approved. The virus replication starts with the specific binding of the S protein to cellular host receptors. Several receptors have now been identified for the respective coronaviruses: The aminopeptidase N (APN) for HCoV-229E, angiotensin-converting enzyme 2 (ACE2) for HCoV-NL63, SARS-CoV and the novel SARS-CoV-2, and dipeptidyl peptidase 4 (DPP4) for MERS-CoV. The expression and tissue distribution of entry receptors consequently influence viral tropism and pathogenicity.⁸⁹

The complete life cycle beginning with the entry (Chapter 1.3.3) to genomic replication, formation of mature virions and ending with exocytosis of the coronavirus are depicted below (**Figure 1.9**).

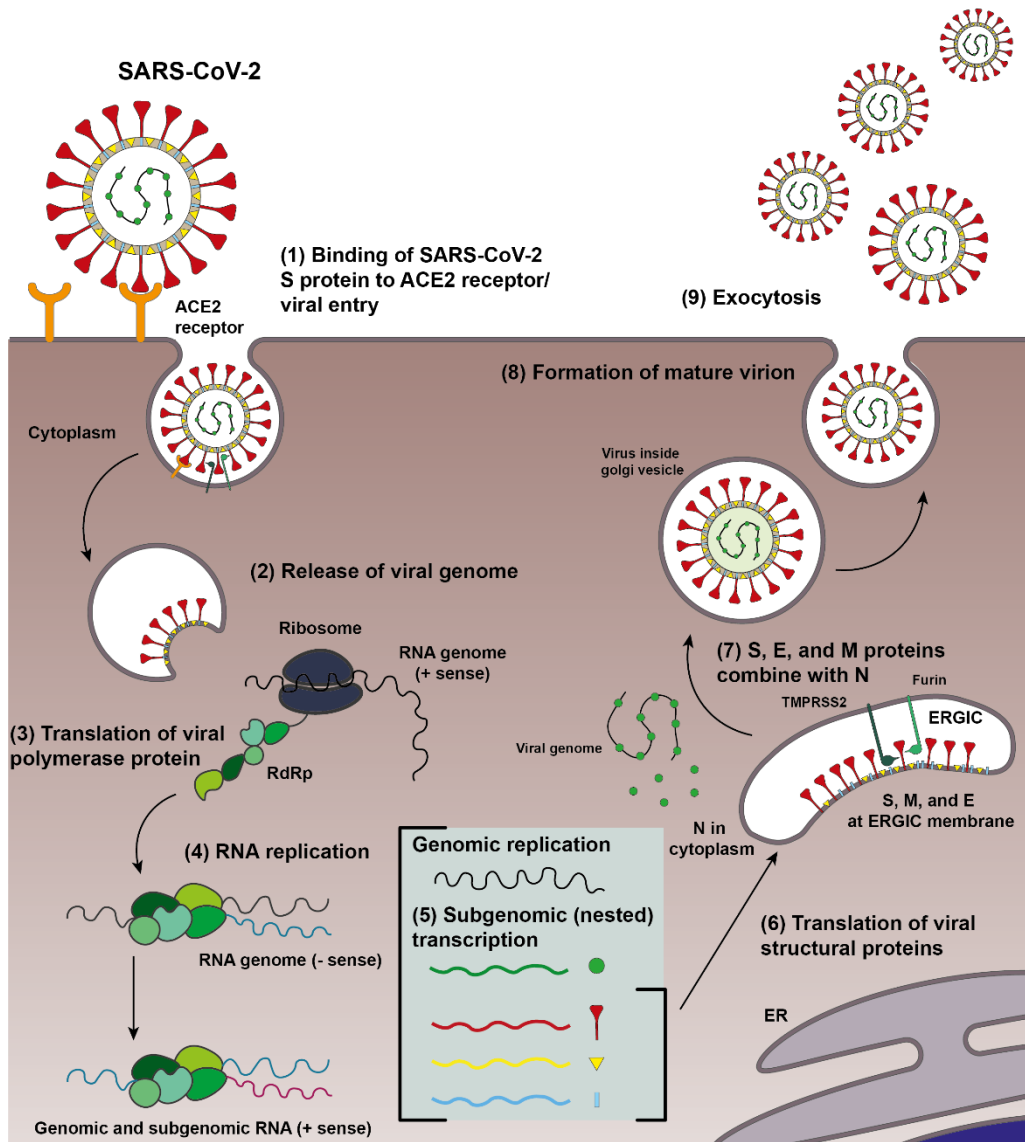


Figure 1.9 Life cycle of SARS-CoV-2. (1) The S protein of SARS-CoV-2 binds to the ACE2 and the virus enters the host cell via direct membrane fusion or endocytosis. (2) Thereupon, the viral RNA is released into the cytoplasm. (3) Then, the replicase gene is translated from the genomic RNA. The genome encodes two large overlapping open reading frames, ORF1a and ORF1ab, which express polyproteins pp1a and pp1ab. These polyproteins, pp1a and pp1ab, contain nonstructural proteins (nsps) 1–11 and 1–16, respectively. Both polyproteins are further processed by viral proteases (papain-like proteases (PL^{pro}), Mpro protease (chymotrypsin-like protease (3CL^{pro}))) into 16 nonstructural proteins, which are required for viral RNA synthesis. All in all, nsps play a crucial role in many processes in viruses and host cells.^{85,90} (4) For RNA replication and transcription of subgenomic RNAs, this requires many of the nsps to assemble into the replicase–transcriptase complex (RTC) to create an environment suitable for RNA synthesis, especially RNA-dependent RNA polymerase (RdRP/nsp12) activity mediates replication and transcription of the viral genome. During replication, RTC drives the production full length (–)RNA copies of the genome, which is used as templates for the full-length (+) RNA genomes and subgenomic RNAs (sgRNAs) as intermediate products, that are mainly mediated by RdRp. (5) In coronavirus transcription, there is a discontinuous step (fragmented transcription) which is unique among the other known RNA viruses, and an ultimate nested set of subgenomic mRNAs (sgmRNAs) with 5' and 3' terminal is produced.⁹¹ (6) Afterwards, these subgenomic proteins become translated into structural and accessories proteins such as M, S, and E proteins, which are subsequently inserted into the endoplasmic reticulum-Golgi intermediate compartment (ERGIC). Meanwhile, nucleocapsid proteins are assembled in the cytoplasm. (7) Structural proteins and nucleocapsid containing viral genome meet in the ERGIC. Finally, to form mature virions, viral genomes encapsulated by the N protein bud in membranes of the ERGIC containing viral structural proteins. (8) After the assembly of mature virion, the virion containing vesicles are transported to the cell surface, fused with the plasma membrane, (9) and then released from the infected cell by exocytosis. A figure from the literature served as a template.⁹²

1.3.3 Viral entry – the structure and furin cleavage site of the spike protein

It is important for the development of drugs and vaccines for treatment COVID-19, to firstly understand how SARS-CoV-2 enters human cells to curb its rapid spread. The entry of SARS-CoV-2 depends on binding of the viral surface spike glycoprotein to cellular receptors; in this case to its host receptor, namely ACE2 (**Figure 1.10**). To accomplish this task, the spike protein must be in an open state/up conformation (**Figure 1.11B**) to present its RBD for proper binding to ACE2.⁹³ For a complete activation of the spike protein, proteolytic cleavage by specific human proteases is required. Genomic analysis of the new CoV revealed that despite a high similarity to the genome sequence with the old SARS-CoV, a furin-like cleavage site occurs between the S1 and S2 domains in the S protein of SARS-CoV-2.^{76,94,95}

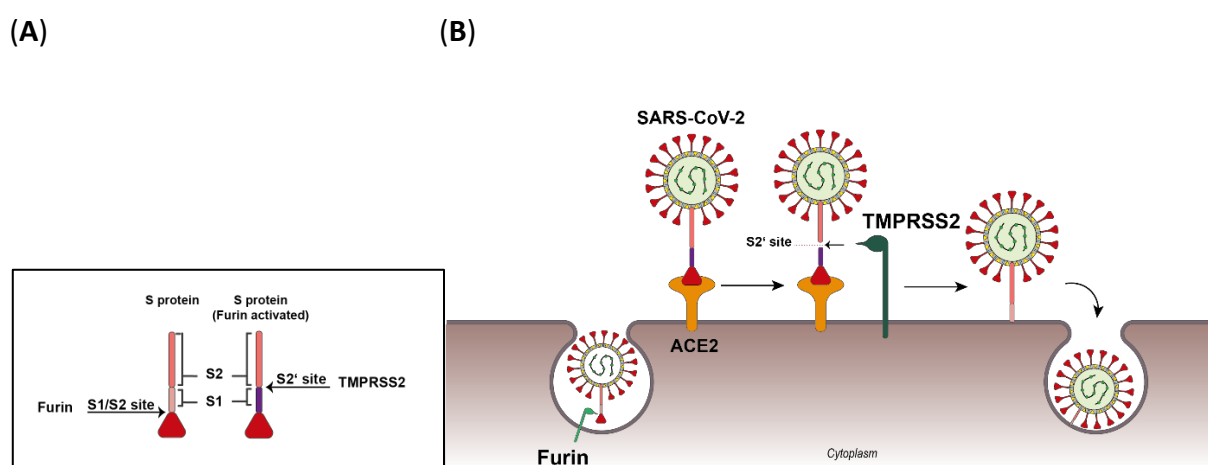


Figure 1.10 Process of viral entry –locking on with the spike. (A) Prior proteolytic cleavage at two sites is required to initiate S protein fusion activity. (B) The first cleavage site by the protease furin is at the S1/S2 boundary and results in a conformation of the spike protein that shows structural changes in the S2 domain. To activate the full fusion process and allow release of the nucleocapsid-coated RNA genome into the cytoplasm, the S2' site must be cleaved by TMPRSS2. A figure from the literature served as a template.⁸³

Depicted in **Figure 1.11A/C**, the spike protein is a large trimeric $\approx 180\text{--}200$ kDa type I transmembrane^{96,97} and class I fusion⁹⁸ glycoprotein that is divided into two domains: the S1 and S2 domains. The subunit S1 contains a RBD and N-terminal domain (NTD) while the subunit S2 comprises a membrane fusion domain, which includes the fusion peptide (FP), heptapeptide repeat sequence 1 (HR1), heptapeptide repeat sequence 2 (HR2), transmembrane domain (TM), and cytoplasmic tail (CT).⁹⁹ Using cryo-electron microscopy, recent studies showed that the spike glycoprotein forms a clove-shaped spike with three S1 heads and a trimeric S2 stem and revealed different conformations of the spike RBD in opened (RBD up) and closed (RBD down) states (**Figure 1.11B-C**).⁹³

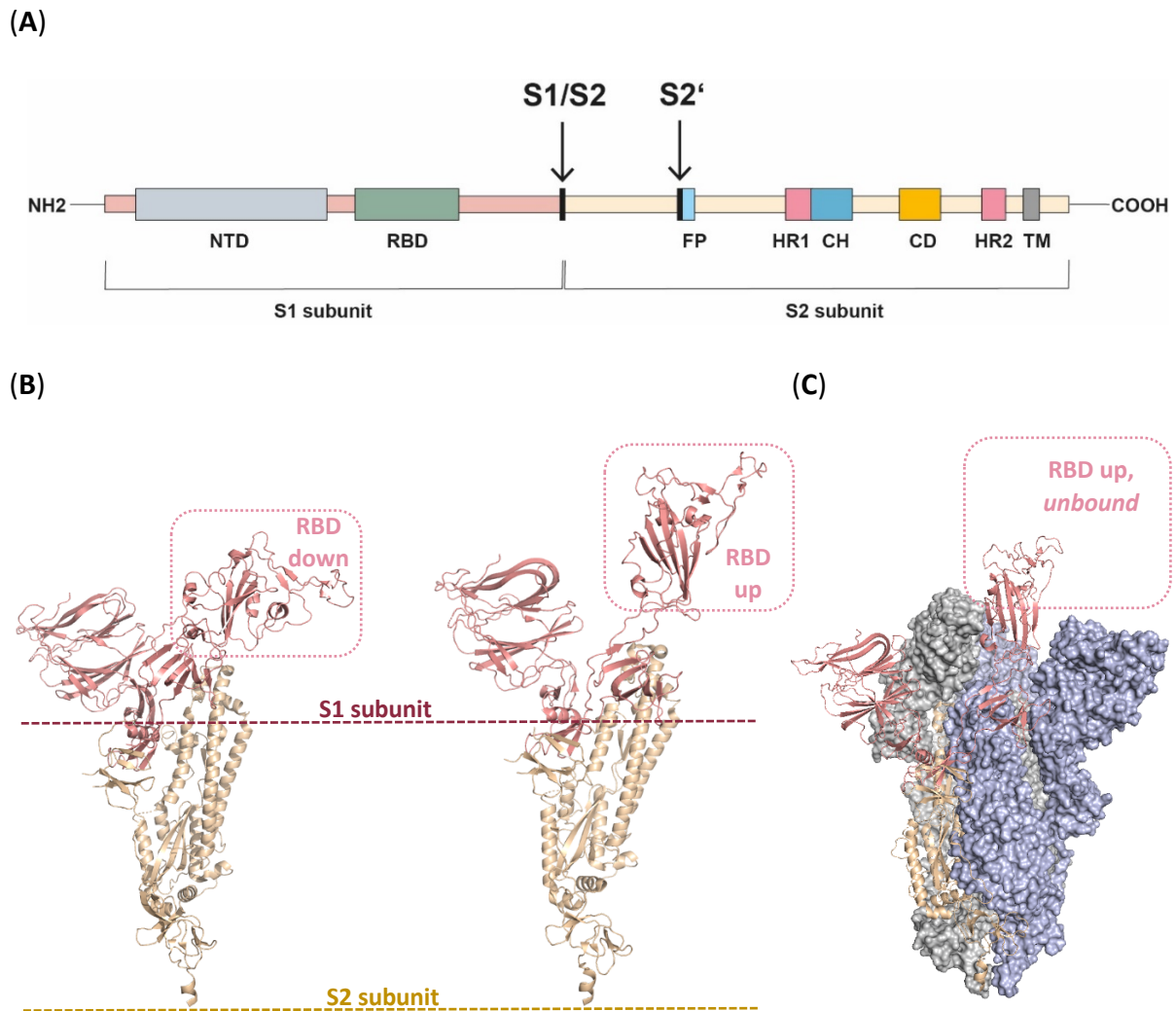


Figure 1.11 Structure of SARS-CoV-2 S protein. (A) Schematic representation of SARS-CoV-2 S protein with its S1 and S2 subunits and cleavage sites S1/2 and S2' (black stroke/arrow). (B) Single protomer of SARS-CoV-2 S protein with the RBD in the down (left, PDB ID: 6ZGE) and up conformation (right, PDB ID: 6ZGG). (C) View of S trimer (grey, purple, pink) with a single RBD in the opened unbound conformation (PDB ID: 6ZGG).⁹³

Once the RBD of the subunit S1 interacts with the host cell by recognizing the receptor ACE2, viral fusion follows. This fusion of viral with host cell membranes results in the release of the viral genome into the host cell. Recent studies showed that SARS-CoV-2 S protein contains a four residues long insertion exhibiting two additional basic residues (Pro-Arg-Arg-Ala-Arg) at the S1/2 site and thereby forming a new furin cleavage site, which was not present in SARS-CoV or other SARS-like CoVs. In addition, the S2' cleavage site of the spike protein is cleaved by TMPRSS2, a trypsin-like serine protease. The importance of the proper activation of both cleavage sites by furin and TMPRSS2 for the replication of SARS-CoV-2 is described in our publication⁷⁸ (Chapter 4.3) and in Section 3.3.

1.4 Furin inhibitors

Furin is involved in numerous physiological as well as pathological processes. Hence, effective inhibitors of this protease could be potential drugs for the treatment of furin-dependent diseases. The already known furin inhibitors can be divided in different groups based on their molecular weight and chemical structure. Selected inhibitor types are listed below (**Table 1.2**).

Table 1.2 Classification of known furin inhibitors.

Macromolecules (Proteins)	Peptides	Modified Peptides	Non-peptide inhibitors
<i>α 1-antitrypsin variant portland</i> ¹⁰⁰	Furin prodomain derivatives ^{101,102}	Chloromethyl ketone derivatives ^{57,103}	Diterpines of <i>Andrographis paniculata</i> ¹⁰⁴
<i>turkey ovomucoid third domain</i> ¹⁰⁵	nona-L-arginine ¹⁰⁶	Ketomethylene derivatives ¹⁰⁷	Chelate complexes, e.g., Cu(TTP*)Cl ₂ Zn(TTP*)Cl ₂ ¹⁰⁸
Eglin c mutants ¹⁰⁹	nona-D-arginine ¹⁰⁶	Eneidyryl peptide derivatives ¹¹⁰	Dicoumarol derivatives ¹¹¹
Inter-alpha-inhibitor proteins ¹¹² <i>α2-macroglobulin</i> ¹¹⁶	Hemagglutinin-derived peptides ¹¹³	Cyclic polyarginine peptides ¹¹⁴	Naphthofluorescein derivatives ¹¹⁵
		Peptides with P1-arginine mimetics ¹¹⁷ 58,120,121	2,5-dideoxystreptamine derivatives ¹¹⁸
Human proteinase inhibitor 8 ¹¹⁹		Elongated and shortened peptide-based furin inhibitors ¹²²	Aminohydrazone derivatives ^{111,123}
Non-competitive furin-inhibiting nanobodies ¹²⁴			Diminazene (Triazene derivative) ¹²⁵

* TTP is 4'-[p-tolyl]-2,2':6',2''-terpyridine

1.5 Crystal structures of furin in complex with inhibitors

The first crystal structure of mouse furin in complex with its irreversible inhibitor decanoyl-Arg-Val-Lys-Arg-chloromethyl ketone was determined by the Than group.¹²⁶ At that time, the commercially available dec-RVKR-CMK was the most often used furin inhibitor, although CMK-derivatives generally suffer from a very short half-life of only few minutes in blood¹²⁷ and are only suitable for biochemical studies. The used truncated soluble furin construct consisted of the catalytic and P domain. Based on this crystal structure, the overall binding mode of such substrate-analogue ligands and characteristic interactions of the individual inhibitor residues with furin were elucidated. Furthermore, the availability of the crystal structure enabled for the first time a rational structure-based design of new improved furin inhibitors.

During the following years, our group has developed numerous highly potent substrate-analogue and reversible binding furin inhibitors containing a C-terminal 4-amidinobenzylamide (4-Amba) group as Arg mimetic.^{58,120,128} In 2014, the first crystal structure of human furin in complex with the noncovalent inhibitors 3-guanidinomethyl-Phac-Arg-Val-Arg-4-Amba (**1**) (PDB: 4OMC) could be determined.²⁶ With a K_i value of 8 pM, this compound was one of the most potent furin inhibitors at that time.^{26,58}

In a subsequent publication, the even more potent furin inhibitor 4-guanidinomethyl-phenylacteyl-Arg-Tle-Arg-4-Amba (**2/MI-1148**) (K_i value of 5.5 pM) containing the unnatural amino acid residue *tert*-leucine (Tle) in P3 position was described. Its crystal structure in complex with furin is shown in **Figure 1.12**.¹²¹

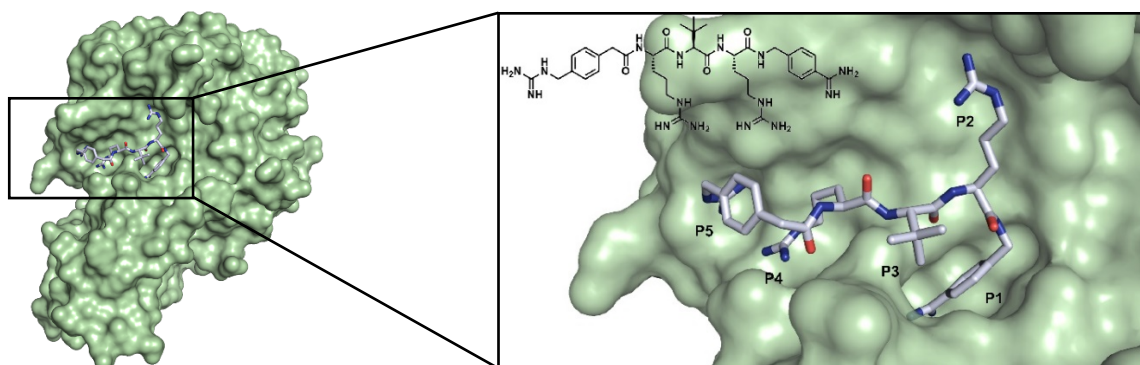


Figure 1.12 Crystal structure of human furin (shown with its solvent-exposed surface in green) in complex with inhibitor **2/MI-1148** (PDB ID: 4RYD).¹²¹

A short time later, the crystal structure of an unliganded form of furin suitable for soaking experiments could be determined. In the ligand-free state, named as “off-state”, numerous changes in furin’s active site have been observed when compared with the so-called “on-state” in presence of substrate-analogue ligands.¹²⁹ A lack of hydrogen bonding between Ser253 and the catalytic Ser368 is causing a rotation of the Ser368 side chain, which disrupts the essential hydrogen bond to His194 in ligand-free furin. The resulting geometrical change within the catalytic triad in the off-state together with a displacement of the backbone from the so-called alignment template (residues Ser253-Pro256) leads to a catalytically inactive form of furin. The catalytically competent state of furin is further stabilized by a Ca^{2+} ion located below the S1 pocket, which accommodates the P1 residue, e.g., arginine or 4-amidinobenzylamide. In absence of this Ca^{2+} the side chain of Asn295, which is part of furin’s oxyanion hole, is rotated. This also leads to a loss of the catalytic activity.

Other groups have synthesized peptidic furin inhibitors with additional basic residues within their P5 to P8 segment.^{117,130} This stimulated work in our group to prepare N-terminally elongated inhibitors containing a nearly constant P4-P1 segment (Arg-Val/Tle-Arg-4-Amba).¹²² Also with these extended inhibitors crystal structures in complex with furin could be determined, e.g., with the hexapeptide inhibitor H-Arg-Arg-Arg-Val-Arg-4-Amba (**3**)(**Figure 13**).¹³¹ The structure revealed the exact binding mode of the P5 and P6 residues, whereas the guanidino group of the P5 Arg is placed on the same position as observed before for the N-terminal guanidine in complex with inhibitor **2/MI-1148**. Surprisingly, due to a turn of the P5-P6-backbone, the P6 side chain is backwards oriented and comes in relatively close contact to the P2 side chain. This suggested the design of inhibitors containing a cyclization between their P6 and P2 side chains.¹³²

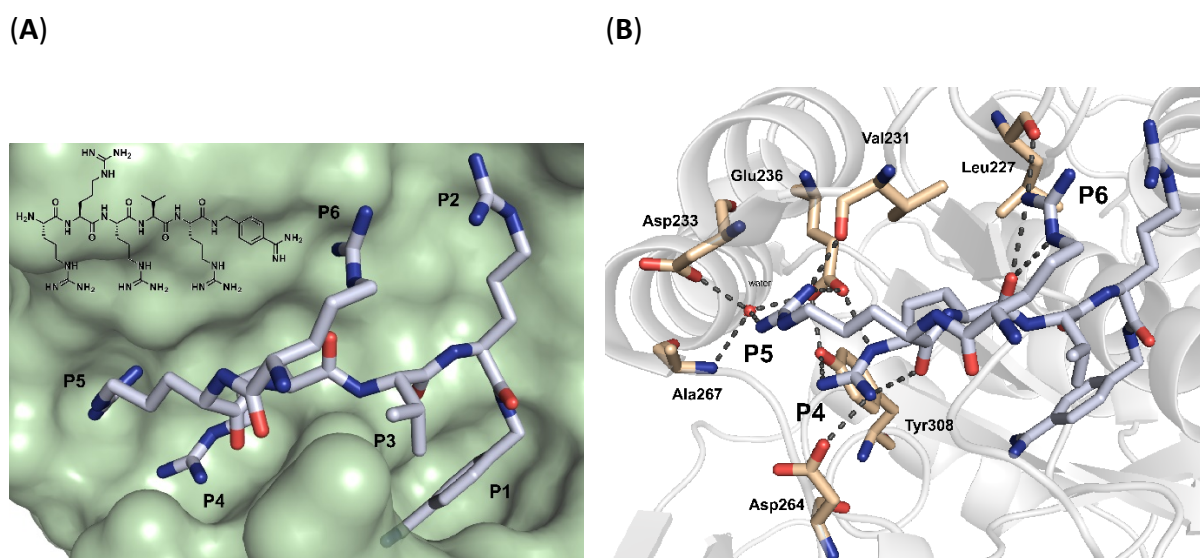


Figure 1.13 Crystal structure of the elongated inhibitor **3** (shown with carbon atoms in gray) in complex with human furin (solvent-exposed surface in green (A) and cartoon representation in light grey (B), PDB ID: 6EQX) showing the inhibitor structure and overall binding mode (A), as well as (B) the formed polar interactions of the P4-P6 inhibitor segment.¹³¹ The involved furin residues are shown with carbon atoms in beige.

Besides peptidic inhibitors, non-peptidic small molecule inhibitors can overcome the disadvantages such as high molecular weight, poor permeability, stability as well as toxic properties. For examples, in 2006, guanidinylated aryl derivatives of 2,5-dideoxystreptamine were described.¹¹⁸ These derivatives are comparable to peptidomimetic inhibitors and exhibit K_i values in the nanomolar range. The crystal structure of the triaryl derivatives (**Figure 1.14**) with furin were solved.¹³³

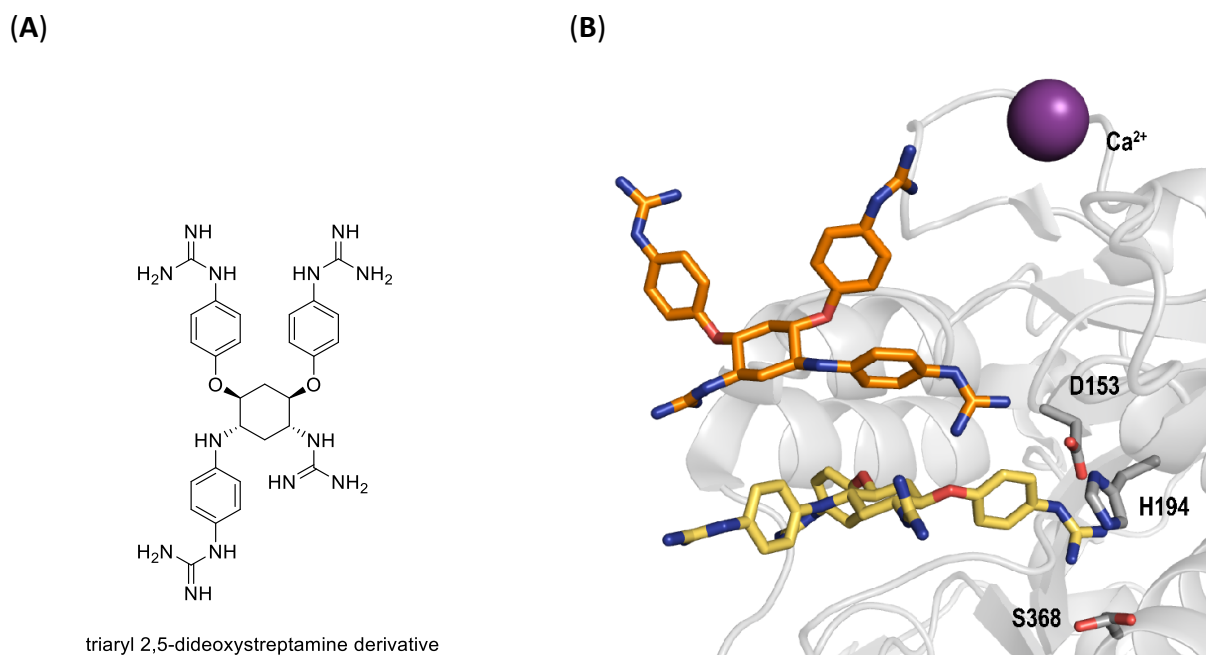


Figure 1.14 Structure of furin in complex with the triaryl 2,5-dideoxystreptamine derivative (PDB ID:5MIM). (A) Chemical structure of the inhibitor. (B) In the complex, two inhibitor molecules bind simultaneously to furin and are shown as a stick model with carbons in orange and yellow. Furin is depicted as a cartoon representation coloured in grey. Side chains of the catalytic residues are presented as a stick model with carbons in dark grey.

1.6 Toxicity study in mice

Toxicity studies in mice have been performed with some of these substrate-analogue inhibitors. A significant toxicity was determined for the most potent furin inhibitor **2/MI-1148** of this series. While the mice accepted an *ip.* dose of 2.5 mg kg⁻¹, all died at 5 mg kg⁻¹.¹³⁴ Its P2 Lys analogue 4-guanidinomethyl-phenylacetyl-Arg-Tle-Lys-4-Amba (**4/MI-1554**) showed a similar inhibitory potency against furin (K_i of 8.5 pM) and was slightly better tolerated (all mice accepted an *ip.* dose of 5 mg kg⁻¹, but died at 10 mg kg⁻¹). Furthermore, due to the significantly reduced toxicity of analogous inhibitors lacking the guanidine in P5 position or the P1-amidine (in both cases the mice tolerated a dose of 10 mg kg⁻¹) it was assumed that the severe toxic effects of inhibitor **2/MI-1148** are caused by the combined presence of the four strongly basic groups in this specific inhibitor. Furthermore, the toxicity of the tested inhibitors could not be correlated with the strength of the furin inhibition, which suggested that the severe toxicity of compound **2/MI-1148** must be caused by addressing a so far unidentified off-target.¹³⁴ More importantly, these results justified the further development of furin inhibitors as potential drugs.

2 Aim of the thesis

Over the past 10 years, several substrates, and numerous effective, reversibly binding, substrate-analogous inhibitors of furin had already been developed in our group. However, the most potent furin inhibitor **2/MI-1148** suffered from a significant toxicity in mice and rats. Therefore, new, potent, and well-tolerable furin inhibitors should be developed and characterized during this thesis, using the following strategies:

- A common approach to improve the stability and bioavailability of peptidic drugs is their cyclization. In the past, first cyclic PC inhibitors had been developed by various groups.^{114,135,136} Therefore, starting from the crystal structure of inhibitor **3** (H-Arg-Arg-Arg-Val-Arg-4-Amba) in complex with furin¹³¹ new types of cyclized inhibitors should be rationally developed, synthesized and characterized.
- Furthermore, based on the results from previous studies¹³⁴, where the toxicity of the furin inhibitors correlated with the number of their strongly basic guanidine and amidine groups, new effective furin inhibitors with reduced basicity should be developed, e.g., by replacement of arginine residues with the unnatural amino acid canavanine.
- In cooperation with other groups, the inhibitors should be tested for cytotoxicity and their antiviral potency in cell culture infected with various furin dependent viruses such as RSV and SARS-CoV-2 (in the group of Prof. Eva Böttcher-Friebertshäuser, Institute of Virology at the Philipps University Marburg) or flaviviruses like Dengue virus and West-Nil virus (in the group of Prof. Ralf Bartenschlager, Molecular Virology at the University Heidelberg).
- The most promising compound(s) should be tested for their toxicity in mice (studies performed by Eurofins Panlabs Taiwan Ltd.) and used for pharmacokinetic studies in rats (performed by Pharmacelsus GmbH, Saarbrücken).
- The best compound should be prepared in a 500 mg scale for first efficacy studies in infected animals studies.
- In addition to the inhibitor studies, novel improved fluorogenic substrates for enzyme kinetic measurements with basic PCs should be developed and characterized with available PCs (furin, PC1, PC2, PC5, and PC7).

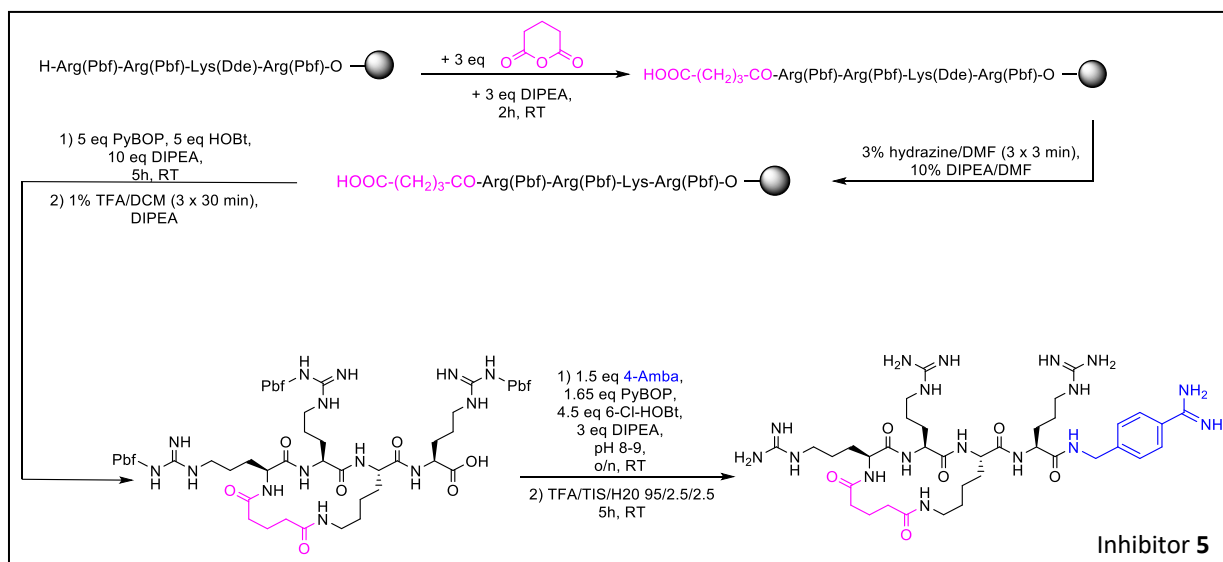
- For characterizing the potential S1/S2 and S2' cleavage sites in the spike protein of SARS-CoV, MERS-CoV, and SARS-CoV-2, a set of fluorescence resonance energy transfer (FRET) substrates should be prepared and examined for their cleavage efficiency by furin.

3 Results and discussion

3.1 Novel macrocyclic inhibitors of the basic proprotein convertase furin

The area of peptide therapeutics began in year 1922 with the extraction of insulin from animal pancreas. Since then, around 80 peptide drugs are commercially available on the global market. In recent years, the search for new peptide therapeutics has increased continuously with already more than 150 peptides in clinical development and another 400-600 peptides in preclinical studies.^{137,138} Nevertheless, peptides are generally considered as poor drug candidates due to their low oral bioavailability and tendency to be rapidly metabolized. These disadvantages often limit their further development for therapeutic use. To overcome these limitations of peptidic drugs, different strategies have been developed to improve their *in vivo* properties. For example, many cyclic peptides have been developed over the last years to improve their potency, bioavailability, selectivity, and stability, as well as to reduce their elimination. For instance, numerous cyclized peptidomimetic inhibitors of the viral NS3/4A serine protease like simeprevir, paritaprevir, grazoprevir, voxilaprevir, and glecaprevir have been approved for the therapy of hepatitis C infections.¹³⁹

There are already developments of cyclized peptidic inhibitors for the basic PC furin. Ramos-Molina *et al.* reported their findings on cyclic peptides containing several alternating arginine and hydrophobic tryptophan residues and few other cyclic derivatives, which showed only a moderate furin inhibition with K_i values between 0.1 and 1 μM .¹¹⁴ In a rational approach, the Kolmar group succeeded in engineering a monocyclic derivative of the bicyclic sunflower trypsin inhibitor into a potent furin inhibitor with an inhibition constant of 0.49 nM.¹³⁶ Using a structure-based approach starting from the crystal structure of furin in complex with the inhibitor **3** (Chapter 4.1, Figure 1)^{122,131}, several series of cyclic furin inhibitors have been prepared in this first publication.¹³² Different types of cyclizations have been performed; one between the side chains of the P6 and P2 residues by inserting a linker segment (Chapter 4.1; Scheme 1, Type 3a), one between the P5 backbone NH and the P3 side chain (**Scheme 3.1**), and another between the P6 backbone NH and the P3 side chain (Chapter 4.1; Scheme 1, Type 2). These cyclizations were introduced without steric conflict of the canonical binding mode of the P6/P5-P1 inhibitor segment to furin.



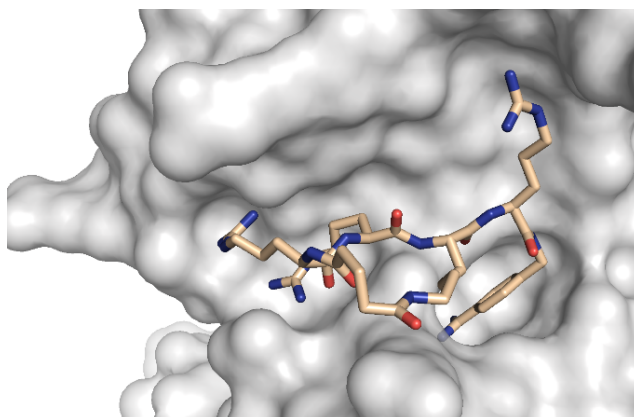
Scheme 3.1 Synthesis of inhibitor **5** cyclized between the P5 backbone NH and the P3 side chain via a glutaryl linker (in pink). After mild acidic liberation of the cyclized P6-P2 segment from the resin, the P1 4-Amba group (blue) was coupled in solution. Synthesis details are described in Chapter 4.1 in Scheme 1, Type 1.

In an additional approach, a known cyclic cell-penetrating peptide (CPP) containing a succinylated Phe-2-naphthylalanyl-(Arg)_n segment ($n = 3, 4$ or 5)^{140,141} of different length was fused with a P3-Lys side chain of a furin inhibitor. In the next inhibitor series, a head-to-tail cyclization of peptides with 6, 8 or 10 arginine residues was performed.

The synthesis of these different types of cyclization is summarized in Scheme 1 of Section 4.1.

The crystal structure determination of selected cyclized inhibitors in complex with human furin was performed by Dr. S. Dahms (University Salzburg) as previously described.¹³¹ In total, seven new crystal structures of cyclic inhibitors with furin have been determined. In general, both backbone and side chains of the P1-P5 segment of these cyclized inhibitors show almost identical intermolecular contacts to furin, when compared with the structure of the linear hexapeptide-derived inhibitor **3**.¹³¹ As an example, the structure of inhibitor **5** in complex with furin is shown in **Figure 3.1**. A complete electron density map could be generated for inhibitor **5**, also showing the exact positions of the more flexible glutaryl linker segment. The linker segment is solvent-exposed and not involved in polar contacts with furin. Unlike the crystal structure with inhibitor **3**, in this type of cyclization the carbon atom of the side-chain carboxyl group of Glu257 is rotated by approximately 120° to a more parallel orientation relative to the linker segment, presumably to avoid a steric clash with the amide bond of the linker.

(A)



(B)

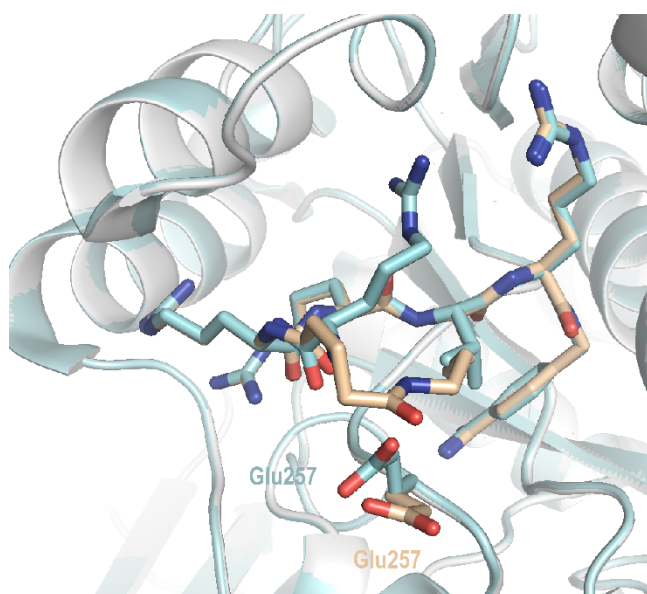


Figure 3.1 (A) Crystal structure of inhibitor **5** (stick model, carbons in beige) in complex with furin (PDB ID: 6HZA). (B) Alignment of inhibitor **5** and the hexapeptide inhibitor **3** (PDB ID: 6HZA, stick model, carbons in light blue). The glutaryl linker of inhibitor **5** is solvent-exposed and the Glu257 side chain is rotated, resulting in a parallel orientation to the linker segment.

Due to their higher flexibility, not all linker segments in the other complexes showed a clear electron density. This applies to complexes with two inhibitors containing the above mentioned cyclic CPP derived from the Phe-2-Nal-(Arg)_n sequence and two compounds possessing a P6-P2 cyclization via a piperazine-derived linker or a 4-aminomethyl-phenylacetyl linker. Nonetheless, the complete P1-P6 segment and P7 backbone atoms (if present) could be refined (shown in Chapter 4.1, Supporting information, Figure S1).

The inhibition constants of these inhibitors were obtained either under tight-binding conditions at similar enzyme and inhibitor concentrations (calculated by using the Morrison equation shown in Chapter 4.1., Supporting Information) or under classical conditions, where the lowest inhibitor concentration was at least ten times higher than the furin concentration.

The most potent inhibitor (c[succinyl-Phe-2-Nal-Arg₄-Lys]-Arg-4-Amba) of this publication, containing a cyclic CPP sequence, exhibits a K_i value of 54 pM. Compounds with cyclization between the P5 or P6 backbone NH and the P3 Lys side chain via a glutaryl spacer possess inhibition constants between 0.5 – 1 nM. A similar or slightly reduced potency was determined for compounds containing a linker-mediated cyclization between the P2 and P6 Lys sidechains. A significantly weaker potency was determined for all cyclic oligoarginines (K_i values > 20 nM) when compared with their non-cyclized analogues (K_i values between 5 and 10 nM). Our best novel cyclic furin inhibitors have stronger potencies compared to the already known cyclic PC inhibitors.^{135,136}

However, all these macrocyclic furin inhibitors revealed a negligible antiviral activity in cells infected with RSV (chapter 4.1, Figure 6), whereas a significant antiviral efficacy was found for the non-cyclized reference inhibitor **2/MI-1148** and for its P2 Lys analogue **4/MI-1554**. The lack of antiviral activity may be caused by the increased molecular weight of the inhibitors resulting in a reduced cell permeability, which prohibits a sufficient addressing of furin in the TGN, where the activation of the RSV fusion protein F occurs.

In summary, different types of cyclized furin inhibitors could be prepared, some of them are highly potent picomolar furin inhibitors *in vitro*. Crystal structures in complex with furin revealed the binding mode of several derivatives and confirmed that their P1-P5 or P1-P6 segment bind in a nearly identical way to furin as the non-cyclized hexapeptide H-Arg-Arg-Arg-Val-Arg-4-Amba (**3**).¹³¹ Nevertheless, all of these cyclized inhibitors showed only a negligible antiviral activity against RSV in cell culture studies.

For further details about this publication see section 4.1:

Thuy Van Lam van, Teodora Ivanova, Kornelia Harges, Miriam Ruth Heindl, Rory E. Morty, Eva Böttcher-Friebertshäuser, Iris Lindberg, Manuel E. Than, Sven O. Dahms, and Torsten Steinmetzer (2019) Design, synthesis, and characterization of macrocyclic inhibitors of the proprotein convertase furin. *ChemMedChem* 14(6), 673-685

3.2 Development of improved furin inhibitors with reduced basicity residues showing potent antiviral activity against SARS-CoV-2 in human airway cells

In cell culture, the replication of numerous furin-dependent viruses like the bird flu strains H5N1 and H7N1,^{58,142} chikungunya virus,¹²² West Nile and Dengue 2 virus,¹³⁴ mumps virus,¹⁴³ or respiratory syncytial virus (RSV)¹³² was significantly inhibited by our most potent multibasic furin inhibitor **2 /MI-1148**. However, this compound suffers from a significant toxicity in rats and mice. Its maximum tolerated dose (MTD) in mice is 2.5 mg kg⁻¹. A severe toxicity in mammals, e.g., non-specific side effects that can vary from acute hypotension^{144,145} to cardiac arrhythmias¹⁴⁶ and pseudo allergic reactions,^{145,147} have been also described for other polycationic compounds. Toxic effects of structurally related furin inhibitors were also described by a Canadian group and it was postulated that it is mainly or even solely depending on the presence of the C-terminal P1 4-Amba group in these inhibitors, while analogous compounds containing different P1 residues were less toxic.^{117,148} Nevertheless, derivatives containing the 4-Amba residue were also tolerated in mice at extremely high doses, e.g., the urokinase-type plasminogen activator inhibitor benzylsulfonyl-D-Ser-Ser-4-Amba was accepted up to an *ip.* dose of 100 mg kg⁻¹ in mice.¹⁴⁹ Furthermore, there exist approved benzamidine drugs such as the antiprotozoal pentamidine or the thrombin inhibitors dabigatran and melagatran, although the latter was later withdrawn from market. These data suggest that the toxicity of these furin inhibitors seems not to be attributed to the presence of the 4-Amba residue alone. However, besides the P1 benzamidine, inhibitor **2/1148** contains three additional strongly basic group, the guanidines in P2, P4, and P5 positions. Our previous studies with structurally closely related inhibitors suggested that the toxicity of these compound can be rather correlated with the number of these strongly basic groups, but not only with the presence of the benzamidine moiety and more importantly, not with the strength of furin inhibition.

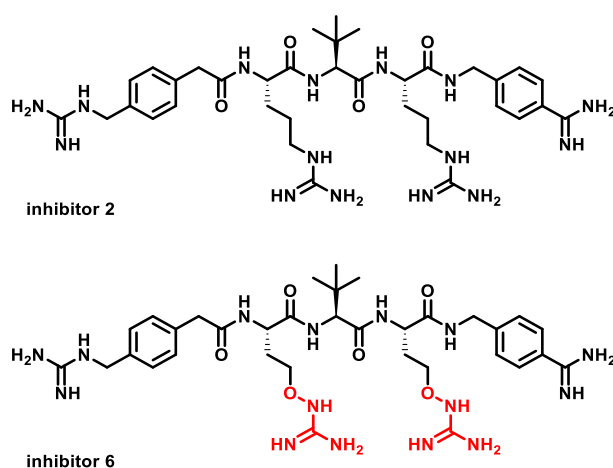
However, it is still unclear, which mechanism triggers the toxicity and which off-target could be responsible. To achieve an antiviral activity in cell cultures, the P2 and P4 side chains of the furin inhibitors must be protonated in the TGN at a pH of approximately 6.0. We hypothesized that the same fully protonated inhibitor species can also address the hypothetical off-target in the circulation at a pH close to 7.4. In this publication we exploited the pH difference in the TGN of the cells and blood circulation to design some kind of compartment-specific furin inhibitors. Ideally, the inhibitors should be almost fully protonated and fourfold positively

charged in the TGN under slightly acidic conditions, whereas they should be only partially charged in the circulation and extracellular space, which should lead to a weaker binding of the postulated off-target (Chapter 4.2., TOC-graphic).

A radical drop in the pK_a value of the P2 and P4 Arg residues was achieved by replacing one or both of them with the noncanonical amino acid Canavanine (Cav).¹⁵⁰ Due to the presence of the electronegative oxygen, the oxyguanidine sidechain of Cav possesses a considerably reduced pK_a value of 7.01 when compared with Arg (pK_a close to 13.5). The most potent inhibitor of this novel inhibitor series (Chapter 4.2., Table 1) obtains two Cav residues in P2 and P4 positions, while maintaining the P5 guanidine moiety and the P1 4-Amba residue (inhibitor **6/MI-1851**, **Figure 3.2A**). This inhibitor obtains a K_i value of 10.1 pM, which is comparable to its arginine analogue inhibitor **2/MI-1148**. Due to its strong potency, only inhibitor **6/MI-1851** is discussed in the following paragraphs of this chapter. For more details on all Cav-derived furin inhibitors, see Section 4.2.

By comparison with the previously determined crystal structure of inhibitor **2/MI-1148** in complex with furin, an identical side chain conformation and a well-defined electron density of the P1-P4 segment was observed for inhibitor **6/MI-1851**. In contrast, a less well-defined electron density was observed for the P5 4-guanidinomethyl-phenylacetyl residue, which exists in two conformations with similar occupancy, depicted as P5A and P5B in Chapter 4.2, Figure 1D. The conformation P5A is identical with the placement of the P5 group in inhibitor **2/MI-1148** leading to the same polar interactions with furin as found for inhibitor **2/MI-1148**, whereas these contacts are lacking in case of conformation P5B, which may explain the twofold weaker K_i value of inhibitor **6/MI-1851** (**Figure 3.2B**).

(A)



(B)

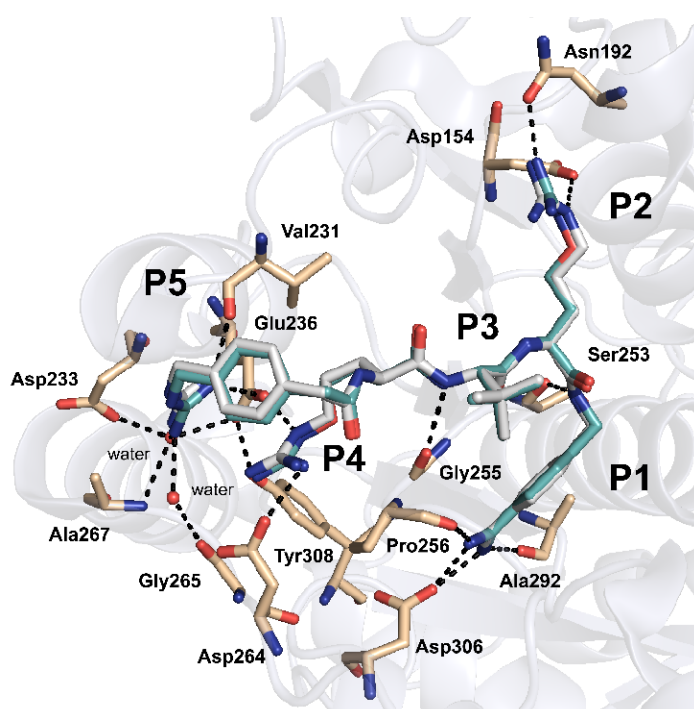


Figure 3.2 (A) Structures of inhibitors **2/MI.1148** and **6/MI-1851** (oxyguanidine groups of Cav in red). (B) Crystal structure of furin (carbon atoms of important active site residues are coloured in beige, the furin backbone is shown in cartoon style in white) in complex with inhibitor **6** (carbons in cyan, PDB ID: 6YD4) superimposed with analogue **2** (carbons in white, PDB ID: 4RYD), indicating the polar interactions. The conformation P5A is involved in several polar contacts to furin, which are absent in conformation P5B. The conformation PC5B is not shown (see Chapter 4.2.).

Like inhibitor **2/MI-1148**, the Cav analogue **6/MI-1851** belongs to the so-called tight-binding inhibitors (**Figure 3.3**). In contrast to classical inhibitors, tight-binding inhibitors already reveal a significant inhibitory effect while their concentrations are in the range of the used enzyme concentration. For such inhibitors, an apparent K_i^* value at a constant substrate concentration

can be calculated via the Morrison equation, which can be further converted to a true K_i value considering the substrate protection term (see Section 4.2, Supporting information).¹⁵¹

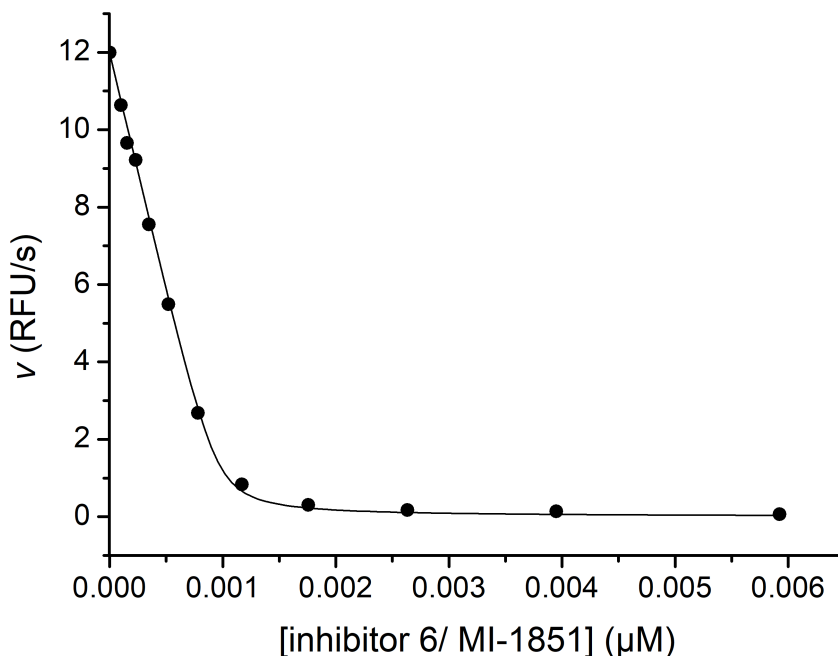


Figure 3.3 Inhibition of furin by inhibitor **6/MI-1851**. Measurements were performed under tight-binding condition in presence of substrate Phac-Arg-Val-Arg-Arg-AMC (12.5 μM in assay) using a furin concentration of 0.95 nM. The determined steady-state rates were fitted as function of the inhibitor concentration using the Morrison's equation for tight-binding inhibitors (see Section 4.2, Supporting information, Chapter 6, Equation 1).

For inhibitor **6/MI-1851**, a strong antiviral activity was found in a multicycle replication assay in A549 human lung cancer cells infected with RSV (**Figure 3.4**), as well as in HuH-7 cells infected with Dengue or West Nile virus (Chapter 4.2, Figure 4). In case of RSV, furin activates the precursor of the fusion protein F and in case of numerous pathogenic flaviviruses the prM precursor of the membrane protein M. The inhibition of both steps leads to an antiviral effect. Last year it was found that the enhanced transmissibility and pathogenicity of the novel SARS-CoV-2 is caused by the insertion of four residues in its spike protein at the S1/S2 site, which can be activated by furin (Chapter 3.3 or Section 4.3).

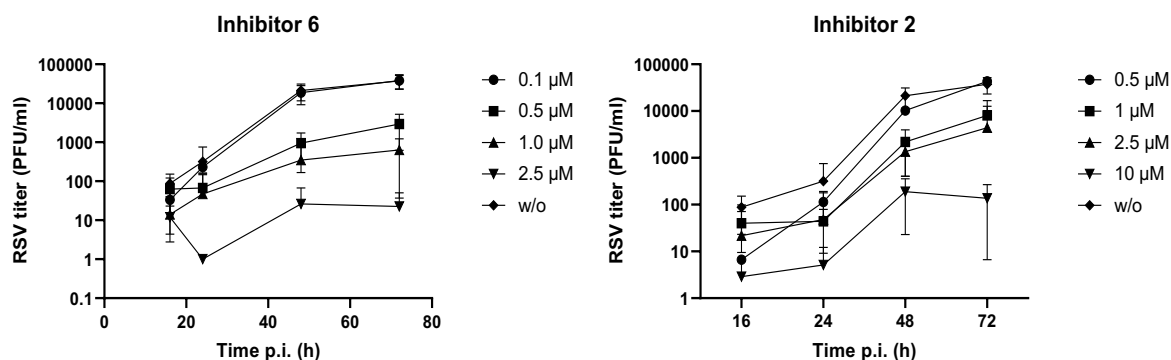


Figure 3.4 Inhibition of multicycle replication of RSV in A549 cells using different concentrations of inhibitors **6** and **2**. After indicated times the virus titers were determined by a plaque assay.

Compound **6/MI-1851** was also tested for toxicity in mice. After intraperitoneal treatment in mice at day 1 with a dose of 2.5 mg kg^{-1} inhibitor **6/MI-1851**, all four mice survived. While the doses were consistently increased via 5, 10, and 15 mg kg^{-1} at time intervals of 24 hours, all mice survived without any mentionable signs of side effects suggesting a significantly reduced toxicity compared to inhibitor **2/MI-1148** (see Table 2 in Chapter 4.2). Considering the reduced toxicity and significant antiviral activity against RSV, DENV-2 and WNV (**Figure 3.4**) as well as the rather similar K_i value of 10.1 pM for compound **6/MI-1851** and its isostructural Arg analogue **2/MI-1148** ($K_i = 5.5 \text{ pM}$), it can be concluded that the toxicity of these compounds is not caused by the inhibition of intracellular furin. This result has strengthened our assumption that the toxicity of the strongly multibasic inhibitor **2/MI-1148** depends on addressing of an unknown off-target and can be reduced by deleting some of the strongly basic guanidine groups.

In summary, by replacing arginine with canavanine residues, we succeeded in synthesizing new highly potent furin inhibitors that show a very similar binding mode as previously seen with their arginine analogues. These canavanine inhibitors show a significant reduction of viral titer in cells infected with furin-dependent viruses. The most suitable overall profile was found for inhibitor **6/MI-1851**.

It was demonstrated in an additional publication that inhibitor **6/MI-1851** strongly suppresses the multicyclic replication of SARS-CoV-2 in human Calu-3 airway cells. This result revealed the crucial contribution of furin in activating the S protein of SARS-CoV-2. The effective cleavage of the S1/S2 site in S of SARS-CoV-2 could be additionally demonstrated by in vitro studies with soluble furin and newly synthesized FRET substrates derived from the S1/2 site sequences

of various coronaviruses. In contrast, FRET substrates derived from the S2' site, which is most likely activated by the trypsin-like serine protease TMPRSS2 revealed a negligible cleavage by furin (see Chapter 3.3 and 4.3).⁷⁸ Both proteases, furin as well as TMPRSS2 are essential for the S activation of the newly emerged SARS-CoV-2 in human airway epithelial cells. Moreover, inhibitor **6/MI-1851** in combination with a TMPRSS2 inhibitor showed an enhanced antiviral activity against SARS-CoV-2 in human respiratory cells compared to the single treatments. Thus, a combination of inhibitors of both S activating proteases or even with a third antiviral agent may represent a suitable therapeutic strategy for the treatment of SARS-CoV-2 infections. Such combination therapies should allow a reduction of the individual inhibitor doses leading to reduced side effects. Although the available data from cell culture studies justify a further preclinical characterization of the furin inhibitor **6/MI-1851** as potential broad spectrum antiviral agent, its efficacy has also to be demonstrated in an appropriate animal model infected with furin-dependent viruses, e.g., SARS-CoV-2.

For further details about these publications see sections 4.2 and 4.3:

Thuy Van Lam van, Miriam Ruth Heindl, Christine Schlutt, Eva Böttcher-Friebertshäuser, Ralf Bartenschlager, Gerhard Klebe, Hans Brandstetter, Sven O. Dahms, and Torsten Steinmetzer (2021) The basicity makes the difference – Improved canavanine-derived inhibitors of the proprotein convertase furin. *ACS Medicinal Chemistry Letters* 12, 3, 426–432

Dorothea Bestle*, Miriam Ruth Heindl*, Hannah Limburg*, **Thuy Van Lam van**, Oliver Pilgram, Hong Moulton, David A. Stein, Kornelia Hades, Markus Eickmann, Olga Dolnik, Cornelius Rohde, Hans-Dieter Klenk, Wolfgang Garten, Torsten Steinmetzer and Eva Böttcher-Friebertshäuser (2020) TMPRSS2 and furin are both essential for proteolytic activation of SARS-CoV-2 in human airway cells. *Life Science Alliance*. 3(9)

*These authors contributed equally to this work.

3.3 Cleavage of SARS-CoV-2 S1/S2 and S2' site fluorescence resonance energy transfer (FRET)-substrates by furin

3.3.1 S1/S2 site FRET-substrates

Since the outbreak of SARS-CoV-2 infections in late December 2019, a tremendous effort for understanding and treating the new disease COVID-19 was invested by countless groups from all over the world.^{152,153} In contrast to SARS-CoV from 2002/2003 it was postulated only a few weeks later that the host protease furin contributes to the activation of the SARS-CoV-2 S protein.⁷⁶ Based on sequence alignments it was found that the S1/S2 site of SARS-CoV-2 S harbors a potential furin cleavage site through a four amino acids long P-R-R-A insertion directly before Arg685↓). Thus, a series of FRET-substrates derived from the S1/S2 cleavage site of various CoV was synthesized to compare their cleavage efficacy by furin. The structures of the prepared FRET-substrates are shown below (**Figure 3.5**).

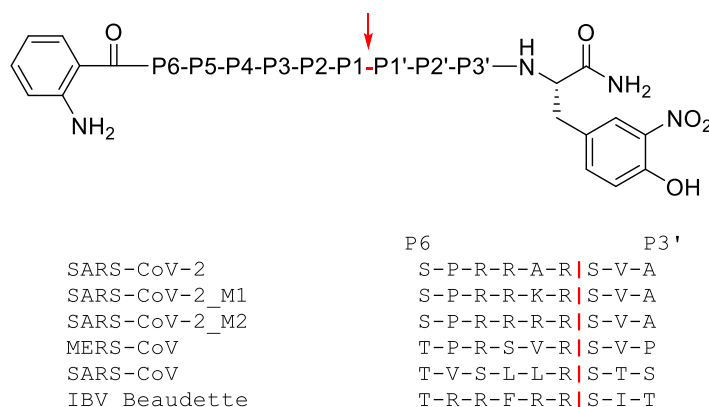


Figure 3.5 FRET-substrates derived from the S1/S2 cleavage site of the indicated CoVs. The substrates contain an N-terminal 2-aminobenzoyl fluorophore in P7 position and a C-terminal 3-nitrotyrosine amide as a P4' residue. Analogous substrates of MERS-CoV, SARS-CoV, and of an avian CoV (infectious bronchitis virus (IBV)) were prepared as reference compounds. Furthermore, two potential mutants of the SARS-CoV-2 cleavage site were synthesized (M1 and M2) to generate even more efficient cleavage sites for furin. The furin cleavage site is shown as arrow or stroke in red.

The protected substrates were synthesized on a Rink-amide-MBHA resin using a standard Fmoc SPPS protocol. After synthesis, the peptide was cleaved from the resin and fully deprotected under strong acidic condition and purified by preparative HPLC. The peptides were obtained as lyophilized TFA salts, their analytical data are summarized in **Table 3.1**.

Table 3.1 Analytical data of synthesized FRET-substrates derived from the S1/2 site of various CoV.

	Substrate	HPLC R_t (min)	MS calc	MS found [M+H] ⁺
SARS-CoV-2	2Abz-SPRRARSVA-Tyr(NO ₂)-NH ₂	27.6	1324.67	1325.81
SARS-CoV-2_M1	2Abz-SPRRKRSVA-Tyr(NO ₂)-NH ₂	25.9	1381.73	461.59 ^[a]
SARS-CoV-2_M2	2Abz-SPRRRRSVA-Tyr(NO ₂)-NH ₂	26.3	1409.74	470.92 ^[a]
MERS-CoV	2Abz-TPRSVRSVP-Tyr(NO ₂)-NH ₂	30.5	1323.67	1324.83
SARS-CoV	2Abz-TVSLLRSTS-Tyr(NO ₂)-NH ₂	38.8	1288.64	1289.60
IBV (Beaudette)	2Abz-TRRFRRSIT- Tyr(NO ₂)-NH ₂	31.4	1517.80	760.10 ^[b]

^[a][M+3H]³⁺/3; ^[b][M+2H]²⁺/2

The cleavage efficiency was determined by enzyme kinetic measurement using human furin (**Figure 3.6**). As predicted, the FRET substrate of the SARS-CoV-2 S1/S2 site was efficiently cleaved by furin. In contrast, a negligible cleavage was found for the monobasic SARS-CoV sequence and a moderate cleavage of the MERS-CoV-derived substrate, which also contains two Arg residues in P1 and P4 positions. As expected, when the P2 Ala residue of the SARS-CoV-2 sequence was mutated to Arg (M1) or Lys (M2), the cleavage efficiency of both tetrabasic substrates was higher as found for the wild type, especially with Arg in P2 position. The reference substrate derived from the CoV-IBV sequence was also very efficiently processed by furin. Summarizing the results, our data showed an efficient cleavage of the S1/S2 site in the S protein of the novel SARS-CoV-2 by furin *in vitro*. Because of the ubiquitous distribution of furin, this might explain the much more efficient transmission of SARS-CoV-2 when compared with SARS-CoV or MERS-CoV, which most likely use different and less abundant host proteases for activating the S1/S2 site.

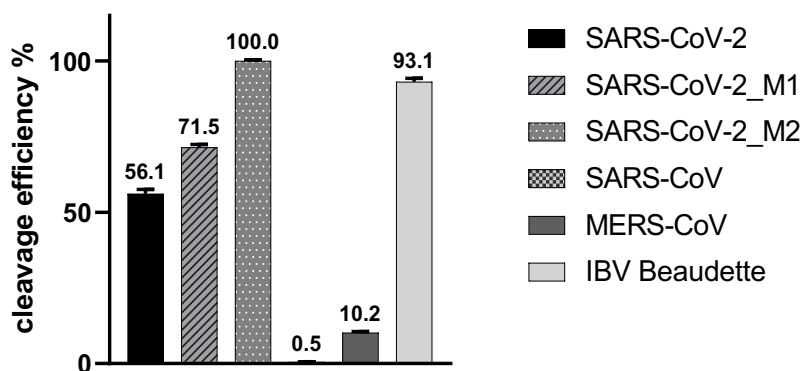


Figure 3.6 Cleavage efficiency of the S1/S2 site-derived FRET substrates from different CoV by furin. The assay was performed with a substrate concentration of 20 μ M in presence of 0.5 nM furin. The cleavage efficiency of the mutant M2 of the SARS-CoV-2 sequence was set as 100%.

3.3.2 S2' site FRET-substrates

Several studies suggested that two different host proteases, TMPRSS2 at the S2' site and furin at the S1/S2 site, are required for the activation of the S protein of SARS-CoV-2.^{76,154,155} However, the S protein of certain other CoV like IBV Beaudette are activated by furin at its S2' site¹⁵⁶ and it was also suggested that furin might be responsible for the S2' activation in case of MERS-CoV S, which possesses two Arg residues in P1 and P4 position before its fusion peptide. In contrast, SARS-CoV-2 S contains a paired basic amino acid motif (KR↓) together with a Lys in P5 position at its S2' site, which might be also activatable to some extent by furin, although furin substrates lacking the important P4 Arg usually requires an additional basic residue in P6 position.²⁴ To clarify furin's role in a potential S2' activation, a series of additional FRET substrates derived from this cleavage site has been prepared (**Figure 3.7**).

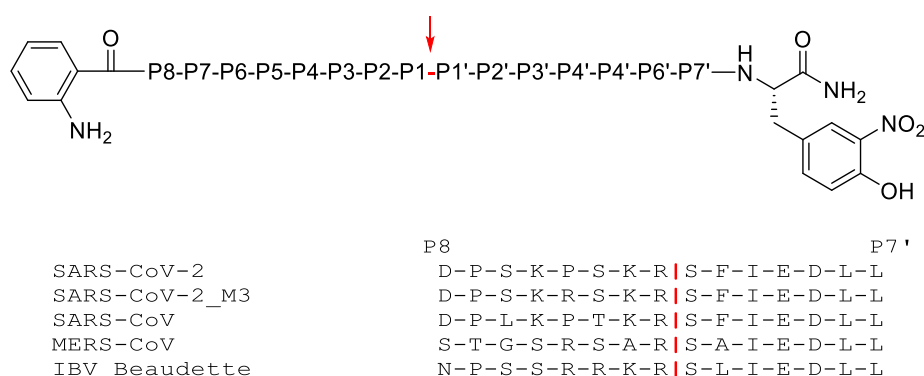


Figure 3.7 Structures of the FRET-substrates derived from the S2' site of certain CoV S proteins. Similar as in the previous S1/S2 site series, all substrates possess an N-terminal 2-aminobenzoyl fluorophore and a C-terminal 3-nitrotyrosine amide. In addition, one mutated substrate of the SARS-CoV-2 sequence at the P4 position was synthesized (M3). The S2' cleavage in front of the fusion peptide is indicated by an arrow or stroke in red.

The preparation of these substrates was performed as described above for the S1/S2-derived FRET-substrates (Chapter 3.3.1). Their analytical data are shown in **Table 3.2**.

Table 3.2 Analytical data of synthesized FRET-substrates derived from the S2' site of certain CoV S proteins.

	Substrate	HPLC R_t (min)	MS calc	MS found [M+H] ⁺
SARS-CoV-2	2Abz-DPSKPSKRSFIEDLL-Tyr(NO ₂)-NH ₂	43.6	2057.02	1029.98 ^[a]
SARS-CoV-2_M3	2Abz-DPSKRSKRSFIEDLL-Tyr(NO ₂)-NH ₂	43.0	2116.07	1059.58 ^[a]
SARS-CoV	2Abz-DPLKPTKRSFIEDLL-Tyr(NO ₂)-NH ₂	46.3	2097.09	1050.20 ^[a]
MERS-CoV	2Abz-STGSRARSFIEDLL-Tyr(NO ₂)-NH ₂	42.6	1887.91	943.9 ^[a]
IBV (Beaudette)	2Abz-NPSSRRKRSFIEDLL-Tyr(NO ₂)-NH ₂	43.3	2109.11	1056.10 ^[a]

^[a][M+2H]²⁺/2

These FRET-substrates were tested in an enzyme kinetic assay with soluble human furin (**Figure 3.8**). When compared with the cleavage efficiency of the IBV Beaudette sequence, the data clearly revealed that the S2' site of SARS-CoV-2 S is only marginally processed by furin.

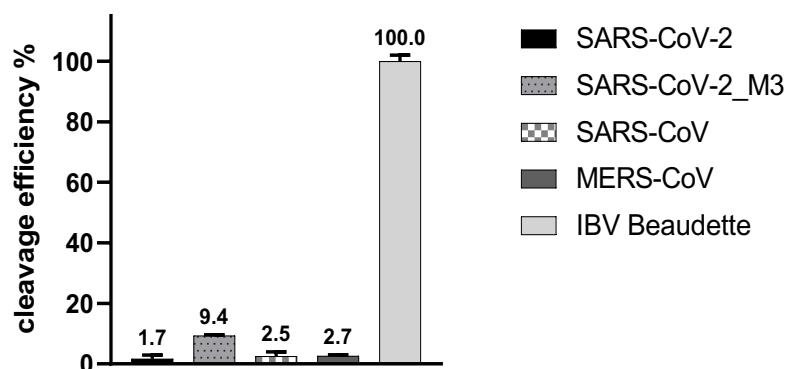


Figure 3.8 Cleavage efficiency of FRET substrates derived from the S2' site of certain CoV S proteins by furin. The kinetic assay was performed with a 20 μ M concentration of the substrates in presence of 0.5 nM furin. The cleavage efficiency of the IBV Beaudette derived substrate was set as 100%.

The mutated substrate M3 containing the P4 Arg is somewhat better cleaved by furin, but also much less than the IBV Beaudette sequence. A marginal activation by furin was also found for the SARS-CoV and MERS-CoV sequences. All these data suggest that another host protease, e.g., the trypsin-like serine protease TMPRSS2, must be involved at the S2' activation of the SARS-CoV, SARS-CoV-2, and MERS-CoV sequences.

For further details about this publication see section 4.3:

Dorothea Bestle*, Miriam Ruth Heindl*, Hannah Limburg*, **Thuy Van Lam van**, Oliver Pilgram, Hong Moulton, David A. Stein, Kornelia Hades, Markus Eickmann, Olga Dolnik, Cornelius Rohde, Hans-Dieter Klenk, Wolfgang Garten, Torsten Steinmetzer, and Eva Böttcher-Friebertshäuser (2020) TMPRSS2 and furin are both essential for proteolytic activation of SARS-CoV-2 in human airway cells. Life Science Alliance. 3(9)

*These authors contributed equally to this work.

3.4 Novel AMC substrates for basic proprotein convertases

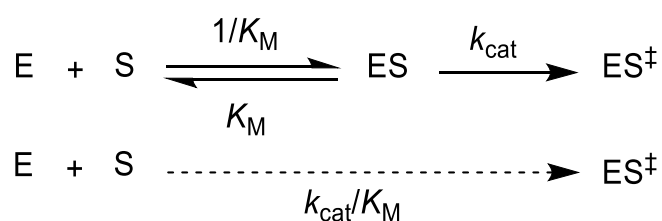
For the biochemical characterization of proteases and inhibitor studies, enzyme kinetic *in vitro* assays with synthetic chromogenic or fluorogenic substrates and recombinant soluble enzymes are usually used. For basic PC, several peptidic substrates with a C-terminal 7-amino-4-methylcoumarin (AMC) fluorophore have been described to date. However, most groups use only one standard substrate (S1/Ref. 1), which is cleaved by all basic PCs, regardless of some differences in their preferred cleavage pattern. Based on results from studies with substrate-analogue inhibitors, 11 new substrates (Table 3.3 or Chapter 4.4) have been synthesized and tested with five available basic PCs. Furthermore, two reference substrates have been used, the commercially available substrate (substrate 1/Ref.1) and our furin standard substrate (S2/Ref.2). The Table 3.4 below shows the kinetic constants including k_{cat}/K_M values, also named as performance constant¹⁵⁷ or enzyme efficiency¹⁵⁸ for very suitable substrates of the tested basic PCs.

Table 3.3 Sequences of the synthesized substrates.

	substrate								
	P7	P6	P5	P4	P3	P2	P1	P1'	
Ref.1			pGlu	Arg	Thr	Lys	Arg	AMC	× 3 AcOH
Ref.2			Phac	Arg	Val	Arg	Arg	AMC	× 3 TFA
S3			Ac	Arg	Val	Arg	Arg	AMC	× 3 TFA
S4			Phac	Arg	Val	Lys	Arg	AMC	× 3 TFA
S5			Phac	Arg	Tle	Arg	Arg	AMC	× 3 TFA
S6			Phac	Arg	Tle	Lys	Arg	AMC	× 3 TFA
S7		Ac	Arg	Arg	Val	Lys	Arg	AMC	× 4 TFA
S8		Ac	Arg	Arg	Tle	Arg	Arg	AMC	× 4 TFA
S9		Ac	Arg	Arg	Tyr	Lys	Arg	AMC	× 4 TFA
S10		Ac	Arg	Arg	Tle	Lys	Arg	AMC	× 4 TFA
S11			H-Arg	Arg	Tle	Lys	Arg	AMC	× 4 TFA
S12	Ac	Arg	Arg	Arg	Tle	Lys	Arg	AMC	× 5 TFA
S13		H-Arg	Arg	Arg	Tle	Lys	Arg	AMC	× 5 TFA

The catalytic rate constant k_{cat} is the turnover number, which describes how many substrate molecules are transformed into product per unit time by an enzyme molecule. In other words, k_{cat} describes the step from the ES complex to the transition state ES^\ddagger , i. e., a small difference of the free energy of both states leads to a large k_{cat} value.¹⁵⁸ In contrast, the K_M value reports the affinity of the substrate to the active site of the enzyme, whereas it mainly refers to the dissociation reaction of the ES complex to free E + S. Contrary, the reciprocal of K_M ($1/K_M$)

refers to the association step from E and S to ES.¹⁵⁸ By combining both constants as the term k_{cat}/K_M , it is possible to describe the catalytic efficiency of an enzyme for a particular substrate. That means, the greater the ratio, the higher the rate of catalysis is. The k_{cat}/K_M term, which corresponds to an apparent second-order rate constant, ultimately describes how well free enzyme and free substrate reach the transition state ES^\ddagger of the reaction.¹⁵⁸ This includes the formation (association) of the ES complex and how the transition state ES^\ddagger is reached starting from ES.



For practical purpose, a suitable substrate should ideally possess a high k_{cat} value providing sufficiently rapid cleavage rates even at low enzyme concentrations, as well as a relative low K_M value. Moreover, at certain substrate concentrations, substrates with lower K_M values provide a stronger protection of the enzyme for inhibition by competitive inhibitors.

With the improved substrate **S8**, it was now possible to perform enzyme kinetic measurements with 10-fold reduced furin concentrations. Compared to our standard furin substrate **Ref.2/S2** (Chapter 4.4.), **S8** possesses a 7-fold reduced K_M value and nearly 2-fold higher k_{cat} value. This enabled inhibition constant determinations of our previously described tight-binding inhibitors with K_i values < 100 pM under classical conditions without the exact knowledge of the enzyme concentration. This allows a more robust determination of K_i values compared to measurements under tight-binding conditions, which requires the precise knowledge of the used enzyme concentration when using the Morrison equation¹⁵⁹ (see Chapter 4.4., Equation 1).

Table 3.4 Selected substrates for furin, PC1, PC2, and PC7 including their determined K_M , k_{cat} , and k_{cat}/K_M values. For PC5A, K_M , V_{max} , and V_{max}/K_M values are shown below.

No.	K_M (μM)	k_{cat} (s^{-1})	k_{cat}/K_M ($\text{M}^{-1} \text{s}^{-1}$)
Furin			
Ref. substrate 1	2.91 ± 0.24	0.296 ± 0.004	1.02×10^5
Ref. substrate 2	5.22 ± 0.18	0.585 ± 0.021	1.12×10^5
S5	11.1 ± 1.4	1.91 ± 0.07	1.72×10^5
S8	0.765 ± 0.012	1.18 ± 0.02	1.55×10^6
PC1			
Ref. substrate 1	19.5 ± 1.2	0.0242 ± 0.0027	1.24×10^3
Ref. substrate 2	34.5 ± 2.4	0.0569 ± 0.0063	1.65×10^3
S3	56.3 ± 2.7	0.0680 ± 0.0056	1.21×10^3
S8	12.9 ± 1.1	0.0311 ± 0.0034	2.40×10^3
PC2			
Ref. substrate 1	38.2 ± 5.6	0.0690 ± 0.0025	1.81×10^3
Ref. substrate 2	46.9 ± 5.2	0.00990 ± 0.00073	211
S6	7.02 ± 0.35	0.0740 ± 0.0063	1.05×10^4
S7	11.2 ± 2.8	0.127 ± 0.006	1.13×10^4
S10	4.11 ± 0.91	0.0439 ± 0.00156	1.07×10^4
S13	5.91 ± 1.55	0.0686 ± 0.0026	1.16×10^4
PC7			
Ref. substrate 1	28.3 ± 1.6	0.275 ± 0.010	9.72×10^3
Ref. substrate 2	2.46 ± 0.92	0.0260 ± 0.0024	1.10×10^4
S10	2.96 ± 0.51	1.46 ± 0.08	4.94×10^5
S11	1.77 ± 0.36	1.38 ± 0.06	7.79×10^5
PC5A			
	K_M (μM)	V_{max} (RFU/s)	V_{max}/K_M (RFU $\times\text{M}^{-1} \text{s}^{-1}$)
Ref. substrate 1	7.10 ± 0.98	13.8 ± 0.7	1.94×10^3
Ref. substrate 2	11.2 ± 1.2	7.78 ± 0.06	6.95×10^5
S4	6.35 ± 1.24	11.5 ± 1.8	1.81×10^6
S5	9.64 ± 2.13	15.8 ± 1.1	1.63×10^6
S8	3.80 ± 0.49	11.4 ± 1.0	3.00×10^6

Moreover, under these conditions when using substrate **S8** at a furin concentration of 95 pM, non-linear progress curves were observed in measurements with inhibitor **2/MI-1148** that were never noticed before with the standard furin substrate **Ref.2/S2** at 10-fold higher furin concentration (Chapter 4.4, Figure 3). The observed slow-binding behaviour of inhibitor **2/1148** allowed for the first time the determination of the association rate constant k_{on} , and the dissociation rate constant k_{off} . The methods and equations used for the determination of K_i , k_{on} , and k_{off} values for inhibitor **2/MI-1148** are described in the publication in Chapter 4.4.

Furthermore, the elongation of the substrates with additional basic residues in P5 and P6 positions increases the $k_{\text{cat}}/K_{\text{M}}$ values in most cases mainly due to considerably reduced K_{M} values. However, this beneficial effect is often impaired by reduced k_{cat} values leading to some kind of k_{cat} and K_{M} compensation.¹⁶⁰ Substrates with low k_{cat} values are not suitable for practical measurements, even though they possess high enzyme efficiency ($k_{\text{cat}}/K_{\text{M}}$).

In summary, in this work several improved peptidic AMC substrates for the basic proprotein convertases furin, PC1, PC2, and PC7 in comparison to commonly used reference substrates **S1** and **S2** could be developed. In contrast, for PC5A the reference substrate **S1** is better suited than the newly prepared compounds.

For further details about this topic see section 4.4:

Thuy Van Lam van, Teodora Ivanova, Iris Lindberg, Eva Böttcher-Friebertshäuser, Torsten Steinmetzer, and Kornelia Hardes - Design, synthesis, and characterization of novel fluorogenic substrates of proprotein convertases furin, PC1, PC2, PC5, and PC7 (Manuscript in preparation; planned for the Journal: Analytical Biochemistry)

4 Publications

4.1 Design, synthesis, and characterization of macrocyclic inhibitors of the proprotein convertase furin

Thuy Van Lam van, Teodora Ivanova, Kornelia Hardes, Miriam Ruth Heindl, Rory E. Morty, Eva Böttcher-Friebertshäuser, Iris Lindberg, Manual E. Than, Sven O. Dahms, and Torsten Steinmetzer (2019)

ChemMedChem. 14(6), 673-685

DOI: 10.1002/cmdc.201800807

Design, Synthesis, and Characterization of Macrocyclic Inhibitors of the Proprotein Convertase Furin

Thuy Van Lam van,^[a] Teodora Ivanova,^[a] Kornelia Harges,^[a] Miriam Ruth Heindl,^[b] Rory E. Morty,^[c] Eva Böttcher-Friebertshäuser,^[b] Iris Lindberg,^[d] Manuel E. Than,^[e] Sven O. Dahms,^[f] and Torsten Steinmetzer*^[a]

The activation of viral glycoproteins by the host protease furin is an essential step in the replication of numerous pathogenic viruses. Thus, effective inhibitors of furin could serve as broad-spectrum antiviral drugs. A crystal structure of an inhibitory hexapeptide derivative in complex with furin served as template for the rational design of various types of new cyclic inhibitors. Most of the prepared derivatives are relatively potent furin inhibitors with inhibition constants in the low nanomolar or even sub-nanomolar range. For seven derivatives the crystal structures in complex with furin could be determined. In three

complexes, electron density was found for the entire inhibitor. In the other cases the structures could be determined only for the P6/P5-P1 segments, which directly interact with furin. The cyclic derivatives together with two non-cyclic reference compounds were tested as inhibitors of the proteolytic activation and replication of respiratory syncytial virus in cells. Significant antiviral activity was found for both linear reference inhibitors, whereas a negligible efficacy was determined for the cyclic derivatives.

Introduction

Peptides are readily accessible and can have wide structural variability, making them attractive tools for the identification and characterization of suitable binding pockets in initial drug design campaigns, e.g., in the field of protease inhibitors. On the other hand, peptidic structures usually suffer from numerous drawbacks such as poor enzymatic stability and rapid elimination; both reasons often limit their further development.^[1] A classical strategy to overcome some of these disadvantages is their modification with N- and C-terminal capping groups and the replacement of proteinogenic amino acids by unusual residues in combination with numerous types of macrocyclization.

Successful examples of approved macrocyclic peptidomimetic drugs are numerous inhibitors of the NS3/4A serine protease of the hepatitis C virus, such as simeprevir, paritaprevir, grazoprevir, voxilaprevir, and glecaprevir,^[2] which are derived from the linear analogues boceprevir, telaprevir, and asunaprevir. Many other examples of potent and selective experimental macrocyclic serine protease inhibitors have been described, including inhibitors of the clotting enzymes thrombin,^[3] factor VIIa^[4–6] or factor XIa,^[7] and of the fibrinolytic protease plasmin.^[8,9] These reports encouraged us to test various macrocyclizations for the design of new furin inhibitors.

Furin belongs to the family of Ca²⁺-dependent proprotein convertases (PCs), all of which contain a subtilisin-like serine protease domain.^[10,11] Furin and the other six basic PCs—PC1, PC2, PC4, PACE4, PC5, and PC7—cleave their substrates at multibasic sequences mainly after arginine, whereas the nonbasic PC site-1 protease (S1P) cleaves preferentially after leucine, valine or isoleucine. Secreted PCSK9, a second nonbasic PC, exists in an enzymatically inactive complex with its inhibitory propeptide. The PCs activate proproteins including hormones, enzymes, receptors or adhesion proteins and are involved in numerous physiological processes. In contrast, PCs also promote cancer progression, osteoarthritis, hypercholesterolemia, and other human pathologies.^[12] Notably, there are also contrary reports describing a protective role of furin in certain cancer types^[13,14] or osteoarthritis.^[15] Furthermore, by activation of viral glycoproteins or bacterial toxins, furin and other PCs contribute to the propagation of certain pathogenic viruses and to the toxicity of some bacteria.^[11,12] Therefore, furin could be a suitable target for short-term treatment of certain PC-dependent infectious diseases.

[a] T. V. Lam van, Dr. T. Ivanova, Dr. K. Harges, Prof. T. Steinmetzer
Institute of Pharmaceutical Chemistry, Philipps University, Marbacher Weg
6, 35032 Marburg (Germany)
E-mail: steinmetzer@uni-marburg.de


[b] M. R. Heindl, Prof. E. Böttcher-Friebertshäuser
Institute of Virology, Philipps University, Hans-Meerwein-Str. 2, 35043 Mar-
burg (Germany)

[c] Dr. R. E. Morty
Department of Lung Development and Remodelling, Max Planck Institute
for Heart and Lung Research, Bad Nauheim (Germany)

[d] Prof. I. Lindberg
Department of Anatomy and Neurobiology, University of Maryland Medical
School, Baltimore, MD 21201 (USA)

[e] Dr. M. E. Than
Protein Crystallography Group, Leibniz Institute on Aging—Fritz Lipmann
Institute, Beutenbergstr. 11, 07745 Jena (Germany)

[f] Dr. S. O. Dahms
Department of Biosciences, University of Salzburg, Billrothstrasse 11, 5020
Salzburg (Austria)

 Supporting information and the ORCID identification number(s) for the
author(s) of this article can be found under:
<https://doi.org/10.1002/cmdc.201800807>.

There are so far three reports regarding cyclized peptidic inhibitors against basic PCs. In an initial study, several cationic cyclized peptides were tested, which were originally designed as cargo molecules with cell-penetrating properties. These peptides contain four or five arginine residues in the ring segment and inhibit furin with K_i values in the range of 0.1–1 μM .^[16] In a second study, various head-to-tail, head-to-side-chain, and side-chain-to-tail cyclizations within multibasic octapeptides were investigated; the best two compounds target furin and PACE4 with slightly improved inhibition constants close to 20 nM and 30 nM, respectively.^[17] In a third approach, several truncated analogues of the bicyclic sunflower trypsin inhibitor (SFTI-1) were developed; the best monocyclic 12-mer peptide of this series contains a lysine as P1 residue and inhibits furin with a K_i value of 0.49 nM.^[18]

To improve the potency of such cyclic analogues, we tried to use a rational, structure-based design strategy by starting from the recently determined crystal structure of inhibitor 1 (H-Arg-Arg-Arg-Val-Arg-4-amidinobenzylamide, $K_i = 33.7 \mu\text{M}$) in complex with furin.^[19,20] The structure (Figure 1) indicates that various cyclizations between the P5 or P6 backbone NH and the P3 side chain (types 1 and 2, Scheme 1), as well as between the side chains of the P6 and P2 residues (type 3), might be feasible without introducing a steric conflict of the canonical binding mode of the P6/P5-P1 inhibitor segment to furin.

Moreover, two additional cyclization strategies were investigated. In a fourth approach, a cyclic cell-penetrating peptide (CPP) containing a Phe-2-naphthylalanyl-(Arg)_x segment with 3, 4, or 5 Arg residues in the ring structure was fused together with the P3 Lys side chain of a furin inhibitory segment via a glutaryl spacer (type 4, Scheme 1). This short cyclic amphiphilic peptide motif rich in arginine and two hydrophobic residues (Phe-2-Nal) was recently developed by Pei and co-workers,^[21,22]

and it was demonstrated to bind strongly to cell membranes followed by subsequent internalization. As a fifth type, we simply performed a head-to-tail cyclization of peptides with 6, 8, or 10 arginine residues and also tested the potency of their linear analogues. Moreover, four additional linear inhibitors were prepared in which the P4-P1 inhibitor segment Arg-Val-Arg-4-Amba was N-terminally elongated with known acetylated CPP sequences derived from penetratin, TAT, transportan, and polyarginine.^[23]

The inhibitory potency of these compounds was determined in enzyme kinetic assays with furin. Selected inhibitors were also tested in infection studies in cells. Moreover, for three analogues, the complete crystal structure could be determined, also showing the flexible solvent-exposed part of the ring segment. For other cyclic analogues, defined electron density could only be found for the inhibitor segment that directly interacts with the furin surface, whereas the density for the more flexible linker part was missing. The results are described below.

Results

Synthesis

Replacement of valine in inhibitor 1 by lysine allows convenient cyclizations between the P5 or P6 backbone NH and the P3 side chain. The various side-chain-protected peptide segments were prepared on 2-chlorotrityl chloride (2-CTC) resin, which was initially loaded either with Fmoc-Arg(Pbf)-OH (for compounds 2, 4, 9–11, and 15–24), Fmoc-Lys(Dde)-OH (for inhibitors 5–8), or Fmoc-Lys(Boc)-OH (for compounds 3 and 12–14), using a standard Fmoc solid-phase peptide synthesis (SPPS) protocol. For type 1, 2 and type 4 inhibitors, the terminal amino group was reacted with glutaric or succinic anhy-

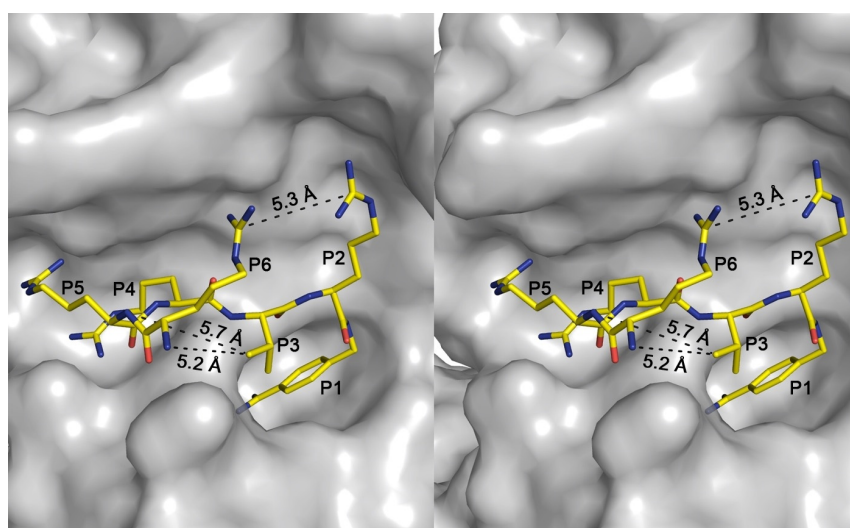
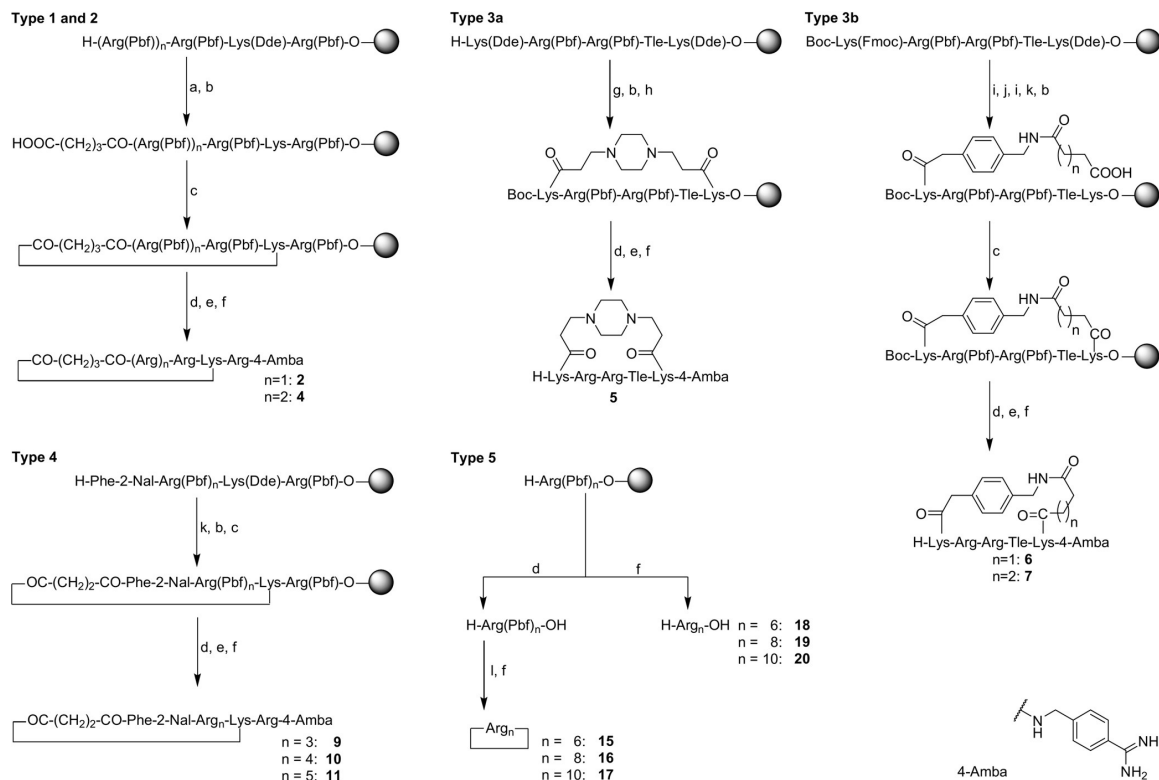


Figure 1. Stereo representation of inhibitor 1 in complex with furin (PDB ID: 6EQX),^[19] indicating the distances between the carbon atoms in the guanidine groups of the P2 and P6 side chains, as well as between the P5 amide nitrogen or P6 amino group and one of the methyl carbons in the side chain of P3 Val.



Scheme 1. Synthesis of the cyclic inhibitors. The shown resin-bound starting materials were prepared by manual peptide synthesis on 2-chlorotrityl chloride resin using a standard Fmoc protocol. Reagents and conditions: a) 3 equiv glutaric anhydride and DIPEA in DMF, 2 h; b) 3% hydrazine-H₂O in DMF (v/v, 3 × 3 min), 5 × washing with DMF; c) 5 equiv PyBOP and 6-Cl-HOBT, 10 equiv DIPEA in DMF, overnight; d) 1% TFA in CH₂Cl₂ (v/v, 3 × 30 min; only in the case of Boc-containing intermediates neutralization by DIPEA); e) 1.5 equiv 4-Amba-2HCl, 1.65 equiv PyBOP, 4.5 equiv 6-Cl-HOBT, 3 equiv DIPEA in DMF (pH ≈ 9), 15 min at 0 °C, 4 h at room temperature; f) TFA/triisopropylsilane/H₂O (95:2.5:2.5, v/v/v), 4.5 h, 40 °C; precipitation in Et₂O, preparative HPLC; g) 4 equiv Boc₂O and DIPEA in DMF, 2 h; h) 1 equiv 3,3'-(piperazine-1,4-diyl)dipropionic acid, 6 equiv 1-[bis(dimethylamino)methylene]-1*H*-1,2,3-triazolo[4,5-*b*]pyridinium-3-oxide hexafluorophosphate (HATU), 12 equiv DIPEA in DMF, 2 h; i) 20% piperidine in DMF, 5 and 15 min; j) 2.5 equiv Fmoc-4-aminomethylphenylacetic acid and 3-[bis(dimethylamino)methyl]yl]-3*H*-benzotriazol-1-oxide hexafluorophosphate (HBTU), 5 equiv DIPEA, 2 h in DMF; k) 4 equiv succinic anhydride (or glutaric anhydride for inhibitor 7) and DIPEA in DMF, 2 h; l) 2 equiv PyBOP and 6-Cl-HOBT, 5 equiv DIPEA (pH ≈ 7–8) in DMF, 48 h.

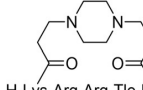
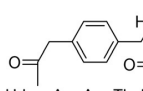
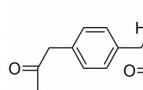
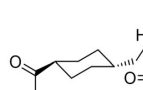
dride, respectively (Scheme 1).^[24,25] After removal of the Dde protection on the indicated lysine residues followed by extensive washing, the resin-bound intermediates were cyclized using benzotriazol-1-yl-oxytrypyrrolidinophosphonium hexafluorophosphate/*N*-hydroxybenzotriazole/diisopropylethylamine (PyBOP/HOBT/DIPEA) in DMF.^[26] The side-chain-protected cyclic peptides were cleaved from the resin under mild acidic conditions, coupled in solution with 4-aminobenzylamine-2HCl, followed by final side chain deprotection under strong acidic conditions, as described previously.^[24,25] Moreover, in addition to the P2 Arg inhibitors 2 and 9–11, their Lys analogues (3 and 12–14) were prepared by an identical strategy (Table 1). Their synthesis started from a Fmoc-Lys(Boc)-2-chlorotrityl resin (not shown).

The preparation of the type 3a inhibitor 5, cyclized between the P6 and P2 Lys side chains, started from the shown resin-bound peptide fragment (Scheme 1). After N-terminal Boc protection the side chain Dde groups on the P2 and P6 Lys residues were removed. The peptides were cyclized on-resin using

the protonatable 3,3'-(piperazine-1,4-diyl)dipropionic acid, which was also previously used for the cyclization of numerous plasmin inhibitors.^[8,9] The following steps were performed as described before. Notably, the synthesis of inhibitor 5 was achieved only with poor yield. After final purification, only ≈ 5 mg were obtained, starting initially from 100 mg of the loaded Fmoc-Lys(Dde)-O-2-chlorotrityl resin. The cyclization of inhibitor 5 is a more complex two-step process. The insertion of the piperazine-dipropionyl fragment starts with an intermolecular reaction, followed by an intramolecular cyclization on the resin. Moreover, to avoid a double acylation of both Lys side chains by two molecules of 3,3'-(piperazine-1,4-diyl)dipropionic acid, this fragment cannot be used in excess, as is normally done in SPPS.

Despite several attempts with slight variations in the amounts of the piperazine derivative, coupling reagent and DIPEA, we could not improve the synthesis of inhibitor 5. Due to these problems, a modified cyclization strategy between the P6 and P2 side chains was investigated (type 3b). After re-

Table 1. Structures, analytical characterization, and potency of the synthesized furin inhibitors. Due to the increased length, the sequences of inhibitors 21–24 are given in one-letter code.

No.	Structure	t_R [min] ^[a]	MS m/z		K_i [nM] ^[b]
			calcd	$[M+H]^+$ found	
2	c[glutaryl-Arg-Arg-Lys]-Arg-4-Amba-4 TFA	15.7	841.51	422.36 ^[c]	0.504 ± 0.097
3	c[glutaryl-Arg-Arg-Lys]-Lys-4-Amba-4 TFA	14.8	813.51	407.93 ^[c]	1.05 ± 0.14
4	c[glutaryl-Arg-Arg-Lys]-Arg-4-Amba-4 TFA	17.5	997.62	998.66	0.68 ± 0.1
5	 H-Lys-Arg-Arg-Tle-Lys-4-Amba · 6 TFA	18.5	1024.68	1025.50	0.491 ± 0.056
6	 H-Lys-Arg-Arg-Tle-Lys-4-Amba · 4 TFA	22.2	1059.65	1060.89	5.04 ± 1.81
7	 H-Lys-Arg-Arg-Tle-Lys-4-Amba · 4 TFA	23.1	1073.66	1074.70	1.17 ± 0.26
8	 H-Lys-Arg-Arg-Tle-Lys-4-Amba · 4 TFA	22.0	1065.69	1066.92	0.99 ± 0.01
9	c[succinyl-Phe-2-Nal-Arg ₃ -Lys]-Arg-4-Amba-5 TFA	33.8	1327.75	665.10 ^[c]	0.378 ± 0.098
10	c[succinyl-Phe-2-Nal-Arg ₄ -Lys]-Arg-4-Amba-6 TFA	32.2	1483.85	743.10 ^[c]	0.0538 ± 0.0059 ^[e]
11	c[succinyl-Phe-2-Nal-Arg ₅ -Lys]-Arg-4-Amba-7 TFA	31.4	1639.95	821.30 ^[c]	0.146 ± 0.032 ^[e]
12	c[succinyl-Phe-2-Nal-Arg ₃ -Lys]-Lys-4-Amba-5 TFA	33.2	1299.75	651.00 ^[c]	0.618 ± 0.002
13	c[succinyl-Phe-2-Nal-Arg ₄ -Lys]-Lys-4-Amba-6 TFA	31.4	1455.85	729.20 ^[c]	0.136 ± 0.020 ^[e]
14	c[succinyl-Phe-2-Nal-Arg ₅ -Lys]-Lys-4-Amba-7 TFA	30.5	1611.95	806.70 ^[c]	0.154 ± 0.047
15	c[Arg ₆]-6 TFA	14.8	936.61	937.60	110.4 ± 1.0
16	c[Arg ₈]-8 TFA	16.8	1248.81	625.50 ^[c]	22.7 ± 0.5
17	c[Arg ₁₀]-10 TFA	18.2	1561.01	781.70 ^[c]	27.8 ± 1.2
18	H-Arg ₆ -OH-7 TFA	13.7	954.62	955.80	9.4 ± 2.3
19	H-Arg ₈ -OH-9 TFA	15.0	1266.82	634.40 ^[c]	6.0 ± 0.4
20	H-Arg ₁₀ -OH-11 TFA	17.0	1579.02	790.90 ^[c]	9.3 ± 1.2
21	Ac-RQIKIWFQNRMRMKWKKRVR-4-Amba-10 TFA	31.8	2829.66	944.82 ^[d]	19.0 (1.86 ± 0.03) ^[f]
22	Ac-YGRKKRRQRRRVR-4-Amba-10 TFA	20.1	1987.22	663.70 ^[d]	11.0 (2.04 ± 0.13) ^[f]
23	Ac-AGYLLGKINLKALAALAKKILRVR-4-Amba-7 TFA	44.6	2765.76	923.27 ^[d]	22.8 (1.51 ± 0.24) ^[f]
24	Ac-RRRRRRRVR-4-Amba-9 TFA	19.4	1695.08	566.22 ^[d]	10.7 (1.69 ± 0.31) ^[f]

[a] HPLC retention time; the gradient started at 1% solvent B (see Experimental Section for details). [b] Data are the mean ± SD obtained for at least three independent measurements. [c] $[M+2H]^{2+} \cdot 2^{-1}$. [d] $[M+3H]^{3+} \cdot 3^{-1}$. [e] K_i values were determined under tight-binding conditions. [f] Data are IC_{50} values (average of two measurements) determined in the presence of the substrate Phac-Arg-Val-Arg-Arg-AMC at 12.5 μ M; the Hill coefficients ± SD are given in brackets.

removal of the Fmoc group, the P6 side chain was elongated by coupling of Fmoc-4-aminomethyl-phenylacetic acid (performed only with 2.5-fold excess of amino acid and HBTU in the presence of 5 equiv DIPEA) in the case of compounds **6** and **7** or Fmoc-tranexamic acid for compound **8**. After Fmoc deprotection, the free amino group was treated with glutaric or succinic anhydride, followed by Dde removal and cyclization of the peptide on resin. The synthesis was completed using the identical steps as described before. Except for compound **5**, all other cyclic inhibitors were prepared without problems by a single intramolecular cyclization using well-established proto-

cols;^[26] in most cases ~15–25 mg of the purified inhibitors could be obtained. The cyclization of the polyarginine inhibitors **15–17** of type 5 was performed in solution. Their linear analogues **18–20** were prepared as reference compounds. Derivatives **21–24** containing the N-terminal elongation with CPP sequences were synthesized by automated SPPS also starting from Fmoc-Arg(Pbf)-O-2-chlorotrityl resin. After completion of the synthesis the side-chain-protected peptides were cleaved from the resin under mild acidic conditions maintaining the side chain protection. The crude intermediates were coupled with 4-amidinobenzylamine, followed by complete deprotec-

tion under strong acidic conditions. The analytical data of the prepared peptides are summarized in Table 1.

Furin inhibition

Inhibitors **2** and **3**, cyclized between the P5 backbone NH and the P3 Lys side chain via a glutaryl spacer (type 1), were characterized as classical competitive inhibitors with K_i values of approximately 0.5 nM and 1 nM, respectively (Table 1). Their potency is significantly stronger than that of the previously published cyclic PC inhibitors^[17] and somewhat lower than the linear P5-P1 inhibitor H-Arg-Arg-Val-Arg-4-Amba ($K_i = 0.11$ nM).^[20] The slight drop in potency might be caused by replacement of Val at the P3 position with Lys, which was required to enable a convenient cyclization to the P5 amino group via the glutaryl spacer. It is known that this P3 substitution usually results in an approximate four-fold decrease in furin inhibition.^[27] Similar potency was also determined for the analogous P6-P3 cyclized inhibitor **4** (type 2).

In compounds **5–8** *tert*-leucine (Tle) was incorporated as P3 residue, which leads to enhanced inhibitory potency relative to Val.^[24] Although inhibitor **5** (type 3a) lacks a basic P2 residue, which is a common prerequisite for potent substrate-analogue furin inhibitors, its potency ($K_i = 0.5$ nM) is nearly identical to that of compounds **2–4**. We speculate that insertion of the protonatable piperazine fragment can partially compensate for the elimination of the basicity at the P2 side chain. A slightly decreased potency was observed for the other analogues **6–8**, which were also cyclized between the P6 and P2 side chains (type 3b).

An even stronger inhibition was determined for most of the type 4 inhibitors (**9–14**), where the furin inhibitor segment was fused to the cyclic CPP sequence. The inhibition constants of compounds **10**, **11**, and **13** (< 150 μ M) were determined under tight-binding conditions, as shown in Figure 2 for the most

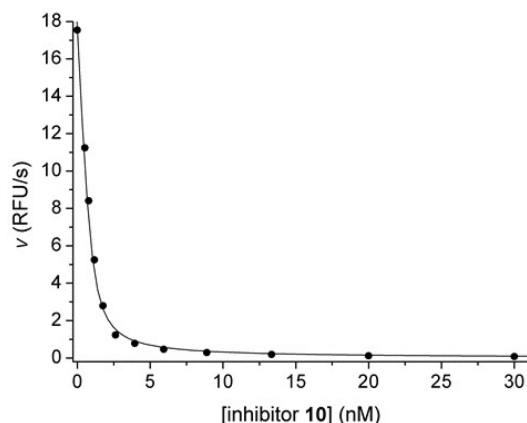


Figure 2. Inhibition of furin (0.95 nM in the assay) by inhibitor **10**. The measurements were performed in the presence of the substrate Phac-Arg-Val-Arg-Arg-AMC (12.5 μ M, $K_M = 5.3$ μ M). The data were fitted to the Morrison equation for tight-binding inhibitors.^[28]

potent analogue **10**. The equations used for K_i value calculations are described in the Supporting Information.

All other inhibition constants were obtained under classical conditions, where the lowest inhibitor concentration was at least ten times higher than the furin concentration. The data also confirm a previous observation that the incorporation of Lys instead of Arg as P2 residue in otherwise identical compounds results in a slightly decreased furin inhibition.^[25,29] Relatively weak potency was obtained for the cyclic polyarginine derivatives **15–17** ($K_i > 20$ nM), whereas their linear analogues **18–20** are somewhat more efficient furin inhibitors, with K_i values < 10 nM.

For the linear inhibitors **21–24** containing the N-terminal CPP sequences, nonlinear dependencies were observed in Dixon plots. This observation indicates a deviation from a normal competitive reversible binding mode. The unknown inhibition mechanism prohibited calculation of K_i values for these compounds and only allowed determination of their IC_{50} values at a constant substrate concentration. Notably, relatively steep concentration–response curves with slope factors larger than unity (between 1.5 and 2) were determined for these four inhibitors (Table 1).

Structure determination

The preparation and purification of homogeneously glycosylated human furin,^[30] as well as the crystallization of its unliganded form, soaking of selected inhibitors and structure determination was performed as described previously.^[19,31] Seven different structures were determined. In all complexes, one asymmetric unit contained one inhibitor-bound furin molecule. Data collection and refinement statistics are summarized in Supporting Information Table S1. The backbone and side chains of the P5-P1 segment of the inhibitors adopted a very similar conformation and make nearly identical intermolecular contacts to furin and surrounding water molecules, as previously observed for the analogous P5-P1 segment in the complex with the linear hexapeptide inhibitor **1** (H-Arg-Arg-Arg-Val-Arg-4-Amba, PDB ID: 6EQX).^[19] For example, the root-mean-square deviation (RMSD) values between the furin complexes with inhibitors **1** and **2** are 0.08 Å for the furin $C\alpha$ atoms and 0.07 Å for the P5-P1 segments of both inhibitors, or 0.09 Å and 0.08 Å in comparison between the inhibitor **1** and **3** complexes, respectively (Figure 3a).

Despite increased B-factors for the more flexible linker segment (Figure 3b), a complete electron density map was obtained for the cyclic inhibitors **2** and **3** (Supporting Information Figure S1 a,b). The glutaryl linker segment and amide connection to the P3 Lys side chain is solvent-exposed in both complexes and is not involved in any polar contact with furin. Notably, this type of cyclization leads to a different side chain conformation of the furin residue Glu257. To avoid a steric clash with the amide bond of the linker, the carbon atom of the side chain carboxyl group of Glu257 is rotated by nearly 120° (Figure 3a). This reorientation results in a parallel orientation of the carboxyl group of Glu257 with the peptide bond between the glutaryl moiety and the P3 side chain.

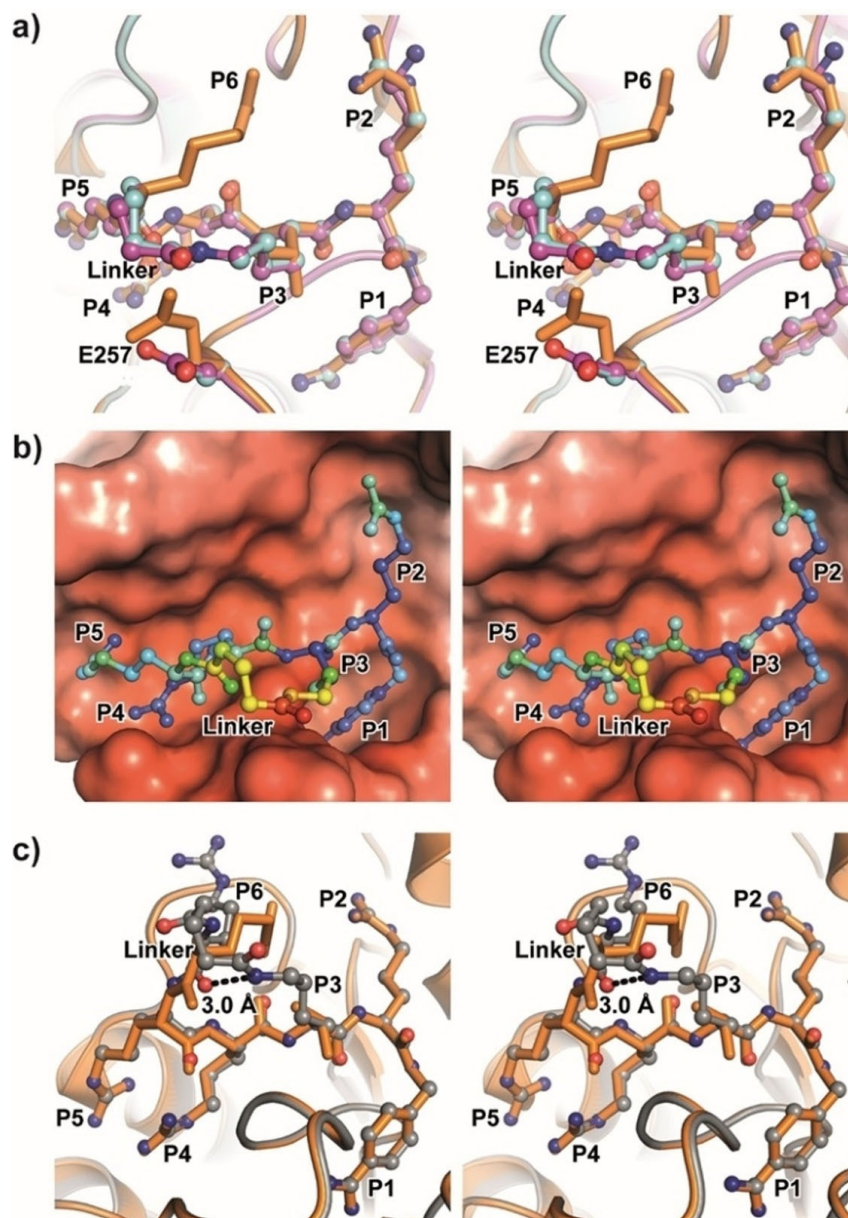


Figure 3. Stereo representation of furin in complex with inhibitors 2, 3, and 4. a) Structural alignment of inhibitors 2 (carbons in cyan) and 3 (carbons in magenta) with compound 1 (orange). The protein backbone of furin is shown as cartoon representation. b) Furin is shown with its solvent-exposed surface colored by its electrostatic potential (negative in red, -10 kT/e; positive in blue, $+10$ kT/e) and inhibitor 2 as ball-and-stick model colored by its B-factors (from 17 \AA^2 in blue to 67 \AA^2 in red). c) Structural alignment of compound 4 (carbons in gray) with inhibitor 1 (orange). The protein backbone is shown as cartoon representation. A hydrogen bond between the P5-P6 inhibitor backbone amide oxygen and the NH of the P3-glutaryl amide bond is given as a dashed line together with hydrogen bonding distance.

Inhibitor 4, elongated with an additional Arg residue at the P6 position, was also well defined in the electron density map, again indicating the typical P5-P1 structure of inhibitor 1 as well as a defined conformation of the linker segment (Supporting Information Figure S1 c). The latter is stabilized by an addi-

tional hydrogen bond between the carbonyl oxygen atom of the P5-P6 peptide bond and the amide nitrogen atom of the P3-glutaryl amide bond (Figure 3 c). The P6 backbone atoms of inhibitor 4, however, are slightly shifted relative to inhibitor 1. Therefore, the P6 side chain of inhibitor 4 cannot properly

bind to the canonical S6 site, instead adopting an alternative position parallel to the peptide bond between Gly229 and Glu230.

In contrast, no clear electron density was obtained for the linker segments in the complexes with inhibitors **5**, **7**, **10**, and **12**, probably due to their high flexibility (Supporting Information Figure S1 d–g). In the complex with inhibitor **10** the complete structure of the P1–P6 segment and the backbone atoms of the P7 residue could be refined, whereas the electron density of the P7 side chain and the succinyl-Phe-2-Nal segment of the ring structure and the connection to the P3 side chain are missing (Supporting Information Figure S1 f). The distance between the P7 backbone NH and the N ϵ of the P3 Lys side

chain is approximately 5.8 Å, which can be spanned by the relatively flexible succinyl-Phe-2-Nal segment containing ten backbone atoms. The P1–P6 segment of the bound inhibitor **10** adopts a nearly identical conformation as previously determined in the complex with inhibitor **1** (Figure 4a) and therefore makes similar polar and electrostatic contacts with furin.^[19]

Relative to inhibitor **10**, the analogous derivative **12** contains Lys at the P2 position, and its ring structure is shortened by one Arg residue. Electron density was found for all atoms of the P6–P1 segment, the backbone of the P7 2-Nal residue and the P7 C β atom, but not for the naphthyl ring and the succinyl-Phe segment including the amide bond to the P3 side chain (Supporting Information Figure S1g). Most backbone and side

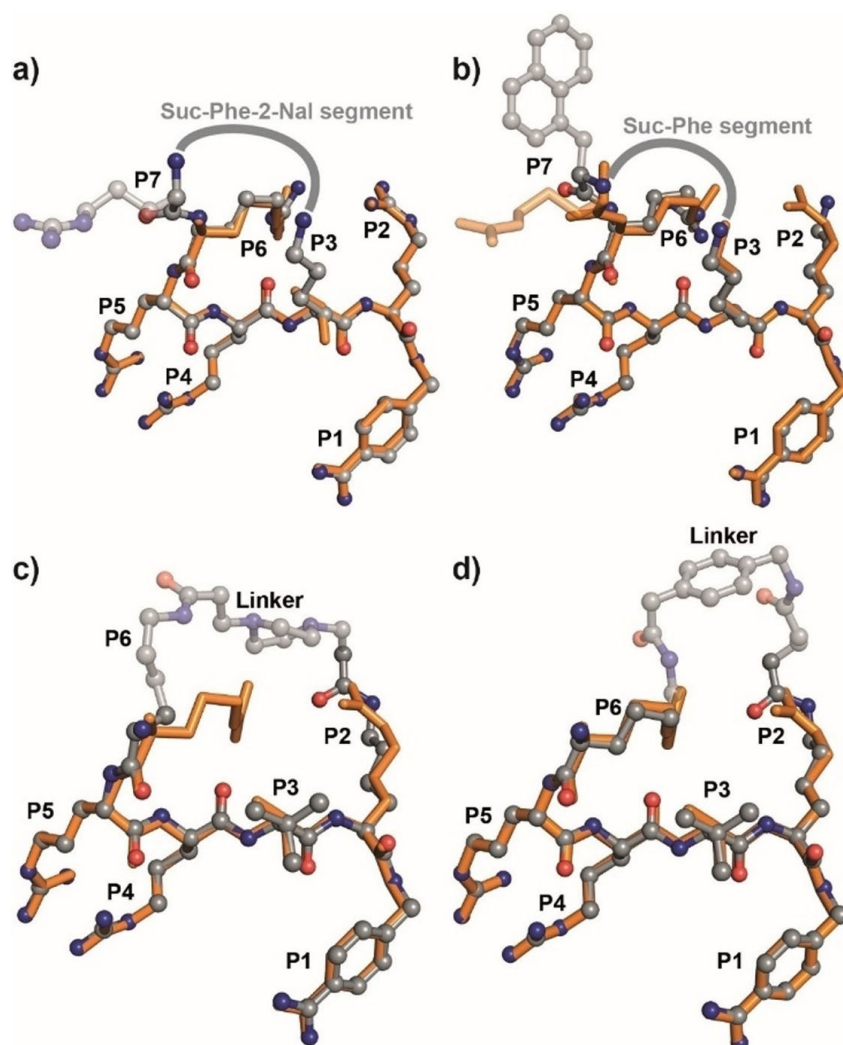


Figure 4. Furin in complex with inhibitors **5**, **7**, **10**, and **12**. Atoms that were modeled with zero occupancy are shown in light colors. Missing residues of the cyclic peptides are marked as gray line between connecting amino acids. a) Superposition of inhibitors **10** (ball-and-stick model, gray carbons) and **1** (orange). b) Superposition of compounds **12** (ball-and-stick model, gray carbons) and **10** (orange). c) Superposition of inhibitors **5** (ball-and-stick model, gray carbons) and **1** (orange). d) Superposition of derivatives **7** (ball-and-stick model, gray carbons) and **1** (orange).

chains atoms of the P6-P1 segment are very similarly placed as found in the complex with inhibitor **10** (Figure 4b). However, the P6-P7 amide group and P7 backbone of inhibitor **12** are somewhat displaced, which leads to a slightly shorter distance between the P7 NH and the nitrogen of the P3 Lys side chain (5.4 Å). When assuming that three backbone atoms roughly span a distance of 3 Å, the seven atoms of the succinyl-Phe segment are sufficient for ring closure.

The structures of the bound inhibitors **5** and **7** could be refined for the complete P5-P1 segment. In addition, we observed electron density for the P6 backbone atoms as well as the P6 C β atom of inhibitor **5** and the P6 C β , C γ , and C δ atoms of inhibitor **7** (Supporting Information Figure S1 d,e). The P5-P1 segments adopted the prototypic conformation as observed for inhibitor **1** (Figure 4c,d). No electron density was observed for the linker segments including the piperazine-dipropionyl moiety of inhibitor **5** (Supporting Information Figure S1 d) and glutaryl-4-aminomethyl-Phac of inhibitor **7** (Supporting Information Figure S1 e). As a result of the peptide bond between the P2 side chain and the linker segment of both inhibitors, the electrostatic P2 interactions are disrupted. This might tolerate multiple conformations of the linkers and thus contribute to increased flexibility.

Inhibition of respiratory syncytial virus propagation

Respiratory syncytial virus (RSV) is an important pathogen and can cause acute lower respiratory tract infections. Such infections can lead to bronchiolitis and pneumonia, especially in younger infants. In 2015, about 3.2 million hospital admissions and 59600 in-hospital deaths in children younger than five years were reported; approximately 45% of these cases occurred in children younger than six months.^[32] There is still no vaccine available for RSV. Current treatment of RSV infections includes palivizumab, a neutralizing monoclonal antibody against the RSV fusion protein F, and inhaled ribavirin. RSV is an enveloped virus containing a non-segmented negative-sense single-stranded RNA genome that belongs to the family of Pneumoviridae.^[32] The surface of the virion contains three glycoproteins: the fusion protein F, the attachment protein G, and a so-called small hydrophobic protein SH. F is a type I protein and mediates the fusion between the virion coat and the plasma membrane of the host cell. After an initial infection, the F protein can also be expressed on the surface of cells and mediates fusion with neighboring cells leading to syncytia formation. The F protein is synthesized as a fusion-incompetent F0 precursor (72 kDa) and forms a homotrimer. The F0 precursor becomes activated by furin or other basic PCs in the trans-Golgi network (TGN) during transport through the secretory pathway, providing two disulfide-linked subunits, an N-terminal F2 (22 kDa) and C-terminal F1 (50 kDa) unit. The N-terminal hydrophobic segment of F1 acts as a fusion peptide and inserts into the host cell membrane. In contrast to other viruses of the Paramyxoviridae and Pneumoviridae families, the RSV F0 precursor contains two preferred multibasic furin cleavage sites. The first is located directly at the N-terminal site of the fusion peptide after residue 136 (Lys131-Lys-Arg-Lys-Arg-Arg136↓),

and the second –27 residues upstream in the F2 subunit after position 109 (Arg106-Ala-Arg-Arg109↓). Cleavage at both sites is required for activation of membrane fusion.^[33,34] Moreover, a peptide of 27 residues (pep27) is released upon cleavage at both sites and has been shown to be converted into the biologically active tachykinin in the case of bovine respiratory syncytial virus (BRSV).^[33,35]

The RSV biosynthetic pathway suggests that efficient inhibition of the furin-catalyzed F0 activation should decrease virus replication. Therefore, selected inhibitors were investigated in a multicycle replication assay in A549 human lung cancer cells infected with the RSV A2 strain. Our previously described furin inhibitors **MI-1148** (4-guanidinomethyl-Phac-Arg-Tle-Arg-4-Amba, $K_i=5.5$ μM , compound **19** in Hardes et al.)^[24] and its P2 Lys analogue **MI-1554** (4-guanidinomethyl-Phac-Arg-Tle-Lys-4-Amba, $K_i=8.5$ μM , compound **27** in Ivanova et al.)^[29] served as reference compounds. All inhibitors tested were well tolerated, because at the concentrations used, no significant cytotoxicity (<10%) was observed. In initial experiments, we found that both linear reference inhibitors **MI-1148** and **MI-1554** decreased the processing of the F0 precursor in A549 cells infected with RSV A2 in a concentration-dependent manner (Figure 5).

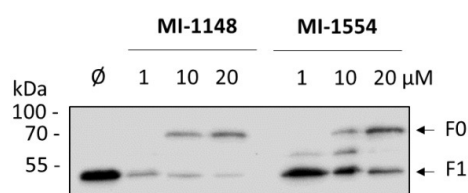


Figure 5. Inhibition of F0 cleavage by the linear reference compounds **MI-1148** and **MI-1554** at indicated concentrations relative to a control in the absence of inhibitor. A549 cells were infected with the RSV A2 strain at a multiplicity of infection (MOI) of 5. At 24 h post-infection cells were treated with inhibitor and further incubated in the presence of inhibitor for 24 h. At 48 h post-infection proteins F0 (72 kDa) and mature F1 (50 kDa) were immunologically detected with an F-specific antibody after SDS-PAGE followed by western blot analysis.

For both linear reference compounds, significant concentration-dependent inhibition of RSV replication was also found in subsequent tests. The virus growth curves obtained in infected cells are shown in Figure 6a,b. However, a complete lack of antiviral efficacy was observed for all of the tested cyclic derivatives (Figure 6c–g) and the noncyclic octa-Arg compound **19** (Figure 6h). Surprisingly, for the two derivatives **10** and **13** fused to the cyclic amphiphilic CPP segment, and for the cyclic octa-Arg compound **16**, enhanced virus replication was observed at higher inhibitor concentrations (Figure 6e–g). Because many transfection agents also possess an amphiphilic or multibasic structure, we speculate that incubation of cells with these CPP derivatives could promote virus uptake and thereby contribute to virus growth. Due to their weak furin inhibition, the linear CPP-inhibitor conjugates **21–24** were not been tested for their antiviral potency.

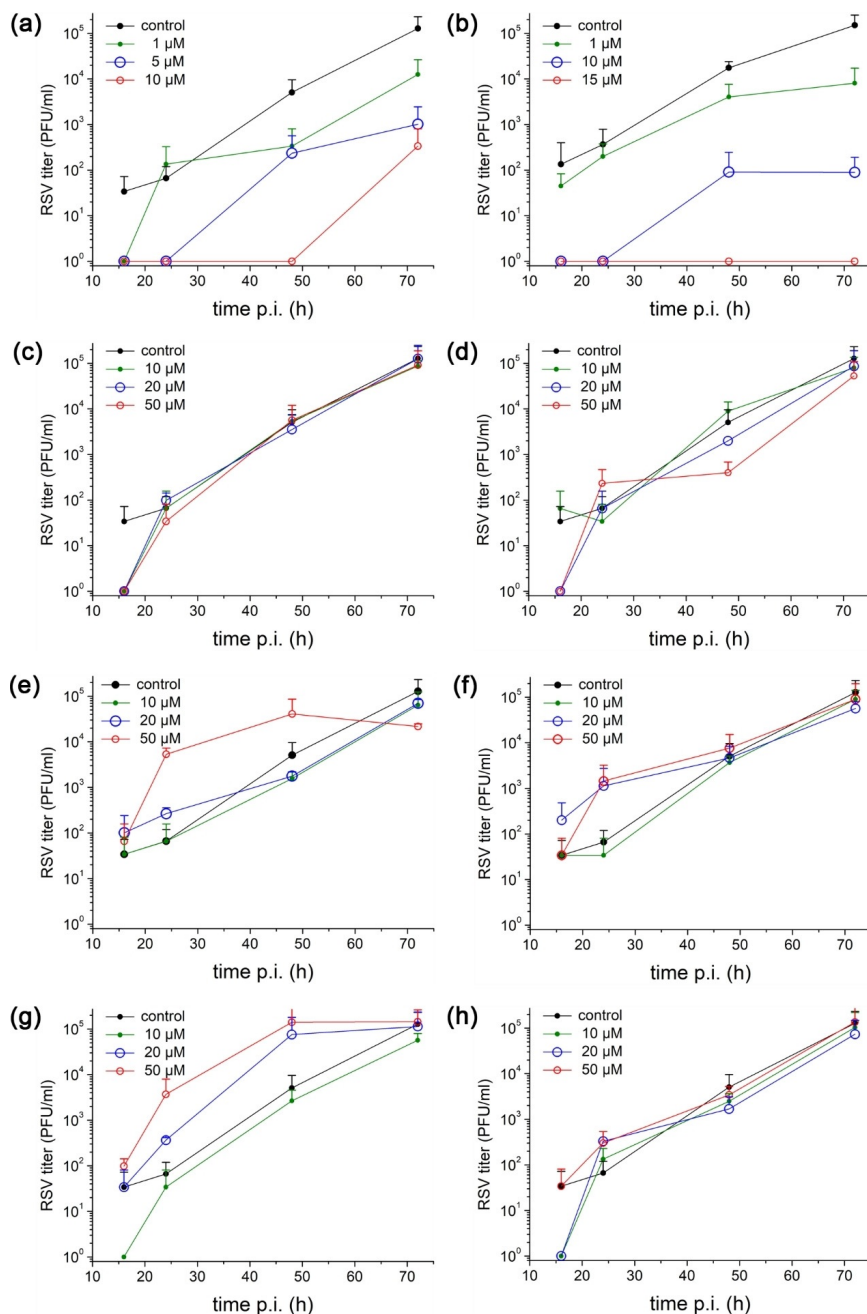


Figure 6. Multicycle replication of RSV A2 in inhibitor-treated A549 human lung cells. A549 cells were inoculated with RSV A2 at a MOI of 1 for 1 h, washed and incubated in the presence of the linear reference inhibitors MI-1148 (a) and MI-1554 (b), the cyclic inhibitors 2 (c), 5 (d), 10 (e), 13 (f), 16 (g), and of the linear octa-Arg compound 19 (h) at indicated concentrations for 72 h. Slightly different concentrations were used for the reference inhibitors MI-1148 and MI-1554. At 16, 24, 48 and 72 h post-infection cell supernatants were collected and viral titers \pm standard deviation ($n=2$) were analyzed by plaque assay (plaque-forming units (PFU) per mL).

Discussion

Our previously described linear inhibitors revealed a significant activity against numerous furin-dependent pathogenic viruses

in cell culture experiments at lower micromolar concentrations.^[20,24,29,36–39] Due to limited tolerability of the most potent compounds in mice,^[29] we prepared different types of new macrocyclic analogues to find alternative inhibitor structures

and determined their potency against furin. The development of these compounds began with the crystal structure of the hexapeptide derivative **1** in complex with furin. Most cyclizations between the P6 or P5 backbone amide and the P3 side chain or between the P6 and P2 side chains provided relatively strong inhibitors with K_i values in the low nanomolar range or even better, thereby confirming the suitability of our structure-based inhibitor design. Despite some differences, similar inhibitory activities were found for compounds **2–8** in enzyme kinetic studies. The data suggest that the potency of these cyclic analogues mainly results from interactions of their very similar P6/P5-P1 segments, whereas the different types of macrocyclization do not confer a beneficial effect with respect to furin inhibition. This assumption could be confirmed by crystal structure determinations of analogues **2–4** in complex with furin. Despite increased B-factors, the electron densities for the glutaryl spacer and the flanking amide bonds were clearly visible in these complexes (Supporting Information Figure S1 a–c), although all three linker segments are solvent-exposed and lack any specific polar contact with furin. That suggests that further variations of the linker, for instance, by incorporation of the shorter ornithine, α,γ -diaminobutyric acid, and α,β -diaminopropionic acid or the elongated homolysine at the P3 position in combination with numerous dicarboxylic acids, should have a rather small effect on inhibitory potency.

A relatively strong potency with K_i values around 1 nM was also found for the P6-P2 side-chain-bridged inhibitors **5–8**, despite acylation and thereby elimination of the basic P2 side chain. This was a somewhat surprising result, because electrostatic interactions in the S2 site are normally an essential prerequisite for high furin affinity. Crystal structures were also determined for analogues **5** and **7**, although the electron density for the P6-P2 side-chain-connecting segment in both furin complexes is missing. This suggests a rather flexible conformation of the linker segment. It is therefore impossible to predict whether the loss of the electrostatic interaction in the S2 pocket could be partially compensated for by new polar contacts of the linker, or by stabilization of the bound inhibitor conformation caused by the cyclization.

The most potent compounds **10** and **13** were obtained by combining a cyclic cell-penetrating amphiphilic hexapeptide containing four consecutive Arg residues with a P3-P1 Lys-Arg/Lys-4-Amba segment. However, as with all other cyclic analogues and despite an excellent inhibition constant of $\approx 54 \mu\text{M}$ for derivative **10**, a complete lack of antiviral activity on the replication of RSV was observed for both compounds in cell culture experiments. Surprisingly, the data for both CPP-derived inhibitors **10** and **13**, as well as for the cyclic octa-Arg derivative **16** even reveal a slightly enhanced RSV replication in the presence of higher inhibitor concentrations (20 and 50 μM) at the beginning of the growth curves (Figure 6 e–g). It might be possible that such CPP-derived derivatives simply act as transfection vehicles^[40–42] thereby contributing to an improved initial virus uptake.

In contrast, significant low micromolar antiviral potency against RSV was determined for the first time with our previously developed linear inhibitors **MI-1148**^[24] and **MI-1554**,^[29]

which were used as reference compounds in these cell culture studies (Figure 6 a,b). This confirms previous reports with the irreversible inhibitor decanoyl-Arg-Val-Lys-Arg-chloromethyl ketone, in which furin was identified as the major host protease for activation of the F0 precursor of RSV.^[34] The lack of any antiviral activity determined for the cyclic analogues suggests that insufficient amounts of these inhibitors reach furin in the secretory pathway, where F0 processing occurs. This is probably caused by the increased molecular weight of the cyclic derivatives. An additional reason for the lack of antiviral potency could also be the lower inhibitory potency of the cyclic derivatives relative to the single-digit picomolar tight-binding inhibitors **MI-1148** and **MI-1554**. Although we do not have any information regarding the furin concentrations in the TGN, we know from enzyme kinetic studies that even very low concentrations of the tight-binding inhibitors **MI-1148** and **MI-1554** around 1 nM are sufficient for considerable inhibition of furin in our standard assay, when the enzyme is used at a very similar concentration of 0.95 nM. The remarkable inhibitory potency of compounds such as **MI-1148** may therefore compensate, to some extent, the poor cellular uptake of these multibasic polar compounds, a phenomenon which does not occur with less potent inhibitors possessing K_i values in the range of 0.1–1 nM. Alternatively, the specific chemical structure of **MI-1148** and other close linear analogues might enable enhanced cellular uptake, providing improved intracellular inhibitory potency. This issue deserves further study.

Conclusions

In summary, we developed various types of new cyclic furin inhibitors. Despite few structural differences in the linker segments used and resulting ring size of the tested macrocyclic inhibitors, they possess closely related P6/P5-P1 segments. For certain analogues, we were able to identify the complete binding mode in complex with furin, which revealed similar interactions in the active site cleft to those of the linear inhibitor **1** in our previous study.^[19] This seems to be the reason that most of these compounds inhibit furin with similar inhibition constants between 0.5 and 1 nM, whereas the specific linker segment has rather little influence on affinity, despite differences in ring size. In contrast, especially inhibitor **10** ($K_i = 54 \mu\text{M}$), which can be considered a chimeric derivative consisting of a furin-inhibitory moiety merged with a cyclic CPP segment, possesses significantly improved potency relative to previously described macrocyclic PC inhibitors. However, all of the newly prepared macrocyclic derivatives including the highly potent inhibitor **10** containing the cyclic CPP segment possess negligible antiviral activity in cells infected with RSV, whereas our linear reference inhibitors **MI-1148**^[24] and **MI-1554**^[29] significantly decrease virus replication at low micromolar concentrations. So far, we can only speculate that the lack of intracellular potency of the cyclic compounds is caused by their decreased inhibitory potency or reduced cellular uptake, when compared with the noncyclic reference compounds.

Experimental Section

Reagents: Protected Fmoc-amino acids, coupling reagents, resins, further chemicals, and solvents were obtained from Orpegen Peptide Chemicals (Heidelberg, Germany), Bachem AG (Bubendorf, Switzerland), IRIS Biotech (Marktredwitz, Germany), Sigma–Aldrich Chemie GmbH (Munich, Germany), Alfa Aesar (Karlsruhe, Germany), and Acros Organics (Geel, Belgium). Fmoc-4-aminomethylphenylacetic acid was purchased from PolyPeptide Laboratories (Strasbourg, France) and Fmoc-tranexamic acid was prepared by reaction of tranexamic acid with Fmoc-OSu. 3,3-(Piperazine-1,4-diyl)di-propanoic acid was from previous studies.^[8]

Standard analytical methods and preparative HPLC: The used methods were recently described in detail.^[20,24] In short, standard analytical reversed-phase HPLC measurements were performed on a Shimadzu LC-10A system (column: Nucleodur C₁₈, 5 μ m, 100 \AA , 4.6 \times 250 mm (Machery-Nagel, Düren, Germany); solvents: (A) 0.1% TFA in water, (B) 0.1% TFA in acetonitrile; gradient: 1% increase solvent B per min, for final inhibitors start at 1% solvent B; flow rate: 1 mL min⁻¹; detection at 220 nm). The final inhibitors were purified (\geq 95% based on detection at 220 nm) using the same solvents on a preparative Varian HPLC system (column: Nucleodur C₁₈, 5 μ m, 100 \AA , 32 \times 250 mm (Machery-Nagel, Düren, Germany); gradient: 0.5% increase solvent B per min; flow rate: 20 mL min⁻¹). All peptides were finally obtained as TFA salts after lyophilization. The molecular mass of the synthesized compounds was determined on a QTrap 2000 ESI spectrometer (Applied Biosystems, now Life Technologies, Carlsbad, CA).

Peptide synthesis: All peptides were prepared on 2-CTC resin, which was either loaded with Fmoc-Arg(Pbf)-OH, Fmoc-Lys(Boc)-OH, or Fmoc-Lys(Dde)-OH. The following residues were coupled by manual Fmoc-SPPS in 2 mL polypropylene syringes with filter frits (inhibitors 2–8) or by automated synthesis (peptides 9–24) in 2 mL syringes on a Syro 2000 peptide synthesizer (MultiSynTech, Witten, Germany). For couplings, a 4-fold excess of Fmoc-amino acid, HBTU, and HOBt in the presence of 8 equiv DIPEA was used (coupling time 1.5 h, single couplings in manual synthesis and double couplings in automated synthesis).

In the case of the resin-bound intermediates for peptides 2–4 and 6–14, after final Fmoc removal the liberated amino group was treated with succinic or glutaric anhydride, followed by Dde cleavage and on-resin cyclization. The cyclized peptide was cleaved from the resin under mild acidic conditions, the obtained crude side-chain-protected intermediates were coupled with 4-Amba-2HCl in solution. After complete side chain deprotection under strong acidic conditions, the final inhibitors were purified by preparative reversed-phase HPLC and obtained as lyophilized TFA salts. The synthesis of the most potent inhibitor 10 is described in the following paragraph in detail.

c[Succinyl-Phe-2-Nal-Arg₄-Lys]-Arg-4-Amba-6 TFA (10): 1.6 mmol (1.04 g, 1 equiv) Fmoc-Arg(Pbf)-OH were dissolved in 20 mL dry CH₂Cl₂ and treated with 1.11 mL (6.4 mmol, 4 equiv) DIPEA. The mixture was added to 1 g 2-CTC resin (loading 1.6 mmol g⁻¹) in a glass reaction vessel with a filter frit. The resin was shaken for 2 h at room temperature, followed by washing with dry CH₂Cl₂ and capping with 20 mL of a mixture of CH₂Cl₂/MeOH/DIPEA (17:2:1, v/v/v, 3 \times 1 min). The resin was subsequently washed with CH₂Cl₂, DMF, and CH₂Cl₂ (3 \times 1 min, respectively) and dried in vacuo (1.42 g). This loaded resin (100 mg; loading \approx 0.7 mmol g⁻¹) was transferred into 2 mL polypropylene syringes with filter frits, the following steps were performed by automated peptide synthesis. After Fmoc removal with 20% piperidine in DMF (5 and 15 min),

7 \times washing with DMF, the following residues (Fmoc-Lys(Dde)-OH, 4 \times Fmoc-Arg(Pbf)-OH, Fmoc-2-Nal-OH, and Fmoc-Phe-OH) were successively coupled using 4.0 equiv of Fmoc-protected amino acid, HBTU, and HOBt, respectively, and 8.0 equiv of DIPEA (double coupling, 2 \times 1.5 h). After washing with DMF (4 \times 1 min), Fmoc cleavage and subsequent washing with DMF (7 \times 1 min), the following steps were conducted by manual synthesis. The resin-bound peptide was treated with a mixture of 28.2 mg (0.28 mmol, 4 equiv) succinic anhydride and 49 μ L (0.28 mmol, 4 equiv) DIPEA, dissolved in 1.5 mL DMF. The syringe was shaken for 2 h, the resin was washed with DMF (3 \times 1 min), followed by Dde removal with 3% hydrazine in DMF (v/v, 3 \times 3 min). The resin was washed with DMF (5 \times 1 min), 10% DIPEA in DMF (v/v, 3 \times 1 min), and DMF (3 \times 1 min). For cyclization, the resin was treated with a mixture of 182 mg (0.35 mmol, 5 equiv PyBOP), 59 mg (0.35 mmol, 5 equiv) 6-Cl-HOBt, and 122 μ L (0.7 mmol, 10 equiv) DIPEA, dissolved in 1.5 mL DMF.^[26] The resin was shaken at room temperature overnight, washed with DMF (3 \times 1 min) and CH₂Cl₂ (4 \times 1 min). The side-chain protected peptide was cleaved from the resin under mild acidic conditions with 1% TFA in CH₂Cl₂ (v/v, 3 \times 30 min). The solvent was removed in vacuo. The oily intermediate (HPLC: elution at 50.7 min, start at 40% solvent B) was dissolved in 1.5 mL DMF and coupled with 23 mg (0.105 mmol, 1.5 equiv) 4-Amba-2HCl in the presence of 60 mg (0.12 mmol, 1.65 equiv) PyBOP, 53 mg (0.32 mmol, 4.5 equiv) 6-Cl-HOBt, and 36.5 μ L (0.21 mmol, 3 equiv) DIPEA at room temperature for 2 h. The solvent was removed in vacuo (HPLC: elution at 44.1 min, start at 40% solvent B). The obtained intermediate was deprotected under strong acidic conditions with a mixture of 1.5 mL TFA/triisopropylsilane/H₂O (95:2.5:2.5, v/v/v, 4.5 h at room temperature). After addition of Et₂O, the precipitated crude product was obtained by centrifugation and washed twice with Et₂O. The product was purified by preparative HPLC, the product containing fractions were evaporated and the product lyophilized from water (22 mg white powder, purity 99% based on HPLC at 220 nm, HPLC: 32.2 min, start at 1% B, MS (ESI, positive): calcd: 1483.85; found *m/z*: 743.10 [*M* + 2H]²⁺ / 2).

Inhibitor 5: The synthesis started from 125 mg Fmoc-Lys(Dde)-resin (loading \approx 0.75 mmol g⁻¹). The following Fmoc-amino acids (Fmoc-Tle-OH, 2 \times Fmoc-Arg(Pbf)-OH, and Fmoc-Lys(Dde)-OH) were coupled by manual SPPS in 2 mL syringes, using the same steps as described above for inhibitor 10. After final Fmoc deprotection the terminal amino group was protected with Boc₂O (102 mg, 0.47 mmol, 5 equiv) in the presence of DIPEA (8 μ L, 0.47 mmol, 5 equiv). After 4 h coupling, the resin was washed with DMF (5 \times 1 min), followed by removal of both Dde protecting groups with 3% hydrazine in DMF and subsequent washing as described above. For cyclization, the resin was treated with a mixture of 28.5 mg (0.094 mmol, 1 equiv) 3,3-(piperazine-1,4-diyl)di-propanoic acid, 214 mg (0.56 mmol, 6 equiv) HATU and 196 μ L (1.128 mmol, 12 equiv) DIPEA in 2 mL DMF. After 2 h coupling, the resin was washed with DMF and CH₂Cl₂ (3 \times 1 min, respectively). The following steps (mild acidic cleavage, HPLC elution of the intermediate at 46.3 min, start at 10% solvent B; coupling of 4-Amba, HPLC elution of the intermediate at 41.8 min, start at 10% solvent B; strong acidic cleavage and final purification by HPLC) were performed as described above for inhibitor 10 (5 mg white powder, purity 95% based on HPLC at 220 nm, HPLC: 18.5 min, start at 1% B, MS (ESI, positive): calcd: 1024.68; found *m/z*: 1025.50 [*M* + H]⁺).

Inhibitors 15–17: The oligo-Arg(Pbf)-peptides were prepared by automated Fmoc-SPPS always starting from 120 mg Fmoc-Arg(Pbf)-resin (loading \approx 0.6 mmol g⁻¹) as described before for in-

hibitor **10**. After final Fmoc deprotection, the peptides were either cleaved from the resin under strong acidic conditions to yield inhibitors **18–20** or under mild acidic conditions providing the intermediates for inhibitors **15–17**. After evaporation of the solvent, the obtained oily intermediates were dissolved in 60 mL DMF (concentration ≈ 1.2 mM)^[43] and treated with 63 μ L (0.36 mmol, 5 equiv) DIPEA. In parallel, 74.9 mg (0.144 mmol, 2 equiv) PyBOP, and 24.4 mg (0.144 mmol, 2 equiv) 6-Cl-HOBt were dissolved in 2 mL DMF. For cyclization, this mixture was added dropwise to the peptide solution over a period of 40 min.^[26] After stirring at room temperature for 48 h (pH ≈ 7 –8) the solvent was evaporated to ≈ 2 –3 mL. The side-chain-protected peptide was precipitated by addition of water and isolated by centrifugation. At the end, the Pbf groups were removed under strong acidic conditions, followed by preparative purification of the cyclized oligo-Arg peptides and lyophilization (yield: 11 mg for inhibitor **15**, 23.5 mg for **16**, 12.9 mg for **17**, 13.1 mg for **18**, 14.3 mg for **19**, 10.8 mg for **20**). The analytical data of the peptides are summarized in Table 1.

Inhibitors 21–24: The synthesis was performed by automated peptide synthesis, followed by coupling of 4-Amba in solution, as described previously^[20] (yield: 19.6 mg for inhibitor **21**, 40.1 mg for **22**, 10.4 mg for **23**, and 24.9 mg for **24**). The analytical data of the peptides are summarized in Table 1.

Protein crystallography: Homogenously glycosylated human furin^[30] (≈ 9 mg mL⁻¹ in 10 mM HEPES, pH 7.5, 100 mM NaCl, 2 mM CaCl₂) was mixed with equal volumes of crystallization solution (100 mM MES, 200 mM K/NaH₂PO₄, pH 5.5–6.0 and 2 M NaCl) and equilibrated against 3.0–3.6 M NaCl in the reservoir of vapor diffusion experiments at 20 °C similar to the procedures described previously.^[19,31] The crystals were soaked for ≈ 16 h in soaking solution (3.13 M NaCl, 100 mM Mes/NaOH, pH 5.5, 200 mM NaH₂PO₄, 1 mM CaCl₂, 20% DMSO) supplemented with inhibitor **2** (5 mM), **3** (5 mM), **4** (5 mM), **5** (5 mM), **7** (5 mM), **10** (1 mM), or **12** (1 mM). Soaked crystals were directly flash cooled in liquid N₂. Diffraction data collection was performed at the synchrotron beamlines ID29^[44] and ID30A-3 (MASSIF-3)^[45] of the European Synchrotron Radiation Facility (ESRF) at 100 K. The data were processed using XDS (v.01/2018)^[46] with XDS-APP (v.2.0)^[47] and the CCP4 program suite (v.7.0.019).^[48] COOT (v.0.8.3)^[49] was used for model building. Refinement was performed in PHENIX (v.1.11.1)^[50] using the structure of furin in complex with inhibitor **1** (PDB ID: 6EQX)^[19] as initial model. The R_{free}-set was always transferred from PDB ID: 6EQX. Geometry restraints for refinement of the inhibitors were generated using the PRODRG server.^[51] Electron density omit maps were calculated in PHENIX (v.1.11.1)^[50] performing positional refinement with simulated annealing of the structures with omitted inhibitors. Molecular graphics and structure alignments were calculated in PYMOL (<http://www.pymol.org>). The coordinates and structure factors of the furin complexes with inhibitors **2**, **3**, **4**, **5**, **7**, **10**, and **12** have been deposited at the World Wide Protein Data Bank with the PDB IDs 6HZA, 6HZB, 6HZD, 6HLE, 6HZC, 6HLB, and 6HLD, respectively.

RSV infections and inhibition of multicycle replication: RSV A2 strain was kindly provided by Christine Krempf, Institute of Virology and Immunobiology, University of Würzburg, Würzburg, Germany. Cell growth and incubations occurred at 37 °C and 5% CO₂. All infection experiments were performed in minimal essential medium (MEM, Gibco, Thermo Fisher Scientific, Paisley, UK) supplemented with 5% fetal calf serum (FCS), penicillin, streptomycin, and glutamine. To generate virus stocks RSV A2 was propagated in Hep-2 cells. Concentrated virus stocks were prepared at the peak of syncytia formation from both cell supernatant and infected cells. Infected cells were mechanically disrupted by vortexing to release

cell-associated virus. The cell suspension and the virus-containing Hep-2 cell culture supernatant were cleared by low-speed centrifugation, subsequently combined, supplemented with 0.1 M MgSO₄ and 0.05 M HEPES and stored as virus stock at -80 °C. Multicycle virus replication in the presence of inhibitors was analyzed in A549 human lung cancer cells. A549 cells were infected with RSV A2 at a multiplicity of infection (MOI) of 1 for 1 h, cells were then washed with PBS to remove the inoculum and were incubated in fresh medium with or without inhibitors for 72 h. At 16, 24, 48 and 72 h post-infection cell supernatants were collected and viral titers determined by plaque assay in Vero76 cells with Avicel overlay.^[52] Briefly, cells were incubated with 10-fold serial dilutions of the supernatants in MEM supplemented with 5% FCS, antibiotics and glutamine for 1 h, washed with PBS and incubated with Avicel overlay for 72 h. Cells were washed, fixed and permeabilized and immunostained using a mouse serum against RSV A2 (NCL-RSV3, Leica), peroxidase-conjugated secondary antibodies and the peroxidase substrate TrueBlue (SeraCare, Milford, USA).

SDS-PAGE and western blot: A549 cells were infected with RSV A2 at a MOI of 5 and incubated in the absence of inhibitors for 24 h. Cells were then treated with inhibitors at the indicated concentrations and incubated in the presence of inhibitors for 24 h. Subsequently, cells were washed with PBS, lysed in reducing SDS-PAGE sample buffer, and heated at 95 °C for 10 min. Cell lysates were subjected to SDS-PAGE (12% gel), transferred to a polyvinylidene difluoride (PVDF) membrane (GE Healthcare, Freiburg, Germany), and detected by incubation with a mouse antibody against F (Novus Biologicals, Centennial, USA) followed by a mouse-specific peroxidase-conjugated secondary antibody. Proteins were visualized using the ChemiDoc XRS+ system with Image Lab software (Bio-Rad).

Acknowledgements

T.S. and E.B.-F. obtained funding from the LOEWE Center DRUID (Novel Drug Targets against Poverty-Related and Neglected Tropical Infectious Diseases). E.B.-F. and M.R.H. were supported by the Deutsche Forschungsgemeinschaft (DFG), Projektnummer 284237345-KFO309. The authors acknowledge provision of synchrotron beam time by the European Synchrotron Radiation Facility (ESRF) and thank the scientific staff at the beamlines ID29 and ID30A-3 (MASSIF-3) for assistance.

Conflict of interest

The authors declare no conflict of interest.

Keywords: furin inhibitors · macrocyclization · proprotein convertases · respiratory syncytial virus · X-ray crystallography

- [1] K. Fosgerau, T. Hoffmann, *Drug Discovery Today* **2015**, *20*, 122–128.
- [2] P. de Leuw, C. Stephan, *Expert Opin. Pharmacother.* **2018**, *19*, 577–587.
- [3] P. G. Nantermet, J. C. Barrow, C. L. Newton, J. M. Pellicore, M. Young, S. D. Lewis, B. J. Lucas, J. A. Krueger, D. R. McMasters, Y. Yan, L. C. Kuo, J. P. Vacca, H. G. Selnick, *Bioorg. Med. Chem. Lett.* **2003**, *13*, 2781–2784.
- [4] E. S. Priestley, D. L. Cheney, I. DeLuca, A. Wei, J. M. Luetgen, A. R. Rendina, P. C. Wong, R. R. Wexler, *J. Med. Chem.* **2015**, *58*, 6225–6236.
- [5] X. Zhang, P. W. Glunz, J. A. Johnson, W. Jiang, S. Jacutin-Porte, V. Ladziata, Y. Zou, M. S. Phillips, N. R. Wurtz, B. Parkhurst, A. R. Rendina, T. M.

- Harper, D. L. Cheney, J. M. Luetzgen, P. C. Wong, D. Seiffert, R. R. Wexler, E. S. Priestley, *J. Med. Chem.* **2016**, *59*, 7125–7137.
- [6] N. R. Wurtz, B. L. Parkhurst, I. DeLucca, P. W. Glunz, W. Jiang, X. Zhang, D. L. Cheney, J. M. Bozarth, A. R. Rendina, A. Wei, T. Harper, J. M. Luetzgen, Y. Wu, P. C. Wong, D. A. Seiffert, R. R. Wexler, E. S. Priestley, *Bioorg. Med. Chem. Lett.* **2017**, *27*, 2650–2654.
- [7] J. R. Corte, T. Fang, H. Osuna, D. J. Pinto, K. A. Rossi, J. E. Myers, Jr., S. Sheriff, Z. Lou, J. J. Zheng, T. W. Harper, J. M. Bozarth, Y. Wu, J. M. Luetzgen, D. A. Seiffert, C. P. Decicco, R. R. Wexler, M. L. Quan, *J. Med. Chem.* **2017**, *60*, 1060–1075.
- [8] S. M. Saupe, S. Leubner, M. Betz, G. Klebe, T. Steinmetzer, *J. Med. Chem.* **2013**, *56*, 820–831.
- [9] S. Hinkes, A. Wuttke, S. M. Saupe, T. Ivanova, S. Wagner, A. Knörlein, A. Heine, G. Klebe, T. Steinmetzer, *J. Med. Chem.* **2016**, *59*, 6370–6386.
- [10] G. Thomas, *Nat. Rev. Mol. Cell Biol.* **2002**, *3*, 753–766.
- [11] N. G. Seidah, A. Prat, *Nat. Rev. Drug Discovery* **2012**, *11*, 367–383.
- [12] F. Couture, F. D'Anjou, R. Day, *Biomol. Concepts* **2011**, *2*, 421–438.
- [13] E. J. Müller, R. Caldelari, H. Posthaus, *J. Mol. Histol.* **2004**, *35*, 263–275.
- [14] J. Declercq, B. Brouwers, V. P. Pruniau, P. Stijnen, K. Tuand, S. Meulemans, A. Prat, N. G. Seidah, A. M. Khatib, J. W. Creemers, *Biomed. Res. Int.* **2015**, 148651.
- [15] H. Lin, E. Hay, A. Latourte, T. Funck-Brentano, W. Bouaziz, H. K. Ea, A. M. Khatib, P. Richette, M. Cohen-Solal, *Sci. Rep.* **2018**, *8*, 10488.
- [16] B. Ramos-Molina, A. N. Lick, A. N. Shirazi, D. Oh, R. Tiwari, N. S. El-Sayed, K. Parang, I. Lindberg, *PLoS One* **2015**, *10*, e0130417.
- [17] T. Lepek, A. Kwiatkowska, F. Couture, K. Ly, R. Desjardins, Y. Dory, A. Pahl, R. Day, *Eur. J. Cell Biol.* **2017**, *96*, 476–485.
- [18] H. Fittler, A. Depp, O. Avrutina, S. O. Dahms, M. E. Than, M. Empting, H. Kolmar, *ChemBioChem* **2015**, *16*, 2441–2444.
- [19] S. O. Dahms, K. Harges, T. Steinmetzer, M. E. Than, *Biochemistry* **2018**, *57*, 925–934.
- [20] K. Harges, T. Ivanova, B. Thaa, G. M. McInerney, T. I. Klokk, K. Sandvig, S. Künzel, I. Lindberg, T. Steinmetzer, *ChemMedChem* **2017**, *12*, 613–620.
- [21] Z. Qian, T. Liu, Y. Y. Liu, R. Briesewitz, A. M. Barrios, S. M. Jhiang, D. Pei, *ACS Chem. Biol.* **2013**, *8*, 423–431.
- [22] W. Lian, B. Jiang, Z. Qian, D. Pei, *J. Am. Chem. Soc.* **2014**, *136*, 9830–9833.
- [23] K. M. Stewart, K. L. Horton, S. O. Kelley, *Org. Biomol. Chem.* **2008**, *6*, 2242–2255.
- [24] K. Harges, G. L. Becker, Y. Lu, S. O. Dahms, S. Köhler, W. Beyer, K. Sandvig, H. Yamamoto, I. Lindberg, L. Walz, V. von Messling, M. E. Than, W. Garten, T. Steinmetzer, *ChemMedChem* **2015**, *10*, 1218–1231.
- [25] G. L. Becker, F. Sielaff, M. E. Than, I. Lindberg, S. Routhier, R. Day, Y. Lu, W. Garten, T. Steinmetzer, *J. Med. Chem.* **2010**, *53*, 1067–1075.
- [26] A. Thakkar, T. B. Trinh, D. Pei, *ACS Comb. Sci.* **2013**, *15*, 120–129.
- [27] G. L. Becker, K. Harges, T. Steinmetzer, *Bioorg. Med. Chem. Lett.* **2011**, *21*, 4695–4697.
- [28] J. W. Williams, J. F. Morrison, *Methods Enzymol.* **1979**, *63*, 437–467.
- [29] T. Ivanova, K. Harges, S. Kallis, S. O. Dahms, M. E. Than, S. Künzel, E. Böttcher-Friebertshäuser, I. Lindberg, G. S. Jiao, R. Bartenschlager, T. Steinmetzer, *ChemMedChem* **2017**, *12*, 1953–1968.
- [30] S. O. Dahms, K. Harges, G. L. Becker, T. Steinmetzer, H. Brandstetter, M. E. Than, *ACS Chem. Biol.* **2014**, *9*, 1113–1118.
- [31] S. O. Dahms, M. Arciniega, T. Steinmetzer, R. Huber, M. E. Than, *Proc. Natl. Acad. Sci. USA* **2016**, *113*, 11196–11201.
- [32] E. Rey-Jurado, A. M. Kalergis, *Int. J. Mol. Sci.* **2017**, *18*, 556.
- [33] L. Gonzalez-Reyes, M. B. Ruiz-Arguello, B. Garcia-Barreno, L. Calder, J. A. Lopez, J. P. Albar, J. J. Skehel, D. C. Wiley, J. A. Melero, *Proc. Natl. Acad. Sci. USA* **2001**, *98*, 9859–9864.
- [34] G. Zimmer, L. Budz, G. Herrler, *J. Biol. Chem.* **2001**, *276*, 31642–31650.
- [35] G. Zimmer, M. Rohn, G. P. McGregor, M. Schemann, K. K. Conzelmann, G. Herrler, *J. Biol. Chem.* **2003**, *278*, 46854–46861.
- [36] G. L. Becker, Y. Lu, K. Harges, B. Strehlow, C. Levesque, I. Lindberg, K. Sandvig, U. Bakowsky, R. Day, W. Garten, T. Steinmetzer, *J. Biol. Chem.* **2012**, *287*, 21992–22003.
- [37] Y. Lu, K. Harges, S. O. Dahms, E. Böttcher-Friebertshäuser, T. Steinmetzer, M. E. Than, H. D. Klenk, W. Garten, *Antiviral Res.* **2015**, *120*, 89–100.
- [38] J. Kouretova, M. Z. Hammamy, A. Epp, K. Harges, S. Kallis, L. Zhang, R. Hilgenfeld, R. Bartenschlager, T. Steinmetzer, *J. Enzyme Inhib. Med. Chem.* **2017**, *32*, 712–721.
- [39] N. Krüger, C. Sauder, S. Huttli, J. Papies, K. Voigt, G. Herrler, K. Harges, T. Steinmetzer, C. Orvell, J. F. Drexler, C. Drosten, S. Rubin, M. A. Müller, M. Hoffmann, *Cell Rep.* **2018**, *25*, 312–320.
- [40] S. Sabouri-Rad, R. K. Oskuee, A. Mahmoodi, L. Gholami, B. Malaek-Nikouei, *Bioimpacts* **2017**, *7*, 139–145.
- [41] P. Arukuusk, L. Pärnaste, N. Oskolkov, D.-M. Copolovici, H. Margus, K. Padari, K. Möll, J. Maslovskaia, R. Tegova, G. Kivi, A. Tover, M. Pooga, M. Ustav, Ü. Langel, *Biochim. Biophys. Acta Biomembr.* **2013**, *1828*, 1365–1373.
- [42] G. Bajaj, A. M. Hau, P. Hsu, P. R. Gafken, M. I. Schimerlik, J. E. Ishmael, *Biochem. Biophys. Res. Commun.* **2014**, *444*, 588–594.
- [43] M. A. Dechantsreiter, E. Planker, B. Matha, E. Lohof, G. Holzemann, A. Jonczyk, S. L. Goodman, H. Kessler, *J. Med. Chem.* **1999**, *42*, 3033–3040.
- [44] D. de Sanctis, A. Beteva, H. Caserotto, F. Dobias, J. Gabadinho, T. Giraud, A. Gobbo, M. Guijarro, M. Lentini, B. Lavault, T. Mairs, S. McSweeney, S. Petitdemange, V. Rey-Bakaikoa, J. Surr, P. Theveneau, G. A. Leonard, C. Mueller-Dieckmann, *J. Synchrotron Radiat.* **2012**, *19*, 455–461.
- [45] P. Theveneau, R. Baker, R. Barrett, A. Beteva, M. W. Bowler, P. Carpentier, H. Caserotto, D. D. Sanctis, F. Dobias, D. Flot, M. Guijarro, T. Giraud, M. Lentini, G. A. Leonard, M. Mattenet, A. A. McCarthy, S. M. McSweeney, C. Morawe, M. Nanao, D. Nurizzo, S. Ohlsson, P. Pernot, A. N. Popov, A. Round, A. Royant, W. Schmid, A. Snigirev, J. Surr, C. Mueller-Dieckmann, *J. Phys. Conf. Ser.* **2013**, *425*, 012001.
- [46] W. Kabsch, *Acta Crystallogr. Sect. D* **2010**, *66*, 125–132.
- [47] K. M. Sparta, M. Krug, U. Heinemann, U. Mueller, M. S. Weiss, *J. Appl. Crystallogr.* **2016**, *49*, 1085–1092.
- [48] M. D. Winn, C. C. Ballard, K. D. Cowtan, E. J. Dodson, P. Emsley, P. R. Evans, R. M. Keegan, E. B. Krissinel, A. G. Leslie, A. McCoy, S. J. McNicholas, G. N. Murshudov, N. S. Pannu, E. A. Potterton, H. R. Powell, R. J. Read, A. Vagin, K. S. Wilson, *Acta Crystallogr. Sect. D* **2011**, *67*, 235–242.
- [49] P. Emsley, B. Lohkamp, W. G. Scott, K. Cowtan, *Acta Crystallogr. Sect. D* **2010**, *66*, 486–501.
- [50] P. D. Adams, P. V. Afonine, G. Bunkoczi, V. B. Chen, I. W. Davis, N. Echols, J. J. Headd, L. W. Hung, G. J. Kapral, R. W. Grosse-Kunstleve, A. J. McCoy, N. W. Moriarty, R. Oeffner, R. J. Read, D. C. Richardson, J. S. Richardson, T. C. Terwilliger, P. H. Zwart, *Acta Crystallogr. Sect. D* **2010**, *66*, 213–221.
- [51] A. W. Schüttelkopf, D. M. van Aalten, *Acta Crystallogr. Sect. D* **2004**, *60*, 1355–1363.
- [52] M. Matrosovich, T. Matrosovich, W. Garten, H. D. Klenk, *Virol. J.* **2006**, *3*, 63.

Manuscript received: December 20, 2018

Revised manuscript received: January 18, 2019

Accepted manuscript online: January 25, 2019

Version of record online: February 20, 2019



Supporting Information

Design, Synthesis, and Characterization of Macrocyclic Inhibitors of the Proprotein Convertase Furin

Thuy Van Lam van,^[a] Teodora Ivanova,^[a] Kornelia Harges,^[a] Miriam Ruth Heindl,^[b] Rory E. Morty,^[c] Eva Böttcher-Friebertshäuser,^[b] Iris Lindberg,^[d] Manuel E. Than,^[e] Sven O. Dahms,^[f] and Torsten Steinmetzer*^[a]

cmdc_201800807_sm_miscellaneous_information.pdf

1. Enzyme kinetics

The following equations have been used for the calculation of K_i and IC_{50} values.

Equation describing the **reversible competitive inhibition**, which was used for the calculation of the K_i values of inhibitors **2-9**, **12**, and **14-20**:

$$v_i = \frac{V_{max} \times [S]}{K_M \times \left(1 + \frac{[I]}{K_i}\right) + [S]}$$

with

v_i = steady-state reaction rate in the presence of a certain inhibitor concentration,

V_{max} = maximal rate of the uninhibited reaction,

$[S]$ = substrate concentration,

$[I]$ = inhibitor concentration,

K_M = Michaelis-Menten constant, and

K_i = inhibitory constant

Three-parameter equation used for calculating the IC_{50} values of inhibitors **21-24**:

$$v_i = \frac{v_0}{1 + \left(\frac{[I]}{IC_{50}}\right)^p}$$

with

v_i = steady-state reaction rate in the presence of a certain inhibitor concentration,

v_0 = rate of the uninhibited reaction at the used constant substrate concentration,

$[I]$ = inhibitor concentration,

IC_{50} = half maximal inhibitory concentration, and

p = slope factor.

Morrison equation for calculation of K_i^{app} values of tight-binding inhibitors **10**, **11**, and **13** possessing K_i values < 0.15 nM:

$$v_i = v_0 \times \frac{[(K_i^{app} + [I]_t - [E]_t)^2 + 4 \times K_i^{app} \times [E]_t]^{1/2} - (K_i^{app} + [I]_t - [E]_t)}{2 \times [E]_t}$$

The substrate-independent true K_i values were calculated from the K_i^{app} values according to the following formula:

$$K_i = \frac{K_i^{app}}{1 + \frac{[S]}{K_M}}$$

with

v_i = steady-state reaction rate in the presence of a certain inhibitor concentration,

v_0 = rate of the uninhibited reaction at the fixed substrate concentration,

K_i^{app} = apparent inhibitory constant,

$[I]_t$ = total inhibitor concentration,

$[E]_t$ = total enzyme concentration,

K_i = inhibitory constant,

$[S]$ = substrate concentration, and

K_M = Michaelis-Menten constant.

2. Structure determination of furin in complex with inhibitors 2, 3, 4, 5, 7, 10, and 12

Table S1. Data collection and refinement statistics.

Data collection statistics	2	3	4	5	7	10	12
PDB ID	6HZA	6HZB	6HZD	6HLE	6HLC	6HLB	6HLD
Wavelength	0.9677	0.9677	0.9677	0.9942	0.9677	0.9942	0.9942
Space group	P6 ₃ 22						
Unit cell parameters							
a (Å), b (Å), c (Å)	131.4, 131.4, 155.2	131.6, 131.6, 155.6	131.6, 131.6, 155.3	133.1, 133.1, 157.6	131.7, 131.7, 155.3	133.3, 133.3, 157.4	133.4, 133.4, 157.4
Resolution range ^a (Å)	45.9-1.9 (2.01-1.90)	43.09-1.9 (2.01-1.90)	45.9-1.9 (2.01-1.90)	43.6-2.0 (2.12-1.99)	46.0-1.9 (2.01-1.90)	47.8-2.0 (2.12-2.00)	46.6-2.1 (2.23-2.10)
R _{meas} ^a (%)	14.7 (129.7)	14.5 (138.2)	11.0 (126.2)	12.3 (81.8)	13.5 (134.8)	8.1 (87.3)	12.4 (93.5)
I/σ(I) ^a	17.6 (2.7)	20.1 (2.7)	23.8 (2.9)	11.2 (2.5)	20.2 (2.6)	17.5 (2.7)	11.3 (2.2)
Completeness ^a	98.5 (98.3)	98.1 (97.9)	95.9 (95.9)	99.5 (98.1)	94.4 (95.8)	98.7 (97.5)	99.5 (99.0)
No. of observations	1,159,582/61,782	1,131,359/61,892	1,126,847/60,391	309,055/56,219	1,058,666/59,568	371,014/55,572	266,431/48,535
Refinement statistics							
No. of non-hydrogen atoms	4,150	4,150	4,163	4,127	4,162	4,028	4,067
protein/inhibitor/other	3,653/60/437	3,653/58	3,653/71/439	3,643/73/411	3,653/77/432	3,594/75/359	3,626/77/364
R _{work} /R _{free}	16.6/18.6	16.5/18.2	16.4/18.3	16.7/19.1	16.4/18.3	16.9/18.7	17.0/19.6
B-factors (Å ²)							
Overall/Wilson plot	28.6/31.0	28.2/30.7	31.5/33.7	30.6/33.0	29.4/31.9	36.4/38.5	35.9/37.6
protein/inhibitor/other	27.7/29.4/36.4	27.2/30.8/35.5	30.6/33.1/38.8	29.6/33.5/38.6	28.4/33.7/36.8	35.7/38.8/43.6	35.1/41.8/42.4
RMSD bond length (Å)	0.006	0.007	0.006	0.008	0.007	0.009	0.008
RMSD bonded B-factors (Å ²)	3.9	3.5	3.2	3.8	3.6	3.6	4.0

^a Values of the highest resolution shell are given in parentheses

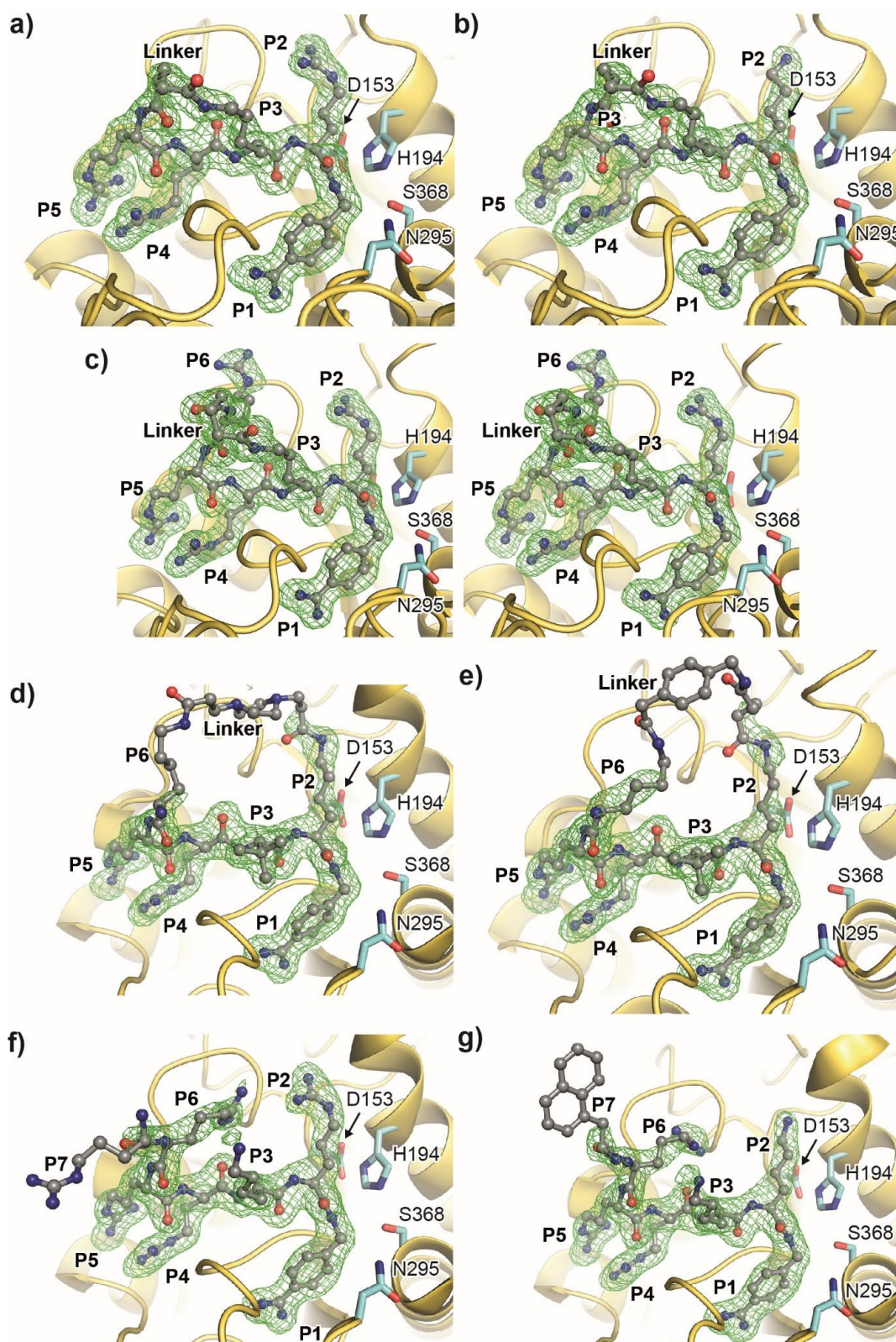


Figure S1. Electron density maps of the furin-bound inhibitors **2** (a), **3** (b), **4** (c, stereo representation), **5** (d), **7** (e) **10** (f) and **12** (g). The protein backbone of furin is given as cartoon representation (golden). The residues of the catalytic triad (Ser368, His194, and Asp153) as well as Asn295 of the oxyanion hole are shown as stick model with carbon atoms in cyan. Inhibitors are shown as ball-and-stick models. The F_o-F_c simulated annealing omit electron density maps (green mesh, atoms of the inhibitors were deleted for map calculation to avoid model bias) are contoured at 3σ . The linker segments of inhibitors **5** and **7** as well as the P7 side chains of inhibitors **10** and **12** were built and refined with zero occupancy. The linker segments of inhibitors **10** and **12** are missing in the structure.

4.2 The basicity makes the difference – Improved canavanine-derived inhibitors of the proprotein convertase furin

Thuy Van Lam van, Miriam Ruth Heindl, Christine Schlutt, Eva Böttcher-Friebertshäuser, Ralf Bartenschlager, Gerhard Klebe, Hans Brandstetter, Sven O. Dahms, and Torsten Steinmetzer
(2021)

ACS Medicinal Chemistry Letters. 2021

DOI: 10.1021/acsmchemlett.0c00651

The Basicity Makes the Difference: Improved Canavanine-Derived Inhibitors of the Proprotein Convertase Furin

Thuy Van Lam van, Miriam Ruth Heindl, Christine Schlutt, Eva Böttcher-Friebertshäuser, Ralf Bartenschlager, Gerhard Klebe, Hans Brandstetter, Sven O. Dahms, and Torsten Steinmetzer*

Cite This: *ACS Med. Chem. Lett.* 2021, 12, 426–432

Read Online

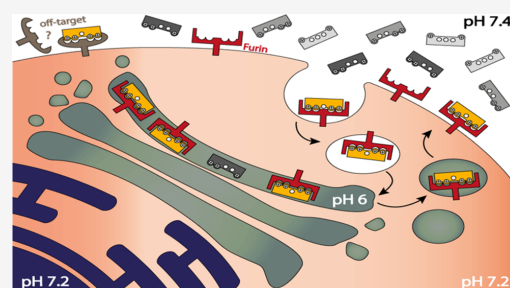
ACCESS |

Metrics & More

Article Recommendations

Supporting Information

ABSTRACT: Furin activates numerous viral glycoproteins, and its inhibition prevents virus replication and spread. Through the replacement of arginine by the less basic canavanine, new inhibitors targeting furin in the trans-Golgi network were developed. These inhibitors exert potent antiviral activity in cell culture with much lower toxicity than arginine-derived analogues, most likely due to their reduced protonation in the blood circulation. Thus, despite its important physiological functions, furin might be a suitable antiviral drug target.



KEYWORDS: furin inhibitors, proprotein convertases, canavanine, crystal structure analysis, proteolytic activation of viruses

Furin belongs to the basic proprotein convertases (PCs), a family of seven Ca^{2+} -dependent human subtilisin-like serine proteases. It activates a huge number of proproteins at characteristic multibasic recognition sequences, including proforms of hormones, enzymes, adhesion proteins, and various receptors.^{1,2} Given these important physiological functions, the whole body knockout of furin in mice is not tolerated and causes embryonic lethality 11 days after gestation. In contrast, an inducible liver-specific knockout in adult mice is well-tolerated, and no morphological abnormalities were found.³ As host protease, furin also activates various toxins of pathogenic bacteria as well as surface glycoproteins of numerous furin-dependent viruses. The cleavage of these viral glycoproteins is essential to ensure cell entry and fusion competence of virus particles, thus contributing to their pathogenicity.⁴ Therefore, furin emerged as a potential target for the development of broad-spectrum antivirals, at least for a short-term administration during acute infections. Based on sequence analysis⁵ and modification of the furin cleavage site,⁶ it was recently suggested that furin also contributes to the activation of the spike protein of the new SARS-coronavirus 2 (SARS-CoV-2) at the S1/S2 site, although a second cleavage by the trypsin-like serine protease TMPRSS2 at the S2' site is required to unmask the fusion peptide.^{7,8}

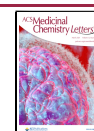
With our previously described 4-aminobenzylamide (Amba) derived inhibitor **1**⁹ and its analogues, we could inhibit the replication of numerous furin-dependent viruses in cell culture, like highly pathogenic bird flu strains H5N1 and H7N1,^{10,11} Chikungunya virus,¹² West Nile and Dengue-2

virus,¹³ mumps virus,¹⁴ or respiratory syncytial virus (RSV).¹⁵ Although these inhibitors revealed only a negligible toxicity in all used cell cultures up to concentrations of 50 μM , they exhibited a significant toxicity in mice. While an intraperitoneal dose of 2.5 mg/kg of inhibitor **1** was accepted, all mice died within the first hour at the next higher dose of 5 mg/kg.¹³ A significant toxicity in mice for structurally related Amba-derived furin-like PC inhibitors was also reported by a different group.^{16,17} Because of previously or presently approved benzamidine derivatives like the prodrugs of melagatran and dabigatran or pentamidin, we assumed that the toxicity of compound **1** is not simply caused by the P1 Amba anchor, but also by the presence of the three additional strongly basic guanidine groups. This was confirmed by deletion or replacements of the individual guanidine and amidine moieties, which all provided less toxic analogues.¹³ However, most of these compounds exhibited a considerably weaker inhibitory potency against furin in enzyme kinetic measurements and strongly reduced or complete lack of any antiviral activity in infected cell cultures. Only the replacement of the P2 Arg in

Received: December 15, 2020

Accepted: February 5, 2021

Published: February 9, 2021



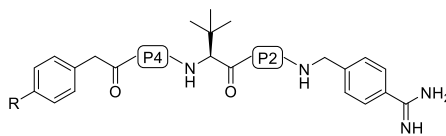
inhibitor **1** by Lys in case of compound **2** was tolerated and provided a slightly less toxic compound.¹³

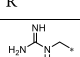
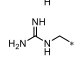
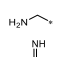
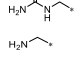
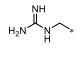
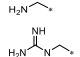
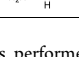
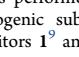
This also raised the question of whether toxicity in mice is either generally caused by the inhibition of the physiological relevant furin itself, which activates most viral glycoproteins and physiological substrates in the trans-Golgi-network (TGN),^{1,2} or by addressing a different, so far unknown off-target in the blood circulation. For an antiviral effect through an effective inhibition of furin, the P2 and P4 side chains of substrate analogue inhibitors must be protonated in the TGN at a pH close to 6.0.^{18,19} Furthermore, we assumed that only the same completely protonated inhibitor species can address the hypothetical off-target in the circulation at a pH around 7.4. Therefore, we propose the hypothesis that this pH difference can be utilized to develop compartment-specific furin inhibitors by replacing the strongly basic P2 and P4 arginines with a residue that is almost completely protonated and positively charged under slightly acidic conditions in the TGN while only partially charged in the circulation and extracellular space. This strategy provided improved furin inhibitors with a stronger antiviral activity in cell culture and reduced toxicity in mice at the same time.

INHIBITOR DESIGN

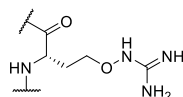
A drastic drop in the pK_a value of alkyl guanidines can be achieved by replacing the methylene group next to the guanidine with oxygen. Such oxyguanidine groups were incorporated in various thrombin inhibitors to improve their bioavailability.^{20,21} Based on this strategy, we prepared a new inhibitor series (Table 1) by replacing the P2 and/or P4

Table 1. Structures and Potencies of the Synthesized Furin Inhibitors



No.	R	P4	P2	K_i (pM) ^a
1 ^b		Arg	Arg	5.5 ± 0.3
2 ^b		Arg	Lys	8.8 ± 4.9
3		Arg	Cav ^c	76.8 ± 14.9
4		Arg	Cav	13.1 ± 1.6
5		Cav	Lys	114 ± 25.9
6		Cav	Lys	36.3 ± 11.2
7		Cav	Cav	34.2 ± 5.1
8		Cav	Cav	10.1 ± 3.2

^aThe assay was performed using recombinant soluble human furin and the fluorogenic substrate Phac-Arg-Val-Arg-Arg-AMC.⁹ ^bThe reference inhibitors **1**⁹ and **2**¹³ were described previously. ^c



residues of inhibitors **1** and **2** by canavanine (Cav). Canavanine is an unusual amino acid containing a weakly basic oxyguanidine group with a pK_a value of 7.01.^{22,23} It should be largely protonated at pH 6.0 suitable for the inhibition of furin in the TGN, whereas it is only partially protonated at pH 7.4, thereby reducing the concentration of the completely protonated species addressing the unknown off-target in the circulation and improving the bioavailability. For instance, based on the Henderson–Hasselbalch equation, it can be roughly calculated for compound **8**, which contains two independently protonatable Cav residues, that at pH 6.0, approximately 80% of the inhibitor exists as the fully 4-fold protonated species, while at pH 7.4, it is only approximately 9%.

The replacement of the P2 Arg in inhibitor **1** provided the Cav derivative **4**, which possesses a 2.4-fold reduced potency in the enzyme kinetic assay, which was performed under our standard conditions at pH 7.0,⁹ where the Cav side chain should be incompletely protonated. The aminomethyl derivative **3** was prepared as an additional analogue lacking the guanidine substitution on the P5 phenylacetyl (Phac) group, although we knew from previous studies that this modification leads to a slightly reduced furin inhibition and weaker antiviral activity in cell culture.^{9,10} Compound **6** is the P4 Cav derivative of inhibitor **2**, whereas compounds **7** and **8** contain two Cav residues in the P2 and P4 position. Especially compounds **4** and **8** are still very potent furin inhibitors with K_i values <15 pM.

Notably, the replacement of the P2 and P4 Arg residues in inhibitor **1** with Cav further reduces the inhibitory potency of this compound type against trypsin. While compound **1** is still a relatively effective trypsin inhibitor possessing a K_i value of 52 nM,²⁴ the affinity of inhibitor **8** is 10-fold reduced (K_i for trypsin 690 nM). Furthermore, a negligible potency ($K_i > 3 \mu\text{M}$) was found for the other tested trypsin-like serine proteases thrombin, factor Xa, and plasmin (Table S3).

CRYSTAL STRUCTURE DETERMINATION

Due to the sp^3 hybridization of the oxygen, we expected that the side chain of Cav can adopt an identical geometry like arginine in the P4 position, which is a prerequisite for an efficient furin inhibition by substrate analogue structures. This assumption could be proven by crystal structures of inhibitors **4**–**6** and **8**, which were determined after soaking the compounds into crystals of ligand-free furin.²⁵ Resolutions between 1.7–2.0 Å have been observed for all complexes, as well as good stereochemistry and R-factors (Table S2). In all crystal structures, furin was found to adopt the “ON”-state enabling a canonical protease-ligand interaction pattern (Figure 1A–D). This includes a specific change of the conformation of the alignment template and of the catalytic triad triggered by ligand binding.²⁵ The observed $C\alpha$ -RMSD values between the structures are lower than 0.1 Å, indicating high overall similarity.

An identical side chain conformation was observed for the P2 Cav-derived inhibitors **4** and **8** (Figure 1A, D) when compared with the previously determined crystal structure of the P2 arginine analogue **1** in furin.⁹ The same applies for the incorporation of Cav in the P4 position as found in the complexes with inhibitors **5**, **6**, and **8** (Figure 1B, C).

Interestingly, the P4-Cav was found to affect the binding of the N-terminal P5-group in the case of inhibitors **5**, **6**, and **8**, which was found to adopt two prevailing conformations with

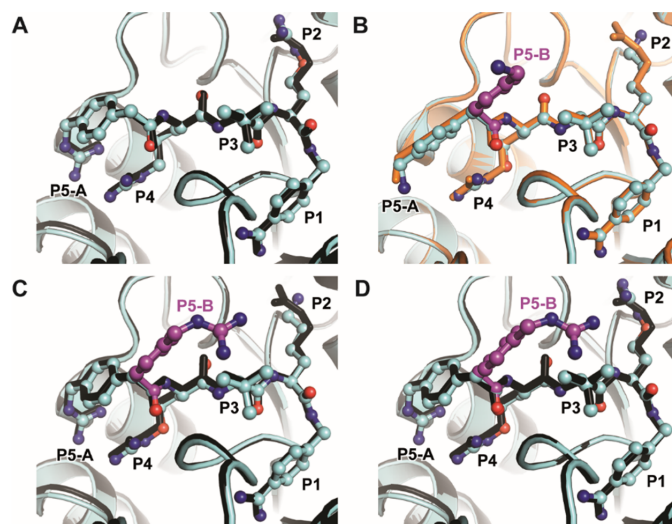


Figure 1. Crystal structures of furin in complex with Cav-based inhibitors. Furin and the inhibitors are shown as cartoon and ball-and-stick models, respectively (cyan). (A, C, D) Furin in complex with inhibitors 4 (A), 6 (C), and 8 (D) all superimposed to the structure of furin (cartoon, black) in complex with analogue **1**⁹ (stick model, black). (B) Furin in complex with inhibitor 5 superimposed to the structure of furin (cartoon, black) in complex with 4-aminomethyl-phenylacetyl-Arg-Tle-Arg-Amba²⁶ (stick model, orange). (A–D) The major conformation of the P5 residue is labeled as P5-A, alternative conformations are shown in magenta (P5-B).

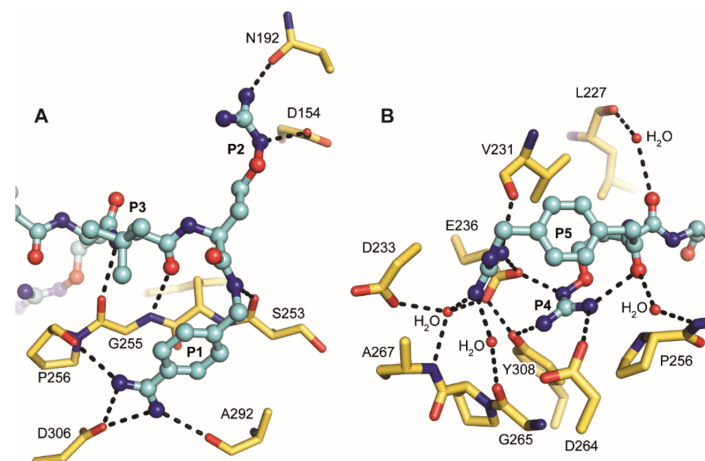


Figure 2. Polar interactions of inhibitor **8** (ball-and-stick model with carbons in cyan) with furin shown as a stick model with yellow carbons, hydrogen bonds are shown as black dashed lines. (A) Polar interactions of the inhibitor's P3–P1 segment. The P1 amidine forms a salt bridge to Asp306 and two additional hydrogen bonds with the carbonyl oxygens of Pro256 and Ala292. The P1 backbone NH binds to the carbonyl oxygen of Ser253. The oxyguanidino moiety of the P2 residue interacts with the carbonyl of Asp154 and the side chain of Asn192, respectively. The P3 backbone makes antiparallel beta-sheet-like hydrogen bonds with Gly255. (B) Polar interactions of the inhibitor's P5–P4 segment. The P4 Cav side chain contacts Asp264, Glu236, and Tyr308, respectively, whereas the P4 carbonyl binds to Leu227 via a water molecule. The P5 guanidino group makes electrostatic interactions with the carboxyl of Glu236 and a hydrogen bond to the carbonyl of Val231. An intramolecular hydrogen bond is formed between the P4 side chain and P5 carbonyl oxygen. Water bridges interactions are found between the P5 carbonyl oxygen and Glu257 NH and from the P5 guanidino group to Gly265, Asp233, and Ala267. It is noteworthy that these interactions of the P5 guanidino group are only observed for conformation A, whereas conformation B is not involved in polar contacts.

similar occupancies (Figure 1B–D). In comparison to their P1–P4 segments, we observed a less well-defined electron density map for the conformation P5-A of these inhibitors with occupancies of 0.5, 0.5, and 0.57, respectively (Figure S1B–D). It is noteworthy that the minor conformation P5-B does not mediate specific attractive interactions with furin. This effect

was observed for both the aminomethyl-Phac (inhibitor 5, Figure 1B) and the guanidinomethyl-Phac group (inhibitors 6 and 8, Figure 1C, D) at the P5 position. In contrast, if arginine was present at P4 (inhibitor 4, Figure 1A), P5 was found in its typical conformation known from inhibitor **1**⁹ as indicated by the well-defined electron density map (Figure S1A).

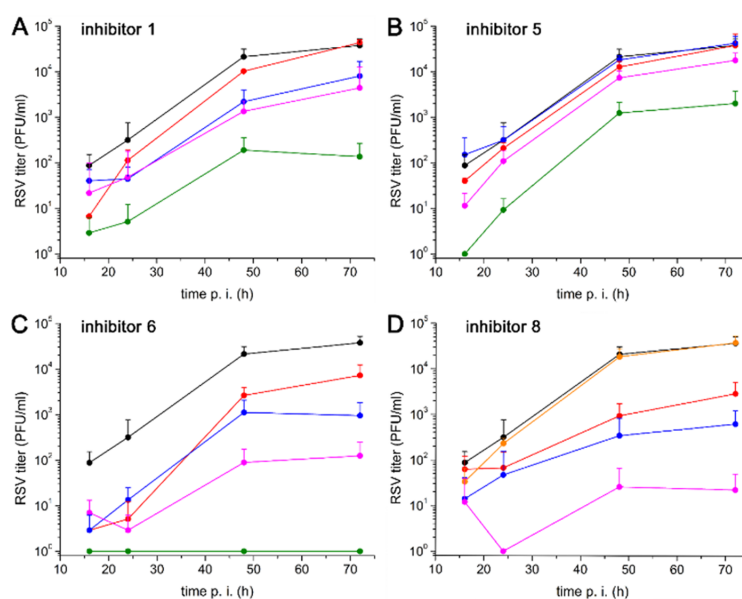


Figure 3. Multicycle replication of RSV in A549 cells. Cells were inoculated with an MOI of 1 for 1 h. After washing, the cells were incubated with various concentrations (control without inhibitor (black), 10 μM (green), 2.5 μM (pink), 1.0 μM (blue), and 0.5 μM (red) of the reference inhibitor 1 (A) and the canavanine-containing analogues 5 (B) and 6 (C). In case of inhibitor 8 (D), the 10 μM concentration was replaced with a 0.1 μM (orange) concentration. At 16, 24, 48, and 72 h post infection, cell supernatants were collected, and viral titers \pm standard deviation ($n = 3$) were determined by plaque assay (plaque-forming units (PFU) per mL).

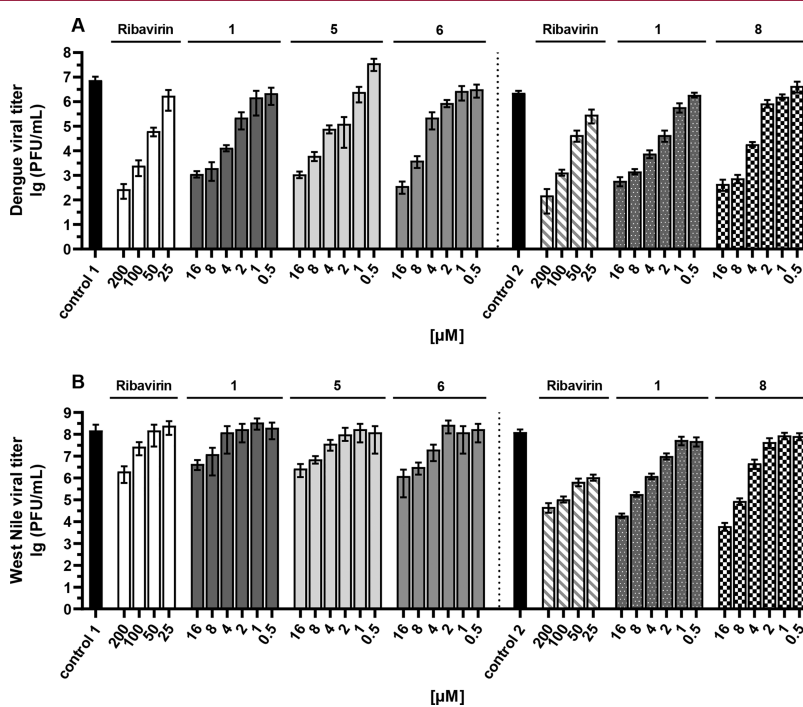


Figure 4. Infection of Huh-7 cells with DENV-2 (A) and WNV (B) in the presence of selected inhibitors. Cell culture supernatants were harvested 48 h postinfection, and virus titers \pm standard deviation ($n = 2$) were determined by plaque assay in VeroE6 cells. The effects of the reference compounds 1 and ribavirin as well as details of the assay methods used have been described recently.^{13,32}

Interestingly, we observed either no deteriorating effect (inhibitor 4 vs 8) on the K_i value or only a moderate drop in inhibitory potency (inhibitor 2 vs 6) due to these alternative P5 conformations caused by the exchange of Arg by Cav at P4. This observation was unexpected because in previous studies we found a strong contribution of the guanidinomethyl-substituted P5 group of up to two orders of magnitude on the K_i value compared with the unsubstituted Phac derivative.¹⁰ A potential loss of binding affinity at P5, as suggested by the distorted P5 residue in the structures with inhibitors 5, 6, and 8, might be compensated by a stronger contribution of P4-Cav, consistent with an increased binding affinity of compound 7 compared with that of inhibitor 3. The Cav side chain shows a different charge distribution compared to arginine because of the electronegative oxygen atom of its oxyguanidino moiety, which might fit better to the S4 pocket of furin. Another explanation might be an impact of P4 Cav to the binding thermodynamics of P5. The alternative occupation of the P5 residue indicates a reduced contribution of hydrogen bonds and electrostatic interactions and thus a reduction of the binding enthalpy. However, the flexibility of the P5 residue is increased in this setting and might compensate the loss of enthalpy by a gain in entropy while keeping the Gibbs free energy virtually unchanged. Figure 2 shows the polar contacts of inhibitor 8 in complex with furin.

ANTIVIRAL ACTIVITY

Among many viral glycoproteins,^{2,27} furin activates the precursor of the fusion protein F of RSV at two multibasic sequences. One of them is directly located at the N-terminal side of the fusion peptide (Lys131-Lys-Arg-Lys-Arg-Arg136↓) and the second 27 residues upstream at the Arg106-Ala-Arg-Arg109↓ segment.^{28,29} Both cleavages and the concomitant release of a 27-mer peptide are essential for the fusion capacity of F and productive infection of target cells. RSV infects nearly all children by two years of age and in some cases, especially in very young children, this can lead to airway inflammation, bronchiolitis, and pneumonia. Worldwide, approximately 3.2 million hospitalizations leading to around 66 000 in-hospital deaths annually in infants younger than 5 years have been reported.^{30,31} The replication mechanism of RSV suggests a furin inhibition as potential antiviral therapy. Therefore, we investigated selected inhibitors in a multicycle replication assay in A549 human lung cancer cells infected with the RSV A2 strain, as reported previously for inhibitor 1,¹⁵ which was used as a reference compound. Compared with inhibitor 1, a reduced RSV inhibition was observed with compound 5, possessing a 4-aminomethyl substitution on the P5 Phac group, while the 4-guanidinomethyl analogue 6 was slightly more potent than the reference inhibitor (Figure 3A–C). The strongest antiviral efficacy was found for inhibitor 8. Based on initial tests, in which a complete inhibition of virus replication was found at 10 μM of inhibitor 8, 0.1 μM was used as lowest concentration for this compound (Figure 3D).

Furthermore, the host protease furin activates the prM precursor of the membrane protein M of numerous pathogenic flaviviruses like Dengue, West Nile, Zika, Yellow fever, Japanese encephalitis, St. Louis encephalitis virus, and others. Furin cleavage of prM is essential to render virus particles infectious. Therefore, the antiviral activity of compounds 5 and 6 was tested in Huh-7 cells infected with dengue virus (strain 16681) or with West-Nile virus, as described previously.^{15,32} In a second experiment, inhibitor 8 was also included (Figure 4).

Inhibitor 1 and the nucleoside analogue ribavirin were used as reference compounds. Also with these viruses, a significant antiviral potency was observed for inhibitors 5, 6, and 8 (Figure 4). For compound 1, EC_{50} values of 0.76 and 0.91 μM were determined for the inhibition of DENV-2 and WNV replication, respectively. Slightly higher EC_{50} values of 1.50 μM (DENV-2) and 1.46 μM (WNV) were calculated for inhibitor 8. For both compounds, the cytotoxicity in Huh-7 cells (CC_{50}) is >50 μM (highest tested concentration). This provided a selectivity index ($\text{SI} = \text{CC}_{50}/\text{EC}_{50}$) >33 for compound 8 against both flaviviruses, the SI values for the reference inhibitor 1 are >65 (DENV-2) and >55 (WNV).

TOXICITY STUDIES

Three Cav-derived inhibitors, converted into their physiologically more acceptable hydrochlorides as described previously,¹³ were tested for toxicity after intraperitoneal (*ip*) treatment in mice. On the first day, the mice were treated with 2.5 mg/kg inhibitor and only, if all four mice survived, with the next higher dose always 24 h later (5, 10, or 15 mg/kg). In contrast to the reference inhibitors 1 and 2, a reduced toxicity was found for all three Cav derivatives (Table 2). Together

Table 2. Toxicity Study in Mice

no.	tolerated dose (mg/kg)	number of deaths at next higher dose ^a
1 ^b	2.5	4 of 4 at 5 mg/kg
2 ^b	5	4 of 4 at 10 mg/kg
5	15	no higher dose tested
6	10	1 of 4 at 15 mg/kg
8	15	no higher dose tested

^aIn each group, four mice (two female and two male) were intraperitoneally treated. ^bPublished previously¹³

with the results from antiviral testing, where compounds 6 and 8 were nearly equipotent to inhibitor 1, it can be concluded that the toxicity of this compound type does not correlate with the inhibition of intracellular furin, leading to an antiviral activity. So far, we cannot explain the exact mechanism leading to the reduced toxicity of the less basic Cav-containing inhibitor 8 compared to its isostructural Arg analogue 1. Notably, similar plasma levels were obtained after intravenous treatment of rats with 1 mg/kg of both compounds. However, two of three rats died within 90 min after *iv* treatment with inhibitor 1 at this concentration (data not shown), whereas compound 8 was well-accepted in all three rats without any signs of side effects, which is a significant advantage compared to our previous inhibitors. Hence, we suspect that a different, so far unknown off-target must be responsible for the toxicity of these benzamidine derivatives, which confirms our previous results.¹³

For further characterization, the best compound 8 was investigated for its pharmacokinetic (PK) properties in rats. The inhibitor was given intravenously (1 mg/kg) and displayed a half-life of 0.9 h and a total body clearance of 442 mL/(h·kg). After intraperitoneal treatment (2.5 mg/kg), a half-life of 1.6 h, a total body clearance of 273 mL/(h·kg), and a maximal concentration (C_{max}) of 3156 ng/mL after 0.5 h were determined. This provided plasma levels >1000 ng/mL ($\sim 1.3 \mu\text{M}$) over a period of approximately 3 h (Figure S6). Such a concentration is close to the range of the EC_{50} values determined for the inhibition with DENV-2 and WNV replication in cell culture studies.

The replacement of arginine by canavanine provided a new series of highly potent furin inhibitors which exhibit a binding mode similar to that found previously in crystal structures of furin in complex with their arginine analogues. The tested compounds possess a significant antiviral activity against furin-dependent viruses, like RSV, WNV, and Dengue-2 virus. The strongest efficacy against RSV was found for inhibitor **8**. This compound also exhibits an efficient inhibition of WNV and Dengue-2 virus replication and possesses a considerably reduced toxicity in mice and rats compared to compound **1**.

Our results prove that the toxicity of these substrate-analogue furin inhibitors does not correlate with the strength of the intracellular furin inhibition. Despite its manifold physiological functions, this makes furin a suitable therapeutic target, especially for the short-term treatment of certain acute infectious diseases. As described recently, treatment with the furin inhibitor **8** also provided a significant reduction of the SARS-CoV-2 replication in infected Calu-3 cells due to the inhibition of the S1/S2 cleavage in its spike surface protein.⁸ Moreover, in previous studies using cell cultures infected with highly pathogenic avian influenza strains,¹¹ we demonstrated a beneficial antiviral effect when the inhibitors of the host protease furin were used in combination with additional drugs addressing viral proteins. This strategy allowed a further reduction of the individual inhibitor concentrations while improving the antiviral efficacy. We are confident that the new and less toxic canavanine-derived furin inhibitors, like compound **8**, are suited for similar combination therapies, which should further reduce drug-related side effects *in vivo* and the rapid development of resistant virus strains.

■ ASSOCIATED CONTENT

SI Supporting Information

The Supporting Information is available free of charge at <https://pubs.acs.org/doi/10.1021/acsmmedchemlett.0c00651>.

Synthesis¹³ and analytical characterization of the inhibitors; protein crystallography with furin including the soaking of the inhibitors into ligand free crystals of furin;²⁵ diffraction data collection, data processing, model building and refinement;²⁶ conditions of the enzyme kinetic measurements; determination of the antiviral activity against RSV,¹⁵ Dengue-2 virus,³² and West Nile virus³² in infected cell cultures; toxicity studies in mice;¹³ and details of the PK study with inhibitor **8** in rats (PDF).

Accession Codes

PDB IDs: 6YD7 (4), 6YD2 (5), 6YD3 (6), and 6YD4 (8).

■ AUTHOR INFORMATION

Corresponding Author

Torsten Steinmetzer – Institute of Pharmaceutical Chemistry, Philipps University, 35032 Marburg, Germany; orcid.org/0000-0001-6523-4754; Email: steinmetzer@uni-marburg.de

Authors

Thuy Van Lam van – Institute of Pharmaceutical Chemistry, Philipps University, 35032 Marburg, Germany
Miriam Ruth Heindl – Institute of Virology, Philipps University, 35043 Marburg, Germany
Christine Schlutt – Institute of Pharmaceutical Chemistry, Philipps University, 35032 Marburg, Germany

Eva Böttcher-Friebertshäuser – Institute of Virology, Philipps University, 35043 Marburg, Germany

Ralf Bartenschlager – Department of Infectious Diseases, Molecular Virology, Heidelberg University and German Center for Infection Research, 69120 Heidelberg, Germany

Gerhard Klebe – Institute of Pharmaceutical Chemistry, Philipps University, 35032 Marburg, Germany; orcid.org/0000-0002-4913-390X

Hans Brandstetter – Department of Biosciences, University of Salzburg, 5020 Salzburg, Austria; orcid.org/0000-0002-6089-3045

Sven O. Dahms – Institute of Pharmaceutical Chemistry, Philipps University, 35032 Marburg, Germany; Department of Biosciences, University of Salzburg, 5020 Salzburg, Austria

Complete contact information is available at:

<https://pubs.acs.org/10.1021/acsmmedchemlett.0c00651>

Notes

The authors declare no competing financial interest.

■ ACKNOWLEDGMENTS

We thank Iris Lindberg for providing the furin used in enzyme kinetic measurements. The authors acknowledge the provision of synchrotron beamtime at the ESRF (ID30A-3) and at the Helmholtz-Zentrum Berlin (HZB, BL14.2) and thank the scientific staff for assistance. We also thank the Helmholtz-Zentrum Berlin for travel support. Furthermore, we thank Heike Lang-Henkel, Stephanie Kallis, Micha Fauth, and Heeyoung Kim for excellent technical assistance. T.S., E.B.-F., and G.K. obtained funding from the LOEWE Center DRUID (Novel Drug Targets against Poverty-Related and Neglected Tropical Infectious Diseases). S.O.D. obtained funding from the Austrian Science Fund (FWF): M 2730, which is gratefully acknowledged.

■ ABBREVIATIONS

Amba, 4-amidinobenzylamide; Cav, canavanine; DENV-2, Dengue virus serotype 2; *ip*, intraperitoneal; *iv*, intravenous; MOI, multiplicity of infection; PC, proprotein convertase; Phac, phenylacetyl; RMSD, root mean square deviation; RSV, respiratory syncytial virus; TGN, trans-Golgi network; Tle, *tert*-leucine; WNV, West-Nile virus

■ REFERENCES

- (1) Thomas, G. Furin at the cutting edge: from protein traffic to embryogenesis and disease. *Nat. Rev. Mol. Cell Biol.* **2002**, *3* (10), 753–66.
- (2) Seidah, N. G.; Prat, A. The biology and therapeutic targeting of the proprotein convertases. *Nat. Rev. Drug Discovery* **2012**, *11* (5), 367–83.
- (3) Roebroek, A. J.; Taylor, N. A.; Louagie, E.; Pauli, I.; Smeijers, L.; Snellinx, A.; Lauwers, A.; Van de Ven, W. J.; Hartmann, D.; Creemers, J. W. Limited redundancy of the proprotein convertase furin in mouse liver. *J. Biol. Chem.* **2004**, *279* (51), 53442–50.
- (4) Klenk, H. D.; Garten, W. Host cell proteases controlling virus pathogenicity. *Trends Microbiol.* **1994**, *2* (2), 39–43.
- (5) Coutard, B.; Valle, C.; de Lamballerie, X.; Canard, B.; Seidah, N. G.; Decroly, E. The spike glycoprotein of the new coronavirus 2019-nCoV contains a furin-like cleavage site absent in CoV of the same clade. *Antiviral Res.* **2020**, *176*, 104742.
- (6) Walls, A. C.; Park, Y. J.; Tortorici, M. A.; Wall, A.; McGuire, A. T.; Veasley, D. Structure, Function, and Antigenicity of the SARS-CoV-2 Spike Glycoprotein. *Cell* **2020**, *183*, 1735.

- (7) Hoffmann, M.; Kleine-Weber, H.; Schroeder, S.; Krüger, N.; Herrler, T.; Erichsen, S.; Schiergens, T. S.; Herrler, G.; Wu, N. H.; Nitsche, A.; Müller, M. A.; Drosten, C.; Pöhlmann, S. SARS-CoV-2 Cell Entry Depends on ACE2 and TMPRSS2 and Is Blocked by a Clinically Proven Protease Inhibitor. *Cell* **2020**, *181*, 271.
- (8) Bestle, D.; Heindl, M. R.; Limburg, H.; Van Lam van, T.; Pilgram, O.; Moulton, H.; Stein, D. A.; Hards, K.; Eickmann, M.; Dolnik, O.; Rohde, C.; Klenk, H. D.; Garten, W.; Steinmetzer, T.; Böttcher-Friebertshäuser, E. TMPRSS2 and furin are both essential for proteolytic activation of SARS-CoV-2 in human airway cells. *Life science alliance* **2020**, *3* (9), e202000786.
- (9) Hards, K.; Becker, G. L.; Lu, Y.; Dahms, S. O.; Köhler, S.; Beyer, W.; Sandvig, K.; Yamamoto, H.; Lindberg, I.; Walz, L.; von Messling, V.; Than, M. E.; Garten, W.; Steinmetzer, T. Novel furin inhibitors with potent anti-infectious activity. *ChemMedChem* **2015**, *10* (7), 1218–31.
- (10) Becker, G. L.; Lu, Y.; Hards, K.; Strehlow, B.; Levesque, C.; Lindberg, I.; Sandvig, K.; Bakowsky, U.; Day, R.; Garten, W.; Steinmetzer, T. Highly potent inhibitors of proprotein convertase furin as potential drugs for treatment of infectious diseases. *J. Biol. Chem.* **2012**, *287* (26), 21992–22003.
- (11) Lu, Y.; Hards, K.; Dahms, S. O.; Böttcher-Friebertshäuser, E.; Steinmetzer, T.; Than, M. E.; Klenk, H. D.; Garten, W. Peptidomimetic furin inhibitor MI-701 in combination with oseltamivir and ribavirin efficiently blocks propagation of highly pathogenic avian influenza viruses and delays high level oseltamivir resistance in MDCK cells. *Antiviral Res.* **2015**, *120*, 89–100.
- (12) Hards, K.; Ivanova, T.; Thaa, B.; McInerney, G. M.; Klok, T. I.; Sandvig, K.; Künzel, S.; Lindberg, I.; Steinmetzer, T. Elongated and Shortened Peptidomimetic Inhibitors of the Proprotein Convertase Furin. *ChemMedChem* **2017**, *12* (8), 613–620.
- (13) Ivanova, T.; Hards, K.; Kallis, S.; Dahms, S. O.; Than, M. E.; Künzel, S.; Böttcher-Friebertshäuser, E.; Lindberg, I.; Jiao, G. S.; Bartenschlager, R.; Steinmetzer, T. Optimization of Substrate-Analogue Furin Inhibitors. *ChemMedChem* **2017**, *12* (23), 1953–1968.
- (14) Krüger, N.; Sauder, C.; Huttli, S.; Papiés, J.; Voigt, K.; Herrler, G.; Hards, K.; Steinmetzer, T.; Orvell, C.; Drexler, J. F.; Drosten, C.; Rubin, S.; Müller, M. A.; Hoffmann, M. Entry, Replication, Immune Evasion, and Neurotoxicity of Synthetically Engineered Bat-Borne Mumps Virus. *Cell Rep.* **2018**, *25* (2), 312–320.
- (15) Van Lam van, T.; Ivanova, T.; Hards, K.; Heindl, M. R.; Morty, R. E.; Böttcher-Friebertshäuser, E.; Lindberg, I.; Than, M. E.; Dahms, S. O.; Steinmetzer, T. Design, Synthesis, and Characterization of Macrocyclic Inhibitors of the Proprotein Convertase Furin. *ChemMedChem* **2019**, *14* (6), 673–685.
- (16) Gagnon, H.; Beauchemin, S.; Kwiatkowska, A.; Couture, F.; D'Anjou, F.; Levesque, C.; Dufour, F.; Desbiens, A. R.; Vaillancourt, R.; Bernard, S.; Desjardins, R.; Malouin, F.; Dory, Y. L.; Day, R. Optimization of furin inhibitors to protect against the activation of influenza hemagglutinin H5 and Shiga toxin. *J. Med. Chem.* **2014**, *57* (1), 29–41.
- (17) Kwiatkowska, A.; Couture, F.; Levesque, C.; Ly, K.; Beauchemin, S.; Desjardins, R.; Neugebauer, W.; Dory, Y. L.; Day, R. Novel Insights into Structure-Activity Relationships of N-Terminally Modified PACE4 Inhibitors. *ChemMedChem* **2016**, *11* (3), 289–301.
- (18) Paroutis, P.; Touret, N.; Grinstein, S. The pH of the secretory pathway: measurement, determinants, and regulation. *Physiology* **2004**, *19*, 207–15.
- (19) Casey, J. R.; Grinstein, S.; Orłowski, J. Sensors and regulators of intracellular pH. *Nat. Rev. Mol. Cell Biol.* **2010**, *11* (1), 50–61.
- (20) Kim, K. S.; Moquin, R. V.; Qian, L.; Morrison, R. A.; Seiler, S. M.; Roberts, D. G. M.; Ogletree, M. L.; Youssef, S.; Chong, S. Preparation of Argatroban analog thrombin inhibitors with reduced basic guanidine moiety. *Med. Chem. Res.* **1996**, *6* (6), 377–383.
- (21) Tomczuk, B.; Lu, T.; Soll, R. M.; Fedde, C.; Wang, A.; Murphy, L.; Crysler, C.; Dasgupta, M.; Eisenngel, S.; Spurlino, J.; Bone, R. Oxyguanidines: application to non-peptidic phenyl-based thrombin inhibitors. *Bioorg. Med. Chem. Lett.* **2003**, *13* (8), 1495–8.
- (22) Boyar, A.; Marsh, R. E. l-Canavanine, a paradigm for the structures of substituted guanidines. *J. Am. Chem. Soc.* **1982**, *104* (7), 1995–1998.
- (23) Pajpanova, T.; Stoev, S.; Golovinsky, E.; Krauss, H. J.; Miersch, J. Canavanine derivatives useful in peptide synthesis. *Amino Acids* **1997**, *12* (2), 191–204.
- (24) Löw, K.; Hards, K.; Fedeli, C.; Seidah, N. G.; Constam, D. B.; Pasquato, A.; Steinmetzer, T.; Roulin, A.; Kunz, S. A novel cell-based sensor detecting the activity of individual basic proprotein convertases. *FEBS J.* **2019**, *286* (22), 4597–4620.
- (25) Dahms, S. O.; Arciniega, M.; Steinmetzer, T.; Huber, R.; Than, M. E. Structure of the unliganded form of the proprotein convertase furin suggests activation by a substrate-induced mechanism. *Proc. Natl. Acad. Sci. U. S. A.* **2016**, *113* (40), 11196–11201.
- (26) Dahms, S. O.; Hards, K.; Steinmetzer, T.; Than, M. E. X-ray Structures of the Proprotein Convertase Furin Bound with Substrate Analogue Inhibitors Reveal Substrate Specificity Determinants beyond the S4 Pocket. *Biochemistry* **2018**, *57* (6), 925–934.
- (27) Klenk, H. D.; Garten, W. Activation cleavage of viral spike proteins. In *Cellular receptors for animal viruses. Monograph* 28, Wimmer, E., Ed.; Gold Spring Harbor Laboratory Press: 1994; pp 241–280.
- (28) Gonzalez-Reyes, L.; Ruiz-Arguello, M. B.; Garcia-Barreno, B.; Calder, L.; Lopez, J. A.; Albar, J. P.; Skehel, J. J.; Wiley, D. C.; Melero, J. A. Cleavage of the human respiratory syncytial virus fusion protein at two distinct sites is required for activation of membrane fusion. *Proc. Natl. Acad. Sci. U. S. A.* **2001**, *98* (17), 9859–64.
- (29) Zimmer, G.; Budz, L.; Herrler, G. Proteolytic activation of respiratory syncytial virus fusion protein. Cleavage at two furin consensus sequences. *J. Biol. Chem.* **2001**, *276* (34), 31642–50.
- (30) Battles, M. B.; McLellan, J. S. Respiratory syncytial virus entry and how to block it. *Nat. Rev. Microbiol.* **2019**, *17* (4), 233–245.
- (31) Cockerill, G. S.; Good, J. A. D.; Mathews, N. State of the Art in Respiratory Syncytial Virus Drug Discovery and Development. *J. Med. Chem.* **2019**, *62* (7), 3206–3227.
- (32) Kouretova, J.; Hammamy, M. Z.; Epp, A.; Hards, K.; Kallis, S.; Zhang, L.; Hilgenfeld, R.; Bartenschlager, R.; Steinmetzer, T. Effects of NS2B-NS3 protease and furin inhibition on West Nile and Dengue virus replication. *J. Enzyme Inhib. Med. Chem.* **2017**, *32* (1), 712–721.

Supporting Information

The basicity makes the difference – Improved canavanine-derived inhibitors of the proprotein convertase furin

Thuy Van Lam van¹, Miriam Ruth Heindl², Christine Schlutt¹, Eva Böttcher-Friebertshäuser², Ralf Bartenschlager^{3,4}, Gerhard Klebe¹, Hans Brandstetter⁵, Sven O. Dahms^{1,5}, Torsten Steinmetzer^{1*}

¹Institute of Pharmaceutical Chemistry, Philipps University, Marbacher Weg 6, D-35032 Marburg, Germany

²Institute of Virology, Philipps University, Hans-Meerwein-Str. 2, Marburg, Germany

³Department of Infectious Diseases, Molecular Virology, Heidelberg University, Im Neuenheimer Feld 344, 69120 Heidelberg, Germany

⁴German Center for Infection Research, Heidelberg Partner Site, Im Neuenheimer Feld 344, 69120 Heidelberg, Germany

⁵Department of Biosciences, University of Salzburg, Billrothstrasse 11, A-5020 Salzburg, Austria

Content

1.	Used analytical methods and synthesis	S3
2.	Analytical data of final inhibitors	S7
3.	Protein crystallography	S11
4.	Structure determination of human furin in complex with inhibitors 4, 5, 6, and 8	S12
5.	Structures of furin in complex with inhibitors 4, 5, 6, and 8	S13
6.	Enzyme kinetic measurements with furin and selected trypsin-like serine proteases	S14
7.	RSV infections and inhibition of multicycle replication	S17
8.	Inhibition of Dengue-2 virus and West Nile virus	S19
9.	Acute toxicity study in mice	S20
10.	Pharmacokinetic characterization of inhibitor 8 in rats	S21
11.	Abbreviations used in the supporting information	S23
12.	References	S23

1. Used analytical methods and synthesis

General

Protected Fmoc-amino acids, coupling reagents, and the used 2-chlorotriethylchloride (2-CTC) resin for peptide synthesis were obtained from IRIS Biotech (Marktredwitz, Germany), ChemPur Feinchemikalien und Forschungsbedarf GmbH (Karlsruhe, Germany), and Bachem AG (Bubendorf, Switzerland). Solvents and standard reagents for synthesis were purchased from Sigma-Aldrich (Taufkirchen, Germany) and Thermo Fisher GmbH (Kandel, Germany), and used without further purification.

Analytical HPLC

Analytical HPLC experiments were performed on a Primaide (VWR, Hitachi) system (column, NUCLEODUR C18 ec, 5 μm , 100 \AA , 4.6 mm \times 250 mm, Macherey-Nagel, Düren, Germany). Water (solvent A) and acetonitrile (solvent B), both containing 0.1 % TFA, were used as eluents with a linear gradient (increase of 1 % solvent B/min) and a flow rate of 1 mL/min. The detection was performed at 220 nm.

Preparative HPLC

The final inhibitors were purified via preparative HPLC (pumps, Varian PrepStar model 218 gradient system; detector, ProStar model 320; fraction collector, Varian model 701) using a reversed phase column (NUCLEODUR C₁₈ ec, 5 μm , 100 \AA , 32 mm \times 250 mm, Macherey-Nagel, Düren, Germany) with identical solvents as described for the analytical HPLC and a linear gradient at a flow rate of 20 mL/min (detection at 220 nm). The inhibitors were obtained as TFA salts after lyophilization on a freeze-drier (Martin Christ Gefriertrocknungsanlagen GmbH, Osterode am Harz, Germany). All final inhibitors possess a purity > 95 % based on HPLC-detection at 220 nm.

Mass spectrometry

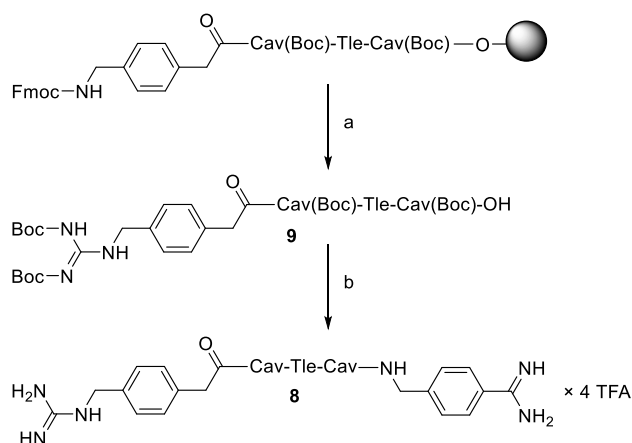
The molecular mass of the synthesized compounds was determined using a QTrap 2000 ESI spectrometer (Applied Biosystems).

NMR spectroscopy

The ¹H NMR and ¹³C NMR spectra for these inhibitors were defined by using a Jeol-ECX500 (Jeol Inc., Peabody, MA).

Synthesis

The synthesis of the inhibitors was performed as described below in detail for compound **8** (Scheme S1).



Scheme S1. Synthesis of inhibitor **8** on 2-CTC resin, loaded with Fmoc-Cav(Boc)-OH. The following P3, P4, and P5 residues were coupled by a standard Fmoc-SPPS protocol using a 2.0-fold excess of Fmoc amino acids, HBTU, and HOBt in presence of 4 equiv DIPEA. The Fmoc deprotection was always performed with 20 % piperidine in DMF. Reagents and conditions: (a) (i) 20 % piperidine in DMF, (ii) 3.0 equiv of *N,N'*-Bis-Boc-1-guanylpyrazole, 4.0 equiv. of DIPEA, DMF, overnight, (iii) 1 % TFA in DCM, 3 × 30 min; neutralization by DIPEA (b) (i) 1.0 equiv. of 4-amidinobenzylamide · 2 HCl, HBTU, and 3 equiv. of DIPEA and 6-Cl-HOBt; (ii) TFA/TIS/H₂O (95:2.5:2.5 v/v/v), 2 h at rt, precipitation in diethyl ether, followed by preparative RP-HPLC.

The side chain protected P5-P2 segment of inhibitor **8** was prepared by solid phase peptide synthesis (SPPS) on 2-chlorotriylchloride (2-CTC) resin, as described previously.¹ In brief, 500 mg of the 2-CTC-resin (loading 1.6 mmol/g, absolute 0.8 mmol) was treated with 399 mg (0.8 mmol) Fmoc-Cav(Boc)-OH dissolved in 8 mL dry DCM and 0.557 ml (3.2 mmol, 4 equiv) diisopropylethylamine (DIPEA) in a 10 mL polypropylene syringe with filter frit (Multisyntech GmbH, Witten, Germany). The resin was shaken for 2 hours, and subsequently washed (3 × 1 min) with DCM/MeOH/DIPEA (17:2:1, v/v/v), 3 × with DCM, 3 × with DMF, 4 × with DCM. Afterwards, the resin was dried *in vacuo* providing 720 mg Fmoc-Cav(Boc)-resin (loading 0.661 mmol/g).

100 mg of this Fmoc-Cav(Boc)-resin (loading 0.661 mmol/g, absolute 0.0661 mmol) was used for the following SPPS steps using a standard Fmoc protocol performed in a 2 mL polypropylene syringe with filter frit. The Fmoc group was always removed by treatment with 20 % piperidine in DMF (5 and 15 min), followed by subsequent washing with DMF (7×1 min). For the coupling of the following residues (Fmoc-Tle-OH, Fmoc-Cav(Boc)-OH, and Fmoc-4-aminomethyl-phenylacetic acid) a 2.0-fold excess of Fmoc amino acids, HBTU, and HOBt in presence of 4 equiv DIPEA was used. When using a higher excess of Fmoc amino acids, a considerable amount of side product was observed due to an additional acylation on the Boc protected Cav side chain. This indicated that the Fmoc-Cav(Boc)-OH is an acceptable building block for the synthesis of short peptide segments, but is not perfectly suited for longer sequences, when using standard SPPS conditions with 3- or 4-fold excess of Fmoc-amino acids and coupling reagent.

After the final coupling of Fmoc-4-aminomethyl-phenylacetic acid, washing with DMF (4×1 min), Fmoc deprotection, and subsequent washing with DMF (5×1 min), the resin was treated with 62 mg (0.198 mmol, 3.0 equiv) of *N,N'*-Bis-Boc-1-guanylpiperazine² and 46 μ l (0.264 mmol, 4.0 equiv) of DIPEA dissolved in 1.5 mL DMF for the conversion of the N-terminal aminomethyl substituent into a bis-Boc-protected guanidinomethyl group. The resin was shaken overnight and subsequently washed with DMF (3×1 min) and DCM (5×1 min). The protected intermediate **9** (Scheme S1) was removed from the resin under mild acidic conditions with 1.5 ml of 1 % TFA in DCM (3×30 min). After each cleavage step, the solution was immediately neutralized by treatment with DIPEA. The solvent was removed in vacuo providing an oily residue (HPLC retention time 23.47 min, start at 30 % solvent B; MS calcd m/z 1036.56, found m/z 1037.56, (M+H)⁺).

The crude intermediate **9** was treated with 22 mg (0.0992 mmol, 1.5 equiv based on the initial resin loading) 4-aminobenzylamide $\cdot 2$ HCl,³ 52 mg (0.0992 mmol, 1.5 equiv) PyBOP, 50.5 mg (0.298 mmol, 4.5 equiv) 6-Cl-HOBT, and 43 μ L (0.248 mmol, 3.75 equiv) DIPEA dissolved in 2 mL DMF. The mixture was stirred at room temperature overnight, afterwards the solvent was removed in vacuo. The remaining oily residue (HPLC retention time 20.12 min, start at 30 % solvent B) was deprotected under strong acidic conditions using 3 mL TFA/H₂O/triisopropylsilane (95:2.5:2.5, v/v/v) for 2 hours. The solution was subsequently dropwise added to cold diethyl ether. The precipitated crude peptide obtained after centrifugation was purified by preparative reversed-phase HPLC, providing 22.3 mg (0.018 mmol, 27.5 % based on the used 100 mg Fmoc-Cav(Boc)-resin) of the final inhibitor **8** as TFA

salt after lyophilization (purity > 95 % based on HPLC-detection at 220 nm, HPLC retention time 21.4 min, start at 1 % solvent B; MS calcd m/z 767.43, found m/z 768.40, (M+H)⁺).

For all other inhibitors, very similar yields between 19-24 mg were obtained, when starting from 100 mg of the loaded Fmoc-Cav(Boc)-resin (for inhibitors **3**, **4**, and **7**) or Fmoc-Lys(Boc)-resin (for compounds **5** and **6**).

2. Analytical data of final inhibitors

Table S1. Analytical data of the newly synthesized inhibitors **3-8**.

No.	Chemical formula	HPLC (min) ^a	MS calc.	MS found [M+H] ⁺
3	C ₃₄ H ₅₃ N ₁₃ O ₅	20.0	723.43	724.45
4	C ₃₅ H ₅₅ N ₁₅ O ₅	21.1	765.45	766.37
5	C ₃₄ H ₅₃ N ₁₁ O ₅	17.0	695.42	696.44
6	C ₃₅ H ₅₅ N ₁₃ O ₅	20.2	737.44	738.30
7	C ₃₃ H ₅₁ N ₁₃ O ₆	20.3	725.41	726.40
8	C ₃₄ H ₅₃ N ₁₅ O ₆	21.4	767.43	768.40

^astart at 1 % solvent A

NMR spectroscopy

The ¹H NMR spectra for inhibitors **3 – 8** and the ¹³C NMR spectra for the most potent furin inhibitors **6** and **8** were recorded by using a Jeol-ECX500 (Jeol Inc., Peabody, MA). Samples were dissolved in DMSO-*d*₆ and the solvent residual signal was used as reference (¹H-NMR: 2.50 ppm, ¹³C-NMR: 39.52 ppm).⁴ Chemical shifts δ are given in the unit ppm, coupling constants *J* in the unit Hz.

Inhibitor **3**

¹H NMR (500 MHz, [D₆] DMSO) δ = 11.21 (s, 1H), 9.19 (d, *J* = 60.0 Hz, 4H), 8.64 (t, *J* = 6.1 Hz, 1H), 8.42 (d, *J* = 8.0 Hz, 1H), 8.31 – 8.05 (m, 4H), 7.89 – 7.63 (m, 7H), 7.57 (d, *J* = 9.0 Hz, 1H), 7.51 – 7.22 (m, 10H), 4.51 – 4.31 (m, 4H), 4.24 (d, *J* = 9.0 Hz, 1H), 3.99 (s, 2H), 3.82 (t, *J* = 6.5 Hz, 2H), 3.59 – 3.43 (m, 2H), 3.08 (dt, *J* = 12.7, 6.6 Hz, 2H), 2.06 (dq, *J* = 14.1, 7.3 Hz, 1H), 1.97 – 1.85 (m, 1H), 1.76 – 1.63 (m, 1H), 1.59 – 1.34 (m, 3H), 0.88 ppm (s, 9H).

Inhibitor **4**

¹H NMR (500 MHz, [D₆] DMSO) δ = 11.22 (s, 1H), 9.26 (s, 2H), 9.14 (s, 2H), 8.65 (t, *J* = 6.1 Hz, 1H), 8.42 (d, *J* = 8.0 Hz, 1H), 8.25 (d, *J* = 7.5 Hz, 1H), 8.03 (t, *J* = 6.2 Hz, 1H), 7.84 – 7.63 (m, 7H), 7.56 (d, *J* = 9.0 Hz, 1H), 7.50 – 7.38 (m, 3H), 7.23 (h, *J* = 9.2 Hz, 11H), 4.48 – 4.19 (m, 7H), 3.82 (t, *J* = 6.3 Hz, 2H), 3.57 – 3.40 (m, 2H), 3.09 (dq, *J* = 12.1, 6.7, 6.1 Hz, 2H), 2.12 – 2.00 (m, 1H), 1.96 – 1.83 (m, 1H), 1.75 – 1.63 (m, 1H), 1.60 – 1.38 (m, 3H), 0.87 ppm (s, 9H).

Inhibitor **5**

¹H NMR (500 MHz, [D₆] DMSO): δ = 11.26 (s, 1H), 9.25 (d, *J* = 12.9 Hz, 4H), 8.57 (t, *J* = 6.0 Hz, 1H), 8.49 (d, *J* = 8.1 Hz, 1H), 8.21 (s, 3H), 8.11 (d, *J* = 7.5 Hz, 1H), 7.90 – 7.73 (m, 9H), 7.65 (d, *J* = 9.3 Hz, 1H), 7.45 (d, *J* = 8.5 Hz, 2H), 7.36 (d, *J* = 8.3 Hz, 2H), 7.28 (d, *J* = 8.3 Hz, 2H), 4.59 – 4.39 (m, 2H),

4.35 – 4.18 (m, 3H), 4.00 (s, 2H), 3.80 (t, $J = 6.7$ Hz, 2H), 3.60 – 3.45 (m, 2H), 2.75 (s, 2H), 2.11 – 1.96 (m, 1H), 1.87 (dt, $J = 14.3, 7.4$ Hz, 1H), 1.73 – 1.47 (m, 4H), 1.41 – 1.20 (m, 2H), 0.87 ppm (s, 9H).

Inhibitor 6

^1H NMR (500 MHz, $[\text{D}_6]$ DMSO) $\delta = 11.31$ (s, 1H), 9.31 (d, $J = 32.6$ Hz, 4H), 8.57 (t, $J = 6.0$ Hz, 1H), 8.48 (d, $J = 8.0$ Hz, 1H), 8.16 (t, $J = 6.1$ Hz, 1H), 8.11 (d, $J = 7.5$ Hz, 1H), 7.83 (s, 7H), 7.76 (d, $J = 8.5$ Hz, 2H), 7.63 (d, $J = 9.1$ Hz, 1H), 7.45 (d, $J = 8.5$ Hz, 2H), 7.23 (q, $J = 8.3$ Hz, 8H), 4.54 – 4.18 (m, 7H), 3.80 (t, $J = 6.6$ Hz, 2H), 3.63 – 3.43 (m, 2H), 2.74 (s, 2H), 2.04 (m, 1H), 1.87 (dd, $J = 14.3, 8.5$ Hz, 1H), 1.76 – 1.47 (m, 4H), 1.40 – 1.19 (m, 2H), 0.86 ppm (s, 9H).

^{13}C NMR (126 MHz, $[\text{D}_6]$ DMSO) $\delta = 171.55, 170.77, 170.53, 169.70, 165.44, 158.45, 156.97, 145.77, 135.33, 135.28, 129.18, 127.94, 127.25, 127.10, 126.43, 73.20, 59.63, 52.69, 49.65, 43.69, 41.71, 41.52, 38.62, 34.29, 31.08, 29.83, 26.64, 26.48, 22.35$ ppm.

Inhibitor 7

^1H NMR (500 MHz, $[\text{D}_6]$ DMSO) $\delta = 11.25$ (d, $J = 29.2$ Hz, 2H), 9.25 (d, $J = 17.4$ Hz, 4H), 8.64 (s, 1H), 8.50 (d, $J = 8.1$ Hz, 1H), 8.33 – 8.13 (m, 4H), 7.82 – 7.72 (m, 10H), 7.66 (d, $J = 9.0$ Hz, 1H), 7.46 (d, $J = 8.5$ Hz, 2H), 7.36 (d, $J = 8.3$ Hz, 2H), 7.28 (d, $J = 8.2$ Hz, 2H), 4.51 (td, $J = 8.6, 5.3$ Hz, 1H), 4.46 – 4.32 (m, 3H), 4.25 (d, $J = 9.0$ Hz, 1H), 4.04 – 3.96 (m, 2H), 3.81 (dt, $J = 19.1, 6.8$ Hz, 3H), 3.58 – 3.47 (m, 3H), 2.04 (tt, $J = 13.5, 7.3$ Hz, 2H), 1.96 – 1.80 (m, 2H), 0.88 ppm (s, 9H).

Inhibitor 8

^1H NMR (500 MHz, $[\text{D}_6]$ DMSO) $\delta = 11.36$ (s, 1H), 11.28 (s, 1H), 9.33 (s, 2H), 9.27 (s, 2H), 8.65 (t, $J = 6.1$ Hz, 1H), 8.50 (d, $J = 8.1$ Hz, 1H), 8.27 (d, $J = 7.4$ Hz, 1H), 8.14 (t, $J = 6.1$ Hz, 1H), 7.83 (s, 8H), 7.76 (d, $J = 8.5$ Hz, 2H), 7.64 (d, $J = 9.0$ Hz, 1H), 7.46 (d, $J = 8.5$ Hz, 4H), 7.29 – 7.18 (m, 6H), 4.54 – 4.30 (m, 6H), 4.24 (d, $J = 9.0$ Hz, 1H), 3.82 (dt, $J = 17.7, 6.6$ Hz, 4H), 3.50 (d, $J = 2.1$ Hz, 2H), 2.11 – 2.00 (m, 2H), 1.95 – 1.82 (m, 2H), 0.87 ppm (s, 9H).

^{13}C NMR (126 MHz, $[\text{D}_6]$ DMSO) $\delta = 171.29, 170.81, 170.60, 169.98, 165.44, 158.50, 156.97, 145.53, 135.33, 135.27, 129.18, 127.97, 127.24, 127.10, 126.50, 73.22, 72.93, 59.69, 49.78, 49.56, 43.70, 41.78, 41.52, 39.85, 34.25, 29.98, 29.78, 26.46$ ppm.

As examples, the ^1H and ^{13}C NMR spectra of inhibitors **6** (Figure S1) and **8** (Figure S2) are shown below. The structures of the inhibitors are provided in their fourfold protonated form obtained after preparative HPLC under acidic conditions (pH approximately 1.9). The provided chemical formulas below the structures are calculated without the trifluoroacetate counterions.

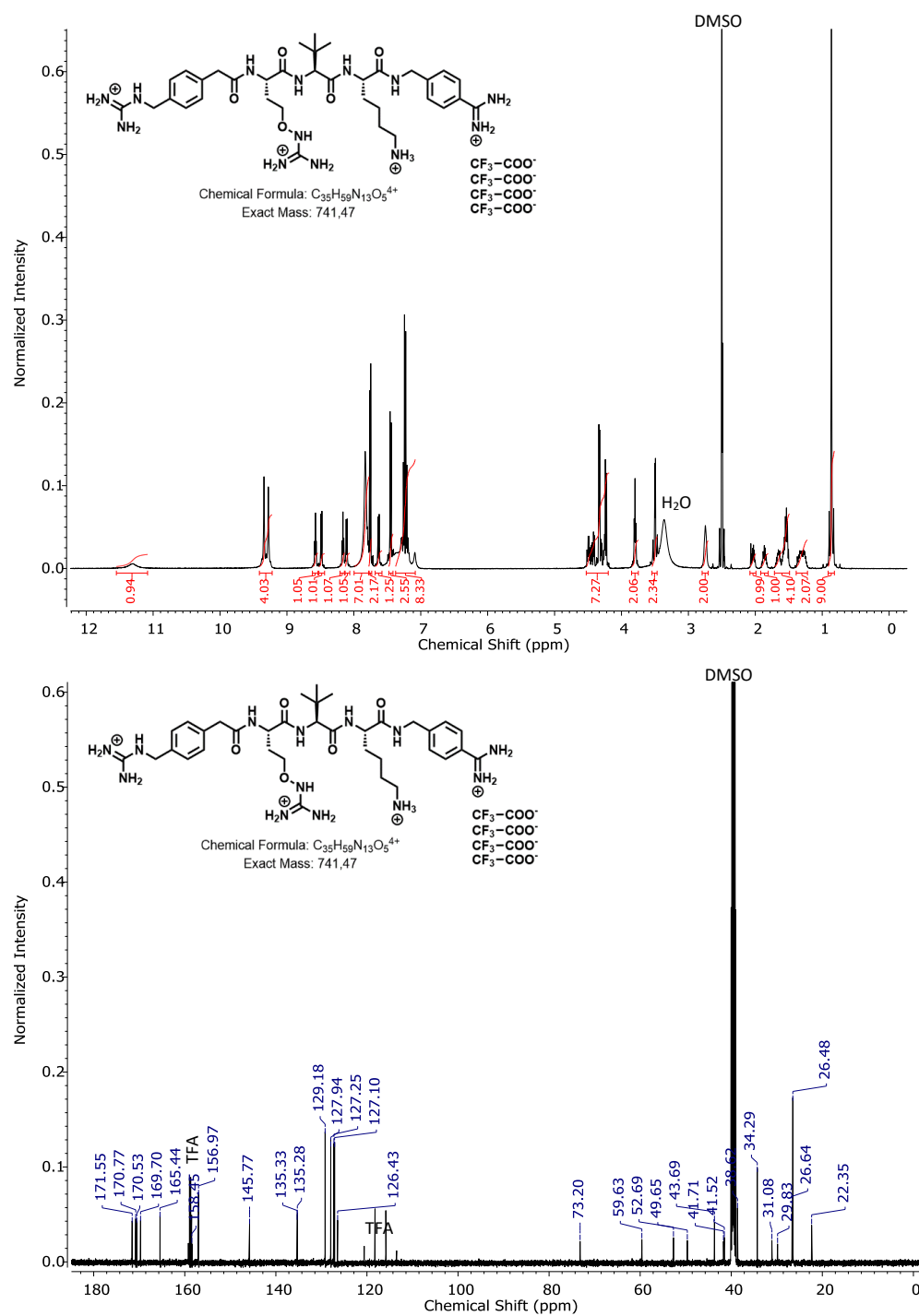


Figure S1. ¹H- and ¹³C-NMR spectra of inhibitor 6 · 4 TFA in DMSO-*d*₆.

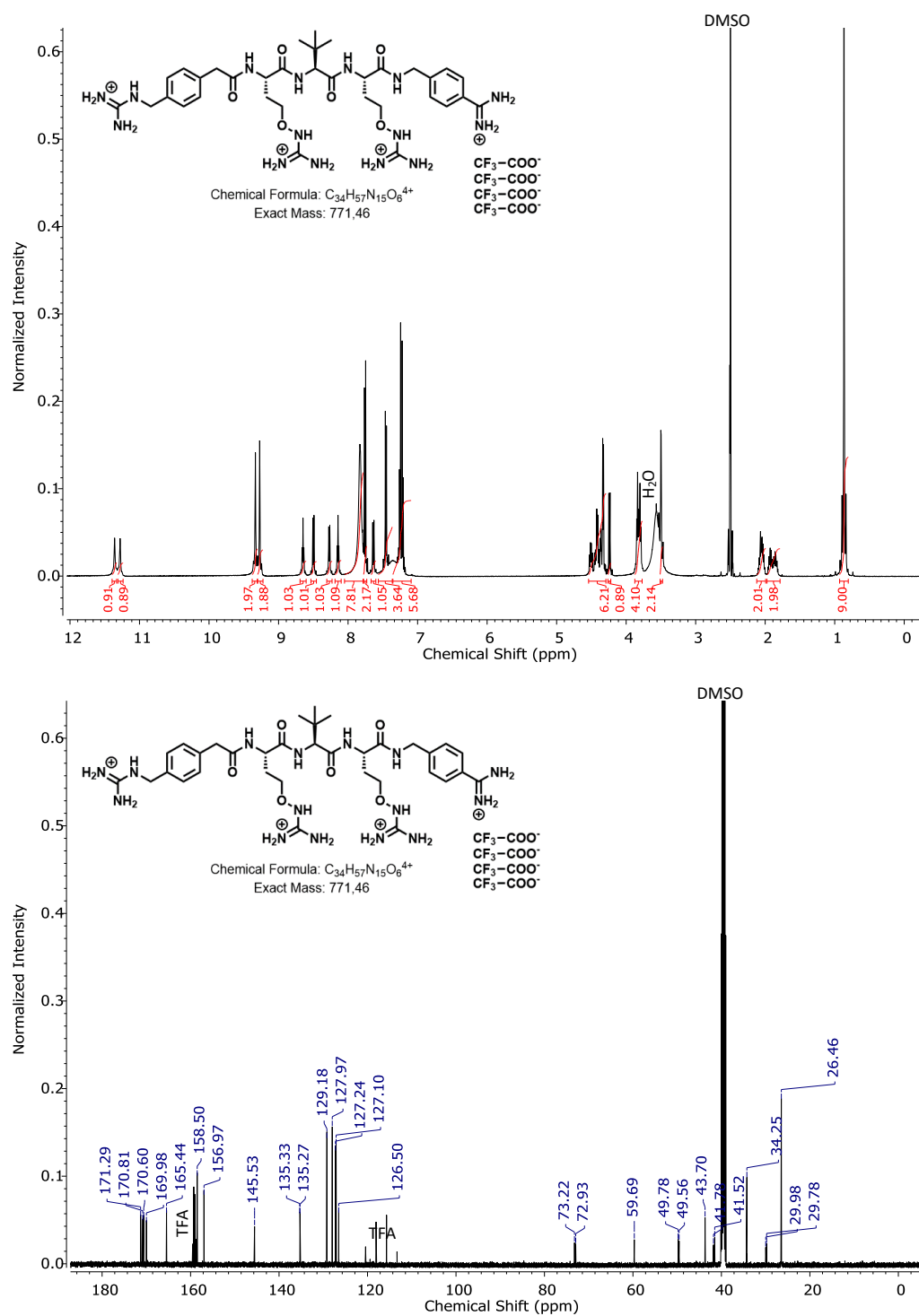


Figure S2. ¹H- and ¹³C-NMR spectra of inhibitor 8 · 4 TFA in DMSO-*d*₆.

S10

3. Protein crystallography

Equal volumes of homogeneously glycosylated human furin,⁵ ~9 mg/mL in 10 mM Hepes pH 7.5, 100 mM NaCl, 2 mM CaCl₂ and crystallization solution (100 mM MES, 200 mM K/NaH₂PO₄, pH 5.5-6.0 and 2 M NaCl) were mixed and equilibrated against the reservoir (3.0-3.6 M NaCl) in vapor diffusion experiments at 18-20°C as described previously.⁶⁻⁷

The soaking solution (3.13 M NaCl; 100 mM Mes/NaOH; pH 5.5; 200 mM NaH₂PO₄; 1 mM CaCl₂; 20% DMSO) was supplemented with 5 mM of inhibitors **5**, **6**, **7** or **8**. Crystals were soaked for ~16 h and flash cooled in liquid N₂. Diffraction data were collected at the synchrotron beam line MASSIF-3 (ID30A-3⁸) of the European Synchrotron Radiation Facility (ESRF) and at BL14.2⁹ (BESSY-II) of the Helmholtz-Zentrum Berlin (HZB). The data were processed using XDS¹⁰ (v.03/2019) with XDS-APP¹¹ (v2.0) and the CCP4 program suite¹² (v.7.0.078). COOT¹³ (v.0.8.9.2) was used for model building. Refinement was performed in PHENIX¹⁴ (v.1.17.1) using the PDB-ID 6EQX⁶ as initial model. One specific R_{free}-set (initially generated up to 1.0 Å⁷) was transferred to the data sets prior refinement start. Geometry restraints of the inhibitors were obtained from the PRODRG-server.¹⁵ Electron density omit maps were calculated in PHENIX¹⁴ (v.1.17.1). PYMOL was used for molecular graphics (<http://www.pymol.org>). The coordinates and structure factors of furin in complex with **5**, **6**, **7** and **8** have been deposited at the World Wide Protein Data Bank with the PDB IDs 6YD2, 6YD3, 6YD4 and 6YD7, respectively.

4. Structure determination of human furin in complex with inhibitors 4, 5, 6, and 8

Table S2. Data collection and refinement statistics.

	4	5	6	8
Data collection statistics				
PDB ID	6YD7	6YD2	6YD3	6YD4
Wavelength	0.9184	0.9677	0.9677	0.9184
Space group	P6 ₃ 22	P6 ₃ 22	P6 ₃ 22	P6 ₃ 22
Unit cell parameters: a = b, c	131.8, 155.4	131.5, 155.2	131.6, 155.3	131.7, 155.5
Resolution range ^a (Å)	47.2-1.8 (1.91-1.80)	43.1-1.8 (1.91-1.80)	43.1-2.0 (2.12-2.00)	47.2-1.7 (1.80-1.70)
R _{meas} ^a (%)	14.1 (160.9)	13.7 (203.9)	21.4 (139.8)	11.7 (197.0)
I/σI ^a	21.24 (2.4)	19.2 (1.8)	12.1 (2.1)	22.21 (2.0)
Completeness ^a	98.6 (97.6)	98.4 (98.3)	97.9 (98.6)	99.9 (99.5)
No. of observations	1473091 / 73093	1,244,968 / 72,501	905,715 / 52,910	1754091 / 87466
Refinement statistics				
No. of non-hydrogen atoms	4,211	4,179	4,159	4,237
protein/inhibitor/other	3670 / 55 / 465	3,653 / 61 / 444	3,653 / 67 / 418	3,670 / 69 / 477
R _{work} /R _{free}	15.4 / 17.1	15.8 / 17.7	16.0 / 18.5	15.3 / 16.9
B-factors (Å²)				
Overall/Wilson plot	29.7 / 30.4	32.1 / 32.4	32.0 / 31.3	31.2 / 31.3
protein/inhibitor/other	28.6 / 25.8 / 38.1	31.1 / 27.3 / 40.3	31.4 / 25.7 / 38.4	30.1 / 26.8 / 40.2
RMSD bond length (Å)	0.009	0.010	0.011	0.009
RMSD bonded B-factors	4.4	4.5	4.8	4.3

^a Values of the highest resolution shell are given in parentheses

5. Structures of furin in complex with inhibitors 4, 5, 6, and 8

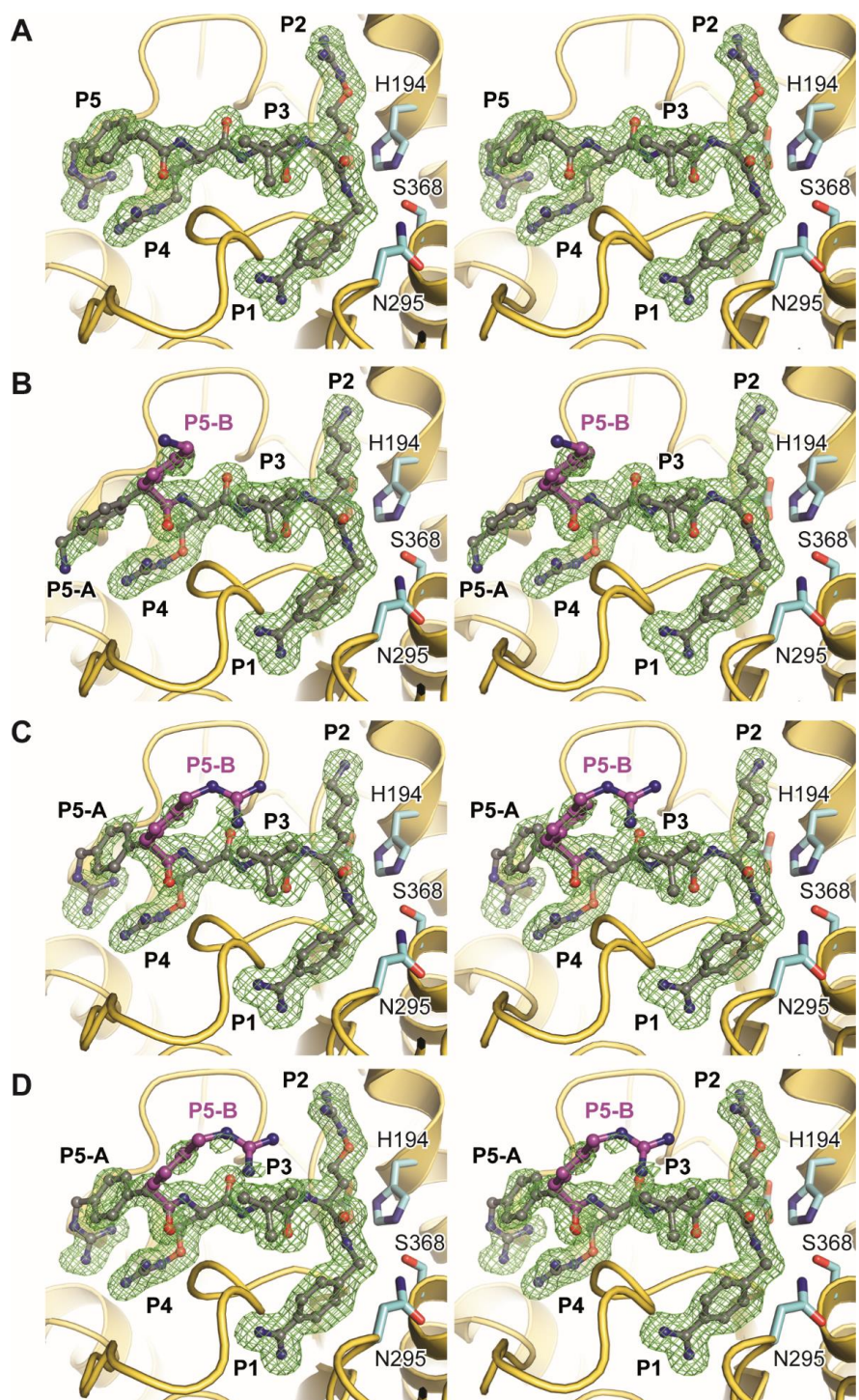


Figure S3. Stereo representation of the difference electron density maps of the furin-bound inhibitors **4** (A), **5** (B), **6** (C), and **8** (D). The protein backbone of furin is given as cartoon representation (golden). The residues Ser368 and His194 of the catalytic triad as well as Asn295 of the oxyanion hole are shown as stick model with carbon atoms in cyan. Inhibitors are shown as ball-and-stick models. The $F_o - F_c$ simulated annealing omit electron density maps (green mesh, atoms of the inhibitors were deleted for map calculation to avoid model bias) are contoured at 3σ . The alternative conformations of the P5 residue in the complexes shown in panels B-D are colored in magenta.

6. Enzyme kinetic measurements with furin and selected trypsin-like serine proteases

Measurements with furin

All measurements were performed in black 96-well plates (Nunc, Langensfeld, Germany) at room temperature with a microplate reader Safire 2 (Tecan, Switzerland) at λ_{ex} 380 nm and λ_{em} 460 nm as described previously.¹⁶ Each well contained 2 μ L inhibitor solution (dissolved in DMSO), 20 μ L of Phac-Arg-Val-Arg-Arg-AMC as substrate (dissolved in water, 12.5 μ M in assay) and 160 μ L buffer (100 mM HEPES, 0.2 % Triton X-100, 2 mM CaCl₂, 0.02 % sodium azide und 1 mg/mL BSA, pH 7.0). The measurements were started by addition of 20 μ L furin¹⁷ solution (0.95 nM in assay). Using the slopes of the linear progress curves the rates were calculated, which were fitted as function of the inhibitor concentration using equation (1) for tight-binding inhibitors,¹⁸ whereby v_0 is the velocity in absence of an inhibitor, I_t is the total inhibitor concentration, E_t is the total enzyme concentration, and K_i^* is the apparent inhibition constant at the used substrate concentration.

$$v = v_0 \times \frac{[(K_i^* + I_t - E_t)^2 + 4 \times K_i^* \times E_t]^{1/2} - (K_i^* + I_t - E_t)}{2 \times E_t} \quad (1)$$

The apparent K_i^* was converted into the true K_i using equation (2), whereby S is the constant concentration (12.5 μ M in assay) of the AMC-substrate Phac-Arg-Val-Arg-Arg-AMC and K_m describes the value of Michaelis constant.

$$K_i = \frac{K_i^*}{1 + \frac{S}{K_m}} \quad (2)$$

The provided K_i values are the average \pm standard deviation of at least three measurements.

Measurements with selected trypsin-like serine proteases

For selectivity studies, the inhibitors were also tested against four trypsin-like serine proteases including trypsin, the clotting proteases thrombin and factor Xa, and the fibrinolytic plasmin (Table S3). The

S14

reference inhibitors **1** and **2** still possess a relatively potent inhibition of trypsin with K_i values of 52 nM and 100 nM, whereas both compounds are only poor inhibitors of the other three tested proteases (K_i values $> 3 \mu\text{M}$). Notably, a more than 10 fold reduced trypsin inhibition was found for the canavanine-derived inhibitors **5-8**, they also possess a negligible inhibitory potency against thrombin, factor Xa, and plasmin.

Table S3. Selectivity measurements with trypsin-like serine proteases, the K_i values for furin are provided as reference. Only for trypsin, an additional selectivity ratio (SR) compared to the furin inhibition is provided in brackets below the K_i value. For the other tested proteases the SR is further increased (not calculated).

No.	furin (pM)	K_i			
		trypsin (μM) SR (K_i trypsin/ K_i furin)	thrombin (μM)	factor Xa (μM)	plasmin (μM)
1	5.5 ± 0.3	0.052 ± 0.0049 (9454)	20 ± 3.2	7.1 ± 0.37	3.5 ± 0.33
2	8.8 ± 4.9	0.10 ± 0.018 (11364)	44 ± 17	8.0 ± 0.57	8.8 ± 0.62
3	76.8 ± 14.9	0.21 ± 0.002 (2734)	13 ± 0.09	28 ± 0.37	3.3 ± 0.25
4	13.1 ± 1.6	0.22 ± 0.2 (16794)	9.6 ± 0.18	15 ± 3.5	3.1 ± 0.26
5	114 ± 25.9	1.3 ± 0.049 (11403)	10 ± 0.06	18 ± 0.60	21 ± 0.87
6	36.3 ± 11.2	0.55 ± 0.012 (15152)	61 ± 3.4	26 ± 0.41	28 ± 0.44
7	34.2 ± 5.1	1.3 ± 0.1 (38012)	25 ± 0.59	47 ± 2.1	19 ± 0.88
8	10.1 ± 3.2	0.69 ± 0.001 (68317)	22 ± 0.52	36 ± 3.5	12 ± 0.21

The measurements with trypsin, thrombin, factor Xa, and plasmin were performed at room temperature in 50 mM Tris × HCl buffer pH 8.0 containing 154 mM NaCl, as described previously¹⁹. The assays were conducted in black 96 well plates using a Fluoroskan Ascent[®] plate reader (Thermo Fisher Scientific, Vantaa, Finland) with λ_{ex} 355 and λ_{em} 460 nm. The measurements were performed with 100 μL buffer containing the inhibitor, 20 μL substrate dissolved in water and were started by addition of 20 μL enzyme solution (total assay volume 140 μL). Mes-DArg-Pro-Arg-AMC²⁰ was used as fluorescence substrate for human fXa (97 pM in assay, molecular weight 46 kDa, Enzyme Research South Bend, Indiana, USA). Tos-Gly-Pro-Arg-AMC was used for bovine thrombin prepared according to Walsmann²¹ (31 pM in assay, molecular weight 33.6 kDa), and Mes-DArg-Gly-Arg-AMC²⁰ for porcine trypsin (30 pM in assay, molecular weight 23.2 kDa, Merck, Darmstadt, Germany). Assays with human plasmin (molecular weight 78 kDa, Chromogenix, Lexington, USA) were performed with an enzyme concentration of 0.35 nM in the assay using the substrate Mes-DArg-Phe-Arg-AMC¹⁹. The provided K_i values are the average \pm standard deviation of three measurements.

7. RSV infections and inhibition of multicycle replication

The influence of the inhibitors on the viability of the used A549 cells was determined by using the CellTiter-Glo[®] assay (Promega GmbH, Mannheim, Germany) according to the instructions of the manufacturer. No cytotoxicity was observed at an inhibitor concentration of 50 μ M (Figure S4).

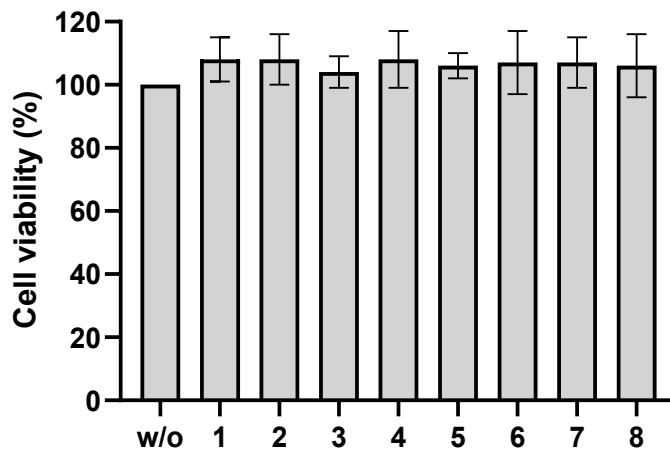


Figure S4. Cytotoxicity of the used inhibitors at a concentration of 50 μ M after 24 hours incubation with A549 cells. The test was performed by the CellTiter-Glo[®] assay.

The experiments were conducted as recently described²². RSV A2 strain was kindly provided by Christine Krempl, Institute of Virology and Immunobiology, University of Würzburg, Würzburg, Germany. Cell growth and incubations occurred at 37 °C and 5 % CO₂. All infection experiments were performed in minimal essential medium (MEM, Gibco, Thermo Fisher Scientific, Paisley, UK) supplemented with 5 % fetal calf serum (FCS), penicillin, streptomycin, and glutamine. RSV was propagated in Hep-2 cells. Concentrated virus stocks were prepared from both cell supernatant and infected cells as described previously.²² Briefly, infected cells were mechanically disrupted by vortexing to release cell-associated virus. The cell suspension and the virus-containing Hep-2 cell culture supernatant were cleared by low-speed centrifugation, subsequently combined, supplemented with 0.1 M MgSO₄ and 0.05 M HEPES and stored as virus stock at -80°C. Multicycle virus replication in the presence of inhibitors was analyzed in A549 human lung cancer cells. A549 cells were infected with RSV at a multiplicity of infection (MOI) of 1 for 1 h. The inoculum was then removed and cells were incubated in fresh medium with or without inhibitors for 72 h. At 16, 24, 48 and 72 h post infection virus

progeny released into the cell supernatants were quantified by plaque assay using Vero76 cells with Avicel overlay.²³ Briefly, cells were incubated with 10-fold serial dilutions of the supernatants in MEM supplemented with 5 % FCS, antibiotics and glutamine for 1 h, washed with PBS and incubated with Avicel overlay for 72 h. Cells were fixed and permeabilized and immunostained using a polyclonal goat antibody against RSV (BIO-RAD Laboratories GmbH, Feldkirchen, Germany), peroxidase-conjugated secondary antibodies and the peroxidase substrate TrueBlue (SeraCare, Milford, USA).

8. Inhibition of Dengue-2 virus and West Nile virus

The influence of the inhibitors on the viability of the used Huh-7 cells was determined by using the CellTiter-Glo[®] assay (Promega GmbH, Mannheim, Germany) according to the instructions of the manufacturer, as described previously.²⁴ A negligible cytotoxicity was observed at the used inhibitor concentrations up to 50 μ M (Figure S5).

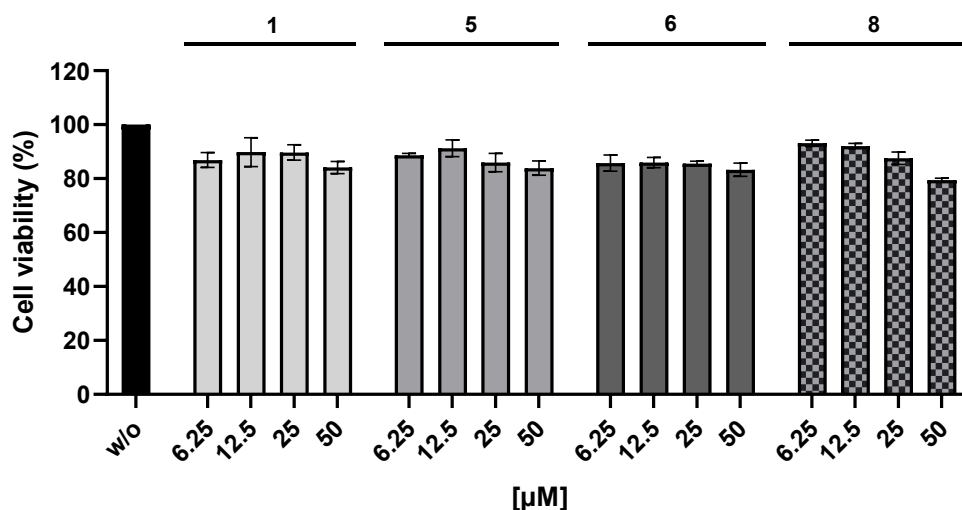


Figure S5. Cytotoxicity of the used inhibitors at the indicated concentrations after 48 hours incubation with Huh-7 cells. The test was performed by the CellTiter-Glo[®] assay.

Antiviral activity of furin inhibitors against Dengue-2 virus (DENV-2) and West Nile virus (WNV) has been described recently.^{1, 25} In brief, DENV-2 replication and spread was determined by plaque assay using Huh-7 cells seeded into 96-well plates.²⁶⁻²⁷ One day after seeding, cells were infected with DENV-2 (strain 16681) at a MOI of 1 PFU/cell. Compounds specified in the results section were dissolved in culture medium and added at different concentrations to the cells together with the virus. After a 2 h incubation at 37°C, media were replaced by fresh medium containing given concentrations of the inhibitors. Virus progeny contained in culture supernatants were quantified 48 h post infection by plaque assay on VeroE6 cells. Ribavirin was included as a reference compound. The analogous plaque assay was used in the case of WNV (strain New York 99; MOI = 0.2 PFU/cell). The impact of compounds on cell viability was determined by using CellTiter-Glo[®] and CytoTox 96[®] assays (Promega GmbH, Mannheim, Germany) following the instructions of the manufacturer.

9. Acute toxicity study in mice

The study was conducted by Eurofins Panlabs Taiwan Ltd. in ICR mice weighing 23 ± 3 g (provided by BioLasco Taiwan under Charles River Laboratories Licensee) according to a standard protocol as described previously.¹ To avoid TFA-related side effects, inhibitors were converted into physiologically more acceptable HCl salts as described previously.¹ All doses were calculated as the free bases of the inhibitors, dissolved in saline, and administered intraperitoneally (*ip.*) at 5 mL/kg to groups of four mice each (two male and two female). The animals received a certain initial dose of each inhibitor (2.5 mg/kg). If the whole group of animals survived for 24 hours, the dose for the same animals was increased (5, 10, and 15 mg/kg). All aspects of this work including housing, experimentation, and animal disposal were performed in general accordance with the “Guide for the Care and Use of Laboratory Animals: Eighth Edition” (National Academies Press, Washington, D.C., 2011) in an AAALAC-accredited laboratory animal facility. In addition, the animal care and use protocol was reviewed and approved by the IACUC at Eurofins Panlabs Taiwan, Ltd.

10. Pharmacokinetic characterization of inhibitor **8** in rats

The study was performed by Pharmacelsus GmbH Germany in adult male Sprague Dawley rats. The animals were housed in a temperature-controlled room (20-24°C) and maintained in a 12 h light/12 h dark cycle. Food and water were available throughout the duration of the study. As described before in the toxicity study, the HCl salt of compound **8** was used for the PK study. Test item formulations were administered either intravenously (*iv.*) at 1 mg/kg to a group of 3 rats or intraperitoneally (*ip.*) at 2.5 mg/kg to 2 rats, respectively. After treatment of all rats, six serial blood samples were obtained from each rat at 5 min, 15 min, 30 min, 1 h, 3 h, and 8 h. At these time points, a volume of 100 µL blood was obtained from the vascular access harness in tubes containing Li-Heparin. After sampling, the plasma was prepared within 10 min and was kept at -20°C until processed for bioanalysis. Both Liquid chromatography (Accela U-HPLC pump, Accela Open Autosampler (Thermo Fisher Scientific, USA)) and mass spectrometry (Q-Exactive mass spectrometer (Orbitrap™ technology with accurate mass)) were used for analysis. All experimental procedures were approved by and conducted in accordance with the regulations of the local Animal Welfare authorities (Landesamt für Gesundheit und Verbraucherschutz, Abteilung Lebensmittel- und Veterinärwesen, Saarbrücken).

The determined plasma concentrations are shown in Figure S6, the pharmacokinetic data are summarized in Table S4.

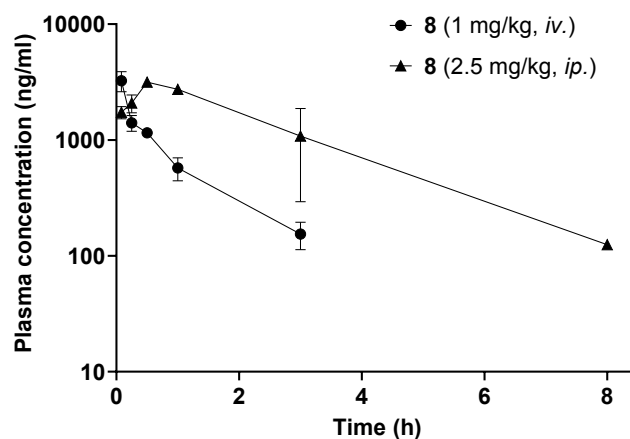


Figure S6. Mean profile of plasma concentrations of the inhibitor **8** after *iv.* (n=3) and *ip.* (n=2) treatment (the lower limit of quantification was set to 120 ng/ml). A plasma level of 1000 ng/ml corresponds to a concentration of approximately 1.3 µM.

Table S4. Pharmacokinetic parameters in male Sprague Dawley rats after treatment with inhibitor **8**. The pharmacokinetic analysis was performed by applying a non-compartment model using the Kinetica 5.0 software (Thermo Scientific, Waltham, USA).

Number of test animals	3	2
Dose route	<i>iv.</i>	<i>ip.</i>
Dosage (mg/kg)	1	2.5
Volume (mL/kg)	5	5
C _{max} (ng/mL)	-	3156
C ₀ (ng/mL)	2076	-
t _{max} (h)	-	0.50
C _z (ng/mL)	154 (after 3h)	126 (after 8h)
t _z (h)	3	8
t _{1/2z} (h)	0.9	1.6
AUC _{0-tz} (ng·h/mL)	2088	9352
AUC _{0-∞} (ng·h/mL)	2291	9642
V _z (mL/kg)	569	
CL (mL/(h·kg))	442	
V _{z/f} (mL/kg)		639
CL/f (mL/(h·kg))		273

Parameters abbreviations:

C _{max} (ng/mL)	maximal concentration
C ₀ (ng/mL)	extrapolated initial concentration
t _{max} (h)	time to reach the maximum concentration
C _z (ng/mL)	last analytically quantifiable concentration
t _z (h)	time of the last sample which has an analytically quantifiable concentration
t _{1/2z} (h)	half life of the terminal slope of a concentration-time curve
AUC _(0-tz) (ng·h/mL)	area under the concentration-time curve up to the time t _z of the last sample
AUC _(0-∞) (ng·h/mL)	area under the concentration-time curve extrapolated to infinity
V _z (mL/kg)	volume of distribution, in case of intravascular administration
CL (mL/(h·kg))	total body clearance, in case of intravascular administration
V _{z/f} (mL/kg)	volume of distribution, in case of extravascular administration
CL/f (mL/(h·kg))	total body clearance, in case of extravascular administration

11. Abbreviations used in the supporting information

Amba, 4-amidinobenzylamide; Cav, canavanine; 2-CTC, 2-chlorotriyl chloride; DCM, dichloromethane; DIPEA, N,N-diisopropylethylamine; DMF, N,N-dimethylformamide; HBTU, 3-[Bis(dimethylamino)methyl]methyl-3H-benzotriazol-1-oxide hexafluorophosphate; HOBT, N-hydroxybenzotriazole; *ip.*, intraperitoneal; *iv.*, intravenous; MOI, multiplicity of infection; PyBOP, (Benzotriazol-1-yloxy)tripyrrolidinophosphonium hexafluorophosphate; RMSD, root mean square deviation; RSV, respiratory syncytial virus; SPPS, solid-phase peptide synthesis; TFA, trifluoroacetic acid; TIS, triisopropylsilane, Tle, *tert*-leucine.

12. References

1. Ivanova, T.; Harges, K.; Kallis, S.; Dahms, S. O.; Than, M. E.; Künzel, S.; Böttcher-Friebertshäuser, E.; Lindberg, I.; Jiao, G. S.; Bartenschlager, R.; Steinmetzer, T., Optimization of Substrate-Analogue Furin Inhibitors. *ChemMedChem* **2017**, *12* (23), 1953-1968.
2. Bernatowicz, M. S.; Wu, Y.; Matsueda, G. R., Urethane protected derivatives of 1-guanylpiperazine for the mild and efficient preparation of guanidines. *Tetrahedron Letters* **1993**, *34* (21), 3389-3392.
3. Becker, G. L.; Sielaff, F.; Than, M. E.; Lindberg, I.; Routhier, S.; Day, R.; Lu, Y.; Garten, W.; Steinmetzer, T., Potent inhibitors of furin and furin-like proprotein convertases containing decarboxylated P1 arginine mimetics. *J Med Chem* **2010**, *53* (3), 1067-75.
4. Gottlieb, H. E.; Kotlyar, V.; Nudelman, A., NMR Chemical Shifts of Common Laboratory Solvents as Trace Impurities. *J Org Chem* **1997**, *62* (21), 7512-7515.
5. Dahms, S. O.; Harges, K.; Becker, G. L.; Steinmetzer, T.; Brandstetter, H.; Than, M. E., X-ray structures of human furin in complex with competitive inhibitors. *ACS Chem Biol* **2014**, *9* (5), 1113-1118.
6. Dahms, S. O.; Harges, K.; Steinmetzer, T.; Than, M. E., X-ray Structures of the Proprotein Convertase Furin Bound with Substrate Analogue Inhibitors Reveal Substrate Specificity Determinants beyond the S4 Pocket. *Biochemistry* **2018**, *57* (6), 925-934.
7. Dahms, S. O.; Arciniega, M.; Steinmetzer, T.; Huber, R.; Than, M. E., Structure of the unliganded form of the proprotein convertase furin suggests activation by a substrate-induced mechanism. *Proc Natl Acad Sci U S A* **2016**, *113* (40), 11196-11201.
8. Theveneau, P.; Baker, R.; Barrett, R.; Beteva, A.; Bowler, M. W.; Carpentier, P.; Caserotto, H.; Sanctis, D. d.; Dobias, F.; Flot, D.; Guijarro, M.; Giraud, T.; Lentini, M.; Leonard, G. A.; Mattenet, M.; McCarthy, A. A.; McSweeney, S. M.; Morawe, C.; Nanao, M.; Nurizzo, D.; Ohlsson, S.; Pernot, P.; Popov, A. N.; Round, A.; Royant, A.; Schmid, W.; Snigirev, A.; Surr, J.; Mueller-Dieckmann, C., The Upgrade Programme for the Structural Biology beamlines at the European Synchrotron Radiation Facility – High throughput sample evaluation and automation. *Journal of Physics: Conference Series* **2013**, *425* (1), 012001.
9. Helmholtz-Zentrum Berlin für Materialien und Energie. (2016). The MX beamlines BL14.1-3 at BESSY II. Journal of large-scale research facilities, 2, A47. <http://dx.doi.org/10.17815/jlsrf-2-64>.

10. Kabsch, W., XDS. *Acta crystallographica. Section D, Biological crystallography* **2010**, *66* (Pt 2), 125-32.
11. Sparta, K. M.; Krug, M.; Heinemann, U.; Mueller, U.; Weiss, M. S., XDSAPP2.0. *Journal of Applied Crystallography* **2016**, *49* (3), 1085-1092.
12. Winn, M. D.; Ballard, C. C.; Cowtan, K. D.; Dodson, E. J.; Emsley, P.; Evans, P. R.; Keegan, R. M.; Krissinel, E. B.; Leslie, A. G.; McCoy, A.; McNicholas, S. J.; Murshudov, G. N.; Pannu, N. S.; Potterton, E. A.; Powell, H. R.; Read, R. J.; Vagin, A.; Wilson, K. S., Overview of the CCP4 suite and current developments. *Acta Crystallogr D Biol Crystallogr* **2011**, *67* (Pt 4), 235-42.
13. Emsley, P.; Lohkamp, B.; Scott, W. G.; Cowtan, K., Features and development of Coot. *Acta crystallographica. Section D, Biological crystallography* **2010**, *66* (Pt 4), 486-501.
14. Adams, P. D.; Afonine, P. V.; Bunkoczi, G.; Chen, V. B.; Davis, I. W.; Echols, N.; Headd, J. J.; Hung, L. W.; Kapral, G. J.; Grosse-Kunstleve, R. W.; McCoy, A. J.; Moriarty, N. W.; Oeffner, R.; Read, R. J.; Richardson, D. C.; Richardson, J. S.; Terwilliger, T. C.; Zwart, P. H., PHENIX: a comprehensive Python-based system for macromolecular structure solution. *Acta crystallographica. Section D, Biological crystallography* **2010**, *66* (Pt 2), 213-21.
15. Schuttelkopf, A. W.; van Aalten, D. M., PRODRG: a tool for high-throughput crystallography of protein-ligand complexes. *Acta Crystallogr D Biol Crystallogr* **2004**, *60* (Pt 8), 1355-63.
16. Hardes, K.; Becker, G. L.; Lu, Y.; Dahms, S. O.; Köhler, S.; Beyer, W.; Sandvig, K.; Yamamoto, H.; Lindberg, I.; Walz, L.; von Messling, V.; Than, M. E.; Garten, W.; Steinmetzer, T., Novel furin inhibitors with potent anti-infectious activity. *ChemMedChem* **2015**, *10* (7), 1218-31.
17. Kacprzak, M. M.; Peinado, J. R.; Than, M. E.; Appel, J.; Henrich, S.; Lipkind, G.; Houghten, R. A.; Bode, W.; Lindberg, I., Inhibition of furin by polyarginine-containing peptides: nanomolar inhibition by nona-D-arginine. *J Biol Chem* **2004**, *279* (35), 36788-94.
18. Williams, J. W.; Morrison, J. F., The kinetics of reversible tight-binding inhibition. *Methods Enzymol* **1979**, *63*, 437-67.
19. Hinkes, S.; Wuttke, A.; Saupe, S. M.; Ivanova, T.; Wagner, S.; Knörlein, A.; Heine, A.; Klebe, G.; Steinmetzer, T., Optimization of cyclic plasmin inhibitors: from benzamidines to benzylamines. *J Med Chem* **2016**, *59* (13), 6370-86.
20. Meyer, D.; Sielaff, F.; Hammami, M.; Böttcher-Friebertshäuser, E.; Garten, W.; Steinmetzer, T., Identification of the first synthetic inhibitors of the type II transmembrane serine protease TMPRSS2 suitable for inhibition of influenza virus activation. *Biochem J* **2013**, *452* (2), 331-343.
21. Walsmann, P., On the purification of thrombin preparations. *Pharmazie* **1968**, *23* (7), 401-402.
22. Van Lam van, T.; Ivanova, T.; Hardes, K.; Heindl, M. R.; Morty, R. E.; Böttcher-Friebertshäuser, E.; Lindberg, I.; Than, M. E.; Dahms, S. O.; Steinmetzer, T., Design, Synthesis, and Characterization of Macrocyclic Inhibitors of the Proprotein Convertase Furin. *ChemMedChem* **2019**, *14* (6), 673-685.
23. Matrosovich, M.; Matrosovich, T.; Garten, W.; Klenk, H. D., New low-viscosity overlay medium for viral plaque assays. *Virology* **2006**, *3*, 63.
24. Nitsche, C.; Zhang, L.; Weigel, L. F.; Schilz, J.; Graf, D.; Bartenschlager, R.; Hilgenfeld, R.; Klein, C. D., Peptide-Boronic Acid Inhibitors of Flaviviral Proteases: Medicinal Chemistry and Structural Biology. *J Med Chem* **2017**, *60* (1), 511-516.

25. Kouretova, J.; Hammamy, M. Z.; Epp, A.; Hardes, K.; Kallis, S.; Zhang, L.; Hilgenfeld, R.; Bartenschlager, R.; Steinmetzer, T., Effects of NS2B-NS3 protease and furin inhibition on West Nile and Dengue virus replication. *J Enzyme Inhib Med Chem* **2017**, *32* (1), 712-721.
26. Nitsche, C.; Schreier, V. N.; Behnam, M. A.; Kumar, A.; Bartenschlager, R.; Klein, C. D., Thiazolidinone-peptide hybrids as dengue virus protease inhibitors with antiviral activity in cell culture. *J Med Chem* **2013**, *56* (21), 8389-403.
27. Weigel, L. F.; Nitsche, C.; Graf, D.; Bartenschlager, R.; Klein, C. D., Phenylalanine and Phenylglycine Analogues as Arginine Mimetics in Dengue Protease Inhibitors. *J Med Chem* **2015**, *58* (19), 7719-33.

4.3 TMPRSS2 and furin are both essential for proteolytic activation of SARS-CoV-2 in human airway cells

Dorothea Bestle*, Miriam Ruth Heindl*, Hannah Limburg*, **Thuy Van Lam van**, Oliver Pilgram, Hong Moulton, David A. Stein, Kornelia Harges, Markus Eickmann, Olga Dolnik, Cornelius Rohde, Hans-Dieter Klenk, Wolfgang Garten, Torsten Steinmetzer, and Eva Böttcher-Friebertshäuser (2020)

Life Science Alliance. 2020, 3(9)

DOI: 10.26508/lsa.202000786

*The authors contributed equally to this work.

Research Article



TMPRSS2 and furin are both essential for proteolytic activation of SARS-CoV-2 in human airway cells

Dorothea Bestle^{1,*}, Miriam Ruth Heindl^{1,*}, Hannah Limburg^{1,*}, Thuy Van Lam van², Oliver Pilgram², Hong Moulton³, David A Stein³, Kornelia Hardes^{2,4}, Markus Eickmann^{1,5}, Olga Dolnik^{1,5}, Cornelius Rohde^{1,5}, Hans-Dieter Klenk¹, Wolfgang Garten¹, Torsten Steinmetzer², Eva Böttcher-Friebertshäuser¹

The novel emerged SARS-CoV-2 has rapidly spread around the world causing acute infection of the respiratory tract (COVID-19) that can result in severe disease and lethality. For SARS-CoV-2 to enter cells, its surface glycoprotein spike (S) must be cleaved at two different sites by host cell proteases, which therefore represent potential drug targets. In the present study, we show that S can be cleaved by the proprotein convertase furin at the S1/S2 site and the transmembrane serine protease 2 (TMPRSS2) at the S2' site. We demonstrate that TMPRSS2 is essential for activation of SARS-CoV-2 S in Calu-3 human airway epithelial cells through antisense-mediated knockdown of TMPRSS2 expression. Furthermore, SARS-CoV-2 replication was also strongly inhibited by the synthetic furin inhibitor MI-1851 in human airway cells. In contrast, inhibition of endosomal cathepsins by E64d did not affect virus replication. Combining various TMPRSS2 inhibitors with furin inhibitor MI-1851 produced more potent antiviral activity against SARS-CoV-2 than an equimolar amount of any single serine protease inhibitor. Therefore, this approach has considerable therapeutic potential for treatment of COVID-19.

DOI [10.26508/lsa.202000786](https://doi.org/10.26508/lsa.202000786) | Received 20 May 2020 | Revised 15 July 2020 | Accepted 15 July 2020 | Published online 23 July 2020

Introduction

In December 2019, a new coronavirus (CoV) emerged and has rapidly spread around the world causing a pandemic never before observed with these viruses. The virus was identified as a new member of the lineage b of the genus *Betacoronavirus*, which also contains the 2002 severe acute respiratory syndrome (SARS)-CoV, and was named SARS-CoV-2 by the World Health Organization. The respiratory disease caused by the virus was designated as coronavirus disease 2019 (COVID-19).

CoVs are a large family of enveloped, single-stranded positive-sense RNA viruses belonging to the order *Nidovirales* and infect a

broad range of mammalian and avian species, causing respiratory or enteric diseases. CoVs have a major surface protein, the spike (S) protein, which initiates infection by receptor binding and fusion of the viral lipid envelope with cellular membranes. Like fusion proteins of many other viruses, the S protein is activated by cellular proteases. Activation of CoV S is a complex process that requires proteolytic cleavage of S at two distinct sites, S1/S2 and S2' (Fig 1), generating the subunits S1 and S2 that remain non-covalently linked (1, 2, 3). The S1 subunit contains the receptor binding domain, whereas the S2 subunit is membrane-anchored and harbors the fusion machinery. Cleavage at the S2' site, located immediately upstream of the hydrophobic fusion peptide, has been proposed to trigger the membrane fusion activity of S (4, 5). In contrast, the relevance of S cleavage at the S1/S2 site is not yet fully understood. Processing of CoV S is believed to occur sequentially, with cleavage at the S1/S2 site occurring first and subsequent cleavage at S2'. Cleavage at the S1/S2 site may be crucial for conformational changes required for receptor binding and/or subsequent exposure of the S2' site to host proteases at the stage of virus entry (reviewed in references 6, 7, and 8).

Many proteases have been found to activate CoVs in vitro, including furin, cathepsin L, and trypsin-like serine proteases such as the transmembrane serine protease 2 (TMPRSS2), TMPRSS11A, and TMPRSS11D (reviewed in references 6, 7, and 8). Among them, TMPRSS2 and furin play major roles in proteolytic activation of a broad range of viruses (reviewed in references 9, 10, and 11). TMPRSS2 is a type II transmembrane serine protease (TTSP) that is widely expressed in epithelial cells of the respiratory, gastrointestinal, and urogenital tract (11, 12). The physiological role of TMPRSS2 is yet unknown, but TMPRSS2-deficient mice lack a discernible phenotype suggesting functional redundancy (13). In 2006, we first identified TMPRSS2 as a virus-activating protease, by demonstrating that it cleaves the surface glycoprotein HA of human influenza A viruses (14). Subsequently, TMPRSS2 was shown to activate the fusion proteins of a number of other respiratory

¹Institute of Virology, Philipps-University, Marburg, Germany ²Institute of Pharmaceutical Chemistry, Philipps-University, Marburg, Germany ³Department of Biomedical Sciences, Carlson College of Veterinary Medicine, Oregon State University, Corvallis, OR, USA ⁴Fraunhofer Institute for Molecular Biology and Applied Ecology, Gießen, Germany ⁵German Center for Infection Research (DZIF), Marburg-Gießen-Langen Site, Emerging Infections Unit, Philipps-University, Marburg, Germany

Correspondence: friebertshaeuser@staff.uni-marburg.de

*Dorothea Bestle, Miriam Ruth Heindl, and Hannah Limburg contributed equally to this work

viruses, including human metapneumovirus, human parainfluenza viruses, and CoVs, including SARS-CoV and Middle East respiratory syndrome (MERS)-CoV in vitro (reviewed in references 8 and 11). TMPRSS2 cleaves at single arginine or lysine residues (R/K↓), and hence, activates viral fusion proteins at the so called monobasic cleavage sites. More recent studies by us and others demonstrated that TMPRSS2-deficient mice do not suffer from pathology when infected with certain influenza A virus strains, SARS-CoV and MERS-CoV due to inhibition of proteolytic activation of progeny virus and consequently inhibition of virus spread along the respiratory tract (15, 16, 17, 18). These studies identified TMPRSS2 as an essential host cell factor for these respiratory viruses and further demonstrated that inhibition of virus activating host cell proteases, particularly TMPRSS2, provides a promising approach for the development of therapeutics to treat respiratory virus infections. The proprotein convertase furin is a type I transmembrane protein that is ubiquitously expressed in eukaryotic tissues and cells. Furin cleaves the precursors of a broad range of proteins, including hormones, growth factors, cell surface receptors, and adhesion molecules during their transport along the secretory pathway at multibasic motifs of the preferred consensus sequence R-X-R/K-R↓ (reviewed in reference 10). Moreover, furin has been identified as an activating protease for the fusion proteins of a broad range of viruses, including highly pathogenic avian influenza A viruses (HPAIV), HIV, Ebola virus, measles virus, and yellow fever virus as well as bacterial toxins such as Shiga toxin or anthrax toxin at multibasic motifs (reviewed in references 9, 10, and 19). Acquisition of a multibasic cleavage site by insertion of basic amino acids has long been known to be a prime determinant of avian influenza A virus pathogenicity in poultry. Activation of the surface glycoprotein HA of HPAIV by furin supports systemic spread of infection with often lethal outcome. In contrast, the HA of low pathogenic avian influenza A viruses (LPAIV) is activated at a monobasic cleavage site by trypsin-like serine proteases. Appropriate proteases are believed to be expressed only in the respiratory and intestinal tract of birds, confining spread of infection to these tissues.

Recent studies indicate that TMPRSS2 is also involved in SARS-CoV-2 S protein activation (20, 21). Transient expression of TMPRSS2 in Vero cells supports cathepsin-independent entry of SARS-CoV-2 pseudotypes. Moreover, pretreatment of human Caco-2 colon and human airway cells with the broad range inhibitor camostat mesylate, which can inhibit TMPRSS2 activity, markedly reduced the entry of SARS-CoV-2 as well as vesicular stomatitis virus pseudotypes containing the SARS-CoV-2 S protein. This suggests that a trypsin-like serine protease is crucial for SARS-CoV-2 entry into these cells. However, sequence analysis of the SARS-CoV-2 S protein suggests that furin may also be involved in S processing (Fig 1B; (22, 23)). The S1/S2 site of SARS-CoV-2 S protein contains an insertion of four amino acids providing a minimal furin cleavage site (R-R-A-R₆₈₅↓) in contrast to the S protein of SARS-CoV. Instead, similar to SARS-CoV the S2' cleavage site of SARS-CoV-2, S possesses a paired dibasic motif with a single KR segment (KR₈₁₅↓) that is recognized by trypsin-like serine proteases.

In the present study, we demonstrate that the S protein of SARS-CoV-2 is activated by TMPRSS2 and furin. We also show that inhibitors against both proteases strongly suppress virus replication in human airway epithelial cells and that the combination of both

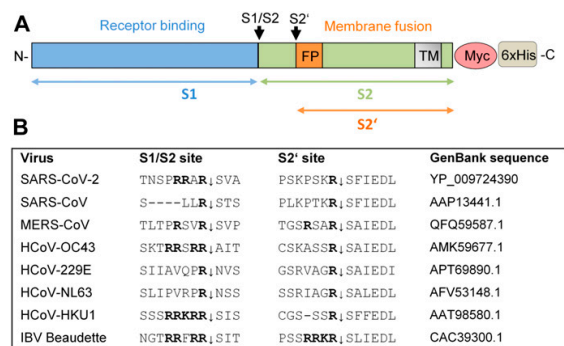


Figure 1. Cleavage of coronavirus S protein.

(A) Schematic representation of the SARS-CoV-2 precursor and the S1 and S2 subunits. Fusion peptide (FP), and transmembrane domain (TM) are indicated. The S1/S2 and S2' cleavage sites and subunits S1, S2, and S2' are indicated by black and colored arrows, respectively. For immunochemical detection, recombinant S is expressed with a C-terminally fused Myc-6xHis-tag peptide in our study.

(B) Alignment of the amino acid sequences at the S1/S2 and S2' cleavage site of the S proteins of different human coronaviruses (HCoV) and avian infectious bronchitis virus strain Beaudette.

types of inhibitors produces a synergistic effect on virus reduction. Our results show that this approach has considerable therapeutic potential for treatment of COVID-19.

Results

Cleavage of SARS-CoV-2 S1/S2 site fluorescence resonance energy transfer (FRET)-substrates by furin

The S1/S2 cleavage site of the novel emerged SARS-CoV-2 has been shown to possess a minimal furin consensus motif of the sequence R-R-A-R↓ with an alanine instead of a basic residue in the P2 position (Fig 1B; (22, 23)). Only few furin substrates possess a nonbasic residue in the P2 position, such as *Pseudomonas aeruginosa* exotoxin A or Shiga toxin (10, 19). To test, whether the S1/S2 sequence of SARS-CoV-2 S protein is efficiently cleaved by furin, a small series of FRET substrates was synthesized (Fig 2A). All compounds possess a 3-nitrotyrosine amide as P4' residue and a 2-amino-benzoyl fluorophore in the P7 position. The analogous sequences of the S proteins from MERS-CoV, SARS-CoV, and avian infectious bronchitis virus (IBV) strain Beaudette were prepared as reference substrates. Moreover, two FRET substrates of the SARS-CoV-2 S1/S2 cleavage site with P2 A → K and A → R mutations were synthesized, to evaluate whether they could constitute even more efficient cleavage sites for furin than the wild type. The FRET substrates were tested in an enzyme kinetic assay with human furin, and their cleavage efficiency is shown in Fig 2B. The FRET substrate of the SARS-CoV-2 S1/S2 cleavage site was efficiently cleaved by recombinant furin. In contrast, the monobasic SARS-CoV FRET substrate was not processed by furin. The MERS-CoV S1/S2 FRET substrate possessing a dibasic R-X-X-R motif was cleaved by furin ~10-fold less efficiently than the best substrates of this FRET

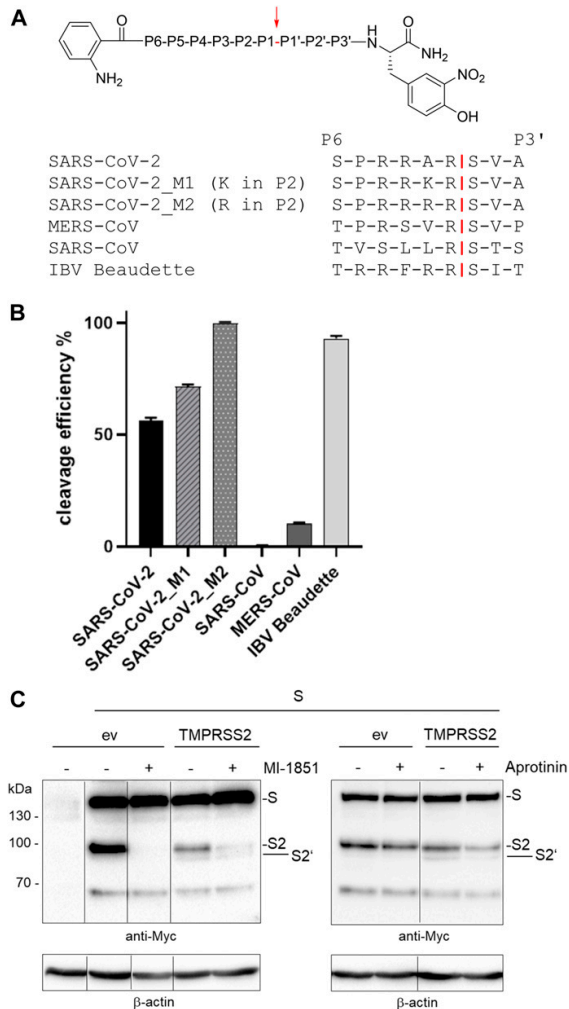


Figure 2. Cleavage of SARS-CoV-2 S by furin and TMPRSS2.

(A) Fluorescence resonance energy transfer substrates of the S protein S1/S2 sites of the indicated CoVs. M1 and M2 are mutants of the SARS-CoV-2 S1/S2 site with substitution of A \rightarrow K or A \rightarrow R in P2 position. IBV, avian infectious bronchitis virus strain Beaudette. Cleavage by furin is indicated in red. (B) Cleavage of the fluorescence resonance energy transfer substrates (20 μ M) by furin (0.5 nM). Cleavage efficiency of SARS-CoV-2_M2 was set as 100%. (C) Cleavage of SARS-CoV-2 S by furin and TMPRSS2 in HEK293 cells. Cells were co-transfected with pCAGGS-S-Myc-6xHis and either empty vector or pCAGGS-TMPRSS2. Cells were then incubated in the absence or presence of aprotinin or furin inhibitor MI-1851 (50 μ M each) for 48 h. Cell lysates were subjected to SDS-PAGE and Western blot analysis using antibodies against the C-terminal Myc-tag. For each Western blot lanes are spliced together from one immunoblot from one experiment. β -actin was used as loading control. Source data are available for this figure.

series. The FRET substrate SARS-CoV-2_M1, which contains an optimized furin recognition site by virtue of an A \rightarrow K mutation in the P2 position, was cleaved with similar efficiency compared with the wild-type sequence. However, substitution of A \rightarrow R in the P2

position strongly enhanced cleavage by furin. As expected, the analogous reference sequence of IBV was also processed by furin very efficiently. The data show that the R-R-A-R motif at the S1/S2 cleavage site of SARS-CoV-2 S is efficiently cleaved by furin in vitro.

SARS-Cov-2 spike protein is cleaved by both furin and TMPRSS2

We next examined whether the SARS-CoV-2 S protein is cleaved by endogenous furin in HEK293 cells. Cells were transiently transfected with pCAGGS plasmid encoding the SARS-CoV-2 S protein with a C-terminal Myc-6xHis-tag and incubated in the absence and presence of the potent synthetic furin inhibitor MI-1851 (cf. Fig S1; manuscript describing its synthesis submitted). At 48 h post transfection, cell lysates were subjected to SDS-PAGE and Western blot analysis using antibodies against the Myc epitope. As shown in Fig 2C (left panel), the uncleaved precursor S and the S2 subunit were detected in the absence of MI-1851, indicating that S is cleaved by endogenous proteases at the S1/S2 site in HEK293 cells. In contrast, S cleavage was efficiently prevented by MI-1851. The S1 subunit cannot be detected by the Myc-specific antibody (cf. Fig 1A). However, S cleavage was not prevented by the trypsin-like serine protease inhibitor aprotinin (Fig 2C, right panel, lane 2). Thus, the data indicate that SARS-CoV-2 S protein is cleaved by furin at the S1/S2 site in HEK293 cells.

We then investigated SARS-CoV-2 S cleavage by TMPRSS2. Because HEK293 cells do not express endogenous TMPRSS2 (unpublished data; see also www.proteinatlas.org), we co-transfected the cells with pCAGGS-S-Myc-6xHis and pCAGGS-TMPRSS2. Then, the cells were incubated in the absence or presence of MI-1851 to suppress S cleavage by endogenous furin. Interestingly, two S cleavage products of ~95 and 80 kDa, respectively, were detected upon co-expression of TMPRSS2 in the absence of MI-1851 (Fig 2C, left panel), most likely S2 and S2', as they can both be detected by the Myc-specific antibody (cf. Fig 1A). In the presence of MI-1851, only a minor S2 protein band was detected. However, the amount of S2' protein present in transient TMPRSS2-expressing cells was similar in MI-1851-treated and untreated cells, suggesting that S cleavage at the S2' site is only caused by TMPRSS2 activity. The small amount of S2 protein detected in TMPRSS2-expressing cells in the presence of MI-1851 was likely due to residual furin activity rather than cleavage of S at the S1/S2 site by TMPRSS2. Cleavage of S by TMPRSS2 at the S2' site was further supported by the reduction of S2' protein in aprotinin treated cells (Fig 2C, right panel). Together, the data show that SARS-CoV-2 S can be cleaved by furin and by TMPRSS2. The data further suggest that the proteases cleave S at different sites with furin processing the S1/S2 site and TMPRSS2 cleaving at the S2' site.

Knockdown of TMPRSS2 prevents proteolytic activation and multiplication of SARS-CoV-2 in Calu-3 human airway epithelial cells

Next, we investigated whether TMPRSS2 is involved in proteolytic activation and multicycle replication of SARS-CoV-2 in Calu-3 human airway epithelial cells. To specifically knockdown TMPRSS2 activity, we previously developed an antisense peptide-conjugated phosphorodiamidate morpholino oligomer (PPMO) (25). PPMOs are

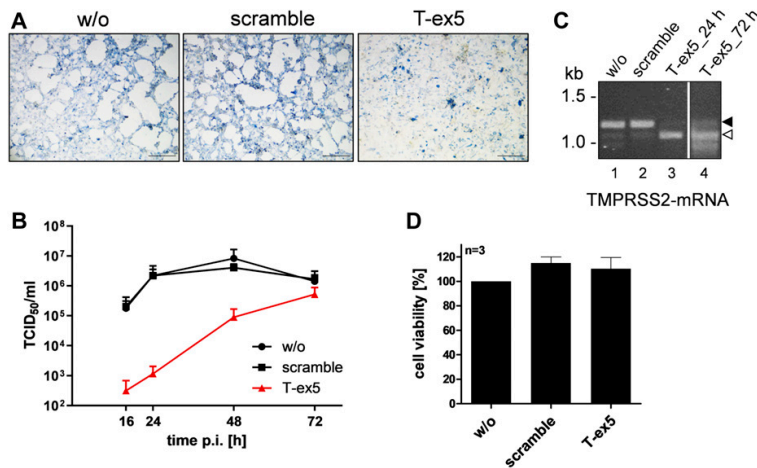


Figure 3. Knockdown of TMPRSS2 expression by PPMO T-ex5 inhibits multicycle replication of SARS-CoV-2 in Calu-3 cells.

(A) Multicycle replication of SARS-CoV-2 in T-ex5-treated Calu-3 cells. Cells were treated with 25 μ M T-ex5 or control PPMO (scramble) for 24 h or remained without treatment (w/o). Cells were then inoculated with SARS-CoV-2 at a MOI of 0.001 for 1 h 30 min, the inoculum was removed and the cells further incubated in the absence of PPMO for 72 h. Cells were fixed and immunostained using a serum against SARS-CoV. Virus-positive cells are stained in blue. Scale bars indicate 500 μ m. (B) Calu-3 cells were treated with PPMO for 24 h and then infected with SARS-CoV-2 for 72 h as described above. Virus titers in supernatants were determined by tissue culture infection dose 50% (TCID₅₀) end point dilution at indicated time points. Results are mean values \pm SD of three independent experiments. (C) Analysis of TMPRSS2-mRNA in PPMO-treated Calu-3 cells. Cells were treated with 25 μ M T-ex5, scramble PPMO or remained untreated (w/o) for 24 h (lanes 1–4). T-ex5-treated cells were inoculated with SARS-CoV-2 as described above and incubated in the absence of PPMO for 72 h (lane 4). Total RNA was isolated and

analyzed by RT-PCR using primers designed to amplify 1,228 nt of full-length TMPRSS2-mRNA. Full-length and truncated PCR products lacking exon 5 are indicated by filled and open arrow heads, respectively. (D) Effect of PPMO treatment on Calu-3 cell viability. Calu-3 cells were treated with scramble or T-ex5 PPMO (25 μ M) for 24 h. Cell viability of untreated (w/o) cells was set as 100%. Results are mean values \pm SD ($n = 3$). Source data are available for this figure.

single-stranded nucleic acid-like compounds, composed of a morpholino oligomer covalently conjugated to a cell-penetrating peptide, and can interfere with gene expression by sterically blocking complementary RNAs. PPMOs are water-soluble and achieve entry into cells and tissues without assisted delivery (reviewed in references 26 and 27). The previously developed PPMO T-ex5 interferes with splicing of TMPRSS2 pre-mRNA, resulting in the production of mature mRNA lacking exon 5 and consequently expression of a truncated TMPRSS2 form that is enzymatically inactive. Using T-ex5 PPMO-mediated knockdown of TMPRSS2 activity, we were able to identify TMPRSS2 as the major influenza A virus activating protease in Calu-3 cells and primary human airway epithelial cells and of influenza B virus in primary human type II pneumocytes (25, 28).

Here, Calu-3 cells were treated once with T-ex5 PPMO for 24 h before infection with SARS-CoV-2 to inhibit the production of normal TMPRSS2-mRNA and deplete enzymatically active TMPRSS2 present in the cells. The cells were then inoculated with SARS-CoV-2 at a low MOI of 0.001, further incubated without additional PPMO treatment for 72 h, and then fixed and immunostained using a rabbit serum originally produced against 2002 SARS-CoV. As shown in Fig 3A, a strong cytopathic effect (CPE) and efficient spread of SARS-CoV-2 infection was visible in Calu-3 cells treated with a negative-control PPMO of nonsense sequence designated as “scramble” as well as untreated cells that were used as controls. In contrast, no CPE and only small foci of infection were observed in T-ex5 PPMO-treated cells at 72 h p.i. (Fig 3A). To examine SARS-CoV-2 activation and multicycle replication in PPMO-treated cells in more detail, Calu-3 cells were treated with PPMO for 24 h before infection, then inoculated with virus at an MOI of 0.001 for 1 h 30 min, and incubated for 72 h in the absence of further PPMO, as described above. At different time points, virus titers in supernatants were

determined by tissue culture infection dose 50% (TCID₅₀) end point dilution. T-ex5 PPMO treatment dramatically reduced virus titers in Calu-3 cells, by 500- and 2,000-fold at 16 and 24 h p.i., respectively, and 90-fold at 48 h p.i. (Fig 3B).

To confirm knockdown of enzymatically active TMPRSS2 expression, Calu-3 cells were treated with PPMO or remained untreated for 24 h, after which TMPRSS2-specific mRNA was isolated and analyzed by RT-PCR as described previously (25). Total RNA was analyzed with primers designed to amplify nucleotides 108–1,336 of TMPRSS2-mRNA. A full-length PCR product of 1,228 bp was amplified from untreated and scramble PPMO-treated Calu-3 cells, whereas a shorter PCR fragment of about 1,100 bp was amplified from T-ex5 PPMO-treated cells (Fig 3C). Sequencing revealed that the truncated TMPRSS2-mRNA lacked the entire exon 5 (data not shown). To further confirm that T-ex5 PPMO single dose treatment before infection still interferes with TMPRSS2-mRNA splicing at 72 h p.i., total RNA was isolated from infected cells at 72 h p.i. and amplified as described above. As shown in Fig 3C, most TMPRSS2-mRNA amplified from T-ex5-treated cells at 72 h p.i. lacked exon 5. The data demonstrate that T-ex5 was very effective at producing exon skipping in TMPRSS2-pre-mRNA and, thus, at inhibiting expression of enzymatically active protease, during the virus growth period in Calu-3 cells. However, a small band of the full-length PCR product was visible after 72 h p.i., indicating low levels of expression of enzymatically active TMPRSS2 at later time points of the virus growth period, which may explain the increase in virus titers observed at 48 h p.i. (cf. Fig 3B). Cell viability was not affected by T-ex5 PPMO treatment of Calu-3 cells, as shown in Fig 3D and described previously (25, 28).

Together, our data identify TMPRSS2 as a host cell factor essential for SARS-CoV-2 activation and multiplication in Calu-3 cells and show that down-regulation of TMPRSS2 activity dramatically blocks SARS-CoV-2 replication.

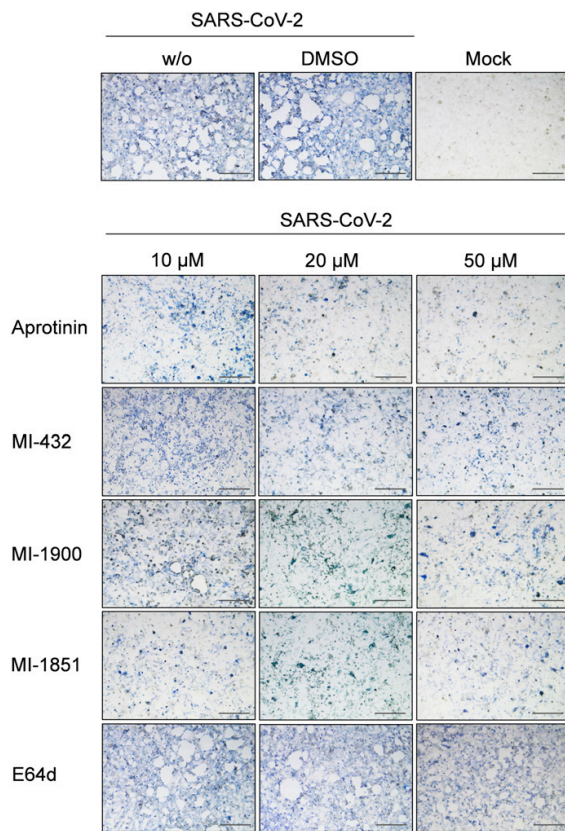


Figure 4. Inhibition of SARS-CoV-2 multiplication in human airway cells by inhibitors of furin and TMPRSS2.

Calu-3 cells were inoculated with SARS-CoV-2 at a low MOI of 0.001 and then incubated in the presence of inhibitors of TMPRSS2 (aprotinin, MI-432, and MI-1900), furin (MI-1851), and endosomal cathepsins (E64d), respectively, at the indicated concentrations. Cells were fixed and immunostained using a rabbit serum against SARS-CoV at 72 h p.i. Virus-positive cells are stained in blue or dark gray depending on the staining intensity. Cells infected in the absence of inhibitors (w/o), in the presence of DMSO (0.5%) and noninfected cells (mock) were used as controls. Scale bars indicate 500 μm . Images are representatives of three independent experiments.

Inhibition of either TMPRSS2 or furin activity suppresses multicycle replication of SARS-CoV-2 in human airway epithelial cells

We next investigated the efficacy of different inhibitors of trypsin-like serine proteases, also inhibiting TMPRSS2, on preventing SARS-CoV-2 activation by TMPRSS2 in Calu-3 cells. We used the natural broad-range serine protease inhibitor aprotinin from bovine lung and two prospective peptide mimetic inhibitors of TMPRSS2, MI-432 (29), and MI-1900 (Fig S1). Aprotinin has long been known to prevent proteolytic activation and multiplication of influenza A virus in cell cultures and mice. Furthermore, inhalation of aerosolized aprotinin by influenza patients markedly reduced the duration of symptoms without causing side effects (30). MI-432 was shown to efficiently

inhibit proteolytic activation and multiplication of influenza A virus in Calu-3 cells (31). The inhibitor MI-1900 is a monobasic and structurally related analog of the dibasic inhibitor MI-432.

To examine the antiviral efficacy of the protease inhibitors against SARS-CoV-2, Calu-3 cells were infected with the virus at a low MOI of 0.001 for 1 h 30 min, after which the inoculum was removed and the cells incubated in the presence of the inhibitors at the indicated concentrations for 72 h. The cells were fixed and immunostained using an antiserum against 2002 SARS-CoV. As shown in Fig 4, strong CPE, with holes visible throughout the monolayer, and efficient spread of SARS-CoV-2 infection was observed in Calu-3 cells in the absence of protease inhibitors. Spread of SARS-CoV-2 infection and virus-induced CPE was efficiently inhibited by aprotinin treatment in a dose-dependent manner and only a few virus-positive cells were visible in Calu-3 cultures treated with 20 and 50 μM aprotinin. Even at a lower concentration of 10 μM , the spread of SARS-CoV-2 was greatly reduced and CPE markedly prevented. Treatment with peptide mimetic TMPRSS2 inhibitors MI-432 and MI-1900 also strongly prevented SARS-CoV-2 multiplication and CPE in Calu-3 cells in a dose-dependent manner, although less potently than aprotinin. At 20 or 50 μM of MI-432 or MI-1900, only small foci of infection were visible. At a concentration of 10 μM , virus spread and CPE in MI-432- or MI-1900-treated cells were still reduced compared with control cells. The data demonstrate that SARS-CoV-2 multiplication in Calu-3 human airway cells can be strongly suppressed by aprotinin and the synthetic TMPRSS2 inhibitors MI-432 and MI-1900.

The observed efficient cleavage of transient expressed SARS-CoV-2 S protein by furin in HEK293 cells prompted us to investigate if furin is involved in SARS-CoV-2 activation in Calu-3 cells. Hence, virus spread in Calu-3 cells was analyzed in the presence of the furin inhibitor MI-1851. Interestingly, MI-1851 strongly inhibited SARS-CoV-2 spread at even the lowest concentration of 10 μM , indicating that furin is critical for SARS-CoV-2 activation and multiplication in these cells (Fig 4). Finally, to examine whether endosomal cathepsins are involved in SARS-CoV-2 activation in Calu-3 cells, multicycle virus replication was determined in the presence of the cathepsin inhibitor E64d. Cathepsin L was shown to cleave the S protein of 2002 SARS-CoV S close to the S1/S2 site (R667) at T678 in vitro (2). Here, strong CPE and foci of infection were observed in E64d-treated cells even at the highest dose of 50 μM , similar to that observed in DMSO-treated as well as untreated control cells, indicating that SARS-CoV-2 activation in Calu-3 cells is independent of endosomal cathepsins.

In sum, our data demonstrate that inhibition of either TMPRSS2 or furin strongly inhibits SARS-CoV-2 in Calu-3 human airway cells, indicating that both proteases are critical for S activation. In contrast, endosomal cathepsins are dispensable or not involved at all in SARS-CoV-2 activation in these cells.

Growth kinetics of SARS-CoV-2 in protease inhibitor-treated Calu-3 cells

To analyze inhibition of SARS-CoV-2 activation and multiplication by the different protease inhibitors in more detail, we performed virus growth kinetics in inhibitor-treated cells. Calu-3 cells were inoculated with SARS-CoV-2 at an MOI of 0.001 and then incubated

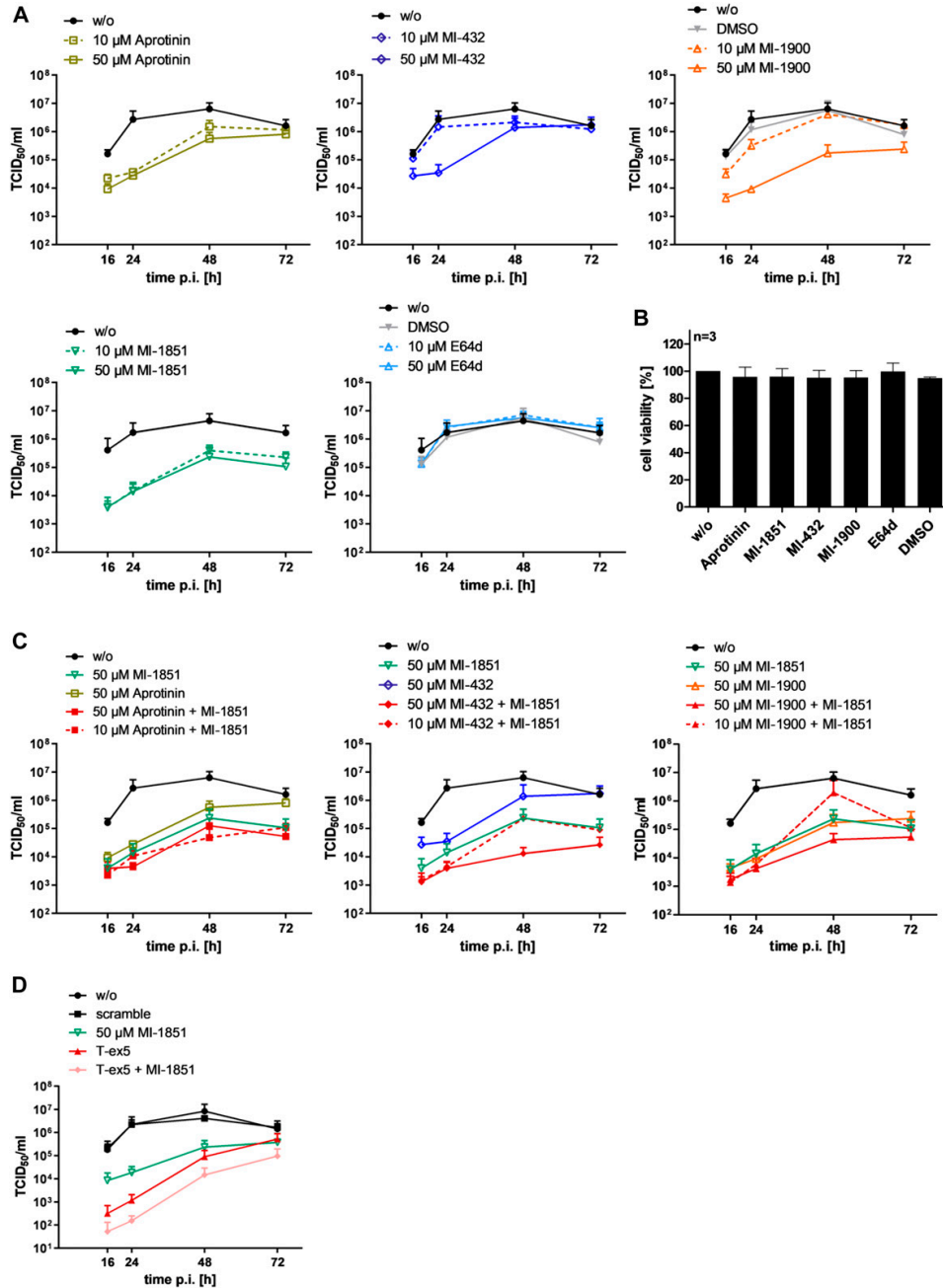


Figure 5. Inhibition of SARS-CoV-2 multicycle replication in human airway epithelial cells by inhibitors of TMPRSS2 and furin.

(A) Calu-3 cells were inoculated with SARS-CoV-2 at a low MOI of 0.001 and then incubated in the absence (w/o) or presence of inhibitors of TMPRSS2 (aprotinin, MI-432, and MI-1900), furin (MI-1851), and endosomal cathepsins (E64d), respectively, or DMSO (0.5%), at the indicated concentrations. At 16, 24, 48, and 72 h postinfection (p.i.), supernatants were collected, and virus replication was determined by tissue culture infection dose 50% ($TCID_{50}$) titration at indicated time points. Data are mean values \pm SD of three to five independent experiments. (B) Effect of inhibitor treatment on cell viability. Calu-3 cells were treated with the indicated protease inhibitor (50 μ M) for 72 h. Untreated cells (w/o) and DMSO treated cells were used as controls. Cell viability of untreated cells was set as 100%. Results are mean values \pm SD (n = 3). (C) Antiviral



in the presence of 10 or 50 μM of the different protease inhibitors. At 16, 24, 48, and 72 h p.i., the viral titer in supernatants was determined by TCID₅₀ titration. Untreated cells and cells treated with DMSO alone were used as controls. SARS-CoV-2 replicated to high titers within 24–48 h in untreated and DMSO-treated cells Calu-3 cells (Fig 5A). Aprotinin suppressed virus replication 25- to 100-fold compared with control cells even at a concentration of 10 μM at 16–48 h p.i. The TMPRSS2 inhibitor MI-432 only slightly affected virus replication at a concentration of 10 μM but reduced virus titers 75-fold at 24 h p.i. at 50 μM . Treatment of cells with TMPRSS2 inhibitor MI-1900 reduced virus titers in a dose-dependent manner and caused strong inhibition of SARS-CoV-2 replication at 50 μM with 35- to 280-fold reduced viral titers compared with control cells. The furin inhibitor MI-1851 efficiently suppressed SARS-CoV-2 multiplication in Calu-3 cells, producing a 30- to 190-fold reduction in virus titers at a dose of 10 μM . In contrast, virus multiplication was not affected by treatment with the cathepsin inhibitor E64d, consistent with the data shown in Fig 4. To provide evidence that inhibition of SARS-CoV-2 replication in inhibitor-treated cells was not caused by cytotoxic effects, we analyzed cell viability in Calu-3 cells treated with 50 μM of the different inhibitors for 72 h. As shown in Fig 5B, evaluation of cell viability revealed no significant cytotoxicity by any of the inhibitors under conditions used in the virus growth experiments.

The data demonstrate that SARS-CoV-2 replication can be efficiently reduced by inhibiting either TMPRSS2 or furin activity, demonstrating that both proteases are crucial for SARS-CoV-2 activation.

Treatment of SARS-CoV-2-infected Calu-3 cells with a combination of TMPRSS2 and furin inhibitors

Finally, we wished to examine whether the combination of inhibitors against TMPRSS2 and furin shows a synergistic antiviral effect. Therefore, Calu-3 cells were infected with virus as described above and incubated in the presence of aprotinin, MI-432, or MI-1900 in combination with MI-1851 at 10 and 50 μM each, respectively, for 72 h. Virus titers in supernatants were determined at indicated time points. Single-dose treatment of each inhibitor and untreated cells were used as controls. As shown in Fig 5C, the combination of 10 μM of MI-1851 with either aprotinin or MI-432 showed enhanced antiviral activity against SARS-CoV-2 and 10- to 30-fold reduced virus titers compared with 10 μM of each inhibitor alone and also reduced viral titer four to eightfold more than that observed with either of the single inhibitors at 50 μM . A combination of 50 μM each of MI-432 and MI-1851 reduced virus titers 10- to 32-fold compared with 50 μM of each inhibitor alone and thereby dramatically suppressed SARS-CoV-2 multiplication 100- to 250-fold compared with untreated or DMSO-treated cells. In contrast, treatment of Calu-3 cells with 50 μM each of MI-1851 and aprotinin did not cause

further suppression of virus titers compared with the combination of 10 μM of each inhibitor. The combination of 10 μM each of MI-1851 and MI-1900 did not show enhanced antiviral activity compared with single inhibitor treatments at 10 μM . However, treatment of cells with 50 μM each of MI-1900 and MI-1851 caused fivefold reduction in viral titers when compared with cells treated with 50 μM of each inhibitor alone and thereby SARS-CoV-2 multiplication in Calu-3 cells was markedly reduced compared to control cells. We furthermore examined the antiviral activity of a combination of T-ex5 PPMO and furin inhibitor MI-1851 against SARS-CoV-2 in Calu-3 cells. As shown in Fig 5D, combined treatment of Calu-3 cells with 25 μM T-ex5 PPMO and 50 μM MI-1851 almost completely blocked SARS-CoV-2 replication with a nearly 15,000-fold reduction in virus titers at 24 h p.i., and reduced virus titers 500-fold at 48 h p.i. compared with control cells. Combination of T-ex5 and MI-1851 was synergistic and caused 30- to 10-fold lower virus titers at 16 and 24 h p.i. compared with single inhibitor-treated cells. The data demonstrate that efficient inhibition of S cleavage by a combination of TMPRSS2 and furin inhibitors can dramatically block SARS-CoV-2 replication in human airway epithelial cells. Furthermore, our data show that combination of TMPRSS2 and furin inhibitors can act synergistically to produce inhibition of SARS-CoV-2 activation and multiplication at lower doses than single protease inhibitor treatment.

In conclusion, our data demonstrate that both TMPRSS2 and furin cleave the SARS-CoV-2 S protein and are essential for efficient virus multicycle replication in Calu-3 human airway cells. The results indicate that TMPRSS2 and furin cleave S at different sites—furin at the S1/S2 site and TMPRSS2 at the S2' site—and suggest that TMPRSS2 and furin cannot compensate for each other in SARS-CoV-2 S activation. Our data further demonstrate that inhibition of either one of these critical proteases can render the S protein of SARS-CoV-2 unable to efficiently mediate virus entry and membrane fusion and, therefore, provides a promising therapeutic approach for treatment of COVID-19.

Discussion

Proteolytic processing of CoV S is a complex process that requires cleavage at two different sites and is yet not fully understood. The amino acid sequence at the S1/S2 and S2' cleavage sites varies among CoVs (Fig 1B), suggesting that differing proteases may be involved in activation of different CoVs. Sequence analyses of the S protein of the emerged SARS-CoV-2 suggested that the R-R-A-R motif at the S1/S2 site may be sensitive to cleavage by furin, whereas the S2' site contains a single R residue that can be cleaved by trypsin-like serine proteases such as TMPRSS2 (20, 22, 23). In the present study, we demonstrate that the SARS-CoV-2 S protein is cleaved by furin and by TMPRSS2. Furthermore, we show that

activity of combinations of TMPRSS2 and furin inhibitors against SARS-CoV-2 in human airway epithelial cells. Calu-3 cells were inoculated with SARS-CoV-2 at an MOI of 0.001 as described above and then incubated in the presence of single protease inhibitors or inhibitor combinations at the indicated concentrations. Virus titers in supernatants were determined by TCID₅₀ at 16, 24, 48, and 72 h p.i. Data are mean values \pm SD of three independent experiments. (D) Calu-3 cells were treated with PPMO for 24 h, then infected with SARS-CoV-2 as described above and incubated in the absence of PPMO (w/o, scramble and T-ex5) and with or without 50 μM of furin inhibitor treatment (MI-1851) for 72 h. At 16, 24, 48, and 72 h p.i., supernatants were collected, and viral titers were determined by TCID₅₀ at indicated time points. Data are mean values \pm SD (n = 2).

multicycle replication of SARS-CoV-2 in Calu-3 human airway cells is strongly suppressed by inhibiting TMPRSS2 and furin activity, demonstrating that both proteases are crucial for S activation in these cells. Our data indicate that furin cleaves at the S1/S2 site, whereas TMPRSS2 cleaves at the S2' site. The effective processing of the S1/S2 site by furin was additionally confirmed by comparing the cleavage rates of various FRET substrates derived from the P6-P3' segments of SARS-CoV-2 and other CoVs. The data clearly revealed that due to the 4-mer PRRA insertion, a well-suited furin cleavage site exists in the S of SARS-CoV-2, which is similarly cleaved as the sequence from the IBV CoV, whereas the analogous substrate of SARS-CoV is not processed by furin. Strong inhibition of SARS-CoV-2 replication in Calu-3 cells by synthetic furin inhibitor MI-1851 furthermore suggests that TMPRSS2 does not compensate for furin cleavage at the S1/S2 site. Likewise, strong inhibition of SARS-CoV-2 replication by knockdown of TMPRSS2 activity using T-ex5 PPMO or treatment of Calu-3 cells with aprotinin, MI-432 and MI-1900, respectively, indicates that furin cannot compensate for the lack of TMPRSS2 in S activation. This was further confirmed by using an analogous FRET substrate derived from the S2' cleavage site of the SARS-CoV-2 S protein (Fig S2). Kinetic measurements clearly revealed that this substrate cannot be cleaved by furin (Fig S2). Thus, we could experimentally demonstrate for the first time that furin only activates the S1/S2 site, as expected from the amino acid sequence at the cleavage sites (22, 23). Together, our data indicate that furin and TMPRSS2 cleave S at different sites and that cleavage by both proteases is crucial to render the S protein active for mediating virus entry and membrane fusion (Fig 6). Iwata-Yoshikawa et al (2019) (18) showed that TMPRSS2-deficient mice do not develop disease symptoms when infected with SARS-CoV and MERS-CoV (18). The data demonstrated that TMPRSS2 is essential for multicycle replication and spread of these CoVs in a manner similar to what we and others have observed for certain influenza A virus strains (15, 16, 17). However, it remains to be determined whether knockout of TMPRSS2 prevents cleavage of the S proteins of SARS-CoV and MERS-CoV at both sites, S1/S2 and S2', or whether another protease is involved in S cleavage, similar to what we have observed here for SARS-CoV-2.

In cell culture, CoVs can enter cells via two distinct routes: the late endosome where S is cleaved by cathepsins or via the cell surface or early endosome using trypsin-like proteases for S cleavage ((2, 32) reviewed in reference 7). However, several recent studies revealed that clinical isolates of human CoV (HCoV) achieve activation by trypsin-like serine proteases and use endosomal cathepsins only in the absence of suitable trypsin-like proteases in cell culture (33, 34). Thus, activation by cathepsins appears to be a mechanism that is acquired by the virus during multiple passaging in cell cultures (34). Congruently, Zhou et al (2015) (35) showed that SARS-CoV pathogenesis in mice was strongly prevented by camostat, a broad-range inhibitor of trypsin-like serine proteases, but not by inhibitors of endosomal cathepsins (35). Here, we show that the cysteine protease inhibitor E64d, which also inhibits cathepsin L and B, did not affect SARS-CoV-2 replication in Calu-3 cells, indicating that endosomal cathepsins are dispensable or not involved at all in SARS-CoV-2 activation in human airway cells.

The presence of a multibasic cleavage site that is processed by ubiquitously expressed furin and, therefore, supports systemic

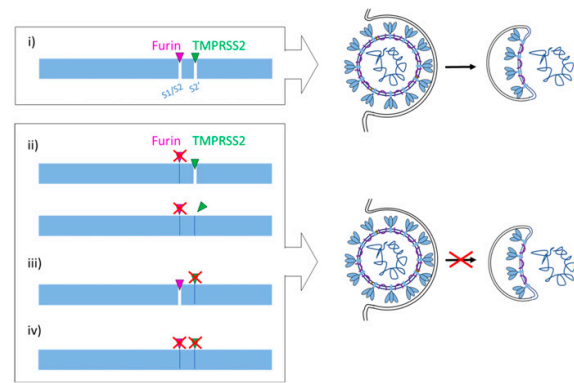


Figure 6. Proposed processing of SARS-CoV-2 spike protein S by TMPRSS2 and furin.

(i) S must be cleaved at two sites, S1/S2 and S2', to trigger fusion of viral and cellular membranes during virus entry to release the virus genome into the host cell. CoV S cleavage is believed to occur sequentially, with cleavage at the S1/S2 site occurring first and subsequent cleavage at the S2' site. Furin processes the S1/S2 site, whereas TMPRSS2 cleaves at the S2' site, and both proteases cannot compensate each other. Inhibition of either furin (ii) or TMPRSS2 (iii) or simultaneous inhibition of both proteases (iv) renders the S protein fusion-inactive and prevents virus entry. Inhibition of TMPRSS2 prevents exposure of the fusion peptide at the N-terminus of the S2' subunit (iii, iv). Inhibition of furin cleavage at the S1/S2 site may directly interfere with virus entry and membrane fusion by steric blockage of conformational changes (ii, upper scheme) or may prevent exposure of the S2' site to TMPRSS2 (ii, lower scheme).

spread of infection, has long been known to be an important determinant of the pathogenicity of HPAIV as well as virulent strains of Newcastle disease virus in poultry (reviewed in references 11 and 36). The S protein of IBV strain Beaudette contains multibasic motifs at the S1/S2 and S2' site (Fig 1B). IBV belongs to the genus *Gammacoronavirus* and causes a highly contagious, acute respiratory disease of chickens. Cleavage of IBV S protein by furin at the S2' site has been associated with neurotropism in chicken (37). Congruently, here, FRET substrates of the S1/S2 and S2' site of the IBV Beaudette S protein were efficiently cleaved by furin (Figs 2B and S2B). However, the contribution of furin-cleavable multibasic motifs at the S1/S2 and/or S2' site with regard to multicycle replication, cellular tropism, and pathogenicity of HCoVs remains to be determined. HCoV-OC43 and HCoV-HKU1 possess a furin cleavage motif at the S1/S2 site. In contrast, the S proteins of the 2002 SARS-CoV, HCoV-229E, and HCoV-NL63 possess single arginine residues at both cleavage sites (see also Figs 2B and S2A). Interestingly, among the S proteins of the seven CoV infecting humans, only SARS-CoV S lacks the 4-mer insertion at the S1/S2 site (Fig 1B; (23)). The S protein of MERS-CoV contains a dibasic motif of the sequence R-X-X-R at both S1/S2 and S2' sites. However, it is still controversial whether MERS-CoV is activated by furin in human airway epithelial cells (38, 39, 40, 41). Other proteases such as the serine protease matriptase/ST14, which also prefers sequences with arginine in the P1 and P4 position, might be involved. Matriptase is expressed in a broad range of cells and tissues and has been shown to activate the HA of H9N2 influenza A viruses possessing the cleavage site motif R-S-S-R ((42), reviewed in reference 11). Interestingly, a study by Park et al. indicated that cleavage of MERS-CoV S by furin or other proprotein



convertases at the S1/S2 site takes place in virus-producing cells before virus release and can impact the cellular localization of membrane fusion and virus entry into a new cell (43). Cleavage of MERS-CoV at the S1/S2 site was postulated as a prerequisite for subsequent cleavage of S at the S2' site by host proteases present at the surface or in early endosomes of human airway cells, thus facilitating virus entry independent of S cleavage by cathepsins in the late endosome. However, other HCoVs, including the 2002 SARS-CoV, are reportedly released with non-cleaved S from infected cells. Hence, S cleavage at both sites, S1/S2 and S2', has to take place at the stage of entry of these viruses.

The present study demonstrates that TMPRSS2 and furin are promising drug targets for the treatment of COVID-19. Furin and/or TMPRSS2 inhibitors could be used alone or in combination to target either or both of these proteases. The TMPRSS2 inhibitors MI-432 and MI-1900 as well as the furin inhibitor MI-1851 provide promising compounds for further drug development. MI-1900 and MI-1851 markedly reduced virus titers even at 72 h p.i., although the cells were treated only once after the inoculum was removed. In aprotinin- or MI-432-treated cells, an increase in viral titers was observed at 48 h p.i., and at 72 h p.i., virus titers were similar to control cells. An additional treatment of cells with protease inhibitors at 24 h p.i. may well have supported efficient blockage of virus inhibition and multiplication at later time points. This needs to be investigated in more detail in future studies. In search for suitable antiviral therapies against SARS-CoV-2 infections, protease inhibitors that have been approved for other applications may be promising for drug repurposing to treat COVID-19. Aprotinin is a broad range serine protease inhibitor isolated from bovine lung, used as a fibrinolysis inhibitor to reduce perioperative bleeding (reviewed in reference 44) and has long been known to inhibit influenza A virus activation and replication in cell culture and in mice in vivo (30). In a clinical trial, inhalation of aerosolized aprotinin in patients with influenza and parainfluenza markedly reduced the duration of symptoms without causing side effects (30). Thus, aprotinin is an inhibitor of TMPRSS2 worthy of consideration for further testing and possible development as a therapeutic treatment for COVID-19. Another promising TMPRSS2 inhibitor candidate for COVID-19 treatment is the broad range protease inhibitor camostat mesylate, which is approved for the treatment of pancreatitis (45, 46). Camostat mesylate has been shown to efficiently inhibit replication of different CoV in cell culture and experimentally infected mice (35, 47, 48). Recently, Hoffmann et al (2020) (20) showed that pretreatment of human Caco-2 colon cells and human airway cells with camostat mesylate markedly reduced entry of SARS-CoV-2 as well as vesicular stomatitis virus pseudotypes containing the SARS-CoV-2 S protein (20).

However, it should be noted that all of these compounds inhibit numerous trypsin-like serine proteases and thus may cause various adverse effects. A specific inhibition of TMPRSS2 activity during an acute SARS-CoV-2 infection would provide the most promising approach to reduce side effects by inhibiting virus activation by host cell proteases. TMPRSS2-deficient mice show no discernible phenotype, indicating functional redundancy or compensation of physiological functions by other protease(s) in the host (13). Unfortunately, there is no crystal structure of TMPRSS2 available so far, which prohibits a rational structure-based design of more efficient inhibitors of this protease. However, first homology models have

been established, which may help for the development of improved TMPRSS2 inhibitors in the future (49, 50 Preprint).

PPMO are highly selective inhibitors of target gene expression. They bind to a complementary sequence in target mRNA and can affect gene expression by steric blockage of translation initiation or pre-mRNA splicing. The demonstration of T-ex5 PPMO efficacy in the present study suggests that reducing TMPRSS2 expression by use of an mRNA-directed approach in general and by PPMO in particular is worthy of further consideration. Importantly, in various experimental animal models of other respiratory virus infections and disease, PPMO were able to be transported to lung tissue after intranasal administration and produced strong reductions in virus growth and virus-induced pathology (51, 52, 53, 54).

Very effective furin inhibitors containing a C-terminal 4-amidinobenzylamide residue have been developed in recent years. Several of these analogs have been successfully used to inhibit the replication of numerous furin dependent human pathogenic viruses such as H5N1 influenza A virus, Chikungunya virus, West Nile virus and dengue-2 virus, mumps virus or respiratory syncytial virus (reviewed in references 49, 55, and 56). So far, these inhibitors have been used only in virus-infected cell cultures and not in animal models. However, the less potent furin inhibitor hexa-D-arginine has been used in mice and rats and protected them against *P. aeruginosa* exotoxin A and anthrax toxemia (57, 58). Therefore, it can be speculated that a specific furin inhibition in the respiratory tract and lungs by inhalative treatment of, for example, MI-1851 or structurally related compounds could be possible without severe side reactions, despite the many physiological functions of furin.

Here, the combination of the TMPRSS2 inhibitors aprotinin or MI-432 with furin inhibitor MI-1851 showed enhanced antiviral activity against SARS-CoV-2 in human airway cells and supported strong reduction of virus multiplication at lower doses compared with treatment with each inhibitor alone. Therefore, the combination of TMPRSS2 and furin inhibitors provides a promising therapeutic strategy for treatment of SARS-CoV-2 infections that not only may enhance antiviral effects but may also reduce drug toxicity and undesirable side effects by allowing reductions of the inhibitor doses. Notably, inhibition of TMPRSS2 and furin acts on the same target and our data show that inhibition of S cleavage at one of the two sites is sufficient to suppress SARS-CoV-2 replication by reducing the production of infectious progeny virus containing inactive S. Thus, the combination of TMPRSS2 and furin inhibitors can act synergistically until S cleavage at one or two sites is prevented. The combination of protease inhibitors with antiviral compounds provides an approach that may produce yet more synergistic antiviral activity at lower drug doses and may furthermore exclude the development of drug-resistant viruses. The combination of TMPRSS2 and furin inhibitors, respectively, with the neuraminidase inhibitor oseltamivir carboxylate has been shown to block influenza A virus replication in human airway cells at remarkably lower concentration of each inhibitor as compared with single inhibitor treatment (59). Combination of a furin inhibitor with oseltamivir carboxylate and the antiviral compounds ribavirin and favipiravir, respectively, efficiently blocked multicycle replication of HPAIV of subtype H5N1 and H7N1 in cell cultures (60, 61). Thus, combination of protease inhibitors (e.g., aprotinin or camostat) and antivirals provides a promising strategy for the treatment of COVID-19 and should be tested in cell cultures and animal models.



In summary, we demonstrate that TMPRSS2 and furin are essential for activation and multiplication of the novel emerged SARS-CoV-2 in human airway epithelial cells and provide promising drug targets for treatment of COVID-19. TMPRSS2 and furin have been shown to be involved in the proteolytic activation of a broad range of viruses. However, the development of host protease inhibitors as a preventative and/or therapeutic strategy for the treatment of virus infections has been minimal to date. Our data demonstrate the high potential of protease inhibitors as drugs for SARS-CoV-2 treatment and highlight the rationale of drug development and repurposing of host protease inhibitors for the treatment of virus infections in general and emerging CoV infections in particular.

Materials and Methods

Cells

Calu-3 human airway epithelial cells (HTB55; ATCC) were cultured in DMEM-Ham F-12 medium (1:1) (Gibco) supplemented with 10% FCS, penicillin, streptomycin, and glutamine, with fresh culture medium replenished every 2–3 d. Vero E6 (CRL-1586; ATCC) and HEK293 (CRL-1573; ATCC) cells were maintained in DMEM supplemented with 10% FCS, antibiotics, and glutamine.

Virus and plasmids

Experiments with SARS-CoV-2 were performed under biosafety level 3 (BSL-3) conditions. The virus used in this study was SARS-CoV-2 isolate Munich 929 (kindly provided by Christian Drosten, Institute of Virology, Charité Universitätsmedizin Berlin). Virus stock was propagated on Vero E6 cells in DMEM medium with 1% FCS for 72 h. Cell supernatant was cleared by low-speed centrifugation and stored at -80°C .

The cDNA encoding the SARS-CoV-2 spike protein of isolate Wuhan-Hu-1 (GenBank accession number [MN908947](https://doi.org/10.1016/j.cels.2020.07.005); codon-optimized, sequence available upon request) with a C-terminal Myc-6xHis-tag was synthesized at Eurofins and subcloned into the pCAGGS expression plasmid using XhoI and NheI restriction sites (pCAGGS-S-Myc-6xHis). Expression plasmid pCAGGS-TMPRSS2 encoding the cDNA of human TMPRSS2 has been described previously (14).

Antibodies

A polyclonal serum against 2002 SARS-CoV was generated by immunization of rabbits with inactivated SARS-CoV. A monoclonal mouse antibody against the C-terminal Myc-tag was purchased from Cell Signaling Technology (2276S). A monoclonal mouse anti- β actin antibody was purchased from Abcam (ab6276). HRP-conjugated secondary antibodies were purchased from DAKO.

PPMO

Phosphorodiamidate morpholino oligomers (PMOs) were synthesized at Gene Tools LLC. PMO sequences (5'–3') were CAGAGTTG-GAGCACTTGCTGCCCA for T-ex5 and CCTCTACCTCAGTTACAATTTATA for scramble. The cell-penetrating peptide (RXR)4 (where R is

arginine and X is 6-aminohexanoic acid) was covalently conjugated to the 3' end of each PMO through a noncleavable linker, to produce peptide-PMO (PPMO), by methods described previously (62).

Protease inhibitors

Aprotinin was purchased from AppliChem and the cysteine protease inhibitor E64d from Sigma-Aldrich (E8640). The synthetic inhibitors of TMPRSS2 and furin were synthesized in-house according to previous methods (29, 63). Stock solutions of protease inhibitors were prepared in double distilled water (aprotinin, MI-432, and MI-1851) or sterile DMSO (MI-1900 and E64d) and stored at -20°C .

Synthesis of FRET substrates

The peptides were synthesized by automated solid phase peptide synthesis on a Syro 2000 synthesizer (MultiSynTech GmbH) using ~ 100 mg Rink-amide-MBHA resin (loading 0.68 mmol/g) for each 2 ml reaction vessel and a standard Fmoc-protocol with double couplings (approximately fourfold excess of Fmoc amino acid, HOBt and HBTU, respectively, and 8 equiv. DIPEA, 2×2 h coupling time) as described recently (64). After final coupling of Boc-2-aminobenzoic acid, the resin was washed with 20% piperidine in DMF (5 and 15 min) to remove an acylation on the 3-nitrotyrosine (65). The peptides were cleaved from the resin and deprotected by a mixture of TFA/triisopropylsilane/water (95/2.5/2.5, vol/vol/v) over 2 h at RT, followed by precipitation in cold diethyl ether. All peptides were purified by preparative reversed-phase HPLC to more than 95% purity based on the detection at 220 nm and finally obtained as lyophilized TFA salts.

Enzyme kinetic measurements with recombinant soluble human furin

The measurements were performed in black 96-well plates (Nunc) at RT with a microplate reader (Safire2, Tecan) at λ_{ex} 320 nm and λ_{em} 405 nm. Each well contained 20 μl of the substrate solution (dissolved in water) and 150 μl buffer (100 mM Hepes, 0.2% Triton X-100, 2 mM CaCl_2 , 0.02% Natriumazid, and 1 mg/ml BSA, pH 7.0). The measurements were started by addition of 20 μl furin (66) solution (0.5 nM in assay). The measurements were performed for 5 min, and the steady-state rates were calculated from the slopes of the progress curves.

RNA isolation, and RT-PCR analysis of exon skipping

For analysis of TMPRSS2-mRNA from PPMO-treated Calu-3 cells, cells were incubated with the indicated concentrations (25 μM) of T-ex5 or scramble PPMO or without PPMO in PPMO medium (DMEM supplemented with 0.1% BSA, antibiotics, and glutamine) for 24 h. Total RNA was isolated at the indicated time points using the RNeasy Mini Kit (QIAGEN) according to the manufacturer's protocol. RT-PCR was carried out with total RNA using the one-step RT-PCR kit (QIAGEN) according to the supplier's protocol. To analyze TMPRSS2-mRNAs for exon skipping, primers TMPRSS2-108fwd (5'-CTA CGA GGT GCA TCC-3') and TMPRSS2-1336rev (5'-CCA GAG GCC CTC CAG CGT CAC CCT GGC AA-3') designed to amplify a full-length PCR product of



1,228 bp from control cells and a shorter PCR fragment of about 1,100 bp lacking exon 5 from T-ex5-treated cells were used (25). RT-PCR products were resolved on a 0.8% agarose gel stained with ethidium bromide.

Infection of cells and multicycle virus replication in the presence of protease inhibitors or PPMO

SARS-CoV-2 infection experiments of Calu-3 cells were performed in serum-free DMEM supplemented with glutamine and antibiotics (DMEM++). For analysis of multicycle replication kinetics Calu-3 cells were seeded in 12-well plates and grown to 90% confluence. Cells were then inoculated with virus at an MOI of 0.001 in DMEM++ for 1 h 30 min, washed with PBS, and incubated in DMEM supplemented with 3% FCS, glutamine, and antibiotics (DMEM+++) with or without addition of protease inhibitors or DMSO to the medium for 72 h. At 16, 24, 48, and 72 h postinfection (p.i.), supernatants were collected, and viral titers were determined by tissue culture infection dose 50% (TCID₅₀) titration as described below. In addition, cells were fixed and immunostained against viral proteins as described below at 72 h p.i. to evaluate virus spread and virus-induced CPE.

For PPMO treatment, Calu-3 cells were incubated with 25 μ M T-ex5 or scramble PPMO or remained untreated in PPMO medium for 24 h before infection. Cells were infected as described above and incubated in DMEM+++ without PPMO for 72 h.

Virus titration by TCID₅₀

Viral supernatants were serially diluted in DMEM++. Each infection time point was titrated in four replicates from 5¹ to 5¹¹. Subsequently, 100 μ l of each virus dilution were transferred to Calu-3 cells grown in 96-well plates containing 100 μ l DMEM+++ and incubated for 72 h. Viral titers were determined with Spearman and Kärber algorithm described in reference 67.

Transient expression of SARS-CoV-2 S protein in HEK293 cells

For transient expression of SARS-CoV-2 S protein 60% confluent HEK293 cells were co-transfected with 1.6 μ g of pCAGGS-S-Myc-6xHis and either 15 ng of empty pCAGGS vector or pCAGGS-TMPRSS2 using Lipofectamine 2000 (Invitrogen) according to the manufacturer's protocol for 48 h. Cells were harvested and centrifuged for 5 min at 8,000g. Subsequently, cells were subjected to SDS-PAGE and Western blot analysis as described below.

SDS-PAGE and Western blot analysis

Cells were washed with PBS, lysed in CellLytic M buffer (Sigma-Aldrich) with a protease inhibitor cocktail (P8340; Sigma-Aldrich), resuspended in reducing SDS-PAGE sample buffer, and heated at 95°C for 10 min. Proteins were subjected to SDS-PAGE (10% acrylamide gel), transferred to a polyvinylidene difluoride (PVDF) membrane (GE Healthcare), and detected by incubation with primary antibodies and species-specific peroxidase-conjugated secondary antibodies. Proteins were visualized using the ChemiDoc XRS system with Image Lab software (Bio-Rad).

Immunohistochemical staining and microscopy

To visualize viral spread in SARS-CoV-2-infected Calu-3 cells, immunohistochemical staining was performed. Calu-3 cells were fixed 72 h postinfection in 4% PFA for 36 h at 4°C. The cells were permeabilized with 0.3% Triton X-100 (Sigma-Aldrich) for 20 min at RT. The cells were incubated with a polyclonal rabbit serum against 2002 SARS-CoV for 1 h 30 min at RT, a species-specific peroxidase-conjugated secondary antibody for 1 h at RT and subsequently stained using the peroxidase substrate KPL TrueBlue (Seracare) and further analyzed on a Leica Dmi1 microscope.

Cell viability assay

Cell viability was assessed by measuring the cellular ATP content using the CellTiterGlo luminescent cell viability assay (Promega). Calu-3 cells grown in 96-well plates were incubated with 25 μ M of each PPMO or 50 μ M of each of the protease inhibitors for 24 and 72 h, respectively. Subsequently, cells were incubated with the substrate according to the manufacturer's protocol. Luminescence was measured using a 96-well plate (Nunc) with a luminometer (Centro LB 960; Berthold Technologies). The absorbance values of PPMO- or inhibitor-treated cells were converted to percentages by comparison with untreated control cells, which were set at 100% cell viability.

Data Availability

Data supporting the findings of this study are available within the article, its supplementary materials, or if stated otherwise available from the corresponding author (Eva Böttcher-Friebertshäuser, friebertshaeuser@staff.uni-marburg.de) upon reasonable request.

Supplementary Information

Supplementary Information is available at <https://doi.org/10.26508/lsa.202000786>.

Acknowledgements

We are grateful to Christian Drosten for providing the virus. We thank Iris Lindberg for providing recombinant furin. We also thank Stephan Becker for support of this study. This work was funded by the LOEWE Center DRUID (project D1), by the German Center for Infection Research (DZIF), and by the Deutsche Forschungsgemeinschaft (DFG, German Research Foundation) SFB 1021 (project B07). We thank Diana Kruhl and Dirk Becker for excellent technical assistance.

Author Contributions

D Bestle: data curation, formal analysis, validation, investigation, methodology, and writing—original draft, review, and editing. MR Heindl: data curation, formal analysis, validation, investigation, methodology, and writing—original draft, review, and editing.



H Limburg: data curation, formal analysis, validation, investigation, methodology, and writing—original draft, review, and editing.

T Van Lam van: data curation, formal analysis, investigation, and methodology.

O Pilgram: data curation, formal analysis, investigation, and methodology.

H Moulton: conceptualization, resources, data curation, formal analysis, investigation, and methodology.

DA Stein: conceptualization, resources, and methodology.

K Hardes: conceptualization, resources, formal analysis, and methodology.

M Eickmann: conceptualization, resources, formal analysis, and methodology.

O Dolnik: resources and methodology.

C Rohde: resources and methodology.

H-D Klenk: conceptualization, resources, methodology, and writing—review and editing.

W Garten: conceptualization and writing—review and editing.

T Steinmetzer: conceptualization, resources, data curation, formal analysis, supervision, funding acquisition, and writing—original draft, review, and editing.

E Böttcher-Friebertshäuser: conceptualization, resources, data curation, formal analysis, supervision, funding acquisition, validation, investigation, methodology, project administration, and writing—original draft, review, and editing.

Conflict of Interest Statement

The authors declare that they have no conflict of interest.

References

- Follis KK, York J, Nunberg JH (2006) Furin cleavage of the SARS coronavirus spike glycoprotein enhances cell-cell fusion but does not affect virion entry. *Virology* 350: 358–369. doi:10.1016/j.virol.2006.02.003
- Bosch BJ, Bartelink W, Rottier PJ (2008) Cathepsin L functionally cleaves the severe acute respiratory syndrome coronavirus class I fusion protein upstream of rather than adjacent to the fusion peptide. *J Virol* 82: 8887–8890. doi:10.1128/jvi.00415-08
- Belouzard S, Chu VC, Whittaker GR (2009) Activation of the SARS coronavirus spike protein via sequential proteolytic cleavage at two distinct sites. *Proc Natl Acad Sci U S A* 106: 5871–5876. doi:10.1073/pnas.0809524106
- Madu IG, Roth SL, Belouzard S, Whittaker GR (2009) Characterization of a highly conserved domain within the severe acute respiratory syndrome coronavirus spike protein S2 domain with characteristics of a viral fusion peptide. *J Virol* 83: 7411–7421. doi:10.1128/jvi.00079-09
- Walls AC, Tortorici MA, Bosch BJ, Frenz B, Rottier PJM, DiMaio F, Rey FA, Veesler D (2016) Cryo-electron microscopy structure of a coronavirus spike glycoprotein trimer. *Nature* 531: 114–117. doi:10.1038/nature16988
- Heald-Sargent T, Gallagher T (2012) Ready, set, fuse! The coronavirus spike protein and acquisition of fusion competence. *Viruses* 4: 557–580. doi:10.3390/v4040557
- Millet JK, Whittaker GR (2015) Host cell proteases: Critical determinants of coronavirus tropism and pathogenesis. *Virus Res* 202: 120–134. doi:10.1016/j.virusres.2014.11.021
- Hoffmann M, Hofmann-Winkler H, Pöhlmann S (2018) Priming time: How cellular proteases arm coronavirus spike proteins. In *Activation of*

Viruses by Host Proteases, Böttcher-Friebertshäuser E, Garten W, Klenk H (eds), pp 71–98. Cham: Springer.

- Klenk HD, Garten W (1994) Host cell proteases controlling virus pathogenicity. *Trends Microbiol* 2: 39–43. doi:10.1016/0966-842x(94)90123-6
- Garten W (2018) Characterization of proprotein convertases and their involvement in virus propagation. In *Activation of Viruses by Host Proteases*, Böttcher-Friebertshäuser E, Garten W, Klenk H (eds), pp 205–248. Cham: Springer.
- Böttcher-Friebertshäuser E (2018) Membrane-anchored serine proteases: Host cell factors in proteolytic activation of viral glycoproteins. In *Activation of Viruses by Host Proteases*, Böttcher-Friebertshäuser E, Garten W, Klenk H (eds), pp 153–203. Cham: Springer.
- Bugge TH, Antalis TM, Wu Q. Type II transmembrane serine proteases (2009) *J Biol Chem* 284: 23177–23181. doi:10.1074/jbc.r109.021006
- Kim TS, Heinlein C, Hackman RC, Nelson PS (2006) Phenotypic analysis of mice lacking the Tmprss2-encoded protease. *Mol Cell Biol* 26: 965–975. doi:10.1128/mcb.26.3.965-975.2006
- Böttcher E, Matrosovich T, Beyerle M, Klenk HD, Garten W, Matrosovich M (2006) Proteolytic activation of influenza viruses by serine proteases TMPRSS2 and HAT from human airway epithelium. *J Virol* 80: 9896–9898. doi:10.1128/JVI.01118-06
- Hatesuer B, Bertram S, Mehnert N, Bahgat MM, Nelson PS, Pöhlmann S, Schughart K (2013) Tmprss2 is essential for influenza H1N1 virus pathogenesis in mice. *PLoS Pathog* 9: e1003774. doi:10.1371/journal.ppat.1003774
- Tarnow C, Engels G, Arendt A, Schwalm F, Sediri H, Preuss A, Nelson PS, Garten W, Klenk HD, Gabriel G, et al (2014) TMPRSS2 is a host factor that is essential for pneumotropism and pathogenicity of H7N9 influenza A virus in mice. *J Virol* 88: 4744–4751. doi:10.1128/jvi.03799-13
- Sakai K, Ami Y, Tahara M, Kubota T, Anraku M, Abe M, Nakajima N, Sekizuka T, Shirato K, Suzuki Y, et al (2014) The host protease TMPRSS2 plays a major role in in vivo replication of emerging H7N9 and seasonal influenza viruses. *J Virol* 88: 5608–5616. doi:10.1128/jvi.03677-13
- Iwata-Yoshikawa N, Okamura T, Shimizu Y, Hasegawa H, Takeda M, Nagata N (2019) TMPRSS2 contributes to virus spread and immunopathology in the airways of murine models after coronavirus infection. *J Virol* 93: e01815–e01818. doi:10.1128/jvi.01815-18
- Rockwell NC, Kysan DJ, Komiyama T, Fuller RS (2002) Precursor processing by kex2/furin proteases. *Chem Rev* 102: 4525–4548. doi:10.1021/cr010168i
- Hoffmann M, Kleine-Weber H, Schroeder S, Krüger N, Herrler T, Erichsen S, Schiergens TS, Herrler G, Wu NH, Nitsche A, et al (2020) SARS-CoV-2 cell entry depends on ACE2 and TMPRSS2 and is blocked by a clinically proven protease inhibitor. *Cell* S0092-8674: 30229–30234. doi:10.1016/j.cell.2020.02.052
- Matsuyama S, Nao N, Shirato K, Kawase M, Saito S, Takayama I, Nagata N, Sekizuka T, Katoh H, Kato F, et al (2020) Enhanced isolation of SARS-CoV-2 by TMPRSS2-expressing cells. *Proc Natl Acad Sci U S A* 117: 7001–7003. doi:10.1073/pnas.2002589117
- Coutard B, Valle C, de Lamballerie X, Canard B, Seidah NG, Decroly E (2020) The spike glycoprotein of the new coronavirus 2019-nCoV contains a furin-like cleavage site absent in CoV of the same clade. *Antiviral Res* 176: 104742. doi:10.1016/j.antiviral.2020.104742
- Walls AC, Park YJ, Tortorici MA, Wall A, McGuire AT, Veesler D (2020) Structure, function, and antigenicity of the SARS-CoV-2 spike glycoprotein. *Cell* S0092-8674: 30262-2. doi:10.1016/j.cell.2020.02.058
- Kassell B, Radicevic M, Ansfield MJ, Laskowski M (1965) The basic trypsin inhibitor of bovine pancreas. IV. The linear sequence of the 58 amino acids. *Biochem Biophys Res Commun* 18: 255–258. doi:10.1016/0006-291x(65)90749-7
- Böttcher-Friebertshäuser E, Stein DA, Klenk HD, Garten W (2011) Inhibition of influenza virus infection in human airway cell cultures by



- an antisense peptide-conjugated morpholino oligomer targeting the hemagglutinin-activating protease TMPRSS2. *J Virol* 85: 1554–1562. doi:10.1128/jvi.01294-10
26. Stein DA (2008) Inhibition of RNA virus infections with peptide-conjugated morpholino oligomers. *Curr Pharm Des* 14: 2619–2634. doi:10.2174/138161208786071290
 27. Moulton HM, Moulton JD (2010) Morpholinos and their peptide conjugates: Therapeutic promise and challenge for duchenne muscular dystrophy. *Biochim Biophys Acta* 1798: 2296–2303. doi:10.1016/j.bbamer.2010.02.012
 28. Limburg H, Harbig A, Bestle D, Stein DA, Moulton HM, Jaeger J, Janga H, Harges K, Koepke J, Schulte L, et al (2019) TMPRSS2 is the major activating protease of influenza A virus in primary human airway cells and influenza B virus in human type II pneumocytes. *J Virol* 93: e00649-19. doi:10.1128/jvi.00649-19
 29. Hammami M, Rühmann E, Maurer E, Heine A, Gütschow M, Klebe G, Steinmetzer T (2012) New 3-amidinophenylalanine-derived inhibitors of matrixprotease. *MedChemComm* 3: 807–813. doi:10.1039/c2md20074k
 30. Zhirnov OP, Klenk HD, Wright PF (2011) Aprotinin and similar protease inhibitors as drugs against influenza. *Antiviral Res* 92: 27–36. doi:10.1016/j.antiviral.2011.07.014
 31. Meyer D, Sielaff F, Hammami M, Böttcher-Friebertshäuser E, Garten W, Steinmetzer T (2013) Identification of the first synthetic inhibitors of the type II transmembrane serine protease TMPRSS2 suitable for inhibition of influenza virus activation. *Biochem J* 452: 331–343. doi:10.1042/bj20130101
 32. Simmons G, Gosalia DN, Rennekamp AJ, Reeves JD, Diamond SL, Bates P (2005) Inhibitors of cathepsin L prevent severe acute respiratory syndrome coronavirus entry. *Proc Natl Acad Sci U S A* 102: 11876–11881. doi:10.1073/pnas.0505577102
 33. Shirato K, Kanou K, Kawase M, Matsuyama S (2016) Clinical isolates of human coronavirus 229E bypass the endosome for cell entry. *J Virol* 91: e01387-16. doi:10.1128/jvi.01387-16
 34. Shirato K, Kawase M, Matsuyama S (2018) Wild-type human coronaviruses prefer cell-surface TMPRSS2 to endosomal cathepsins for cell entry. *Virology* 517: 9–15. doi:10.1016/j.virol.2017.11.012
 35. Zhou Y, Vedantham P, Lu K, Agudelo J, Carrion R, Jr, Nunneley JW, Barnard D, Pöhlmann S, McKerrow JH, Renslo AR, et al (2015) Protease inhibitors targeting coronavirus and filovirus entry. *Antiviral Res* 116: 76–84. doi:10.1016/j.antiviral.2015.01.011
 36. Garten W, Klenk HD (2008) Cleavage activation of the influenza virus hemagglutinin and its role in pathogenesis. In *Avian Influenza*, Klenk HD, Matrosovich MN, Stech J (eds), pp 156–167. Basel: Karger.
 37. Cheng J, Zhao Y, Xu G, Zhang K, Jia W, Sun Y, Zhao J, Xue J, Hu Y, Zhang G (2019) The S2 subunit of QX-type infectious bronchitis coronavirus spike protein is an essential determinant of neurotropism. *Viruses* 11: E972. doi:10.3390/v11100972
 38. Gierer S, Müller MA, Heurich A, Ritz D, Springstein BL, Karsten CB, Schendzielorz A, Gnirß K, Drosten C, Pöhlmann S (2015) Inhibition of proprotein convertases abrogates processing of the middle eastern respiratory syndrome coronavirus spike protein in infected cells but does not reduce viral infectivity. *J Infect Dis* 211: 889–897. doi:10.1093/infdis/jiu407
 39. Burkard C, Verheije MH, Wicht O, van Kasteren SI, van Kuppeveld FJ, Haagmans BL, Peikmans L, Rottier PJ, Bosch BJ, de Haan CA (2014) Coronavirus cell entry occurs through the endo-/lysosomal pathway in a proteolysis-dependent manner. *PLoS Pathog* 10: e1004502. doi:10.1371/journal.ppat.1004502
 40. Matsuyama S, Shirato K, Kawase M, Terada Y, Kawachi K, Fukushi S, Kamitani W (2018) Middle East respiratory syndrome coronavirus spike protein is not activated directly by cellular furin during viral entry into target cells. *J Virol* 92: e00683-18. doi:10.1128/jvi.00683-18
 41. Millet JK, Whittaker GR (2014) Host cell entry of Middle East respiratory syndrome coronavirus after two-step, furin-mediated activation of the spike protein. *Proc Natl Acad Sci U S A* 111: 15214–15219. doi:10.1073/pnas.1407087111
 42. Baron J, Tarnow C, Mayoli-Nüssle D, Schilling E, Meyer D, Hammami M, Schwalm F, Steinmetzer T, Guan Y, Garten W, et al (2013) Matrixprotease, HAT, and TMPRSS2 activate the hemagglutinin of H9N2 influenza A viruses. *J Virol* 87: 1811–1820. doi:10.1128/jvi.02320-12
 43. Park JE, Li K, Barlan A, Fehr AR, Perlman S, McCray PB, Jr, Gallagher T (2016) Proteolytic processing of Middle East respiratory syndrome coronavirus spikes expands virus tropism. *Proc Natl Acad Sci U S A* 113: 12262–12267. doi:10.1073/pnas.1608147113
 44. Steinmetzer T, Pilgram O, Wenzel BM, Wiedemeyer SJA (2020) Fibrinolysis inhibitors: Potential drugs for the treatment and prevention of bleeding. *J Med Chem* 63: 1445–1472. doi:10.1021/acs.jmedchem.9b01060
 45. Tanaka N, Tsuchiya R, Ishii K (1979) Comparative clinical study of FOY and Trasylol in acute pancreatitis. *Adv Exp Med Biol* 120B: 367–378.
 46. Midgley I, Hood AJ, Proctor P, Chasseaud LF, Irons SR, Cheng KN, Brindley CJ, Bonn R (1994) Metabolic fate of 14C-camostat mesylate in man, rat and dog after intravenous administration. *Xenobiotica* 24: 79–92. doi:10.3109/00498259409043223
 47. Kawase M, Shirato K, van der Hoek L, Taguchi F, Matsuyama S (2012) Simultaneous treatment of human bronchial epithelial cells with serine and cysteine protease inhibitors prevents severe acute respiratory syndrome coronavirus entry. *J Virol* 86: 6537–6545. doi:10.1128/jvi.00094-12
 48. Shirato K, Kawase M, Matsuyama S (2013) Middle East respiratory syndrome coronavirus infection mediated by the transmembrane serine protease TMPRSS2. *J Virol* 87: 12552–12561. doi:10.1128/jvi.01890-13
 49. Steinmetzer T, Harges K (2018) The Antiviral Potential of host protease inhibitors. In *Activation of Viruses by Host Proteases*, Böttcher-Friebertshäuser E, Garten W, Klenk H (eds), pp 279–325. Cham: Springer.
 50. Rensi S, Altman RB, Liu T, Lo YC, McInnes G, Derry A, Keys A. (2020) Homology modeling of TMPRSS2 yields candidate drugs that may inhibit entry of SARS-CoV-2 into human. *ChemRxiv*. <https://chemrxiv.org/articles/Homolog>. doi:10.26434/chemrxiv.12009582 (Preprint posted March 20, 2020).
 51. Gabriel G, Nordmann A, Stein DA, Iversen PL, Klenk HD (2007) Morpholino oligomers targeting PB1 and NP genes enhance survival of mice infected with highly pathogenic influenza A H7N9 virus. *J Gen Virol* 89: 939–948. doi:10.1099/vir.0.83449-0
 52. Lupfer C, Stein DA, Mourich DV, Tepper SE, Iversen PL, Pasty M (2008) Inhibition of influenza A H3N8 infections in mice by morpholino oligomers. *Arch Virol* 153: 929–937. doi:10.1007/s00705-008-0067-0
 53. Lai SH, Stein DA, Guerrero-Plata A, Liao SL, Ivancic T, Hong C, Iversen PL, Casola A, Garofalo RP (2008) Inhibition of respiratory syncytial virus infections with morpholino oligomers in cell cultures and in mice. *Mol Ther* 16: 1120–1128. doi:10.1038/mt.2008.81
 54. Opriessnig T, Patel D, Wang R, Halbur PG, Meng XJ, Stein DA, Zhang YJ (2011) Inhibition of porcine reproductive and respiratory syndrome virus infection in piglets by a peptide-conjugated morpholino oligomer. *Antiviral Res* 91: 36–42. doi:10.1016/j.antiviral.2011.04.012
 55. Krüger N, Sauder C, Huttel S, Papias J, Voigt K, Herrler G, Harges K, Steinmetzer T, Orvell C, Drexler JF, et al (2018) Entry, replication, immune evasion, and neurotoxicity of synthetically engineered bat-borne mumps virus. *Cell Rep* 25: 312–320. doi:10.1016/j.celrep.2018.09.018
 56. Van Lam van T, Ivanova T, Harges K, Heindl MR, Morty RE, Böttcher-Friebertshäuser E, Lindberg I, Than ME, Dahms SO, Steinmetzer T (2019) Design, synthesis, and characterization of macrocyclic inhibitors of the proprotein convertase furin. *ChemMedChem* 14: 673–685. doi:10.1002/cmdc.201800807
 57. Sarac MS, Cameron A, Lindberg I (2002) The furin inhibitor hexa-D-arginine blocks the activation of *Pseudomonas aeruginosa* exotoxin A in vivo. *Infect Immun* 70: 7136–7139. doi:10.1128/iai.70.12.7136-7139.2002



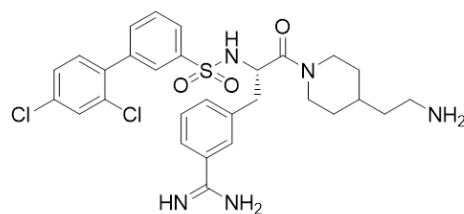
58. Sarac MS, Peinado JR, Leppla SH, Lindberg I (2004) Protection against anthrax toxemia by hexa-D-arginine in vitro and in vivo. *Infect Immun* 72: 602–605. doi:[10.1128/iai.72.1.602-605.2004](https://doi.org/10.1128/iai.72.1.602-605.2004)
59. Böttcher-Friebertshäuser E, Lu Y, Meyer D, Sielaff F, Steinmetzer T, Klenk HD, Garten W (2012) Hemagglutinin activating host cell proteases provide promising drug targets for the treatment of influenza A and B virus infections. *Vaccine* 30: 7374–7380. doi:[10.1016/j.vaccine.2012.10.001](https://doi.org/10.1016/j.vaccine.2012.10.001)
60. Lu Y, Harges K, Dahms SO, Böttcher-Friebertshäuser E, Steinmetzer T, Than ME, Klenk HD, Garten W (2015) Peptidomimetic furin inhibitor MI-701 in combination with oseltamivir and ribavirin efficiently blocks propagation of highly pathogenic avian influenza viruses and delays high level oseltamivir resistance in MDCK cells. *Antiviral Res* 120: 89–100. doi:[10.1016/j.antiviral.2015.05.006](https://doi.org/10.1016/j.antiviral.2015.05.006)
61. Garten W, Braden C, Arendt A, Peitsch C, Baron J, Lu Y, Pawletko K, Harges K, Steinmetzer T, Böttcher-Friebertshäuser E (2015) Influenza virus activating host proteases: Identification, localization and inhibitors as potential therapeutics. *Eur J Cell Biol* 94: 375–383. doi:[10.1016/j.ejcb.2015.05.013](https://doi.org/10.1016/j.ejcb.2015.05.013)
62. Abes S, Moulton HM, Clair P, Prevot P, Youngblood DS, Wu RP, Iversen PL, Lebleu B (2006) Vectorization of morpholino oligomers by the (R-Ahx-R) 4 peptide allows efficient splicing correction in the absence of endosomolytic agents. *J Control Release* 116: 304–313. doi:[10.1016/j.jconrel.2006.09.011](https://doi.org/10.1016/j.jconrel.2006.09.011)
63. Harges K, Becker GL, Lu Y, Dahms SO, Köhler S, Beyer W, Sandvig K, Yamamoto H, Lindberg I, Walz L, et al (2015) Novel furin inhibitors with potent anti-infectious activity. *ChemMedChem* 10: 1218–1231. doi:[10.1002/cmdc.201500103](https://doi.org/10.1002/cmdc.201500103)
64. Harges K, Zouhir Hammamy M, Steinmetzer T (2013) Synthesis and characterization of novel fluorogenic substrates of coagulation factor XIII-A. *Anal Biochem* 442: 223–230. doi:[10.1016/j.ab.2013.07.043](https://doi.org/10.1016/j.ab.2013.07.043)
65. Singh S, Khaytin I, Botsko S, Crossley G, Plank DK, Lefievre Y, Giuffrida F, Pennington MW (2002) Addition of o-aminobenzoic acid during Fmoc solid phase synthesis of a fluorogenic substrate containing 3-nitrotyrosine. *Lett Pept Sci* 9: 221–225. doi:[10.1007/bf02538387](https://doi.org/10.1007/bf02538387)
66. Kacprzak MM, Peinado JR, Than ME, Appel J, Henrich S, Lipkind G, Houghten RA, Bode W, Lindberg I (2004) Inhibition of furin by polyarginine-containing peptides: Nanomolar inhibition by nona-D-arginine. *J Biol Chem* 279: 36788–36794. doi:[10.1074/jbc.m400484200](https://doi.org/10.1074/jbc.m400484200)
67. Hierholzer JC, Killington RA (1996) Virus isolation and quantitation. In *Virology Methods Manual*, Mahy BWJ, Kangro HO (eds), pp 24–32. London, San Diego: Academic Press.



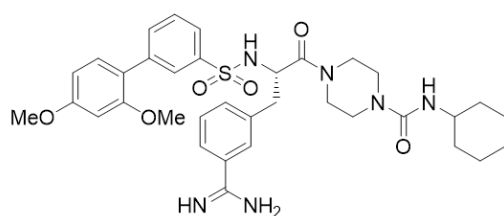
License: This article is available under a Creative Commons License (Attribution 4.0 International, as described at <https://creativecommons.org/licenses/by/4.0/>).

Figure S1

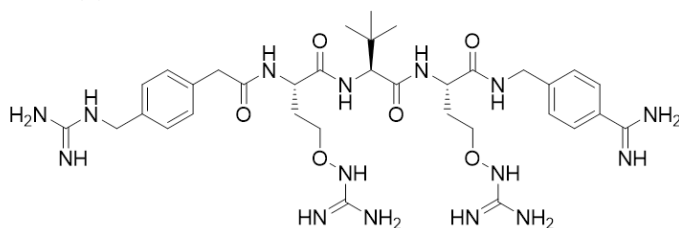
MI-432



MI-1900



MI-1851



Aprotinin

RPDFCLEPPYTGPKARIIRYFYNAKAGLCQTFVYGGCRAKRNNFKSAEDCMRTCGGA

Figure S1: Structural formulas of peptide mimetic inhibitors MI-432, MI-1900 and MI-1851 and the linear amino acid sequence of bovine aprotinin (Kassell et al., 1965).

Figure S2

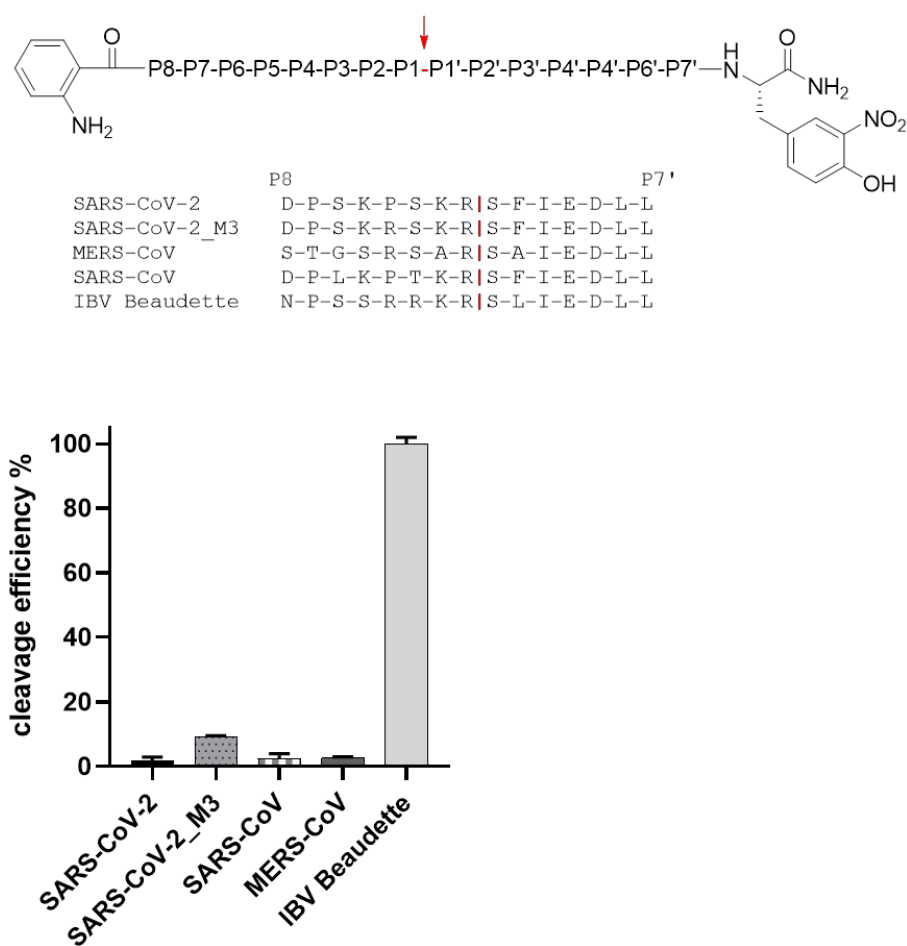


Figure S2: Cleavage analysis of SARS-CoV-2 S2' site by furin. **A)** FRET substrates of the S protein S2' sites of the indicated CoVs. M3 is a mutant of the SARS-CoV-2 S2' site with substitution of P→R in P4 position. IBV: avian infectious bronchitis virus strain Beaudette. Cleavage by furin is indicated in red. **B)** Cleavage of the FRET substrates (20 μM) by furin (0.5 nM). Cleavage efficiency of IBV Beaudette was set as 100%.

4.4 Design, synthesis, and characterization of novel fluorogenic substrates of proprotein convertases furin, PC1, PC2, PC5, and PC7

Thuy Van Lam van, Teodora Ivanova, Iris Lindberg, Eva Böttcher-Friebertshäuser, Torsten Steinmetzer, and Kornelia Harges

(Manuscript in preparation; planned for the Journal: **Analytical Biochemistry**)

Design, synthesis, and characterization of novel fluorogenic substrates of proprotein convertases furin, PC1, PC2, PC5, and PC7

Thuy Van Lam van^a, Teodora Ivanova^a, Iris Lindberg^b, Eva Böttcher-Friebertshäuser^c, Torsten Steinmetzer^a, Kornelia Harges^{a,d*}

^a Institute of Pharmaceutical Chemistry, Philipps University, Marbacher Weg 6, D-35032 Marburg, Germany

^b Department of Anatomy and Neurobiology, University of Maryland, Baltimore, Maryland 21201

^c Institute of Virology, Philipps University, Hans-Meerwein-Straße 2, D-35043 Marburg, Germany

^d Fraunhofer Institute for Molecular Biology and Applied Ecology, Ohlebergsweg 12, D-35394 Giessen, Germany

*corresponding author: Kornelia.Harges@ime.fraunhofer.de

Keywords

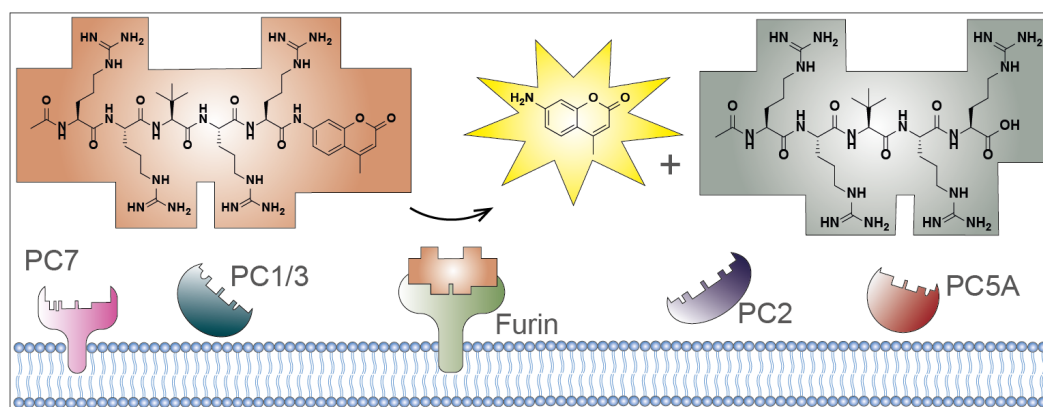
Proprotein convertases, fluorogenic substrates, furin, PC1, PC2, PC5, PC7

Abstract

Proprotein convertases (PCs) are involved in the pathogenesis of various infectious diseases such as COVID-19, which makes them promising drug targets. Most assays for basic PCs have been performed with few standard substrates, regardless of differences in cleavage efficiencies. Derived from our studies on substrate-analogue inhibitors, 11 novel substrates were synthesized and characterized with five basic PCs. H-Arg-Arg-Tle-Lys-Arg-AMC is the most efficiently cleaved furin substrate based on its k_{cat}/K_M value. For further measurements, Ac-Arg-Arg-Tle-Arg-AMC was selected because of its higher k_{cat} value. Compared to our standard conditions, the use of this improved substrate allowed the reduction of the furin concentration, which enabled K_i value determinations of previously described tight-binding inhibitors under classical conditions. Under these circumstances, for the first time a slow-binding behavior was observed for inhibitor **MI-1148**. Besides furin, the substrates were characterized with four additional basic PCs. The most efficiently cleaved PC1 substrate is Ac-Arg-Arg-Arg-Tle-Lys-Arg-AMC. The highest k_{cat}/K_M values for PC2 and PC7 were found for its N-terminally unprotected analogue, although some other substrates possess higher k_{cat} values. The highest performance constant for PC5A was found for substrate Ac-Arg-Arg-Tle-Lys-Arg-AMC. In summary, especially for furin, PC1, PC2, and PC7 suitable substrates have been identified, which can improve further measurements.

Word limit: 200 / Word count: 200

Graphical abstract



Introduction

The family of proprotein convertases (PCs) comprises nine Ca^{2+} -dependent serine endoproteases including the seven basic PCs furin, PC1, PC2, PC4, PACE4, PC5, and PC7, as well as the non-basic PCs SKI-1/S1P and PCSK9.^{1,2} Basic PCs preferentially cleave their substrates at the C-terminus of the minimal consensus sequence $\text{R/K-X}_n\text{-R/K}\downarrow$ (X_n : 0-, 2-, 4-, 6-amino acid spacer, arrow represents the cleavage site).^{2,3} Furin and PC7 are ubiquitously and PACE4 as well as PC5 widely expressed. In contrast, PC1 and PC2 are only found in secretory granules in the neuroendocrine system. Furthermore, PC4 is exclusively expressed in germ cells.² Despite the recognition of similar multibasic motifs and therefore overlapping cleavage pattern, differences in tissue distribution and subcellular localization influence the PC specificity with respect to natural substrates.⁴

PCs are involved in the processing of precursor proteins of hormones, growth factors, enzymes, transcription factors, membrane receptors, and other extracellular or serum proteins.^{2,3} Due to their crucial role, PCs are linked to numerous diseases, including but not limited to cancer, metabolic disorders, and osteoarthritis.⁵ Furthermore, during infections they are hijacked by different pathogens to cleave viral or bacterial protein precursors. Prominent examples are the activation of the spike protein of the severe acute respiratory syndrome coronavirus 2 (SARS-CoV-2) by furin or the hemagglutinin of highly pathogenic avian influenza viruses by furin and PC5.^{6,7} Therefore, the development of efficient inhibitors against these potential drug targets is of great interest.

The conventional approach to identify protease inhibitors is based on enzyme kinetic *in vitro* assays using synthetic chromogenic or fluorogenic substrates and recombinant enzymes. For basic PCs, numerous 7-amino-4-methylcoumarin (AMC) derived substrates have been successfully employed.^{8,9} Most assays have been routinely carried out with the fluorogenic substrates pyroglutamyl-Arg-Thr-Lys-Arg-AMC and Boc-Arg-Val-Arg-Arg-AMC.^{10,11} The latter belongs to one of the first described furin substrates. In contrast to tested tripeptidic Arg-AMC substrates lacking the P4 Arg, it was nearly 100-fold more efficiently cleaved by furin and hence, demonstrated the high relevance of a basic P4 residue.¹¹ This substrate was also used for measurements with purified, recombinant PC2.¹² In contrast to furin, it shows a lower affinity for PC2 with a K_M value of 131 μM and was less efficiently cleaved with a performance constant¹³ corresponding to the k_{cat}/K_M value of $6.2 \times 10^3 \text{ M}^{-1}\text{s}^{-1}$. The k_{cat}/K_M ratio can be also considered as a kind of second order rate constant, describing the reaction of the free enzyme and free substrate until reaching the transition state ES^\ddagger .¹⁴ Furthermore, several AMC substrates based on the cleavage site sequences of native and mutant prorenins were designed.¹⁵ Coupling of pyroglutamic acid (Pyr) as P5 residue provided the already mentioned substrate Pyr-Arg-Thr-Lys-Arg-AMC. In enzyme kinetic measurements with a furin preparation a k_{cat}/K_M ratio of $1.87 \times 10^4 \text{ M}^{-1}\text{s}^{-1}$ was determined for this substrate, which is approximately five times higher compared to the value obtained using Boc-Arg-Val-Arg-Arg-AMC.¹⁵ No cleavage for analogues with Glu in P2 and Phe in P4 position was observed again highlighting the relevance of the basic residues in these positions. Additional AMC substrates were used to determine differences in the substrate specificity of furin and other basic PCs. As expected, the P4 substitution within the substrate Ac-Arg-Ser-Lys-Arg-AMC by Lys or Ornithine resulted in a drop of the performance constants for furin from $8.1 \times 10^3 \text{ M}^{-1}\text{s}^{-1}$ to $1.5 \times 10^1 \text{ M}^{-1}\text{s}^{-1}$ and $2.9 \times 10^1 \text{ M}^{-1}\text{s}^{-1}$, respectively.¹⁶ The introduction of a P3 Glu also resulted in a strongly decreased k_{cat}/K_M value of $5.8 \times 10^1 \text{ M}^{-1}\text{s}^{-1}$. The effects on PC1 were similar albeit less pronounced compared to furin. To further assess the specificity of furin, elongated substrates also comprising the P6 position were tested.¹⁷ The introduction of Arg and Lys as P6 residue significantly increases the performance constants 10-fold compared to the Ala analogue. Therefore, the best substrate of this series Ac-Lys-Ala-Arg-Tyr-Lys-Arg-AMC possesses a performance constant of $2.2 \times 10^6 \text{ M}^{-1}\text{s}^{-1}$, which closely matches values reported for natural substrates. However, these hexapeptides showed a significant substrate inhibition already at relatively low concentrations in the range of 10 μM .

Besides these AMC derivatives, several FRET (fluorescence resonance energy transfer) substrates like 2-aminobenzoyl-Arg-Val-Lys-Arg-Gly-Leu-Ala-Tyr(NO₂)-Asp-OH were synthesized. In contrast to Boc-Arg-Val-Arg-Arg-AMC, its K_M value for furin is decreased by a factor of 14 and the k_{cat} value is 150-fold increased leading to a significantly improved performance constant of $7.7 \times 10^6 \text{ M}^{-1}\text{s}^{-1}$.¹⁸ Furthermore, FRET substrates covering the cleavage sites of classical substrates like hormone precursors, viral coat glycoproteins as well as bacterial protein precursor and thereby closely resembling natural substrates were tested for their cleavage by basic PCs.^{19–21} In a study by Izidoro *et al.* the best furin substrate is derived from the Rous sarcoma virus glycoprotein and possesses an excellent k_{cat}/K_M value of $3.4 \times 10^8 \text{ M}^{-1}\text{s}^{-1}$.²⁰ In comparison to most AMC substrates, these FRET substrates are more efficiently cleaved. However, the conversion of measured changes in fluorescence with such FRET substrates into concentrations is more laborious and can be hampered by a pronounced inner filter effect, especially at high substrate concentrations.²²

In our previous work with substrate analogue furin inhibitors, we found that elongation of our core segment Arg-Val-Arg-Amba with additional Arg residues in the rather distal positions P5 and P6 as well as the incorporation of Tle (*tert*-leucine) in P3 position leads to improved K_i values and therefore emphasizes the importance of these positions for furin binding.^{23–27} Similar trends with selected inhibitors were also observed for PC1 and PC2.²⁴ Therefore, we have prepared a series of 11 novel AMC substrates and characterized them with furin and the related basic PCs PC1, PC2, PC5A, and PC7. The results of these experiments are summarized in this paper.

Results

Design and synthesis of novel PC substrates

For the characterization of our first inhibitors the commercially available substrate **1**, Pyr-Arg-Thr-Lys-Arg-AMC, was used.^{23,28,29} Based on our best inhibitor at that time, Phac-Arg-Val-Arg-Amba²⁸ (K_i value 0.81 nM) substrate **2** was synthesized and used in later measurements with basic PCs.^{24–27,30} Both substrates served as reference compounds in this study. Considering the improved potency of furin inhibitors with *tert*-leucine (Tle) in P3 position compared to Val, analogues **5**, **6**, **8**, and **10–13** were synthesized to further examine the influence of this residue on substrate cleavage. Additionally, Tyr was incorporated in this position in substrate **9**, because it was previously used in a series of related AMC substrates.^{8,17}

Furthermore, numerous inhibitors possess additional basic residues in their P5-P6 segment, sometimes even in P7 and P8 position.^{23,25,31–34} The crystal structure of inhibitor H-Arg-Arg-Arg-Val-Arg-4-amidinobenzylamide²⁵ in complex with furin (PDB: 6EQX³¹) shows that the additional P5 Arg residue is bound in a well-defined S5 pocket in the active site cleft of the protease. However, due to a turn of the peptide backbone, the side chain of the N-terminal Arg in P6 position is oriented rather backwards close to the P2 side chain forming only few interactions to furin (Figure 1).³¹

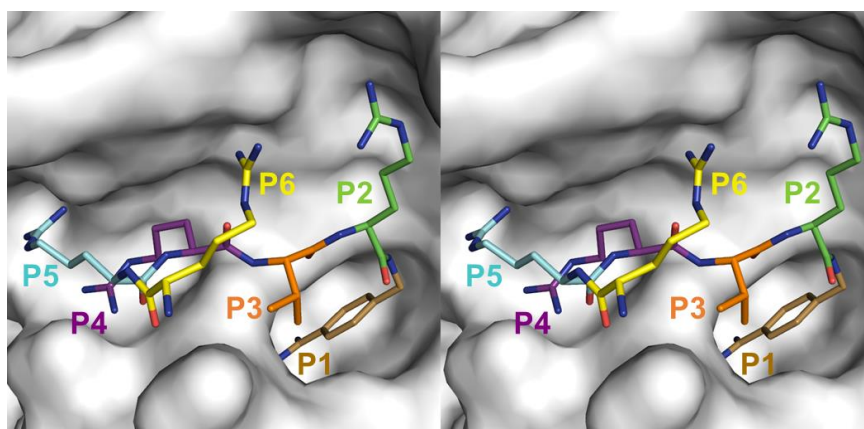


Figure 1. Stereo view of inhibitor H-Arg-Arg-Arg-Val-Arg-4-amidinobenzylamide²⁵ in complex with human furin (PDB: 6EQX³¹). The residues are labelled according to the nomenclature of Schechter and Berger.³⁵

Therefore, the peptidic backbone of substrate **2** was elongated with further Arg residues. Substrates **7** – **11** contain one additional Arg residue in P5 position and compounds **12** and **13** two Arg residues in the P6-P5 segment. Due to the free N-terminus, substrates **11** and **13** possess an additional basic moiety. Furthermore, many physiological substrates possess Lys in P2-position. In substrate analogue inhibitors the exchange of P2-Arg to Lys results in an approximately 2-fold drop in affinity.^{26,28} To examine the influence on substrates, also the P2-Lys substrates **4**, **6**, **7**, and **9** – **13** were synthesized. All substrates were prepared according to a previously described strategy.²⁴ Briefly, the protected N-terminal peptide segment starting from the P2 residue was synthesized on 2-chlorotritylchloride resin with a standard Fmoc SPPS protocol. This segment was cleaved under mild acidic conditions from the resin maintaining the side chain protection, followed by coupling of H-Arg-AMC \times 2 HCl in solution and removal of all protecting groups (Scheme S1 and Figure S1 in Supporting Information). The sequences and analytical data of the substrates are summarized in Table 1.

Table 1. Sequences of the synthesized substrates including their analytical characterization. The known substrates **1** and **2** served as reference compounds.

substrate								HPLC	MS	MS	
P7	P6	P5	P4	P3	P2	P1	P1'	(min)	calc.	(found) [M+H] ⁺	
1		Pyr	Arg	Thr	Lys	Arg	AMC	\times 3 AcOH	Commercially available		
2*		Phac	Arg	Val	Arg	Arg	AMC	\times 3 TFA	21.8	860.48	861.40
3		Ac	Arg	Val	Arg	Arg	AMC	\times 3 TFA	14.9	784.45	262.47 ^a
4		Phac	Arg	Val	Lys	Arg	AMC	\times 3 TFA	21.2	832.47	833.20
5		Phac	Arg	Tle	Arg	Arg	AMC	\times 3 TFA	23.0	874.49	438.40 ^b
6		Phac	Arg	Tle	Lys	Arg	AMC	\times 3 TFA	22.0	846.49	424.44 ^b
7	Ac	Arg	Arg	Val	Lys	Arg	AMC	\times 4 TFA	14.0	912.54	457.40 ^b
8	Ac	Arg	Arg	Tle	Arg	Arg	AMC	\times 4 TFA	15.2	954.56	487.50 ^b
9	Ac	Arg	Arg	Tyr	Lys	Arg	AMC	\times 4 TFA	14.6	976.54	489.40 ^b
10	Ac	Arg	Arg	Tle	Lys	Arg	AMC	\times 4 TFA	17.7	926.56	927.90
11		H-Arg	Arg	Tle	Lys	Arg	AMC	\times 4 TFA	14.7	884.55	885.80
12	Ac	Arg	Arg	Tle	Lys	Arg	AMC	\times 5 TFA	15.3	1082.66	1083.80
13	H-Arg	Arg	Arg	Tle	Lys	Arg	AMC	\times 5 TFA	14.8	1040.60	1041.90

* Previously published²⁴

^a $[M+3H]^{3+}/3$

^b $[M+2H]^{2+}/2$

Enzyme kinetic characterization of the substrates using furin

The commercially available derivative **1** is the most widely used substrate for basic PCs. We determined a K_M value of 2.9 μM and a k_{cat} value of 0.3 s^{-1} resulting in a performance constant of $1.02 \times 10^5 \text{ M}^{-1}\text{s}^{-1}$ (Table 2). A similar k_{cat}/K_M ratio was found for analogue **2**, which was used as standard substrate for furin in our previous work.²⁴⁻²⁷ In contrast to compound **2**, substrate **3** possesses an N-terminal acetyl group, resulting in a slightly enhanced K_M value, which leads to a decreased performance constant of $6.6 \times 10^4 \text{ M}^{-1}\text{s}^{-1}$, despite identical k_{cat} values. In analogues **4**–**6**, containing an N-terminal Phac residue, the P2 and P3 positions were modified. The exchange of the P2 Arg in substrates **2** and **5** to Lys provided compounds **4** and **6** possessing decreased K_M values. In contrast, the substitution of the P3 Val in compound **2** by Ile in analogue **5** resulted in an approximately 2-fold increased K_M value. Both findings were unexpected and are not in line with the results of our furin inhibitor studies. In several series with reversible substrate-analogue competitive inhibitors, we consistently found an opposite tendency, a reduced potency with P2 Lys derivatives^{26,29} and an increased affinity after incorporation of Ile in P3 position.²⁴⁻²⁶ However, the deteriorated K_M constant of the Ile substrate **5** was overcompensated by a 3-fold enhanced k_{cat} providing an improved k_{cat}/K_M value compared to the Val analogue **2**. A similarly 1.5-fold improved performance constant was also observed for the Ile substrate **6**, when compared to the Val compound **4**, both possessing Lys as P2 residue. The replacement of the Phac residue by Ac-Arg (**7-10**) or unprotected Arg (**11** and **13**) leads to significantly reduced K_M values resulting in strongly improved performance constants $> 1 \times 10^6 \text{ M}^{-1}\text{s}^{-1}$. The incorporation of the bulky aromatic Tyr, which was previously used in a related PC substrate series^{8,17}, leads to a declined k_{cat}/K_M ratio in compound **9**. In contrast, as already found for the shorter tetrapeptides, the P2-Lys analog **10** possesses an approximately 2-fold higher performance constant than the P2 Arg substrate **8**. This is due to a 5-fold decreased K_M value, although the k_{cat} value was even reduced. Similar kinetic constants were observed for the compound **11** as well as the further elongated substrates **12** and **13**.

For kinetic measurements high enzymatic activities are beneficial, as found for substrates **5** and **8** with k_{cat} values $> 1 \text{ s}^{-1}$. However, the significantly reduced K_M value leads to an approximately 10-fold higher performance constant for substrate **8** in comparison to compound **5**. Therefore, substrate **8** was selected for further inhibitor measurements.

Table 2. Enzyme kinetic characterization of the synthesized substrates with the basic PCs furin, PC1, PC2, PC5, and PC7.

No	Furin		PC1		PC2		PC5A		PC7	
	K_M (μM)	k_{cat} (s^{-1})	K_M (μM)	k_{cat} (s^{-1})	K_M (μM)	k_{cat} (s^{-1})	K_M (μM)	V_{max} (RFU/s)	K_M (μM)	k_{cat} (s^{-1})
1	2.91 ± 0.24	0.296 ± 0.004	19.5 ± 1.2	0.0242 ± 0.0027	38.2 ± 5.6	0.0690 ± 0.0025	7.10 ± 0.98	13.8 ± 0.7	28.3 ± 1.6	0.275 ± 0.010
2	5.22 ± 0.18	0.585 ± 0.021	34.5 ± 2.4	0.0569 ± 0.0063	46.9 ± 5.2	0.00990 ± 0.00073	11.2 ± 1.2	7.78 ± 0.06	2.46 ± 0.92	0.0260 ± 0.0024
3	8.87 ± 0.28	0.584 ± 0.009	56.3 ± 2.7	0.0680 ± 0.0056	112 ± 18	0.00818 ± 0.00150	17.8 ± 4.1	7.04 ± 0.96	10.2 ± 2.1	0.0493 ± 0.0022
4	2.40 ± 0.11	0.597 ± 0.010	1.28 ± 0.13	0.00610 ± 0.00075	21.3 ± 1.5	0.150 ± 0.007	6.35 ± 1.24	11.5 ± 1.8	9.41 ± 0.08	0.318 ± 0.018
5	11.1 ± 1.4	1.91 ± 0.07	6.60 ± 0.39	0.0191 ± 0.0018	38.7 ± 0.8	0.0436 ± 0.0007	9.64 ± 2.13	15.8 ± 1.1	3.91 ± 1.84	0.116 ± 0.025
6	1.88 ± 0.01	0.698 ± 0.014	0.216 ± 0.012	0.00177 ± 0.00017	7.02 ± 0.35	0.0740 ± 0.0063	2.63 ± 0.38	8.43 ± 0.13	8.69 ± 1.61	0.580 ± 0.032
7	0.170 ± 0.005	0.373 ± 0.016	3.58 ± 0.52	0.0115 ± 0.0012	11.2 ± 2.8	0.127 ± 0.006	1.53 ± 0.46	7.11 ± 0.25	5.10 ± 2.51	0.929 ± 0.035
8	0.765 ± 0.012	1.18 ± 0.02	12.9 ± 1.1	0.0311 ± 0.0034	58.1 ± 15.5	0.0664 ± 0.0109	3.80 ± 0.49	11.4 ± 1.0	1.06 ± 0.54	0.436 ± 0.021
9	0.682 ± 0.033	0.843 ± 0.012	1.15 ± 0.12	0.00614 ± 0.00066	28.9 ± 2.3	0.142 ± 0.001	2.44 ± 0.43	6.51 ± 0.64	2.65 ± 0.99	0.351 ± 0.018
10	0.135 ± 0.035	0.373 ± 0.027	0.615 ± 0.115	0.00334 ± 0.00032	4.11 ± 0.91	0.0439 ± 0.00156	0.442 ± 0.121	4.19 ± 0.16	2.96 ± 0.51	1.46 ± 0.08
11	0.146 ± 0.048	0.583 ± 0.045	0.549 ± 0.101	0.00336 ± 0.00040	48.8 ± 0.5	0.172 ± 0.004	0.586 ± 0.086	2.78 ± 0.09	1.77 ± 0.36	1.38 ± 0.06
12	0.163 ± 0.038	0.450 ± 0.050	0.236 ± 0.071	0.00194 ± 0.00020	4.69 ± 0.06	0.0265 ± 0.0006	0.226 ± 0.036	1.89 ± 0.13	1.04 ± 0.49	0.794 ± 0.067
13	0.126 ± 0.068	0.339 ± 0.026	0.420 ± 0.180	0.00240 ± 0.00026	5.91 ± 1.55	0.0686 ± 0.0026	0.651 ± 0.297	1.31 ± 0.05	0.15 ± 0.03	0.263 ± 0.009

In comparison to our previously used standard conditions with substrate **2** it was possible to reduce the enzyme concentration from approximately 0.95 to 0.095 nM. The use of such reduced enzyme concentrations is particularly beneficial for measurements with highly potent inhibitors to avoid tight binding conditions, which require the exact knowledge of the active enzyme concentration for calculating an apparent inhibition constant using the Morrison **equation 1**. The apparent K_i^* can be converted into the true value by means of **equation 2**.³⁶ In contrast, for more robust K_i value determinations under classical conditions (**equation 3**), where the lowest inhibitor concentration must be at least 10-fold higher than the enzyme concentration used, it is not necessary to know the exact enzyme concentration. Now, using substrate **8** and the reduced furin concentration it was possible to measure our previously described tight-binding inhibitors^{23–26} under classical conditions. Exemplarily, the determination of the K_i values of inhibitors **MI-1579**²⁶ (4-guanidinomethyl-phenylacetyl-Arg-Tle-Arg-3-fluoro-4-amidinobenzylamide) and **MI-1148**²⁴ (4-guanidinomethyl-phenylacetyl-Arg-Tle-Arg-4-amidinobenzylamide) is shown under tight-binding and classical conditions using substrates **2** and **8**, respectively (Figure 2).

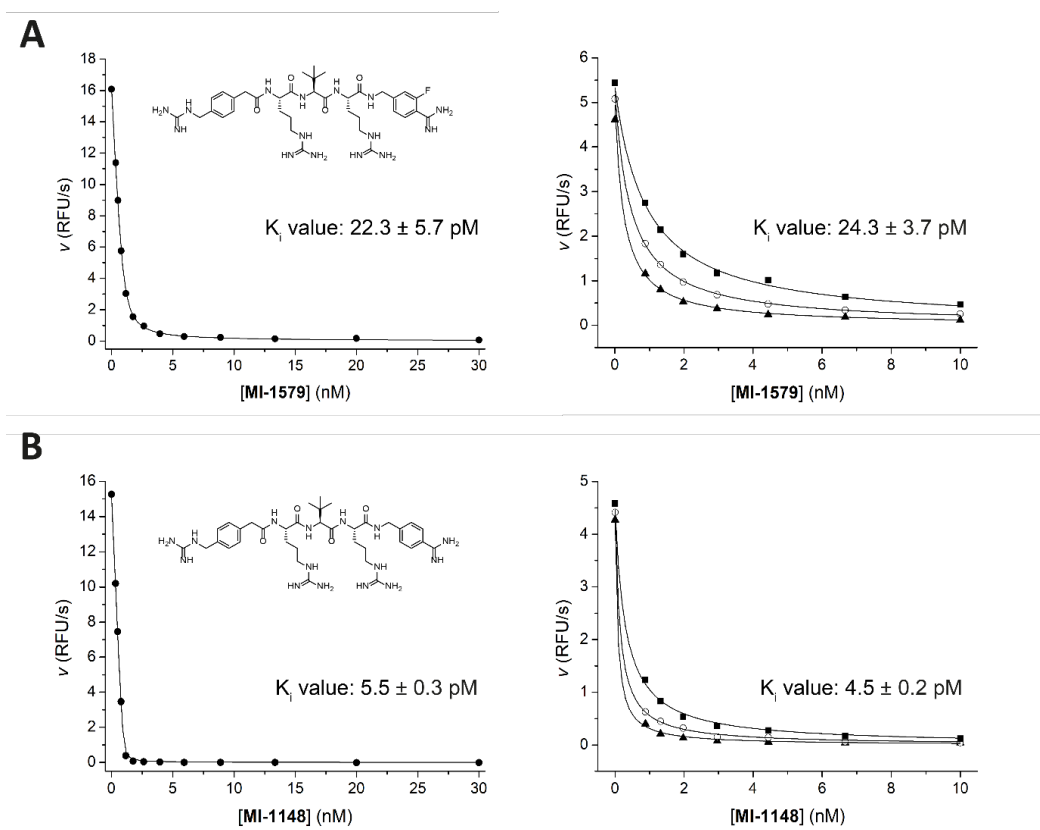


Figure 2. Inhibition of furin by inhibitors **MI-1579** (A) and **MI-1148** (B) under tight-binding conditions in the presence of a single concentration (●, 12.5 μ M) of substrate **2** (0.95 nM furin per well, left side, the data were fitted to **equation 1**) and under classical conditions in presence of substrate **8** (10 (■), 5 (○), and 2.5 (▲) μ M for inhibitor **MI-1579** and 50 (■), 25 (○), and 12.5 (▲) μ M for **MI-1148** and 0.095 nM furin per well (right side, the data were fitted to **equation 3**).

For both inhibitors very similar K_i values were determined with these two methods. An inhibition constant of 5.5 ± 0.3 pM was measured for inhibitor **MI-1148** under tight-binding conditions with

substrate **2**. Under classical conditions with substrate **8** and the reduced furin concentration a K_i value of 4.5 ± 0.2 pM was determined. For inhibitor **MI-1579** a K_i value of 22.3 ± 5.7 pM was calculated under tight-binding conditions and a value of 24.3 ± 3.7 pM using the classical conditions.

During these measurements with substrate **8** at this decreased furin concentration, non-linear progress curves have been observed in presence of lower concentrations of inhibitor **MI-1148** at the used substrate concentrations. After approximately 5-10 min, a nearly linear relationship was obtained, indicating a slow-binding behavior. This kinetic behavior was never observed during previous measurements with substrate **2**, in these cases always linear progress curves have been detected. The obtained progress curves at a substrate **8** concentration of 50 μ M are depicted in Figure 3A.

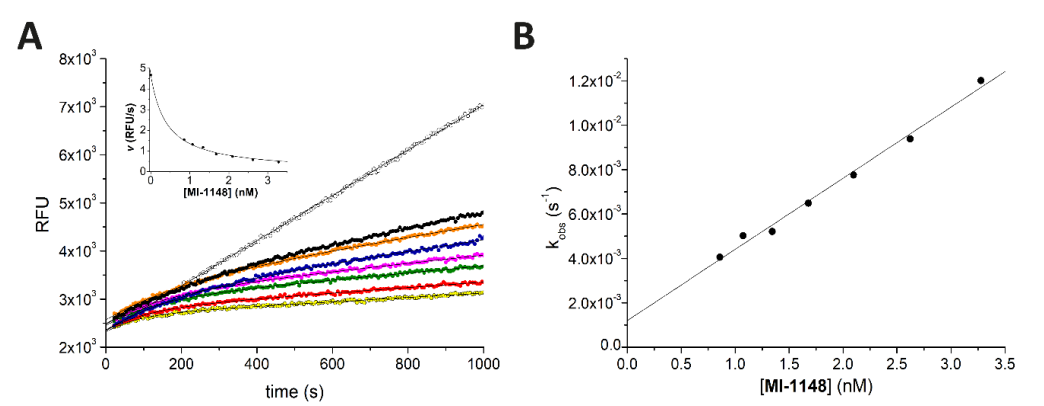


Figure 3. Slow-binding behavior of inhibitor **MI-1148**. (A) Progress curves of the slow-binding inhibition of furin (0.095 nM) by inhibitor **MI-1148** at 3.27 nM (●), 2.62 nM (●), 2.09 nM (●), 1.67 nM (●), 1.34 nM (●), 1.07 nM (●), 0.86 nM (●), and 0 nM (○) in the presence of substrate **8** (50 μ M). The progress curves were fitted to **equation 4**. The inset shows the dependence of the determined steady-state rates v_s from the inhibitor concentration, which was used for K_i value calculation with **equation 3**. (B) The calculated rate constants k_{obs} of each progress curve were fitted as a function of the inhibitor concentrations according to **equation 5** providing the rate constants k_{on} and k_{off} .

In case of slow-binding inhibition the obtained progress curves can be fitted to **equation 4** providing the apparent rate constant k_{obs} , the steady state velocity v_s , and, when lacking a rapid pre-equilibrium, a constant initial velocity v_0 .^{37,38} The v_s values were fitted as a function of the inhibitor concentration to **equation 3** providing a K_i value of 3.08 ± 0.05 pM (Figure 3A, inset). According to **equation 5**, the k_{obs} values were used for the calculation of the rate constants k_{on} and k_{off} (Figure 3B). In addition, **equation 6** allowed the calculation of the dissociation rate constant k_{off} from the determined K_i and k_{on} values. For the measurements shown in Figure 3 a very rapid k_{on} rate of $4.12 \times 10^8 \pm 0.24 \times 10^8$ $M^{-1}s^{-1}$ and a k_{off} value of $1.27 \times 10^{-3} \pm 0.09 \times 10^{-3}s^{-1}$ were determined. In contrast to **MI-1148**, for **MI-1579** only linear progress curves were obtained under the used conditions. Therefore, no association and dissociation rate constants could be determined for this compound.

Enzyme kinetic characterization of the substrates using recombinant murine PC1

Compound **1** is a standard PC1 substrate, which was also used in our previous measurements.²⁴ The determined performance constant of 1.24×10^3 $M^{-1}s^{-1}$ is similar as found by other groups.¹⁶ A comparable relatively low k_{cat}/K_M ratio was also determined for substrate **2** and its acetylated analogue

3, although their k_{cat} values are even higher than those of most other substrates in this series. Concerning the P2 residue, approximately 10-fold increased k_{cat} values were observed for the P2 Arg derivatives compared to their Lys analogues (e.g., substrates **2/4**, **5/6**, and **8/10**). However, this advantage of the P2 Arg substrates was deteriorated by their more than 20-fold increased K_{M} values leading to higher $k_{\text{cat}}/K_{\text{M}}$ ratios for the Lys derivatives. Among the three pairs of substrates possessing Val or Tle in this position (**2/5**, **4/6**, and **7/10**), both k_{cat} and K_{M} values are increased for the Val analogues. Despite some compensation this always resulted in slightly higher performance constants for the Tle substrates. Interestingly, a complete compensation was found for the P3 Tyr derivative **9** when compared to the Tle derivative **10** leading to similar performance constants.

Generally, the elongation with additional basic residues has a positive influence on the performance constants, the highest $k_{\text{cat}}/K_{\text{M}}$ ratio was found for the acetylated substrate **12**. Slightly decreased performance constants were detected for the direct non-acylated analogue **13**, the pentapeptidic substrates **9 – 11** and substrate **6**. However, all of them suffer from very poor k_{cat} values. Due to their higher k_{cat} values, substrates **2**, **3**, and **8** are suitable for routine measurements with PC1.

Enzyme kinetic characterization of the substrates using recombinant murine PC2

Proteomic studies on the cleavage of neuropeptides by PC2 revealed a preference for substrates containing Lys in P2 position compared to Arg.³⁹ This tendency was confirmed with our substrate series, where the P2-Lys compounds **4**, **6**, and **10** have lower K_{M} values than their direct Arg analogs **2**, **5**, and **8**, leading to higher performance constants for the tested Lys derivatives. In a previous study, we had found an improved PC2 inhibition for analogues with Tle instead of Val in P3 position.²⁴ Similar to furin, the incorporation of Tle in substrate **5** resulted in a 4-fold increased k_{cat} value compared to compound **2**, whereas a relatively small influence on the K_{M} value was observed, resulting in a 5-fold improved performance constant. Interestingly, the incorporation of Tyr in P3 position of substrate **9**, lead to an increased k_{cat} value of 0.14 s^{-1} compared to its analogues **7** and **10**. In contrast to furin, the elongation with a further P5-Arg residue in substrate **8** has only a negligible influence on the $k_{\text{cat}}/K_{\text{M}}$ values compared to the shorter analogue **5**, suggesting that this basic moiety is not contributing to a more efficient substrate cleavage. Interestingly, the N-terminally unprotected analogue **11** of substrate **8** possesses a significantly higher k_{cat} value of 0.17 s^{-1} but also a deteriorated K_{M} value when compared with some other substrates, e.g., compounds **6** and **7**. Furthermore, the incorporation of an additional Arg in P6 position in compounds **12** and **13** resulted in decreased k_{cat} values but also lower K_{M} values compared to analogue **11**.

The best performance constants above $1 \times 10^4 \text{ M}^{-1}\text{s}^{-1}$ were found for compounds **6**, **7**, **10**, and **13**, which are approximately 6-fold improved compared to the most widely used PC2 substrate **1**. Due to their high k_{cat} and an acceptable K_{M} value, both, substrates **4** and **7** are suitable candidates for routine measurements with PC2.

Enzyme kinetic characterization of the substrates using PC5A

For PC5A measurements, concentrated supernatants of cells have been used, which were transfected with a plasmid encoding human PC5A. These supernatants were not further purified and due to the limited volume, no enzyme titration could be performed. Therefore, only $V_{\text{max}}/K_{\text{M}}$ values could be calculated for PC5A, although they are proportional to the $k_{\text{cat}}/K_{\text{M}}$ ratios. Similar to PC2, substrates **4** and **6** with a Lys residue possess more than 2-fold higher $V_{\text{max}}/K_{\text{M}}$ values than their Arg counterparts **2** and **5**, caused by their lower K_{M} values. Also in the elongated substrates, the replacement of P2 Arg in substrate **8** by Lys in substrate **10** resulted in a 3-fold improved cleavage efficiency. Furthermore, the incorporation of Tle in substrate **6** also provided a 2-fold improved $V_{\text{max}}/K_{\text{M}}$ value when compared with analogue **4**. Here, in the opposite to the structure-activity-relationship with furin, the incorporation of Tle leads to lower K_{M} values and a reduced V_{max} . Additional basic residues in P5 and P6 position improve

the cleavage efficiency. Elongation of compound **5** with an Arg in substrate **8** leads to an almost 2-fold improved V_{\max}/K_M value. However, the N-terminally unprotected analogues **11** and **13** possess reduced V_{\max}/K_M ratios compared to their acylated counterparts **10** and **12**. The P6 Arg in substrates **12** and **13** results again in the lowest V_{\max} values of this series, which were compensated by low K_M constants.

Based on their V_{\max}/K_M ratio compounds **10** and **12** are the best PC5A substrates. However, due to the higher V_{\max} value, substrates **1**, **4**, **5**, and **8** might be better suited for routine measurements.

Enzyme kinetic characterization of the substrates using PC7

For the commercially available substrate **1** a K_M value of 28.3 μM and a k_{cat} value of 0.28 s^{-1} was determined under our conditions resulting in a k_{cat}/K_M value of $9.72 \times 10^3 \text{ M}^{-1}\text{s}^{-1}$. In comparison to the reference substrate **1**, the k_{cat} values of compounds **2** and **3** are significantly reduced, but compensated by improved K_M values. The incorporation of a P2 Lys in derivative **4** leads to a slightly higher k_{cat} and 3-fold improved K_M value when compared with compound **1**. A further increased performance constant was observed for the P3 Tle analogue **6** and especially for the elongated derivatives **7** – **13**. All these extended compounds possess relatively low K_M values $\leq 5.5 \mu\text{M}$, which suggests that the S5 and S6 sites of PC7 contribute to the binding of the additional Arg residues in these substrates.

The highest performance constant of $1.75 \times 10^6 \text{ M}^{-1}\text{s}^{-1}$ within this series was determined for the N-terminally unprotected hexapeptide **13**, caused by the very low K_M value of 0.15 μM . However, due to the better overall profile with 5- to 6-fold higher k_{cat} values substrates **10** and **11** might be better suited for routine measurements with PC7.

Discussion

Basic furin-like PCs are promising drug targets, especially for the development of broad-spectrum antivirals. For more convenient biochemical and enzyme kinetic studies like the characterization of inhibitors it is beneficial to use efficiently cleaved substrates, which enable measurements at low enzyme concentrations.

Previously published natural and synthetic PC substrates strongly differ in their performance constants. For instance, the protective antigen from anthrax is cleaved by furin after the sequence Arg-Lys-Lys-Arg167 with a k_{cat}/K_M ratio of $5.5 \times 10^6 \text{ M}^{-1}\text{s}^{-1}$.¹¹ In contrast, many of the earlier published shorter AMC derived tetrapeptidic substrates were only moderately cleaved with significantly reduced k_{cat}/K_M values. Therefore, it was initially speculated that the bulky AMC moiety interferes with substrate binding.¹⁸ However, Fuller and coworkers showed that also elongated AMC substrates like Ac-Arg-Ala-Arg-Tyr-Lys-Arg-AMC are cleaved with a similar efficiency compared to physiological and FRET substrates.¹⁷

With furin, we determined a k_{cat}/K_M value of approximately $1 \times 10^5 \text{ M}^{-1}\text{s}^{-1}$ for the reference substrate **1** under our conditions. Compared to literature this value is 3- to 10-fold higher, which might be caused by differences in the composition, pH and ion strength of the used buffer or enzyme preparations.^{15,16,40} Interestingly, for some substrates (e.g., compounds **2** and **5**) we observed that changes in k_{cat} or K_M resulted in similar performance constants revealing a kind $k_{\text{cat}}-K_M$ compensation, previously described also for other enzymes.⁴¹ In case of substrate **2** the K_M value is 2-fold lower compared to its P3 Tle-analogue **5**. At the same time the k_{cat} of substrate **2** is 3-fold reduced, resulting in similar performance constants of $1.12 \times 10^5 \text{ M}^{-1}\text{s}^{-1}$ for compound **2** and of $1.72 \times 10^5 \text{ M}^{-1}\text{s}^{-1}$ for substrate **5**, respectively. This highlights that K_M is influencing the k_{cat} value. A very tight binding substrate, possessing a low free energy of the ES complex (small K_M), often requires a higher activation energy to reach the transition state, which results in reduced k_{cat} values.

All elongated substrates with additional basic P5 and P6 residues exhibit more than 10-fold improved performance constants when compared to their shorter analogues. This tendency is mainly attributed to reduced K_M values, although the pentapeptidic substrate **8** also possesses an enhanced k_{cat} value. Fuller and coworkers described a pronounced substrate inhibition of furin by very similar hexapeptidic AMC substrates like Ac-Lys-Ala-Arg-Tyr-Lys-Arg-AMC containing basic P6 groups, whereas a normal Michaelis-Menten behavior was observed for the shorter tetrapeptides.¹⁷ We could not observe any significant substrate inhibition in our study under the used conditions. For example, the Michaelis-Menten plot of substrate **13** is shown in Figure S2, where substrate concentrations up to 40-fold above the K_M values have been used.

The use of improved furin substrates has several practical advantages for the enzyme kinetic characterization of inhibitors. At first, higher k_{cat} values and performance constants generally allow measurements at lower enzyme concentrations leading to a reduced enzyme consumption. Secondly, due to the use of approximately 10-fold reduced furin concentrations it was now possible to measure our previously described tight-binding inhibitors with K_i values < 100 pM with substrate **8** under classical conditions, where the lowest inhibitor concentration is still approximately 10-fold higher than the used enzyme concentration. When using the less efficiently cleaved substrate **2**, which requires significantly higher enzyme concentrations for kinetic measurements, a K_i determination under classical conditions was only possible for inhibitors with inhibition constants > 100 pM. In general, it is advantageous when inhibition constants can be determined under classical conditions, where the knowledge of the precise enzyme concentration is not required. In contrast, the calculation of K_i values under tight-binding conditions using the Morrison equation depends on the exact enzyme concentration and is very sensitive to minor inaccuracies this parameter.³⁶ Furthermore, for enabling such measurements a high S/K_M ratio is required to achieve a strong protection of the enzyme, thereby reducing the effect of the inhibitor. Due to the very low K_M value of 0.77 μM for substrate **8**, a sufficient substrate protection of furin from inhibition by compound **MI-1579** (K_i approximately 25 pM) could be achieved, when using this substrate at concentrations $\geq 2.5 \mu\text{M}$ during kinetic measurements (Figure 2A). For the even stronger inhibitor **MI-1148** (K_i approximately 4 pM; Figure 2B) higher substrate concentrations $\geq 12.5 \mu\text{M}$ had to be used to achieve a sufficient substrate protection of furin. Notably, very similar inhibition constants have been determined for both inhibitors regardless of the used conditions and calculation methods. Although the k_{cat} of substrate **5** is almost twice as large compared with substrate **8**, it is less suited for such measurements due to its 15-fold higher K_M value, which would lead to a much weaker substrate protection of furin.

The third beneficial result when using the improved substrate **8** at 50 μM and a 10-fold reduced enzyme concentration was the observation of a pronounced slow-binding behavior during kinetic measurements with inhibitor **MI-1148** on a normal plate reader, where we obtain the first data points approximately 25 s after the start of the reaction by the addition of enzyme and a short mixing time. This allowed for the first time the determination of the individual association and dissociation rate constants. For this inhibitor a k_{on} rate constant of $5 \times 10^8 \text{ M}^{-1}\text{s}^{-1}$ and a k_{off} value of $1 \times 10^{-3} \text{ s}^{-1}$ could be determined. Usually, the k_{on} values for protein ligand binding are in the range of 10^5 to $10^8 \text{ M}^{-1}\text{s}^{-1}$.¹⁴ Therefore, this very large k_{on} value is relative close to the diffusion controlled upper limit of association rate constants, which is most likely caused by a rapid electrostatically-driven association process between the 4-fold protonated inhibitor and furin's highly acidic and negatively charged active site.

In contrast to furin, PC1 and PC2 are rather considered as off-targets for inhibitor development. Both enzymes are located in acidic secretory granules in neuroendocrine cells and play a key role in endocrine and neural functions.² They process precursors of many polypeptide hormones such as pro- β -endorphin, proglucagon, and proinsulin.⁵ Due to overlapping cleavage pattern, inhibitors against a certain basic PC like furin have to be also tested for their specificity with the other PC family members.

For kinetic measurements with PC1 and PC2 we used their murine forms, which may cause some differences to their human counterparts. The PC1 k_{cat}/K_M value for the reference substrate **1** is in accordance with the values published by Jean *et al.* and Icimoto and coworkers for the human analogue.^{16,42} In contrast, Fugère *et al.* determined a significantly higher performance constant of $5.19 \times 10^4 \text{ M}^{-1}\text{s}^{-1}$.⁴³ Besides differences in the protease preparation, we saw a strong decline in protease activity already after one freeze-thaw cycle, which also influences the amount of active enzyme. With PC2, we determined a K_M value of $38 \mu\text{M}$, a k_{cat} value of 0.07 s^{-1} and a k_{cat}/K_M value of $1.8 \times 10^3 \text{ M}^{-1}\text{s}^{-1}$ for the reference substrate **1**. Lamango and coworkers determined an approximately 3-fold higher K_M and a k_{cat} value resulting in a performance constant of $6160 \text{ M}^{-1}\text{s}^{-1}$.¹² Furthermore, the progress curves of PC1 showed slight parabolic character despite a pre-incubation of enzyme in buffer for 30 min. For this reason, only the values after 500 s were taken for linear regression to determine the steady-state rates from the progress curves. This behavior might also be a possible reason for differences in the determined values. In general, the elongation with additional basic residues has a positive influence on the catalytic efficiency of PC1 and PC2. Due to a significantly decreased K_M value the highest k_{cat}/K_M ratio of $6.24 \times 10^3 \text{ M}^{-1}\text{s}^{-1}$ with PC1 was found for the N-terminally acylated substrate **12**. However, substrate **12** suffers from a poor k_{cat} value, therefore, analogue **8** or even substrate **3** are more suitable for routine measurements with PC1. In general, compared to other basic PCs, PC1 can be considered as a protease with a relatively weak catalytic activity. In contrast, mainly due to relatively high k_{cat} values substrates **4**, **7**, **9**, and **11** are suitable PC2 substrates in kinetic measurements.

Furthermore, PC5 was used to characterize the novel substrates. The protease is widely distributed and plays a role in various diseases like atherosclerosis or cancer.^{5,44,45} It contributes to embryo implantation and might therefore be an interesting target for hormone free contraception.⁴⁶ There are two isoforms of this protease: PC5A is the soluble form whereas PC5B is a type-1 membrane protein.⁴⁷ We used conditioned medium of HEK293 transfected with a plasmid encoding for human PC5A for kinetic measurements. Therefore, we could not determine the exact enzyme concentration which prohibited the calculation of k_{cat} values. However, the provided V_{max} values are directly proportional to k_{cat} allowing a comparison of the substrates amongst each other. For background correction, the supernatant of cells transfected with the empty vector was used. Similar to PC1, differences in the performance constants amongst all substrates are not high. Substrates **10** and **12**, which are the best substrates of this series and possess V_{max}/K_M values over $8 \times 10^6 \text{ RFU} \times \text{M}^{-1}\text{s}^{-1}$ are only 25-fold more efficiently cleaved than the substrate **3**. Again, these substrates suffer from low V_{max} values and might not be used for routine measurements.

In addition, the substrates were characterized with PC7. In contrast to other basic PCs, in PC7-knockout mice no visible deleterious phenotype was observed suggesting that PC7 is not involved in critical functions during development or physiology.² Most likely, there is some redundancy between furin and PC7, which both share certain substrates.^{48,49} Interestingly, first data suggest, that PC7 plays a role in anxiety, because PC7 knockout mice exhibit an anxiolytic phenotype.² Therefore, PC7 inhibitors could be potential drugs for the treatment of patients with anxiety disorders. For kinetic measurements a commercially available recombinant truncated form of PC7 was used. A k_{cat} value of 0.28 s^{-1} and a K_M value of $28 \mu\text{M}$ was determined for the reference substrate **1** resulting in a k_{cat}/K_M value of $9.72 \times 10^3 \text{ M}^{-1}\text{s}^{-1}$. For a recombinant enzyme lacking the carboxy terminus, Fugère and coworkers determined a K_M value of $62.4 \mu\text{M}$, a k_{cat} value of 0.18 s^{-1} , and a performance constant of $2885 \text{ M}^{-1}\text{s}^{-1}$.⁴³ In contrast, Izaguirre *et al.* found a K_M value of $2.2 \mu\text{M}$, a k_{cat} value of 0.032 s^{-1} and a k_{cat}/K_M value of $1.5 \times 10^4 \text{ M}^{-1}\text{s}^{-1}$ for a PC7 construct up to the P domain.⁴⁰ Before use, the commercially available PC7 is activated by treatment with the metalloprotease thermolysin, which is later inhibited by ortho-phenanthroline. Therefore, differences in the determined values for PC7 might be caused by different enzyme preparations.

Compared to furin, PC7 is less strongly inhibited by our previously published furin inhibitors.¹⁸ However, the introduction of a basic P5 residue also resulted in a stronger inhibition, which suggests that basic residues at least in P5 position contribute to substrate binding. This trend is also observed for the longer substrates with a basic residue in P5 position as well as with analogues containing an additional basic P6 group. Substrate **13** possesses the highest $k_{\text{cat}}/K_{\text{M}}$ ratio of $1.75 \times 10^6 \text{ M}^{-1}\text{s}^{-1}$, which is almost 200-fold higher as found for the standard substrate **1**. Similar to the other PCs, the most efficient substrates suffer from relatively low k_{cat} values. Therefore, especially substrates **10** and **11** with significantly increased k_{cat} values are much better suited for routine measurements. These improved substrates allow a reduction of the PC7 concentration during the measurement and therefore are suitable for the screening of PC7 inhibitors.

In summary, for furin, PC1, PC2, and PC7 one or more suitable AMC substrates compared to the commonly used substrate **1** were identified. These substrates are more efficiently cleaved and thereby allow a reduction of enzyme concentration.

Material and Methods

All reagents, including standard Fmoc amino acids, coupling reagents, resins, solvents, and other chemicals were obtained from Orpegen, Bachem, Iris Biotech, Fluka, Acros, ThermoFisher, or Sigma Aldrich.

Synthesis

The solid phase peptide synthesis of the side-chain protected N-terminal peptide segment lacking the C-terminal Arg-AMC was performed using approximately 120 mg Fmoc-Arg(Pbf)-2-chlorotrityl resin (loading 0.6 mmol/g) or Fmoc-Lys(Boc)-2-chlorotrityl resin (loading 0.7 mmol/g) in a 2 mL reaction vessel and a standard Fmoc protocol^{24–26} with double couplings (approximately 4-fold excess of Fmoc-amino acid, HOBt, and HBTU, respectively, and 8 equivalents DIPEA, 2 × 2 h coupling time, DMF as solvent).

The protected peptide was cleaved from the resin under mild acidic conditions (1 % TFA in DCM, 3 × 30 min) at room temperature. The solvent was removed *in vacuo* yielding an oily intermediate, which was treated with 1.0 equivalent of H-Arg-AMC × 2 HCl, 1.0 equivalent of PyAOP, and 3.0 equivalents of DIPEA in DMF. The mixture was stirred for 15 min at 0 °C and 4 h at room temperature. The solvent was removed *in vacuo* and the protected intermediate was treated with 1.2 mL TFA/TIS/H₂O (95/2.5/2.5, v/v/v) for 3 h at room temperature. The mixture was precipitated in cold diethyl ether and dried *in vacuo*. All peptides were purified by preparative reversed-phase HPLC to more than 95 % purity based on the detection at 220 nm and finally obtained as lyophilized TFA salts.

Analytical HPLC experiments were performed on a Shimadzu LC-10A system (pumps: 2LC-10 ATVP, system controller: SCL-10AVP, auto-injector: SIL-10AXL, detector SPD-M109AVP, degasser: DGU-14A, column oven: CTO-10A, column: Nucleodur C18, 5 μm, 100 Å, 4.6 × 250 mm, Macherey-Nagel, Düren, Germany) using a linear gradient of acetonitrile (10 – 70 % in 60 min, detection at 220 nm) in water containing 0.1 % TFA at flow rate of 1 mL/min. For data acquisition and analysis, the software Shimadzu Class-VP version 7.2.1 SP1 was used. The final substrates were purified by preparative HPLC (pumps: Varian PrepStar Model 218 gradient system, detector: ProStar Model 320, fraction collector: Varian Model 701) using a C18 column (Nucleodur, 5 μm, 32 × 250 mm, Macherey-Nagel, Düren, Germany) and a linear gradient of acetonitrile containing 0.1 % TFA at a flow rate of 20 mL/min. All substrates were finally obtained as TFA salts after lyophilisation (Alpha 2-4 LDplus, Martin Christ Gefriertrocknungsanlagen, Osterode am Harz, Germany). The molecular mass of the synthesized

compounds was determined using a QTrap 2000 ESI spectrometer (Applied Biosystems, Darmstadt, Germany) or a LTQ-FT Ultra (ThermoFisher Scientific, Waltham, Massachusetts, United States)

Enzyme kinetic measurements

All fluorescence measurements were performed in 96 well plates at room temperature using a Tecan Safire² microplate reader (Grödigg, Austria). The substrate cleavage and release of free fluorescent AMC was measured at λ_{ex} 380 nm and λ_{em} 460 nm.

Measurements with recombinant human furin

The measurements were performed with black FluoroNunc F96 MaxiSorp plates (Nunc, Langensfeld, Germany) for 20 min. For measurements in absence of inhibitor each well contained 20 μ L of the respective substrate (dissolved and diluted in water) and 160 μ L buffer (100 mM HEPES, 0.2 % Triton X-100, 2 mM CaCl₂, 0.02 % NaN₃, and 1 mg/mL BSA, pH 7.0). The measurements were started by addition of 20 μ L furin³² solution (final concentration 0.95 nM).

In case of inhibitor measurements, each well was additionally treated with 2 μ L inhibitor dissolved in DMSO. The assays with inhibitors **MI-1148**²⁴ and **MI-1579**²⁶ under tight-binding conditions were performed in presence of a constant concentration of substrate **2** (12.5 μ M in the assay) using an identical furin concentration of 0.95 nM. The measurements provided linear progress curves and steady-state rates were calculated from the slopes of the progress curves. The dependence of the determined steady-state rates from the inhibitor concentration was used to calculate an apparent inhibition constant K_i^* using **equation 1** (v_s is the calculated steady state rate, v_0 is the velocity in absence of an inhibitor, I_t is the total inhibitor concentration, E_t is the total enzyme concentration, and K_i^* is the apparent inhibition constant at the used substrate concentration).³⁶

$$v_s = v_0 \times \frac{[(K_i^* + I_t - E_t)^2 + 4 \times K_i^* \times E_t]^{1/2} - (K_i^* + I_t - E_t)}{2 \times E_t} \quad \text{(Equation 1)}$$

The apparent K_i^* value was converted into the true K_i value using **equation 2**.

$$K_i = \frac{K_i^*}{1 + \frac{S}{K_M}} \quad \text{(Equation 2)}$$

Substrate **8** enabled measurements with inhibitors **MI-1148**²⁴ and **MI-1579**²⁶ under classical conditions using a reduced furin concentration of 0.095 nM. The assays were performed in presence of 10, 5 and 2.5 μ M of substrate **8** for inhibitor **MI-1579** and with 50, 25, and 12.5 μ M of substrates **8** for **MI-1148**. The steady-state rates were calculated from the linear slopes of the progress curves, which were reached after approximately 10 min. The K_i values were obtained by fitting the data to the equation for classical reversible competitive inhibition (**equation 3**), as described previously.²⁸

$$v_s = \frac{V_{max} \times [S]}{K_M \times \left(1 + \frac{[I]}{K_i}\right) + [S]} \quad \text{(Equation 3)}$$

Furthermore, under these conditions, well-formed characteristic non-linear progress curves were obtained for inhibitor **MI-1148** in presence of substrate **8** (50 μ M in the assay) over 15 min. The obtained progress curves were fitted to **equation 4**, where P is the corresponding fluorescence signal of the formed product concentration, v_s is the calculated steady state rate, v_0 is the velocity in absence of an inhibitor, k_{obs} is the apparent first-order rate constant and d the displacement of the fluorescence signal from zero at $t = 0$.

$$[P] = (v_s \times t) + \frac{(v_0 - v_s) \times [1 - \exp^{-k_{obs} \times t}]}{k_{obs}} + d \quad \text{(Equation 4)}$$

The steady-state velocities v_s were used to calculate the K_i value according to **equation 3**.

The k_{obs} values were fitted as function of the inhibitor concentrations using **equation 5** to provide the association rate constant k_{on} from the slope of the plot.

$$k_{obs} = \frac{k_{on} \times [I]}{\left(1 + \frac{[S]}{K_M}\right)} + k_{off} \quad \text{(Equation 5)}$$

The dissociation rate constant k_{off} was calculated from the known K_i and k_{on} values using **equation 6**.

$$K_i = \frac{k_{off}}{k_{on}} \quad \text{(Equation 6)}$$

Measurements with murine PC1

The measurements were performed in opaque 96-well plates 3365 (Corning, Kaiserslautern, Germany). Each well contained 38 μ L PC1 buffer (100 mM NaOAc, 5 mM CaCl₂, 0.1 % Brij35, 0.1 % NaN₃, and 0.01 % BSA; pH 5.5) and 2 μ L of enzyme⁵⁰. Before measurements, the plate was incubated for 30 min at room temperature. Then, 10 μ L of the respective substrate dissolved in water were added, providing a total assay volume of 50 μ L. Due to the parabolic progress curves, only the data from 500 s were taken for linear regression.

The amount of active PC1 in the enzyme preparation was determined by titration with the irreversible inhibitor Dec-Arg-Val-Arg-Lys-CMK (Bachem, Bubendorf, Switzerland; see Figure S3). PC1 was incubated at room temperature with varying concentrations of the inhibitor (750 – 0.37 nM in the assay) in assay buffer for 30 min. Substrate **2** (50 μ M in the assay) was then added. The plot of the initial velocities v versus the five lowest inhibitor concentrations gave a straight line with an intercept of approximately 28 nM corresponding to the enzyme concentration.

Measurements with murine PC2

The measurements were performed in opaque 96-well plates 3365 (Corning, Kaiserslautern, Germany). Each well contained 40 μ L PC2 solution¹² (100 mM NaOAc, 2 mM CaCl₂, 0.1 % Brij35, 0.1 % NaN₃, and 0.01 % BSA; pH 5.0). Before measurements, the plate was incubated for 1 h at room temperature. Then, 10 μ L of the respective substrate dissolved in water were added, providing a total assay volume of 50 μ L.

The amount of active PC2 in the enzyme preparation was determined by titration with the irreversible inhibitor Dec-Arg-Val-Arg-Lys-CMK (Bachem, Bubendorf, Switzerland; see Figure S4). Preactivated PC2 was incubated at room temperature with varying concentrations of the inhibitor (2.9 – 250 nM) in assay buffer for 45 min. Substrate **7** (25 μ M in the assay) was then added. The plot of the initial velocities v versus the four lowest inhibitor concentrations gave a straight line with an intercept of approximately 51 nM corresponding to the enzyme concentration.

Measurements with human PC5A

Transfection of HEK293T cells (T175 cell culture flasks, 30 mL DMEM medium supplemented with 10% fetal calf serum and 1% penicillin/streptomycin/glutamine) with 50 μ g PC5A plasmid (Origene, Rockville, Maryland, United States) or the corresponding empty vector (Origene, Rockville, Maryland, United States) were performed with Lipofectamine3000 (ThermoFisher Scientific, Waltham, Massachusetts, United States) according to the manufacturer's instructions. 48 h post transfection, the supernatant was centrifuged to remove cell debris and concentrated to 4 mL in Amicon ultracentrifugation filters (Merck, Darmstadt, Germany).

The measurements were performed in opaque 96-well plates 3365 (Corning, Kaiserslautern, Germany). Each well contained 75 μ L PC5 buffer (20 mM BisTris, 5 mM CaCl₂; pH 6.5) and 5 μ L substrate solution. The measurements were started by addition of 20 μ L enzyme preparation providing a total assay volume of 100 μ L. The background activity was determined with the empty vector control and subtracted from the values obtained with PC5A.

Measurements with human PC7

The measurements were performed in opaque 96-well plates 3365 (Corning, Kaiserslautern, Germany). Human recombinant PC7 (R&D systems, Minneapolis, Minnesota, United States) was diluted to 50 μ g/mL in buffer (50 mM Tris, 10 mM CaCl₂, 0.15 M NaCl, 0.05 % Brij 35; pH 7.5) and activated by addition of 2.0 μ g/mL thermolysin (R&D systems, Minneapolis, Minnesota, United States) for 4 h at 37 °C. To inhibit thermolysin activity, 1,10-phenanthroline was added at a final concentration of 10 mM. Then, the enzyme was diluted to 13.90 nM with assay buffer (25 mM Tris; pH 7.0). Each well contained 60 μ L PC7 assay buffer and 20 μ L substrate solution. The measurements were started by addition of 20 μ L enzyme solution (2.78 nM in the assay) providing a total assay volume of 100 μ L.

Acknowledgement

Part of this work was supported by the Deutsche Forschungsgemeinschaft (HA 7910/1-1 to K.H.).

Abbreviations

Ac, acetyl; Amba, 4-amidinobenzylamide; AMC, 7-amino-4-methylcoumarin; CMK, chloromethyl ketone; DCM, dichloromethane; DIPEA, *N,N*-diisopropylethylamine; DMF, dimethylformamide; DMSO, dimethyl sulfoxide; Fmoc, 9-fluorenylmethoxycarbonyl; FRET, fluorescence resonance energy transfer; HBTU, *O*-(benzotriazol-1-yl)-tetramethyluronium hexafluorophosphate; HOBt, 1-hydroxybenzotriazole; HPLC, high-performance liquid chromatography; MS, mass spectrometry; PC, proprotein convertase; Phac, phenylacetyl; Pyr, pyroglutamic acid; TFA, trifluoroacetic acid

References

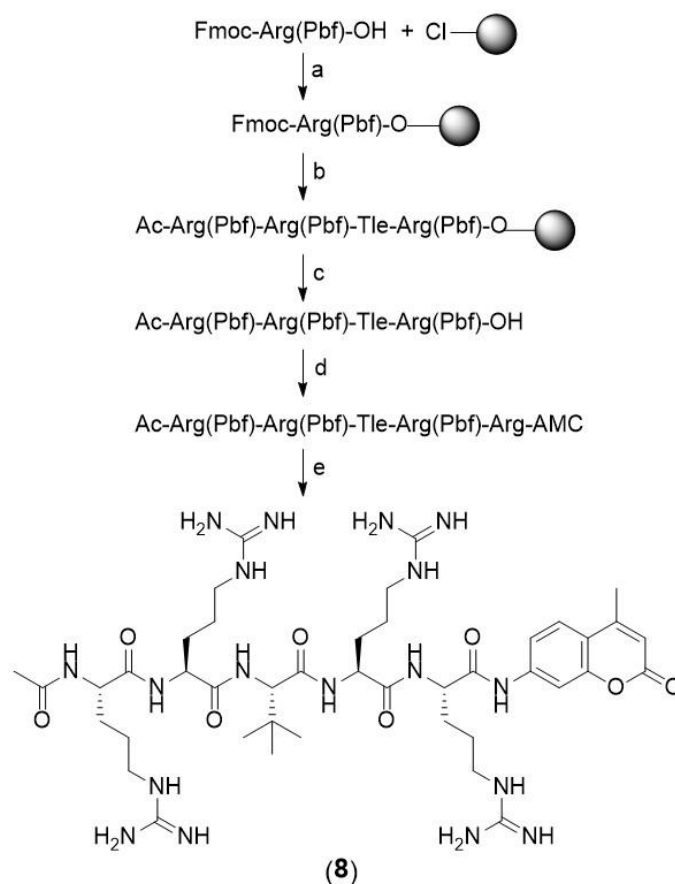
- (1) Seidah, N. G.; Prat, A. Precursor convertases in the secretory pathway, cytosol and extracellular milieu. *Essays in biochemistry* **2002**, *38*, 79–94.
- (2) Seidah, N. G.; Prat, A. The biology and therapeutic targeting of the proprotein convertases. *Nature reviews. Drug discovery* **2012**, *11*, 367–383.
- (3) Seidah, N. G.; Mayer, G.; Zaid, A.; Rousselet, E.; Nassoury, N.; Poirier, S.; Essalmani, R.; Prat, A. The activation and physiological functions of the proprotein convertases. *The international journal of biochemistry & cell biology* **2008**, *40*, 1111–1125.
- (4) Shiryayev, S. A.; Chernov, A. V.; Golubkov, V. S.; Thomsen, E. R.; Chudin, E.; Chee, M. S.; Kozlov, I. A.; Strongin, A. Y.; Cieplak, P. High-resolution analysis and functional mapping of cleavage sites and substrate proteins of furin in the human proteome. *PLoS one* **2013**, *8*, e54290.
- (5) Artenstein, A. W.; Opal, S. M. Proprotein convertases in health and disease. *The New England journal of medicine* **2011**, *365*, 2507–2518.
- (6) Bestle, D.; Heindl, M. R.; Limburg, H.; van Lam van, T.; Pilgram, O.; Moulton, H.; Stein, D. A.; Harges, K.; Eickmann, M.; Dolnik, O.; *et al.* TMPRSS2 and furin are both essential for proteolytic activation of SARS-CoV-2 in human airway cells. *Life science alliance* **2020**, *3*.

- (7) Stieneke-Gröber, A.; Vey, M.; Angliker, H.; Shaw, E.; Thomas, G.; Roberts, C.; Klenk, H. D.; Garten, W. Influenza virus hemagglutinin with multibasic cleavage site is activated by furin, a subtilisin-like endoprotease. *The EMBO journal* **1992**, *11*, 2407–2414.
- (8) Rockwell, N. C.; Krysan, D. J.; Komiyama, T.; Fuller, R. S. Precursor processing by kex2/furin proteases. *Chemical reviews* **2002**, *102*, 4525–4548.
- (9) Basak, A.; Chen, A.; Majumdar, S.; Smith, H. P. In vitro assay for protease activity of proprotein convertase subtilisin kexins (PCSKs): an overall review of existing and new methodologies. *Methods in molecular biology (Clifton, N.J.)* **2011**, *768*, 127–153.
- (10) Munzer, J. S.; Basak, A.; Zhong, M.; Mamarbachi, A.; Hamelin, J.; Savaria, D.; Lazure, C.; Hendy, G. N.; Benjannet, S.; Chrétien, M.; *et al.* In vitro characterization of the novel proprotein convertase PC7. *The Journal of biological chemistry* **1997**, *272*, 19672–19681.
- (11) Molloy, S. S.; Bresnahan, P. A.; Leppla, S. H.; Klimpel, K. R.; Thomas, G. Human furin is a calcium-dependent serine endoprotease that recognizes the sequence Arg-X-X-Arg and efficiently cleaves anthrax toxin protective antigen. *The Journal of biological chemistry* **1992**, *267*, 16396–16402.
- (12) Lamango, N. S.; Zhu, X.; Lindberg, I. Purification and enzymatic characterization of recombinant prohormone convertase 2: stabilization of activity by 21 kDa 7B2. *Archives of biochemistry and biophysics* **1996**, *330*, 238–250.
- (13) Koshland, D. E. The application and usefulness of the ratio $k(\text{cat})/K(\text{M})$. *Bioorganic chemistry* **2002**, *30*, 211–213.
- (14) Copeland, R. A. *Evaluation of enzyme inhibitors in drug discovery: A guide for medicinal chemists and pharmacologists*; Methods of biochemical analysis v. 46; J. Wiley: Hoboken, N.J., 2005.
- (15) Hatsuzawa, K.; Nagahama, M.; Takahashi, S.; Takada, K.; Murakami, K.; Nakayama, K. Purification and characterization of furin, a Kex2-like processing endoprotease, produced in Chinese hamster ovary cells. *The Journal of biological chemistry* **1992**, *267*, 16094–16099.
- (16) Jean, F.; Boudreault, A.; Basak, A.; Seidah, N. G.; Lazure, C. Fluorescent peptidyl substrates as an aid in studying the substrate specificity of human prohormone convertase PC1 and human furin and designing a potent irreversible inhibitor. *The Journal of biological chemistry* **1995**, *270*, 19225–19231.
- (17) Krysan, D. J.; Rockwell, N. C.; Fuller, R. S. Quantitative characterization of furin specificity. Energetics of substrate discrimination using an internally consistent set of hexapeptidyl methylcoumarinamides. *The Journal of biological chemistry* **1999**, *274*, 23229–23234.
- (18) Angliker, H.; Neumann, U.; Molloy, S. S.; Thomas, G. Internally quenched fluorogenic substrate for furin. *Analytical biochemistry* **1995**, *224*, 409–412.
- (19) Basak, A.; Zhong, M.; Munzer, J. S.; Chrétien, M.; Seidah, N. G. Implication of the proprotein convertases furin, PC5 and PC7 in the cleavage of surface glycoproteins of Hong Kong, Ebola and respiratory syncytial viruses: a comparative analysis with fluorogenic peptides. *The Biochemical journal* **2001**, *353*, 537–545.
- (20) Izidoro, M. A.; Gouvea, I. E.; Santos, J. A. N.; Assis, D. M.; Oliveira, V.; Judice, W. A. S.; Juliano, M. A.; Lindberg, I.; Juliano, L. A study of human furin specificity using synthetic peptides derived from natural substrates, and effects of potassium ions. *Archives of biochemistry and biophysics* **2009**, *487*, 105–114.
- (21) Lazure, C.; Gauthier, D.; Jean, F.; Boudreault, A.; Seidah, N. G.; Bennett, H. P.; Hendy, G. N. In vitro cleavage of internally quenched fluorogenic human parathyroid hormone and parathyroid-related peptide substrates by furin. Generation of a potent inhibitor. *The Journal of biological chemistry* **1998**, *273*, 8572–8580.
- (22) Liu, Y.; Kati, W.; Chen, C. M.; Tripathi, R.; Molla, A.; Kohlbrenner, W. Use of a fluorescence plate reader for measuring kinetic parameters with inner filter effect correction. *Analytical biochemistry* **1999**, *267*, 331–335.
- (23) Becker, G. L.; Lu, Y.; Hards, K.; Strehlow, B.; Levesque, C.; Lindberg, I.; Sandvig, K.; Bakowsky, U.; Day, R.; Garten, W.; *et al.* Highly potent inhibitors of proprotein convertase furin as potential

- drugs for treatment of infectious diseases. *The Journal of biological chemistry* **2012**, *287*, 21992–22003.
- (24) Harges, K.; Becker, G. L.; Lu, Y.; Dahms, S. O.; Köhler, S.; Beyer, W.; Sandvig, K.; Yamamoto, H.; Lindberg, I.; Walz, L.; *et al.* Novel Furin Inhibitors with Potent Anti-infectious Activity. *ChemMedChem* **2015**, *10*, 1218–1231.
- (25) Harges, K.; Ivanova, T.; Thaa, B.; McInerney, G. M.; Klock, T. I.; Sandvig, K.; Künzel, S.; Lindberg, I.; Steinmetzer, T. Elongated and Shortened Peptidomimetic Inhibitors of the Proprotein Convertase Furin. *ChemMedChem* **2017**, *12*, 613–620.
- (26) Ivanova, T.; Harges, K.; Kallis, S.; Dahms, S. O.; Than, M. E.; Künzel, S.; Böttcher-Friebertshäuser, E.; Lindberg, I.; Jiao, G.-S.; Bartenschlager, R.; *et al.* Optimization of Substrate-Analogue Furin Inhibitors. *ChemMedChem* **2017**, *12*, 1953–1968.
- (27) van Lam van, T.; Ivanova, T.; Harges, K.; Heindl, M. R.; Morty, R. E.; Böttcher-Friebertshäuser, E.; Lindberg, I.; Than, M. E.; Dahms, S. O.; Steinmetzer, T. Design, Synthesis, and Characterization of Macrocyclic Inhibitors of the Proprotein Convertase Furin. *ChemMedChem* **2019**, *14*, 673–685.
- (28) Becker, G. L.; Sielaff, F.; Than, M. E.; Lindberg, I.; Routhier, S.; Day, R.; Lu, Y.; Garten, W.; Steinmetzer, T. Potent inhibitors of furin and furin-like proprotein convertases containing decarboxylated P1 arginine mimetics. *Journal of medicinal chemistry* **2010**, *53*, 1067–1075.
- (29) Becker, G. L.; Harges, K.; Steinmetzer, T. New substrate analogue furin inhibitors derived from 4-amidinobenzylamide. *Bioorganic & medicinal chemistry letters* **2011**, *21*, 4695–4697.
- (30) van Lam van, T.; Heindl, M. R.; Schlutt, C.; Böttcher-Friebertshäuser, E.; Bartenschlager, R.; Klebe, G.; Brandstetter, H.; Dahms, S. O.; Steinmetzer, T. The Basicity Makes the Difference: Improved Canavanine-Derived Inhibitors of the Proprotein Convertase Furin. *ACS medicinal chemistry letters* **2021**, *12*, 426–432.
- (31) Dahms, S. O.; Harges, K.; Steinmetzer, T.; Than, M. E. X-ray Structures of the Proprotein Convertase Furin Bound with Substrate Analogue Inhibitors Reveal Substrate Specificity Determinants beyond the S4 Pocket. *Biochemistry* **2018**, *57*, 925–934.
- (32) Kacprzak, M. M.; Peinado, J. R.; Than, M. E.; Appel, J.; Henrich, S.; Lipkind, G.; Houghten, R. A.; Bode, W.; Lindberg, I. Inhibition of furin by polyarginine-containing peptides: nanomolar inhibition by nona-D-arginine. *The Journal of biological chemistry* **2004**, *279*, 36788–36794.
- (33) Gagnon, H.; Beauchemin, S.; Kwiatkowska, A.; Couture, F.; D'Anjou, F.; Levesque, C.; Dufour, F.; Desbiens, A. R.; Vaillancourt, R.; Bernard, S.; *et al.* Optimization of furin inhibitors to protect against the activation of influenza hemagglutinin H5 and Shiga toxin. *Journal of medicinal chemistry* **2014**, *57*, 29–41.
- (34) Lewandowska-Goch, M. A.; Kwiatkowska, A.; Łepeck, T.; Ly, K.; Navals, P.; Gagnon, H.; Dory, Y. L.; Prah, A.; Day, R. Design and Structure-Activity Relationship of a Potent Furin Inhibitor Derived from Influenza Hemagglutinin. *ACS medicinal chemistry letters* **2021**, *12*, 365–372.
- (35) Schechter, I.; Berger, A. On the size of the active site in proteases. I. Papain. *Biochemical and biophysical research communications* **1967**, *27*, 157–162.
- (36) Williams, J. W.; Morrison, J. F. The kinetics of reversible tight-binding inhibition. *Methods in enzymology* **1979**, *63*, 437–467.
- (37) Morrison, J. F. The slow-binding and slow, tight-binding inhibition of enzyme-catalysed reactions. *Trends in Biochemical Sciences* **1982**, *7*, 102–105.
- (38) Stein, R. L.; Strimpler, A. M.; Edwards, P. D.; Lewis, J. J.; Mauger, R. C.; Schwartz, J. A.; Stein, M. M.; Trainor, D. A.; Wildonger, R. A.; Zottola, M. A. Mechanism of slow-binding inhibition of human leukocyte elastase by trifluoromethyl ketones. *Biochemistry* **1987**, *26*, 2682–2689.
- (39) Zhang, X.; Pan, H.; Peng, B.; Steiner, D. F.; Pintar, J. E.; Fricker, L. D. Neuropeptidomic analysis establishes a major role for prohormone convertase-2 in neuropeptide biosynthesis. *Journal of neurochemistry* **2010**, *112*, 1168–1179.

- (40) Izaguirre, G.; Arciniega, M.; Quezada, A. G. Specific and Selective Inhibitors of Proprotein Convertases Engineered by Transferring Serpin B8 Reactive-Site and Exosite Determinants of Reactivity to the Serpin α 1PDX. *Biochemistry* **2019**, *58*, 1679–1688.
- (41) Yu, B.; Hunt, J. F. Enzymological and structural studies of the mechanism of promiscuous substrate recognition by the oxidative DNA repair enzyme AlkB. *Proceedings of the National Academy of Sciences of the United States of America* **2009**, *106*, 14315–14320.
- (42) Icimoto, M. Y.; Barros, N. M.; Ferreira, J. C.; Marcondes, M. F.; Andrade, D.; Machado, M. F.; Juliano, M. A.; Júdice, W. A.; Juliano, L.; Oliveira, V. Hysteretic behavior of proprotein convertase 1/3 (PC1/3). *PLoS one* **2011**, *6*, e24545.
- (43) Fugère, M.; Limperis, P. C.; Beaulieu-Audy, V.; Gagnon, F.; Lavigne, P.; Klarskov, K.; Leduc, R.; Day, R. Inhibitory potency and specificity of subtilase-like pro-protein convertase (SPC) prodomains. *The Journal of biological chemistry* **2002**, *277*, 7648–7656.
- (44) Stawowy, P.; Fleck, E. Proprotein convertases furin and PC5: targeting atherosclerosis and restenosis at multiple levels. *Journal of molecular medicine (Berlin, Germany)* **2005**, *83*, 865–875.
- (45) Khatib, A.-M.; Siegfried, G.; Chrétien, M.; Metrakos, P.; Seidah, N. G. Proprotein convertases in tumor progression and malignancy: novel targets in cancer therapy. *The American journal of pathology* **2002**, *160*, 1921–1935.
- (46) Aljofan, M.; Singh, H.; Ho, H.; Xie, S.; Zhu, Y.; Sun, Z.; Guo, X.; Wang, J.; Nie, G. Inhibition of proprotein convertase 5/6 activity: potential for nonhormonal women-centered contraception. *Contraception* **2012**, *85*, 602–610.
- (47) Chrétien, M.; Seidah, N. G.; Basak, A.; Mbikay, M. Proprotein convertases as therapeutic targets. *Expert opinion on therapeutic targets* **2008**, *12*, 1289–1300.
- (48) Seidah, N. G.; Sadr, M. S.; Chrétien, M.; Mbikay, M. The multifaceted proprotein convertases: their unique, redundant, complementary, and opposite functions. *The Journal of biological chemistry* **2013**, *288*, 21473–21481.
- (49) Seidah, N. G. What lies ahead for the proprotein convertases? *Annals of the New York Academy of Sciences* **2011**, *1220*, 149–161.
- (50) Zhou, Y.; Lindberg, I. Purification and characterization of the prohormone convertase PC1(PC3). *The Journal of biological chemistry* **1993**, *268*, 5615–5623.

Supporting Information

Synthesis of substrate **8**

Scheme S1. Synthesis of substrate **8**. (a) loading of 2-chlorotrityl chloride resin with 1 equiv. of Fmoc-Arg(Pbf)-OH, 4 equiv. of DIPEA, dry DCM, 2 h; (b) Fmoc-SPPS, double couplings with 4 equiv. of amino acid, HBTU, HOBT, and 8 equiv. of DIPEA, respectively; (c) cleavage from the resin with 1 % TFA in DCM, three times for 30 min, removal of the solvent in vacuo; (d) 1 equiv. of H-Arg-AMC \times 2 HCl, 1 equiv. of PyAOP, 3 equiv. of DIPEA in DMF, 15 min 0 °C, 4 h at room temperature (e) removal of the protecting groups with TFA/TIS/H₂O (95/2.5/2.5, v/v/v), 3 h, precipitation in cold diethyl ether, purification by preparative HPLC. The substrate was purified by reversed phase preparative HPLC and obtained as lyophilized TFA salt.

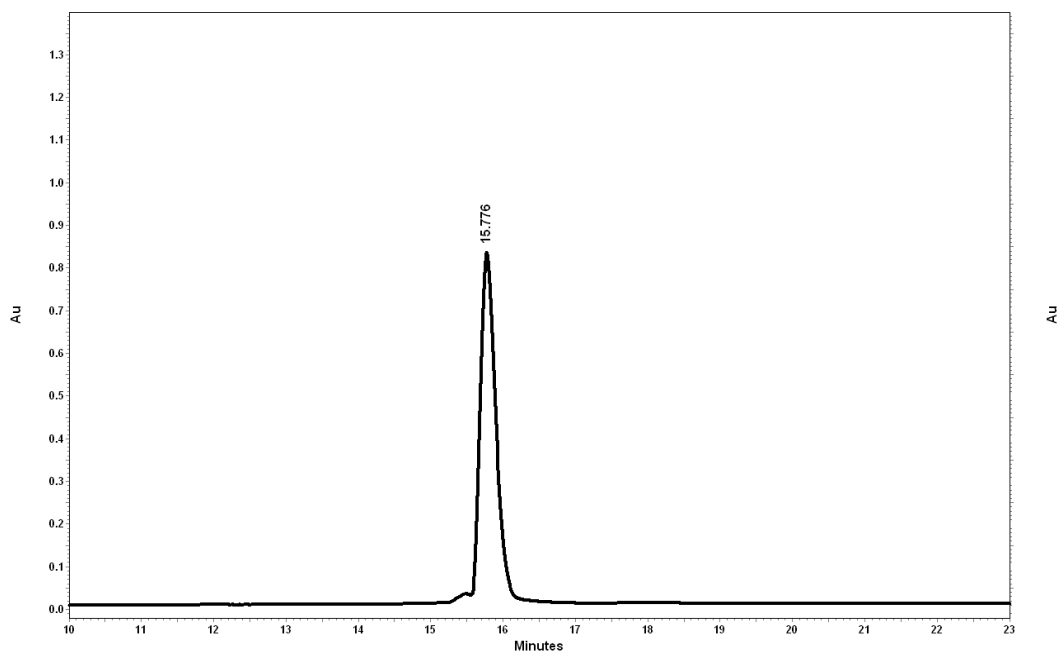
Chromatogram of substrate **8**

Figure S1. Chromatogram of substrate **8** (Ac-Arg-Arg-Tle-Arg-Arg-AMC) (retention time: 15.8 min, start at 10 % acetonitrile).

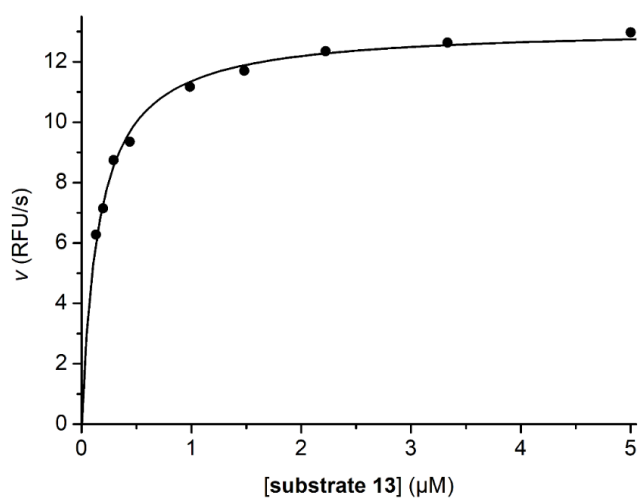
Michaelis-Menten plot of substrate **13** with furin

Figure S2. Michaelis-Menten plot of the furin-catalyzed cleavage of substrate **13** (H-Arg-Arg-Arg-Tle-Lys-Arg-AMC) using an enzyme concentration of 0.95 nM.

Active site titration of mPC1

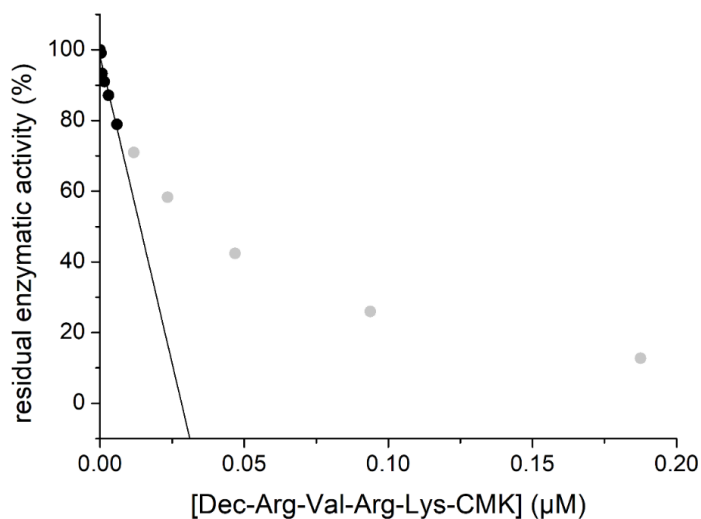


Figure S3. Active site titration of mPC1 using the irreversible inhibitor Dec-Arg-Val-Arg-Lys-CMK. The remaining residual activity was determined in presence of 50 µM substrate **2**.

Active site titration of mPC2

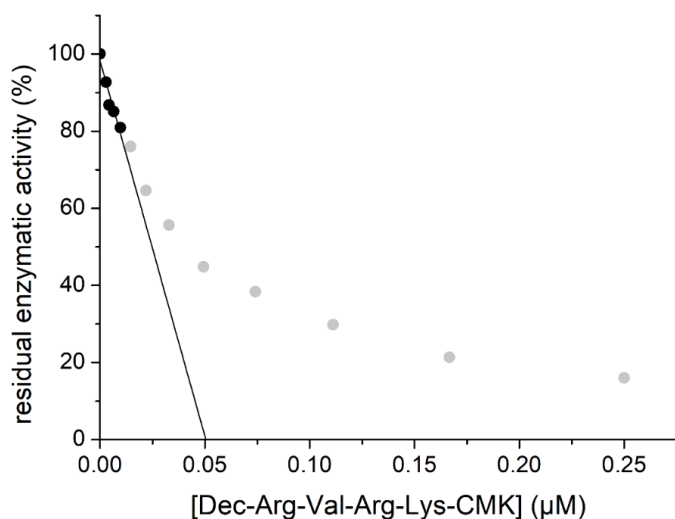


Figure S4. Active site titration of mPC2 using the irreversible inhibitor Dec-Arg-Val-Arg-Lys-CMK. The remaining residual activity was determined in presence of 25 µM substrate **7**.

5 Conclusion and future perspectives

Despite its importance for manifold physiological processes, the basic proprotein convertase furin can be inhibited for a short-term treatment of acute infectious diseases caused by furin-dependent pathogenic viruses. In particular, furin has recently come into the focus as an important drug target, since it is one of the activating host proteases for the SARS-CoV-2 spike protein. The inhibition of furin prohibits the replication of this virus.

Based on the multibasic furin recognition sequence with the consensus motif –Arg–X–Lys/Arg–Arg↓– and previous data from our group, novel substrate-analogue furin inhibitors were synthesized and characterized in this thesis. Furthermore, a set of new fluorogenic substrates of the basic PCs have been prepared and analysed.

Inspired by a crystal structure of a hexapeptide-derived inhibitor containing a C-terminal 4-amidinobenzylamide group (inhibitor **3**) in complex with furin and by numerous reports of approved macrocyclic inhibitors of other proteases, several small series of cyclic furin inhibitors were elaborated in this work. These differ in the cyclization method by using different type of linkers and the positions of the residues involved in the cyclization. Some of the new cyclic inhibitors possess inhibition constants in the low nanomolar or even sub-nanomolar range. Several crystal structures of these cyclized inhibitors in complex with furin were determined in cooperation with a group from the University of Salzburg. However, despite their strong inhibitory potency in enzyme kinetic assays, the cyclic inhibitors did not show any antiviral effect in cells infected by the respiratory syncytial virus (RSV), where furin activates its fusion protein F. In parallel, a significant antiviral efficacy was observed for the non-cyclic reference inhibitor **2/MI-1148** suggesting a reduced membrane permeability and cellular uptake of the considerably larger cyclic inhibitors.

However, inhibitor **2/MI-1148** is poorly tolerated and possesses a severe toxicity in rodents, probably caused by the strongly multibasic character of these compounds. The toxicity of this compound could be reduced by replacing one or two Arg residues by the less basic amino acid canavanine possessing a weakly basic oxyguanidine group in its side chain ($pK_a \approx 7.01$). These compounds exhibit a similar binding mode as previously observed in crystal structures of furin in complex with inhibitor **2/MI-1148**. This likely also explains the comparable K_i value of the new canavanine analogues, e.g., inhibitor **6/MI-1851** possesses only a slightly weaker K_i value

of 10.1 pM but comparable antiviral activity against furin-dependent viruses, such as RSV, WNV, and Dengue-2 virus.

In cooperation with the institute of Virology, inhibitor **6/MI-1851** was also shown to substantially reduce SARS-CoV-2 replication in infected Calu-3 cells due to the inhibition of the furin-catalyzed activation of the S1/S2 site in its spike surface protein. Although postulated before, based on sequence alignments of S protein from different CoV, these data indicated for the first time the crucial importance of furin for the S protein activation in these cells. They were supported by analysing a small series of newly prepared FRET substrates derived from the S1/S2 site of the S protein from certain CoV. It could be verified that the SARS-CoV-2 sequence is efficiently cleaved by furin, whereas a negligible cleavage was found for the SARS-CoV substrate and a 5-fold reduced cleavage of the MERS-CoV sequence. In summary, the current data strongly suggest that an efficient furin inhibition could be a promising therapeutic intervention for the treatment of SARS-CoV-2 infections. Moreover, a similar series of FRET substrates derived from the S2' site of the S protein was prepared. In this case the SARS-CoV-2 sequence very poorly cleaved by furin suggesting that a different host protease must cleave the peptide bond in front of the fusion peptide. Numerous studies suggest that this S2' cleavage is performed by the trypsin-like serine protease TMPRSS2.

To reveal the improvement of canavanine-derived inhibitors, a toxicity study in mice was performed and in case of inhibitor **6/MI-1851** all mice accepted a 6-fold higher *ip.* dose of 15 mg/kg when compared with the linear inhibitor **2/MI-1148**. So far, no higher dose of inhibitor **6/MI-1851** was tested. In combination with the strong antiviral potency of inhibitor **6/MI-1851**, which requires an efficient inhibition of the intracellular furin in the TGN, these results confirmed our hypothesis that the toxicity of these substrate-analogue furin inhibitors does not correlate with the strength of intracellular furin inhibition. The toxicity of these compounds must depend on the addressing of another, as yet unknown, off-target.

These results provided a promising future direction for the development of further improved inhibitors by replacing the remaining guanidine groups on the P5 residues with alternative less basic substituents. Another possibility could be the replacement of the benzamidine group in P1 position with less basic arginine mimetics.

To fully understand the relationship between the overall basicity and toxicity of these inhibitors, the postulated off-target should be identified. In a safety screen with inhibitors

2/MI-1148 using 44 potential receptor or enzyme targets performed at the company Eurofins, no clear off-target could be identified, so far.

Furthermore, a set of new fluorogenic substrates with a C-terminal Arg-AMC moiety has been prepared, which was analysed with five basic PCs. For certain PCs (except PC5A) improved substrates could be identified, which enable measurements with reduced enzyme concentrations in future. Using optimized conditions for furin measurements in presence of an improved substrate and reduced enzyme concentration enabled the determination of inhibition constants of previously identified tight-binding inhibitors under more robust classical conditions without the knowledge of the exact enzyme concentration.

In summary, very potent substrate-analogue reversible furin inhibitors were developed, synthesized, and characterized. The most promising inhibitor **6/MI-1851** containing two less basic canavanine residues showed a significant antiviral activity in infected cell at strongly reduced toxicity in mice and rats when compared to previous compounds from our group. However, further preclinical studies with these furin inhibitors have to be performed to demonstrate their antiviral efficacy in a suitable animal model *in vivo*.

6 References

- (1) Seidah, N. G.; Prat, A. The biology and therapeutic targeting of the proprotein convertases. *Nat Rev Drug Discov* **2012**, *11*, 367–383.
- (2) Ruth Hogue Angeletti. *Proteins: analysis and design*; Elsevier, 1998.
- (3) Puente, X. S.; Sánchez, L. M.; Overall, C. M.; López-Otín, C. Human and mouse proteases: a comparative genomic approach. *Nature reviews. Genetics* **2003**, *4*, 544–558.
- (4) Oda, K. New families of carboxyl peptidases: serine-carboxyl peptidases and glutamic peptidases. *Journal of biochemistry* **2012**, *151*, 13–25.
- (5) Rawlings, N. D.; Waller, M.; Barrett, A. J.; Bateman, A. MEROPS: the database of proteolytic enzymes, their substrates and inhibitors. *Nucleic acids research* **2014**, *42*, D503-9.
- (6) Madala, P. K.; Tyndall, J. D.; Nall, T.; Fairlie, D. P. Update 1 of: Proteases universally recognize beta strands in their active sites. *Chemical reviews* **2010**, *110*.
- (7) Seidah, N. G.; Mayer, G.; Zaid, A.; Rousselet, E.; Nassoury, N.; Poirier, S.; Essalmani, R.; Prat, A. The activation and physiological functions of the proprotein convertases. *Int J Biochem Cell Biol.* **2008**, *40*, 1111–1125.
- (8) Pasquato, A.; Rochat, C.; Burri, D. J.; Pasqual, G.; La Torre, J. C. de; Kunz, S. Evaluation of the anti-arenaviral activity of the subtilisin kexin isozyme-1/site-1 protease inhibitor PF-429242. *Virology* **2012**, *423*, 14–22.
- (9) Creemers, John W M; Khatib, A.-M. Knock-out mouse models of proprotein convertases: unique functions or redundancy? *Frontiers in bioscience : a journal and virtual library* **2008**, *13*, 4960–4971.
- (10) Thomas, G. Furin at the cutting edge: from protein traffic to embryogenesis and disease. *Nat Rev Mol Cell Biol* **2002**, *3*, 753–766.
- (11) Shakya, M.; Lindberg, I. Mouse Models of Human Proprotein Convertase Insufficiency. *Endocrine reviews* **2021**, *42*, 259–294.
- (12) Constam, D. B.; Calfon, M.; Robertson, E. J. SPC4, SPC6, and the novel protease SPC7 are coexpressed with bone morphogenetic proteins at distinct sites during embryogenesis. *J Cell Biol* **1996**, *134*, 181–191.
- (13) Roebroek, Anton J M; Taylor, N. A.; Louagie, E.; Pauli, I.; Smeijers, L.; Snellinx, A.; Lauwers, A.; Van de Ven, Wim J M; Hartmann, D.; Creemers, John W M. Limited redundancy of the proprotein convertase furin in mouse liver. *J Biol Chem* **2004**, *279*, 53442–53450.
- (14) Couture, F.; D'Anjou, F.; Day, R. On the cutting edge of proprotein convertase pharmacology: from molecular concepts to clinical applications. *Biomol Concepts* **2011**, *2*, 421–438.
- (15) Henrich, S.; Lindberg, I.; Bode, W.; Than, M. E. Proprotein convertase models based on the crystal structures of furin and kexin: explanation of their specificity. *J Mol Biol* **2005**, *345*, 211–227.

- (16) Seidah, N. G.; Sadr, M. S.; Chrétien, M.; Mbikay, M. The multifaceted proprotein convertases: their unique, redundant, complementary, and opposite functions. *The Journal of biological chemistry* **2013**, *288*, 21473–21481.
- (17) Seidah, N. G. What lies ahead for the proprotein convertases? *Annals of the New York Academy of Sciences* **2011**, *1220*, 149–161.
- (18) Roebroek, A. J.; Schalken, J. A.; Leunissen, J. A.; Onnekink, C.; Bloemers, H. P.; van de Ven, W. J. Evolutionary conserved close linkage of the c-fes/fps proto-oncogene and genetic sequences encoding a receptor-like protein. *The EMBO Journal* **1986**, *5*, 2197–2202.
- (19) Julius, D.; Brake, A.; Blair, L.; Kunisawa, R.; Thorner, J. Isolation of the putative structural gene for the lysine-arginine-cleaving endopeptidase required for processing of yeast prepro-alpha-factor. *Cell* **1984**, *37*.
- (20) Fuller, R. S.; Brake, A. J.; Thorner, J. Intracellular targeting and structural conservation of a prohormone-processing endoprotease. *Science (New York, N.Y.)* **1989**, *246*, 482–486.
- (21) van de Ven, W. J.; Voorberg, J.; Fontijn, R.; Pannekoek, H.; van den Ouweland, A. M.; van Duijnhoven, H. L.; Roebroek, A. J.; Siezen, R. J. Furin is a subtilisin-like proprotein processing enzyme in higher eukaryotes. *Molecular biology reports* **1990**, *14*, 265–275.
- (22) Thacker, C.; Am Rose. A look at the *Caenorhabditis elegans* Kex2/Subtilisin-like proprotein convertase family. *BioEssays : news and reviews in molecular, cellular and developmental biology* **2000**, *22*.
- (23) Seidah, N. G.; Day, R.; Marcinkiewicz, M.; Chrétien, M. Precursor convertases: an evolutionary ancient, cell-specific, combinatorial mechanism yielding diverse bioactive peptides and proteins. *Annals of the New York Academy of Sciences* **1998**, *839*, 9–24.
- (24) Rockwell, N. C.; Krysan, D. J.; Komiyama, T.; Fuller, R. S. Precursor processing by kex2/furin proteases. *Chem Rev* **2002**, *102*, 4525–4548.
- (25) Siezen, R. J.; Creemers, J. W.; Van, d. V. W. Homology modelling of the catalytic domain of human furin. A model for the eukaryotic subtilisin-like proprotein convertases. *European journal of biochemistry* **1994**, *222*.
- (26) Dahms, S. O.; Harges, K.; Becker, G. L.; Steinmetzer, T.; Brandstetter, H.; Than, M. E. X-ray structures of human furin in complex with competitive inhibitors. *ACS chemical biology* **2014**, *9*, 1113–1118.
- (27) Anderson, E. D.; VanSlyke, J. K.; Thulin, C. D.; Jean, F.; Thomas, G. Activation of the furin endoprotease is a multiple-step process: requirements for acidification and internal propeptide cleavage. *The EMBO Journal* **1997**, *16*, 1508–1518.
- (28) Anderson, E. D.; Molloy, S. S.; Jean, F.; Fei, H.; Shimamura, S.; Thomas, G. The ordered and compartment-specific autoproteolytic removal of the furin intramolecular chaperone is required for enzyme activation. *J Biol Chem* **2002**, *277*, 12879–12890.
- (29) Machen, T. E.; Leigh, M. J.; Taylor, C.; Kimura, T.; Asano, S.; Moore, H.-P. H. pH of TGN and recycling endosomes of H⁺/K⁺-ATPase-transfected HEK-293 cells: implications for pH

regulation in the secretory pathway. *American journal of physiology. Cell physiology* **2003**, *285*, C205-14.

(30) Vey, M.; Schäfer, W.; Berghöfer, S.; Klenk, H. D.; Garten, W. Maturation of the trans-Golgi network protease furin: compartmentalization of propeptide removal, substrate cleavage, and COOH-terminal truncation. *The Journal of cell biology* **1994**, *127*, 1829–1842.

(31) Takahashi, S.; Nakagawa, T.; Banno, T.; Watanabe, T.; Murakami, K.; Nakayama, K. Localization of furin to the trans-Golgi network and recycling from the cell surface involves Ser and Tyr residues within the cytoplasmic domain. *J Biol Chem* **1995**, *270*, 28397–28401.

(32) Braun, E.; Sauter, D. Furin-mediated protein processing in infectious diseases and cancer. *Clinical & translational immunology* **2019**, *8*, e1073.

(33) Izidoro, M. A.; Gouvea, I. E.; Santos, J. A. N.; Assis, D. M.; Oliveira, V.; Judice, W. A. S.; Juliano, M. A.; Lindberg, I.; Juliano, L. A study of human furin specificity using synthetic peptides derived from natural substrates, and effects of potassium ions. *Archives of biochemistry and biophysics* **2009**, *487*, 105–114.

(34) Chakraborti, S.; Dhalla, N. S. *Pathophysiological Aspects of Proteases*; Springer: Singapore, 2017.

(35) Tian, S.; Huang, Q.; Fang, Y.; Wu, J. FurinDB: A database of 20-residue furin cleavage site motifs, substrates and their associated drugs. *International journal of molecular sciences* **2011**, *12*, 1060–1065.

(36) Nakayama, K. Furin: a mammalian subtilisin/Kex2p-like endoprotease involved in processing of a wide variety of precursor proteins. *Biochem J* **1997**, *327 (Pt 3)*, 625–635.

(37) Essalmani, R.; Susan-Resiga, D.; Chamberland, A.; Abifadel, M.; Creemers, J. W.; Boileau, C.; Seidah, N. G.; Prat, A. In vivo evidence that furin from hepatocytes inactivates PCSK9. *The Journal of biological chemistry* **2011**, *286*.

(38) Jin, W.; Fuki, IV; Seidah, N. G.; Benjannet, S.; Glick, J. M.; Rader, D. J. Proprotein convertases are responsible for proteolysis and inactivation of endothelial lipase. *The Journal of biological chemistry* **2005**, *280*.

(39) Roebroek, A. J.; Umans, L.; Pauli, I. G.; Robertson, E. J.; van Leuven, F.; Van de Ven, W J; Constam, D. B. Failure of ventral closure and axial rotation in embryos lacking the proprotein convertase Furin. *Development (Cambridge, England)* **1998**, *125*, 4863–4876.

(40) Kim, W.; Essalmani, R.; Szumska, D.; Creemers, J. W. M.; Roebroek, A. J. M.; D'Orleans-Juste, P.; Bhattacharya, S.; Seidah, N. G.; Prat, A. Loss of endothelial furin leads to cardiac malformation and early postnatal death. *Molecular and cellular biology* **2012**, *32*, 3382–3391.

(41) Giannelli, F.; Green, P. M.; High, K. A.; Sommer, S.; Lillicrap, D. P.; Ludwig, M.; Olek, K.; Reitsma, P. H.; Goossens, M.; Yoshioka, A. Haemophilia B: database of point mutations and short additions and deletions--second edition. *Nucleic Acids Res* **1991**, *19 Suppl*, 2193–2219.

- (42) Chen, Y.; Molloy, S. S.; Thomas, L.; Gambia, J.; Bächinger, H. P.; Ferguson, B.; Zonana, J.; Thomas, G.; Morris, N. P. Mutations within a furin consensus sequence block proteolytic release of ectodysplasin-A and cause X-linked hypohidrotic ectodermal dysplasia. *Proc Natl Acad Sci U S A* **2001**, *98*, 7218–7223.
- (43) Bassi, D. E.; Fu, J.; Lopez De Cicco, Ricardo; Klein-Szanto, A. J. P. Proprotein convertases: "master switches" in the regulation of tumor growth and progression. *Mol Carcinog* **2005**, *44*, 151–161.
- (44) Wu, Y.; Yakar, S.; Zhao, L.; Hennighausen, L.; LeRoith, D. Circulating insulin-like growth factor-I levels regulate colon cancer growth and metastasis. *Cancer research* **2002**, *62*, 1030–1035.
- (45) Syed, V. TGF- β Signaling in Cancer. *Journal of cellular biochemistry* **2016**, *117*.
- (46) Siegfried, G.; Basak, A.; Cromlish, J. A.; Benjannet, S.; Marcinkiewicz, J.; Chrétien, M.; Seidah, N. G.; Khatib, A.-M. The secretory proprotein convertases furin, PC5, and PC7 activate VEGF-C to induce tumorigenesis. *The Journal of clinical investigation* **2003**, *111*, 1723–1732.
- (47) Bassi, D. E.; Lopez De Cicco, R; Mahloogi, H.; Zucker, S.; Thomas, G.; Klein-Szanto, A. J. Furin inhibition results in absent or decreased invasiveness and tumorigenicity of human cancer cells. *Proc Natl Acad Sci U S A* **2001**, *98*, 10326–10331.
- (48) Sounni, N. E.; Devy, L.; Hajitou, A.; Frankenne, F.; Munaut, C.; Gilles, C.; Deroanne, C.; Thompson, E. W.; Foidart, J. M.; Noel, A. MT1-MMP expression promotes tumor growth and angiogenesis through an up-regulation of vascular endothelial growth factor expression. *FASEB J* **2002**, *16*, 555–564.
- (49) Yakala, G. K.; Cabrera-Fuentes, H. A.; Crespo-Avilan, G. E.; Rattanasopa, C.; Burlacu, A.; George, B. L.; Anand, K.; Mayan, D. C.; Corliano, M.; Hernández-Reséndiz, S.; *et al.* FURIN Inhibition Reduces Vascular Remodeling and Atherosclerotic Lesion Progression in Mice. *Arteriosclerosis, thrombosis, and vascular biology* **2019**, *39*, 387–401.
- (50) Lin, H.; Ah Kioon, M.-D.; Lalou, C.; Larghero, J.; Launay, J.-M.; Khatib, A.-M.; Cohen-Solal, M. Protective role of systemic furin in immune response-induced arthritis. *Arthritis and rheumatism* **2012**, *64*, 2878–2886.
- (51) Levesque, C.; Couture, F.; Kwiatkowska, A.; Desjardins, R.; Guérin, B.; Neugebauer, W. A.; Day, R. PACE4 inhibitors and their peptidomimetic analogs block prostate cancer tumor progression through quiescence induction, increased apoptosis and impaired neovascularisation. *Oncotarget* **2015**, *6*, 3680–3693.
- (52) Panet, F.; Couture, F.; Kwiatkowska, A.; Desjardins, R.; Guérin, B.; Day, R. PACE4 is an important driver of ZR-75-1 estrogen receptor-positive breast cancer proliferation and tumor progression. *European journal of cell biology* **2017**, *96*, 469–475.
- (53) Gordon, V. M.; Leppla, S. H. Proteolytic activation of bacterial toxins: role of bacterial and host cell proteases. *Infect Immun* **1994**, *62*, 333–340.

- (54) Koehler, T. M. Bacillus anthracis Physiology and Genetics. *Molecular aspects of medicine* **2009**, *30*, 386–396.
- (55) Hoskisson, P. A. Microbe Profile: Corynebacterium diphtheriae - an old foe always ready to seize opportunity. *Microbiology (Reading, England)* **2018**, *164*, 865–867.
- (56) Zhu, Q.; Li, L.; Guo, Z.; Yang, R. Identification of Shiga-like toxin Escherichia coli isolated from children with diarrhea by polymerase chain reaction. *Chinese medical journal* **2002**, *115*, 815–818.
- (57) Hallenberger, S.; Bosch, V.; Angliker, H.; Shaw, E.; Klenk, H. D.; Garten, W. Inhibition of furin-mediated cleavage activation of HIV-1 glycoprotein gp160. *Nature* **1992**, *360*, 358–361.
- (58) Becker, G. L.; Lu, Y.; Harges, K.; Strehlow, B.; Levesque, C.; Lindberg, I.; Sandvig, K.; Bakowsky, U.; Day, R.; Garten, W.; *et al.* Highly potent inhibitors of proprotein convertase furin as potential drugs for treatment of infectious diseases. *J Biol Chem.* **2012**, *287*, 21992–22003.
- (59) Waxham, M.N.; Server, A. C.; Goodman, H. M.; Wolinsky, J. S. Cloning and sequencing of the mumps virus fusion protein gene. *Virology* **1987**, *159*, 381–388.
- (60) Richardson, C.; Hull, D.; Greer, P.; Hasel, K.; Berkovich, A.; Englund, G.; Bellini, W.; Rima, B.; Lazzarini, R. The nucleotide sequence of the mRNA encoding the fusion protein of measles virus (Edmonston strain): A comparison of fusion proteins from several different paramyxoviruses. *Virology* **1986**, *155*, 508–523.
- (61) Hu, B.; Guo, H.; Zhou, P.; Shi, Z. L. Characteristics of SARS-CoV-2 and COVID-19. *Nature reviews. Microbiology* **2021**, *19*.
- (62) Virology: Coronaviruses. *Nature* **1968**, *220*, 650.
- (63) Tyrrell, D. A.; Almeida, J. D.; Cunningham, C. H.; Dowdle, W. R.; Hofstad, M. S.; McIntosh, K.; Tajima, M.; Zakstelskaya, L. Y.; Easterday, B. C.; Kapikian, A.; *et al.* Coronaviridae. *Intervirology* **1975**, *5*, 76–82.
- (64) Shereen, M. A.; Khan, S.; Kazmi, A.; Bashir, N.; Siddique, R. COVID-19 infection: Origin, transmission, and characteristics of human coronaviruses. *Journal of advanced research* **2020**, *24*, 91–98.
- (65) Cheever, F. S.; Daniels, J. B.; Pappenheimer, A. M.; Bailey, O. T. A Murine Virus (JHM) causing disseminated encephalomyelitis with extensive destruction of myelin: I. Isolation and biological properties of the virus. *The Journal of Experimental Medicine* **1949**, *90*, 181–194.
- (66) Chan, J. F.-W.; Kok, K.-H.; Zhu, Z.; Chu, H.; To, K. K.-W.; Yuan, S.; Yuen, K.-Y. Genomic characterization of the 2019 novel human-pathogenic coronavirus isolated from a patient with atypical pneumonia after visiting Wuhan. *Emerging microbes & infections* **2020**, *9*, 221–236.
- (67) Zhong, N. S.; Zheng, B. J.; Li, Y. M.; Poon, L. L.M.; Xie, Z. H.; Chan, K. H.; Li, P. H.; Tan, S. Y.; Chang, Q.; Xie, J. P.; *et al.* Epidemiology and cause of severe acute respiratory syndrome

- (SARS) in Guangdong, People's Republic of China, in February, 2003. *The Lancet* **2003**, *362*, 1353–1358.
- (68) Drosten, C.; Günther, S.; Preiser, W.; van der Werf, S.; Brodt, H.-R.; Becker, S.; Rabenau, H.; Panning, M.; Kolesnikova, L.; Fouchier, R. A. M.; *et al.* Identification of a novel coronavirus in patients with severe acute respiratory syndrome. *The New England journal of medicine* **2003**, *348*, 1967–1976.
- (69) Am Zaki; van, B. S.; Bestebroer, T. M.; Osterhaus, A. D.; Fouchier, R. A. Isolation of a novel coronavirus from a man with pneumonia in Saudi Arabia. *The New England journal of medicine* **2012**, *367*.
- (70) Petrosillo, N.; Viceconte, G.; Ergonul, O.; Ippolito, G.; Petersen, E. COVID-19, SARS and MERS: are they closely related? *Clinical microbiology and infection : the official publication of the European Society of Clinical Microbiology and Infectious Diseases* **2020**, *26*, 729–734.
- (71) Pillaiyar, T.; Wendt, L. L.; Manickam, M.; Easwaran, M. The recent outbreaks of human coronaviruses: A medicinal chemistry perspective. *Med Res Rev* **2021**, *41*, 72–135.
- (72) Docea, A. O.; Tsatsakis, A.; Albulescu, D.; Cristea, O.; Zlatian, O.; Vinceti, M.; Moschos, S. A.; Tsoukalas, D.; Goumenou, M.; Drakoulis, N.; *et al.* A new threat from an old enemy: Re-emergence of coronavirus (Review). *International Journal of Molecular Medicine* **2020**, *45*, 1631–1643.
- (73) Bchetnia, M.; Girard, C.; Duchaine, C.; Laprise, C. The outbreak of the novel severe acute respiratory syndrome coronavirus 2 (SARS-CoV-2): A review of the current global status. *Journal of infection and public health* **2020**, *13*, 1601–1610.
- (74) Ali, M. J.; Hanif, M.; Haider, M. A.; Ahmed, M. U.; Sundas, F.; Hirani, A.; Khan, I. A.; Anis, K.; Karim, A. H. Treatment Options for COVID-19: A Review. *Frontiers in medicine* **2020**, *7*, 480.
- (75) Wang, M.; Cao, R.; Zhang, L.; Yang, X.; Liu, J.; Xu, M.; Shi, Z.; Hu, Z.; Zhong, W.; Xiao, G. Remdesivir and chloroquine effectively inhibit the recently emerged novel coronavirus (2019-nCoV) in vitro. *Cell research* **2020**, *30*.
- (76) Coutard, B.; Valle, C.; Lamballerie, X. de; Canard, B.; Seidah, N. G.; Decroly, E. The spike glycoprotein of the new coronavirus 2019-nCoV contains a furin-like cleavage site absent in CoV of the same clade. *Antiviral research* **2020**, *176*, 104742.
- (77) Chen, Y.; Guo, Y.; Pan, Y.; Zhao, Z. J. Structure analysis of the receptor binding of 2019-nCoV. *Biochem Biophys Res Commun* [Online early access]. DOI: 10.1016/j.bbrc.2020.02.071. Published Online: Feb. 17, 2020.
- (78) Dorothea Bestle; Miriam Ruth Heindl; Hannah Limburg; Thuy Van Lam van; Oliver Pilgram; Hong Moulton; David A Stein; Kornelia Harges; Markus Eickmann; Olga Dolnik; *et al.* TMPRSS2 and furin are both essential for proteolytic activation of SARS-CoV-2 in human airway cells. *Life Science Alliance* **2020**, *3*.

- (79) Zhou, P.; Yang, X.-L.; Wang, X.-G.; Hu, B.; Zhang, L.; Zhang, W.; Si, H.-R.; Zhu, Y.; Li, B.; Huang, C.-L.; *et al.* A pneumonia outbreak associated with a new coronavirus of probable bat origin. *Nature* **2020**, *579*, 270–273.
- (80) Lu, R.; Zhao, X.; Li, J.; Niu, P.; Yang, B.; Wu, H.; Wang, W.; Song, H.; Huang, B.; Zhu, N.; *et al.* Genomic characterisation and epidemiology of 2019 novel coronavirus: implications for virus origins and receptor binding. *The Lancet* **2020**, *395*, 565–574.
- (81) Zhu, N.; Zhang, D.; Wang, W.; Li, X.; Yang, B.; Song, J.; Zhao, X.; Huang, B.; Shi, W.; Lu, R.; *et al.* A Novel Coronavirus from Patients with Pneumonia in China, 2019. *The New England journal of medicine* **2020**, *382*, 727–733.
- (82) Kim, D.; Lee, J.-Y.; Yang, J.-S.; Kim, J. W.; Kim, V. N.; Chang, H. The Architecture of SARS-CoV-2 Transcriptome. *Cell* **2020**, *181*, 914-921.e10.
- (83) Hartenian, E.; Nandakumar, D.; Lari, A.; Ly, M.; Tucker, J. M.; Glaunsinger, B. A. The molecular virology of coronaviruses. *J Biol Chem* **2020**, *295*, 12910–12934.
- (84) Bahrami, A.; Ferns, G. A. Genetic and pathogenic characterization of SARS-CoV-2: a review. *Future Virology* [Online early access]. DOI: 10.2217/fvl-2020-0129.
- (85) Fehr, A. R.; Perlman, S. Coronaviruses: an overview of their replication and pathogenesis. *Methods in molecular biology (Clifton, N.J.)* **2015**, *1282*, 1–23.
- (86) Robson, B. COVID-19 Coronavirus spike protein analysis for synthetic vaccines, a peptidomimetic antagonist, and therapeutic drugs, and analysis of a proposed achilles' heel conserved region to minimize probability of escape mutations and drug resistance. *Computers in Biology and Medicine* **2020**, *121*, 103749.
- (87) Schoeman, D.; Fielding, B. C. Coronavirus envelope protein: current knowledge. *Virology journal* **2019**, *16*, 69.
- (88) Tai, W.; He, L.; Zhang, X.; Pu, J.; Voronin, D.; Jiang, S.; Zhou, Y.; Du, L. Characterization of the receptor-binding domain (RBD) of 2019 novel coronavirus: implication for development of RBD protein as a viral attachment inhibitor and vaccine. *Cellular and Molecular Immunology* **2020**, 1–8.
- (89) V'kovski, P.; Kratzel, A.; Steiner, S.; Stalder, H.; Thiel, V. Coronavirus biology and replication: implications for SARS-CoV-2. *Nature reviews. Microbiology* **2021**, *19*, 155–170.
- (90) Chen, Y.; Liu, Q.; Guo, D. Emerging coronaviruses: Genome structure, replication, and pathogenesis. *Journal of medical virology* **2020**, *92*, 418–423.
- (91) Sawicki, S. G.; Sawicki, D. L. A new model for coronavirus transcription. *Advances in experimental medicine and biology* **1998**, *440*, 215–219.
- (92) Alanagreh, L.'a.; Alzoughool, F.; Atoum, M. The Human Coronavirus Disease COVID-19: Its Origin, Characteristics, and Insights into Potential Drugs and Its Mechanisms. *Pathogens (Basel, Switzerland)* **2020**, *9*.

- (93) Benton, D. J.; Wrobel, A. G.; Xu, P.; Roustan, C.; Martin, S. R.; Rosenthal, P. B.; Skehel, J. J.; Gamblin, S. J. Receptor binding and priming of the spike protein of SARS-CoV-2 for membrane fusion. *Nature* **2020**, *588*, 327–330.
- (94) Xia, S.; Lan, Q.; Su, S.; Wang, X.; Xu, W.; Liu, Z.; Zhu, Y.; Wang, Q.; Lu, L.; Jiang, S. The role of furin cleavage site in SARS-CoV-2 spike protein-mediated membrane fusion in the presence or absence of trypsin. *Signal transduction and targeted therapy* **2020**, *5*, 92.
- (95) Walls, A. C.; Park, Y.-J.; Tortorici, M. A.; Wall, A.; McGuire, A. T.; Velesler, D. Structure, Function, and Antigenicity of the SARS-CoV-2 Spike Glycoprotein. *Cell* **2020**, *181*, 281-292.e6.
- (96) Tang, T.; Bidon, M.; Jaimes, J. A.; Whittaker, G. R.; Daniel, S. Coronavirus membrane fusion mechanism offers a potential target for antiviral development. *Antiviral research* **2020**, *178*, 104792.
- (97) Ou, X.; Liu, Y.; Lei, X.; Li, P.; Mi, D.; Ren, L.; Guo, L.; Guo, R.; Chen, T.; Hu, J.; *et al.* Characterization of spike glycoprotein of SARS-CoV-2 on virus entry and its immune cross-reactivity with SARS-CoV. *Nature communications* **2020**, *11*, 1620.
- (98) Bosch, B. J.; van der Zee, R.; Haan, C. A. M. de; Rottier, P. J. M. The coronavirus spike protein is a class I virus fusion protein: structural and functional characterization of the fusion core complex. *J Virol* **2003**, *77*, 8801–8811.
- (99) Wrapp, D.; Wang, N.; Corbett, K. S.; Goldsmith, J. A.; Hsieh, C.-L.; Abiona, O.; Graham, B. S.; McLellan, J. S. Cryo-EM structure of the 2019-nCoV spike in the prefusion conformation. *Science (New York, N.Y.)* **2020**, *367*, 1260–1263.
- (100) Anderson, E. D.; Thomas, L.; Hayflick, J. S.; Thomas, G. Inhibition of HIV-1 gp160-dependent membrane fusion by a furin-directed alpha 1-antitrypsin variant. *J Biol Chem* **1993**, *268*, 24887–24891.
- (101) Basak, A.; Chen, A.; Scamuffa, N.; Mohottalage, D.; Basak, S.; Khatib, A.-M. Blockade of furin activity and furin-induced tumor cells malignant phenotypes by the chemically synthesized human furin prodomain. *Current medicinal chemistry* **2010**, *17*, 2214–2221.
- (102) Basak, A.; Lazure, C. Synthetic peptides derived from the prosegments of proprotein convertase 1/3 and furin are potent inhibitors of both enzymes. *Biochem J* **2003**, *373*, 231–239.
- (103) Garten, W.; Stieneke, A.; Shaw, E.; Wikstrom, P.; Klenk, H. D. Inhibition of proteolytic activation of influenza virus hemagglutinin by specific peptidyl chloroalkyl ketones. *Virology* **1989**, *172*, 25–31.
- (104) Basak, A.; Cooper, S.; Roberge, A. G.; Banik, U. K.; Chrétien, M.; Seidah, N. G. Inhibition of proprotein convertases-1, -7 and furin by diterpines of *Andrographis paniculata* and their succinoyl esters. *Biochem J* **1999**, *338*, 107–113.
- (105) Lu, W.; Zhang, W.; Molloy, S. S.; Thomas, G.; Ryan, K.; Chiang, Y.; Anderson, S.; Laskowski, M. Arg15-Lys17-Arg18 turkey ovomucoid third domain inhibits human furin. *J Biol Chem* **1993**, *268*, 14583–14585.

- (106) Cameron, A.; Appel, J.; Houghten, R. A.; Lindberg, I. Polyarginines are potent furin inhibitors. *J Biol Chem* **2000**, *275*, 36741–36749.
- (107) Angliker, H. Synthesis of tight binding inhibitors and their action on the proprotein-processing enzyme furin. *J Med Chem* **1995**, *38*, 4014–4018.
- (108) Podsiadlo, P.; Komiyama, T.; Fuller, R. S.; Blum, O. Furin inhibition by compounds of copper and zinc. *J Biol Chem* **2004**, *279*, 36219–36227.
- (109) Zhi-xue Liu; Hao Fei; Cheng-wu Chi. Two engineered eglin c mutants potently and selectively inhibiting kexin or furin. *FEBS Letters* **2004**, *556*, 116–120.
- (110) Basak, A.; Khatib, A.-M.; Mohottalage, D.; Basak, S.; Kolajova, M.; Bag, S. S.; Basak, A. A novel enediynyl peptide inhibitor of furin that blocks processing of proPDGF-A, B and proVEGF-C. *PloS one* **2009**, *4*, e7700.
- (111) Komiyama, T.; Coppola, J. M.; Larsen, M. J.; van Dort, M. E.; Ross, B. D.; Day, R.; Rehemtulla, A.; Fuller, R. S. Inhibition of furin/proprotein convertase-catalyzed surface and intracellular processing by small molecules. *J Biol Chem* **2009**, *284*, 15729–15738.
- (112) Opal, S. M.; Artenstein, A. W.; Cristofaro, P. A.; Jhung, J. W.; Palardy, J. E.; Parejo, N. A.; Lim, Y.-P. Inter-alpha-inhibitor proteins are endogenous furin inhibitors and provide protection against experimental anthrax intoxication. *Infect Immun* **2005**, *73*, 5101–5105.
- (113) Lewandowska-Goch, M. A.; Kwiatkowska, A.; Łeppek, T.; Ly, K.; Navals, P.; Gagnon, H.; Dory, Y. L.; Prahl, A.; Day, R. Design and Structure-Activity Relationship of a Potent Furin Inhibitor Derived from Influenza Hemagglutinin. *ACS Medicinal Chemistry Letters* **2021**, *12*, 365–372.
- (114) Ramos-Molina, B.; Lick, A. N.; Nasrolahi Shirazi, A.; Oh, D.; Tiwari, R.; El-Sayed, N. S.; Parang, K.; Lindberg, I. Cationic Cell-Penetrating Peptides Are Potent Furin Inhibitors. *PloS one* **2015**, *10*, e0130417.
- (115) Coppola, J. M.; Bhojani, M. S.; Ross, B. D.; Rehemtulla, A. A small-molecule furin inhibitor inhibits cancer cell motility and invasiveness. *Neoplasia (New York, N.Y.)* **2008**, *10*, 363–370.
- (116) van Rompaey, L.; Ayoubi, T.; van de Ven, W.; Marynen, P. Inhibition of intracellular proteolytic processing of soluble proproteins by an engineered alpha 2-macroglobulin containing a furin recognition sequence in the bait region. *Biochem J* **1997**, *326 (Pt 2)*, 507–514.
- (117) Gagnon, H.; Beauchemin, S.; Kwiatkowska, A.; Couture, F.; D'Anjou, F.; Levesque, C.; Dufour, F.; Desbiens, A. R.; Vaillancourt, R.; Bernard, S.; *et al.* Optimization of furin inhibitors to protect against the activation of influenza hemagglutinin H5 and Shiga toxin. *J Med Chem* **2014**, *57*, 29–41.
- (118) Jiao, G.-S.; Cregar, L.; Wang, J.; Millis, S. Z.; Tang, C.; O'Malley, S.; Johnson, A. T.; Sareth, S.; Larson, J.; Thomas, G. Synthetic small molecule furin inhibitors derived from 2,5-dideoxystreptamine. *Proc Natl Acad Sci U S A* **2006**, *103*, 19707–19712.

- (119) Dahlen, J. R.; Jean, F.; Thomas, G.; Foster, D. C.; Kisiel, W. Inhibition of soluble recombinant furin by human proteinase inhibitor 8. *J Biol Chem* **1998**, *273*, 1851–1854.
- (120) Becker, G. L.; Sielaff, F.; Than, M. E.; Lindberg, I.; Routhier, S.; Day, R.; Lu, Y.; Garten, W.; Steinmetzer, T. Potent inhibitors of furin and furin-like proprotein convertases containing decarboxylated P1 arginine mimetics. *J Med Chem* **2010**, *53*, 1067–1075.
- (121) Harges, K.; Becker, G. L.; Lu, Y.; Dahms, S. O.; Kohler, S.; Beyer, W.; Sandvig, K.; Yamamoto, H.; Lindberg, I.; Walz, L.; *et al.* Novel Furin Inhibitors with Potent Anti-infectious Activity. *ChemMedChem* **2015**, *10*, 1218–1231.
- (122) Harges, K.; Ivanova, T.; Thaa, B.; McInerney, G. M.; Klock, T. I.; Sandvig, K.; Künzel, S.; Lindberg, I.; Steinmetzer, T. Elongated and Shortened Peptidomimetic Inhibitors of the Proprotein Convertase Furin. *ChemMedChem* **2017**, *12*, 613–620.
- (123) Sielaff, F.; Than, M. E.; Bevec, D.; Lindberg, I.; Steinmetzer, T. New furin inhibitors based on weakly basic amidinohydrazones. *Bioorg Med Chem Lett* **2011**, *21*, 836–840.
- (124) Zhu, J.; Declercq, J.; Roucourt, B.; Ghassabeh, G. H.; Meulemans, S.; Kinne, J.; David, G.; Vermorken, Alphons J M; Van de Ven, Wim J M; Lindberg, I.; *et al.* Generation and characterization of non-competitive furin-inhibiting nanobodies. *Biochem J* **2012**, *448*, 73–82.
- (125) Wu, C.; Zheng, M.; Yang, Y.; Gu, X.; Yang, K.; Li, M.; Liu, Y.; Zhang, Q.; Zhang, P.; Wang, Y.; *et al.* Furin: A Potential Therapeutic Target for COVID-19. *iScience* **2020**, *23*, 101642.
- (126) Henrich, S.; Cameron, A.; Bourenkov, G. P.; Kiefersauer, R.; Huber, R.; Lindberg, I.; Bode, W.; Than, M. E. The crystal structure of the proprotein processing proteinase furin explains its stringent specificity. *Nature structural biology* **2003**, *10*, 520–526.
- (127) Kaiser, B.; Hauptmann, J. Pharmacology of Synthetic Thrombin Inhibitors of the Tripeptide Type. *Cardiovasc Drug Reviews* **1992**, *10*, 71–87.
- (128) Becker, G. L.; Harges, K.; Steinmetzer, T. New substrate analogue furin inhibitors derived from 4-amidinobenzylamide. *Bioorg Med Chem Lett* **2011**, *21*, 4695–4697.
- (129) Dahms, S. O.; Arciniega, M.; Steinmetzer, T.; Huber, R.; Than, M. E. Structure of the unliganded form of the proprotein convertase furin suggests activation by a substrate-induced mechanism. *Proc Natl Acad Sci U S A* **2016**, *113*, 11196–11201.
- (130) Kacprzak, M. M.; Peinado, J. R.; Than, M. E.; Appel, J.; Henrich, S.; Lipkind, G.; Houghten, R. A.; Bode, W.; Lindberg, I. Inhibition of furin by polyarginine-containing peptides: nanomolar inhibition by nona-D-arginine. *The Journal of biological chemistry* **2004**, *279*, 36788–36794.
- (131) Dahms, S. O.; Harges, K.; Steinmetzer, T.; Than, M. E. X-ray Structures of the Proprotein Convertase Furin Bound with Substrate Analogue Inhibitors Reveal Substrate Specificity Determinants beyond the S4 Pocket. *Biochemistry* **2018**, *57*, 925–934.
- (132) van Lam van, T.; Ivanova, T.; Harges, K.; Heindl, M. R.; Morty, R. E.; Böttcher-Friebertshäuser, E.; Lindberg, I.; Than, M. E.; Dahms, S. O.; Steinmetzer, T. Design, Synthesis,

- and Characterization of Macrocyclic Inhibitors of the Proprotein Convertase Furin. *ChemMedChem* **2019**, *14*, 673–685.
- (133) Dahms, S. O.; Jiao, G.-S.; Than, M. E. Structural Studies Revealed Active Site Distortions of Human Furin by a Small Molecule Inhibitor. *ACS Chem Biol* **2017**, *12*, 1211–1216.
- (134) Ivanova, T.; Harges, K.; Kallis, S.; Dahms, S. O.; Than, M. E.; Künzel, S.; Böttcher-Friebertshäuser, E.; Lindberg, I.; Jiao, G.-S.; Bartenschlager, R.; *et al.* Optimization of Substrate-Analogue Furin Inhibitors. *ChemMedChem* **2017**, *12*, 1953–1968.
- (135) Łepeck, T.; Kwiatkowska, A.; Couture, F.; Ly, K.; Desjardins, R.; Dory, Y.; Prahl, A.; Day, R. Macrocyclization of a potent PACE4 inhibitor: Benefits and limitations. *European journal of cell biology* **2017**, *96*, 476–485.
- (136) Fittler, H.; Depp, A.; Avrutina, O.; Dahms, S. O.; Than, M. E.; Empting, M.; Kolmar, H. Engineering a Constrained Peptidic Scaffold towards Potent and Selective Furin Inhibitors. *Chembiochem : a European journal of chemical biology* **2015**, *16*, 2441–2444.
- (137) Fosgerau, K.; Hoffmann, T. Peptide therapeutics: current status and future directions. *Drug discovery today* **2015**, *20*.
- (138) Lau, J. L.; Dunn, M. K. Therapeutic peptides: Historical perspectives, current development trends, and future directions. *Bioorganic & medicinal chemistry* **2018**, *26*, 2700–2707.
- (139) Leuw, P. de; Stephan, C. Protease inhibitor therapy for hepatitis C virus-infection. *Expert opinion on pharmacotherapy* **2018**, *19*, 577–587.
- (140) Qian, Z.; Liu, T.; Liu, Y.-Y.; Briesewitz, R.; Barrios, A. M.; Jhiang, S. M.; Pei, D. Efficient delivery of cyclic peptides into mammalian cells with short sequence motifs. *ACS Chem Biol* **2013**, *8*, 423–431.
- (141) Lian, W.; Jiang, B.; Qian, Z.; Pei, D. Cell-permeable bicyclic peptide inhibitors against intracellular proteins. *J. Am. Chem. Soc.* **2014**, *136*, 9830–9833.
- (142) Lu, Y.; Harges, K.; Dahms, S. O.; Böttcher-Friebertshäuser, E.; Steinmetzer, T.; Than, M. E.; Klenk, H.-D.; Garten, W. Peptidomimetic furin inhibitor MI-701 in combination with oseltamivir and ribavirin efficiently blocks propagation of highly pathogenic avian influenza viruses and delays high level oseltamivir resistance in MDCK cells. *Antiviral research* **2015**, *120*, 89–100.
- (143) Krüger, N.; Sauder, C.; Hüttel, S.; Papies, J.; Voigt, K.; Herrler, G.; Harges, K.; Steinmetzer, T.; Örvell, C.; Drexler, J. F.; *et al.* Entry, Replication, Immune Evasion, and Neurotoxicity of Synthetically Engineered Bat-Borne Mumps Virus. *Cell reports* **2018**, *25*.
- (144) Kaiser, B.; Hauptmann, J.; Markwardt, F. Untersuchungen zur Pharmakodynamik synthetischer Thrombininhibitoren vom Typ basisch substituierter N alpha-arylsulfonylierter Phenylalaninamide. *Pharmazie* **1987**, *42*, 119–121.
- (145) Peternel, L.; Stempelj, M.; Cerne, M.; Zega, A.; Obreza, A.; Oblak, M.; Drevensek, G.; Budihna, M. V.; Stanovnik, L.; Urleb, U. Direct thrombin inhibitors built on the

azaphenylalanine scaffold provoke degranulation of mast cells. *Thrombosis and haemostasis* **2006**, *95*, 294–300.

(146) ARONOV, A. Predictive in silico modeling for hERG channel blockers. *Drug discovery today* **2005**, *10*, 149–155.

(147) Wang, H.; Wang, H. S.; Liu, Z. P. Agents that induce pseudo-allergic reaction. *Drug discoveries & therapeutics* **2011**, *5*, 211–219.

(148) Kwiatkowska, A.; Couture, F.; Levesque, C.; Ly, K.; Beauchemin, S.; Desjardins, R.; Neugebauer, W.; Dory, Y. L.; Day, R. Novel Insights into Structure-Activity Relationships of N-Terminally Modified PACE4 Inhibitors. *ChemMedChem* **2016**, *11*, 289–301.

(149) Henneke, I.; Greschus, S.; Savai, R.; Korfei, M.; Markart, P.; Mahavadi, P.; Schermuly, R. T.; Wygrecka, M.; Stürzebecher, J.; Seeger, W.; *et al.* Inhibition of urokinase activity reduces primary tumor growth and metastasis formation in a murine lung carcinoma model. *American journal of respiratory and critical care medicine* **2010**, *181*, 611–619.

(150) Boyar, A.; Marsh, R. E. l-Canavanine, a paradigm for the structures of substituted guanidines. *J. Am. Chem. Soc.* **1982**, *104*, 1995–1998.

(151) Morrison, J. F. Kinetics of the reversible inhibition of enzyme-catalysed reactions by tight-binding inhibitors. *Biochimica et Biophysica Acta (BBA) - Enzymology* **1969**, *185*, 269–286.

(152) Klenk, H. D.; Garten, W. Host cell proteases controlling virus pathogenicity. *Trends in microbiology* **1994**, *2*, 39–43.

(153) Garten, W. Characterization of Proprotein Convertases and Their Involvement in Virus Propagation. In *Activation of Viruses by Host Proteases*; Böttcher-Friebertshäuser, E., Garten, W., Klenk, H. D., Eds.; Springer International Publishing: Cham, 2018; pp 205–248.

(154) Hoffmann, M.; Kleine-Weber, H.; Schroeder, S.; Krüger, N.; Herrler, T.; Erichsen, S.; Schiergens, T. S.; Herrler, G.; Wu, N.-H.; Nitsche, A.; *et al.* SARS-CoV-2 Cell Entry Depends on ACE2 and TMPRSS2 and Is Blocked by a Clinically Proven Protease Inhibitor. *Cell* **2020**, *181*, 271-280.e8.

(155) Matsuyama, S.; Nao, N.; Shirato, K.; Kawase, M.; Saito, S.; Takayama, I.; Nagata, N.; Sekizuka, T.; Katoh, H.; Kato, F.; *et al.* Enhanced isolation of SARS-CoV-2 by TMPRSS2-expressing cells. *Proc Natl Acad Sci U S A* **2020**, *117*, 7001–7003.

(156) Cheng, J.; Zhao, Y.; Xu, G.; Zhang, K.; Jia, W.; Sun, Y.; Zhao, J.; Xue, J.; Hu, Y.; Zhang, G. The S2 Subunit of QX-type Infectious Bronchitis Coronavirus Spike Protein Is an Essential Determinant of Neurotropism. *Viruses* **2019**, *11*.

(157) Koshland, D. E. The application and usefulness of the ratio $k(\text{cat})/K(\text{M})$. *Bioorganic chemistry* **2002**, *30*, 211–213.

(158) Copeland, R. A. *Evaluation of Enzyme Inhibitors in Drug Discovery*; Wiley, 2013.

(159) Ivanova, T. *A contribution to the inhibition of the proprotein convertase furin*. Dissertation - Philipps University Marburg, 2017.

(160) Yu, B.; Hunt, J. F. Enzymological and structural studies of the mechanism of promiscuous substrate recognition by the oxidative DNA repair enzyme AlkB. *Proc Natl Acad Sci U S A* **2009**, *106*, 14315–14320.

7 Statutory declaration

Ich, Thuy Van Lam van, versichere, dass ich meine Dissertation:

“Development of enhanced furin inhibitors with reduced toxicity as potential broad spectrum antiviral drugs”

selbstständig, ohne unerlaubte Hilfe angefertigt und mich dabei bei keiner anderen als der von mir ausdrücklich bezeichneten Quellen bedient habe. Alle vollständig oder sinngemäß übernommenen Zitate sind als solche gekennzeichnet.

Die Dissertation wurde in der jetzigen oder ähnlichen Form noch bei keiner anderen Hochschule eingereicht und hat noch keinen sonstigen Prüfungszwecken gedient.

Marburg, den

.....
Thuy Van Lam van

8 Acknowledgment

For the successful completion of this dissertation, which would be impossible without support from various people, my special thanks go to all who encouraged me during my PhD:

First of all, I want to express my greatest appreciation towards my supervisor Professor Dr. Torsten Steinmetzer for welcoming me in his team and giving me the opportunity to work on this project. Thanks for his excellent support, valuable advice, and guidance during this time. At any time, his door was open for me. Even during tough times, we could always find a solution to any problem together. I appreciate this very much - thank you! Likewise, the many fun Betriebsausflüge, especially skiing in Hirschegg, conferences (especially Jena), as well as the selbstgepflückte-Steinpilze-dinner will be remembered forever.

I am very grateful to Professor Dr. Eva Friebertshäuser for the outstanding collaboration during almost the entire period of my doctoral thesis and for her work as second referee and examiner. I would also like to take this opportunity to thank the whole working group of AG Friebertshäuser for the good working during our collaboration.

I owe a deep sense of gratitude to Dr. Kornelia Harges for her tireless extraordinary help and support. From the beginning, I enjoyed this great collaboration, and I am deeply grateful for all that I was able to learn from her. Without you this thesis would not have been possible- Thank you!

A debt of gratitude is also owed to Dr. Teodora Ivanova for the great time we spent together at work as well as privately. She was also a great support for me and could help and show me so much with her expertise. Thank you, Teodora!

My great thanks to Dr. Sven Dahms for determining the crystal structures of my inhibitors in complex with furin and for very interesting discussions, both in person and via Webex meetings.

I would like to especially thank Benjamin Wenzel, Oliver Pilgram, Simon Wiedemeyer, Heike Lang-Henkel, Dorothee Rogge, and Fabian Schneider for their help with synthesis and numerous practical tasks, and Simon Huber for his support with computer chemistry.

Another thanks goes to Stefan Newel for recording the NMR spectra and helping with questions regarding their analysis. A big thank you goes to Nina Zitzer, Lena Ludwig-Radtke, and Rixa Kraut for recording the mass spectra. Especially I would like to thank Nina for the great time we spent together but also for all the personal talks and encouraging words from her.

I thank the whole former and present Erstsemester-Praktikumsassistenten-Gruppe, especially Dr. Armin Reichenberg, Matthäus Drabek, Simon Huber, and Rebecca Feyh for funny and memorable moments in "unten"-Lab with the "kids".

I would like to thank many other colleagues from the Department of Pharmacy who gave me insights into other research areas which allowed me to continuously learn and broaden my experience. For this, I thank AG Bakowsky, AG Klebe, AG Becker, and the former and present AG Steinmetzer.

I am extremely thankful to Dr. Teodora Ivanova and Raquel Reilly for their attentive and detailed proofreading of the thesis. Thanks a lot!

For the time towards the end of this thesis, I would like to say a special thank you to Simon Huber, Rebecca Feyh, Raquel Reilly, Nina Zitzer, and Dr. Stefan Merkel who had to put up with all my emotional outbursts but still always encouraged me – many thanks!

Personally, I thank all my friends outside of work. For the nice evenings during the week with the "Skatmädels", the great summer nights on the terrace with my best and longtime friends from Dortmund and from the pharmacy study time, quite a few hours at the Café Bohne with my "Bestie" as well as the exciting hours on the golf course with the "Golfpro-Crew".

A big thank you also goes out to the staff at Behring-, and Philipps-Apotheke for a great time over the last 9 years. I would especially like to mention and express my sincere thanks to Dr. Nan-Si Brass and Dr. Sascha Brass, who have always believed in me since the beginning of my pharmacy study and no matter what situation I was in, they always had an open ear for me.

I dedicate a thank you to the Hinder family for their constant encourage since the beginning and for giving me a second home here in Hessen.

From the bottom of my heart, I thank Lukas for his wholehearted support that I have been receiving day by day since 2012. In all phases of my life, you are my constant inspire as well as my calm pole in difficult times. Thank you for your patience, trust and especially your love that you give me.

Finally but importantly, I would like to acknowledge with gratitude, the unconditional love and unwavering support of my parents over the past 30 years. Without their encouragement and guidance throughout my life, I would not be where I am now – Thank you very much!

“Ăn trái nhớ kẻ trồng cây.”

When eating fruit, remember the one who planted the tree.

Vietnamese Proverb

9 Curriculum vitae

Personal Information

Surname / First Name: Thuy Van Lam van
Address: Wettergasse 36, 35037 Marburg
Mobil: +49 170 2250203
Date of birth: 21.09.1991
Place of birth: Dortmund, Germany
Nationality: German
Email: thuyvan@gmx.net

Work Experience

July 2017 – present **Pharmacist**
Behring Apotheke, Marburg

Education

August 2017 – present **Ph.D.**
Philipps University Marburg
Institute of Pharmaceutical Chemistry
Doctoral Thesis Title: “Development of enhanced furin
inhibitors with reduced toxicity as potential broad spectrum
antiviral drugs”
Supervisor: Prof. Dr. Torsten Steinmetzer

June 2017
(Graduation after practical year)
bent **Licensed Pharmacist**
Philipps University Marburg

April 2012 – April 2016 **Study Pharmacy**
Philipps University Marburg

October 2011 – March 2012 **Study Biology**
University Duisburg-Essen

2009-2011 **Abitur**
Mallinckrodt-Gymnasium Dortmund